UNIVERSITAT POLITÈCNICA DE VALÈNCIA

INSTITUTO INTERUNIVERSITARIO DE INVESTIGACIÓN DE RECONOCIMIENTO MOLECULAR Y DESARROLLO TECNOLÓGICO

Enzyme-functionalized hybrid mesoporous nanodevices for sensing, controlled release and molecular communication

PhD. THESIS

Submitted by

Antoni Llopis Lorente

PhD. Supervisors:

Prof. Ramón Martínez Máñez
Dr. Félix Sancenón Galarza

Valencia, January 2019

idm
Centro de Reconocimiento
Molecular y Desarrollo Tecnológico

UNIVERSITAT
POLITÈCNICA
DE VALÈNCIA

RAMÓN MARTÍNEZ MÁÑEZ, PhD in Chemistry and Professor at the *Universitat Politècnica de València*, and FÉLIX SANCENÓN GALARZA, PhD in Chemistry and Lecturer at the *Universitat Politècnica de València*.

CERTIFY:

That the work ***"Enzyme-functionalized hybrid mesoporous nanodevices for sensing, controlled release and molecular communication"*** has been developed by Antoni Llopis Lorente under their supervision in the Instituto Interuniversitario de Investigación de Reconocimiento Molecular y Desarrollo Tecnológico (IDM) of the *Universitat Politècnica de València*, as a Thesis Project in order to obtain the degree of PhD in Chemistry at the *Universitat Politècnica de València.*

Valencia, January 8th 2019.

Prof. Ramón Martínez Máñez Dr. Félix Sancenón Galarza

A mi familia,
por todo su apoyo y amor

“*En el fondo, los científicos somos gente con suerte: podemos jugar a lo que queramos durante toda la vida.*”

Lee Smolin

“*You must expect great things of yourself before you can do them.*”

“*I've failed over and over and over again in my life. And that is why I succeed.*”

Michael Jordan

“If I had six hours to cut down a tree, I’d spend the first four sharpening the saw.”

Abraham Lincoln

Acknowledgements

Agradecimientos

En primer lugar, me gustaría dar las gracias a mis directores de tesis, Ramón y Félix. A Ramón, por confiar en mí y darme la oportunidad de unirme a la familia del IDM. Por haber creado un grupo, un Instituto y una infraestructura de investigación en el que se han podido formar tantas personas a lo largo de los años. Sin duda, tu esfuerzo y dedicación son dignos de admirar. Gracias por tus consejos, por animarme a pensar y darme la oportunidad de desarrollar mis propias ideas.

A Félix, por estar siempre ahí, por tu ayuda y amabilidad, por tus consejos, por tus correcciones en tiempos récord para las que cualquiera se tiraría semanas, y por tu buena disponibilidad para solucionar cualquier trámite o papeleo. Gracias también en lo personal, tus visitas diarias al lab en las que charlar o bromear de cualquier cosa, por los buenos momentos fuera del lab, y por alguna cerveza que otra.

Gracias Reynaldo, por invitarme a hacer una estancia en tu laboratorio en Madrid, una estancia que ha contribuido enormemente a los resultados alcanzados en esta tesis. También gracias a la gente del lab de Reynaldo, por vuestra acogida, por enseñarme, y por el buen ambiente.

Thanks Daniela and all members of Wilson's group, for giving me the opportunity to do a stay in your lab, to work in an international environment, and to know the Dutch research system. I feel lucky for my time in the Netherlands, it was a wonderful experience.

Gracias Samuel, por el entusiasmo y energía que demuestras, y por tu interés en iniciar una colaboración juntos. Gracias a la gente del IBEC por vuestra amabilidad y buen trato.

Muchísimas gracias a todos mis compañeros y compañeras del laboratorio 2.6 y del IDM con los que he tenido la oportunidad de compartir estos años. Para los que ya estaban al inicio cuando entré, para los que entraron al principio, para los que fueron llegando, para todos los que vinieron de estancia, y para los más nuevos... muchas gracias!! Para Luis Enrique, Cris M., Lluís, Isabel, Kim, Irene, Núria, Patri, Ravi, Mar, Cris G., Àngela, María Moragues, Edgar, Cris T., Alba, Sameh, Carol, Elena, Loles, Erick, Alberto, Andrea Barba, Almudena, Carlos Fuenmayor, Carmen, Andrea Bernardos, Amelia, Santi, Lorena, Asha, Manoharan, Mirka, Joty, Mónica, Roberto, Ana Calvo, Anita, Luis Pla, Maria Elena, Luis Villaescusa, Alejandro, Bea Lozano, Nati, Adrián, Mónica, Elisa, Regina, Arianna, Andy, Tania, Hazem, Ismael, Bea de Luis, Xente, Eva G., Àngels, Marta, María A., Borja; Juanfran, Pablo, Eva B., Quique, Paula, Elena L., las principesas ... Y a los que me deje, sóis tantos que seguro que se me olvida más de uno. Me siento afortunado por haberos conocido y creo que es una de las mejores cosas de nuestro trabajo. Gracias por vuestra ayuda, y por los buenos momentos dentro y (mejores aún) fuera del lab. Al final, cada persona somos el resultado de las experiencias y las personas que nos encontramos en el camino, y vosotros habéis dejado huella en mí.

Gracias a mis amigos y a mis compañeros del club de basket y del pueblo, por las risas, los buenos momentos, y por ser una fuente de energía desde mucho antes que empezara la tesis.

Muchas gracias a mis padres, a mi hermano Jordi y a mi hermana Tere, por ser ese punto de apoyo que siempre está ahí y por todo vuestro respaldo durante estos años.

Gracias también a mis abuelos y demás familia.

Muchas gracias a Tania, porque la química nos unió y desde el primer momento hubo química entre nosotros y todo fluyó. Gracias por apoyarme y enterderme, por tus ánimos, por tu buen humor y tu forma de ser, por disfrutar conmigo de las pequeñas cosas de la vida y por completarme. También gracias a esa parte de la familia que tengo en Honduras.

Y aunque, probablemente no le llegué el mensaje, me gustaría dar las gracias a mi profesor Joan Pastor, por las clases de Física y Química en el Instituto de Carcaixent que me animaron para adentrarme en este mundo, así como a los buenos profesores que he tenido durante la carrera de Química en la Universidad de Valencia.

Resumen

La presente tesis doctoral titulada “Nanodispositivos mesoporosos híbridos funcionalizados con enzimas para detección, liberación controlada y comunicación molecular” se centra en el diseño, preparación, caracterización y evaluación de distintos nanodispositivos híbridos orgánico-inorgánicos utilizando como soporte nanopartículas tipo Janus de oro y sílice mesoporosa, que se equipan con enzimas, especies fluorescentes y puertas moleculares.

En el primer capítulo se introduce el marco en el que se engloban los estudios realizados donde se combinan distintas herramientas y conceptos relacionados con la nanotecnología, la química supramolecular, el campo de los materiales mesoporos y las puertas moleculares, así como partículas Janus y enzimas. A continuación, se presentan los objetivos generales que son abordados en los siguientes capítulos experimentales.

En el tercer capítulo se presenta un nanodispositivo para liberación controlada en respuesta al neurotransmisor acetilcolina. En concreto, se trata de nanopartículas Janus de oro-sílice mesoporosa funcionalizadas con la enzima acetilcolinesterasa en la parte del oro y con complejos supramoleculares de inclusión entre β-ciclodextrina y benzimidazol en la superfície de la sílice. El complejo supramolecular actúa como tapón o nanoválvula impidiendo la salida de la carga almacenada en el interio de la sílice. La liberación selectiva en respuesta a acetilcolina se produce debido a su hidrólisis mediadada por la enzima, lo cual produce ácido acético e induce la apertura de la nanoválvula por protonación del benzimidazol.

En el cuarto capítulo se presenta un sistema de liberación controlado enzimáticamente basado en la apertura de una puerta sensible a tioles utilizando como soporte nanopartículas Janus oro-sílice mesoporosa. En concreto, la parte mesoporosa está funcionazada con cadenas de oligo(etilen glicol) unidas mediante un puente disulfuro, mientras que la parte del oro se utiliza para pegar la enzima acetilcolinesterasa. Como par sustrato-enzima modelo se utiliza acetiltiocolina-acetilcolinesterasa, ya que en este caso la reacción enzimática produce tiocolina como especie que induce la apertura de la puerta molecular.

Asimismo, se demuestra que la unidad enzimática puede detectar la presencia de inhibidores y como resultado se obtiene una modulación de la liberación. Los estudios en células muestran que el dispositivo es biocompatible cuando está cargado con safranina O. Además, el nanodispotivo muestra una mayor eficiencia para liberar el citotóxico doxorubicina en células cancerosas en presencia de acetiltiocolina.

El quinto capítulo muestra un sistema de comunicación química entre dos nanopartículas Janus distintas que imita el modelo de comunicación interactiva. En concreto, la primera partícula ($S1_{gal}$) está funcionalizada con la enzima β-galactosidasa en la parte del oro, y la parte mesoporosa está cargada con un colorante y tapada con β-ciclodextrina unida a la sílice mediante puentes disulfuro. En el segundo tipo de nanopartícula ($S2_{gox}$), la parte mesoporosa está cargada con un agente reductor (*N*-acetil-L-cisteína) y tapada con una nanoválvula supramolecular (β-ciclodextrina:benzimidazol). El proceso de comunicación se dispara en presencia de lactosa. La lactosa es hidrolizada por la β-galactosidasa sobre la primera partícula ($S1_{gal}$) y la glucosa generada (primer mensajero químico) difunde hacia la segunda nanopartícula ($S2_{gox}$), donde la glucosa oxidasa la transforma en ácido glucónico. Esto resulta en la bajada local del pH, lo cual produce la apertura de la nanoválvula supramolecular y la liberación de *N*-acetil-L-cisteína (segundo mensajero químico), que difunde de vuelta hacia la primera nanopartícula ($S1_{gal}$). La *N*-acetil-L-cisteína induce la ruptura de los puentes disulfuro que tapan la parte mesoporosa de $S1_{gal}$ y esto resulta en la liberación del colorante encapsulado.

En el sexto capítulo se presenta el diseño de nanodispositivos capaces de leer la presencia simultánea de varias biomoléculas del ambiente y actuar mediante el procesamiento de funciones lógicas que resultan en la liberación programada de la carga. En concreto, se prepararon nanopartículas Janus de oro-sílice mesoporosa funcionalizadas con la enzima glucosa deshidrogenasa en la superficie del oro y nanoválvulas supramoleculares (β-ciclodextrina:benzimidazol) como puertas sobre la superficie de la sílice. El nanodispositivo actúa como una puerta lógica AND y es capaz de leer la presencia simultánea de glucosa y NAD^+ para disparar la liberación de la carga. Además, se muestra que se pueden

coinmovilizar glucosa deshidrogenasa y la enzima ureasa para imitar la función lógica INHIBIT, de forma que la función AND se deshabilita en presencia de urea. Finalmente, se muestra que estas nanopartículas pueden liberar un fàrmaco citotóxico en células cancerosas tras detectar la presencia simultánea de glucosa y NAD^+ intracelular.

En el séptimo capítulo, se propone una nueva aproximación para el diseño de nanosensores ópticos basados en el desanclaje mediado enzimáticamente de especies indicadoras. Como prueba de concepto, se presenta un nanosensor para la detección de urea basado en el desanclaje de un oligonucléotido fluorescente desde nanopartículas Janus de oro-sílice mesoporosa. En concreto, las nanopartículas se funcionalizan sobre la sílice con grupos amino (cargados positivamente a pH neutro) a los cuáles se pega el oligonucleótido fluorescente por interacciones electrostáticas, mientras que la parte del oro se utiliza para pegar la enzima ureasa. El mecanismo de sensado se basa en el reconocimiento de urea por la unidad enzimática y su trasformación en amoníaco (mensajero químico), que produce la desprotonación de los grupos amino sobre la superficie de sílice y la liberación del oligonucleótido fluorescente al medio. El nanodispositivo se ha aplicado para la detección de urea en sangre y para la identificación de leche adulterada.

Como conclusión general, los estudios realizados muestran que la incorporación de enzimas sobre nanopartículas permite introducir funciones de reconocimiento con alta especificidad y diseñar nanodispositivos avanzados para distintas finalidades. La combinación de nanopartículas híbridas con grupos orgánicos como puertas moleculares, efectores enzimáticos y especies cromo-fluorogénicas o fármacos puede resultar muy versátil; y se espera que los resultados obtenidos puedan inspirar el desarrollo de nuevos materiales inteligentes con aplicación en distintas áreas como la nanomedicina y la detección de moléculas de interés.

Resum

La present tesi doctoral titulada "Nanodispositius mesoporosos híbrids funcionalitzats amb enzims per a detecció, alliberació controlada i comunicació molecular" es centra en el disseny, preparació, caracterització i avaluació de distints nanodispositius híbrids orgànic-inorgànics utilitzant com a suport nanopartícules tipus Janus d'or i sílice mesoporosa, que s'equipen amb enzims, espècies fluorescents i portes moleculars.

En el primer capítol s'introdueix el marc en el que s'engloben els estudis realitzats on es combinen distintes eines i conceptes relacionats amb la nanotecnologia, la química supramolecular, el camp dels materials mesoporosos i les portes molèculars, així com partícules Janus i enzims. A continuació, es presenten els objectius generals que són abordats en els següents capítols experimentals.

En el tercer capítol, es presenta un nanodispositiu per a l'alliberació controlada en resposta al neurotransmissor acetilcolina. En concret, es tracta de nanopartícules Janus d'or-sílice-mesoporosa funcionalitzades amb l'enzim acetilcolinesterasa en la part de l'or i amb complexes supramolecular d'inclusió entre β-ciclodextrina i benzimidazol en la superfície de la sílice. El complex supramolecular actua como tap o nanovàlvula impedint l'eixida de la càrrega encapsulada a l'interior de la sílice. L'alliberació selectiva en resposta a acetilcolina es produeix degut a la seua hidròlisis catalitzada per l'enzim, el que produeix àcid acètic i indueix l'apertura de la nanovàlvula per protonació del benzimidazol.

En el quart capítol es presenta un sistema d'alliberació controlat enzimàticament basat en la apertura d'una porta sensible a tiols utilitzant com a suport nanopartícules Janus d'or-sílice mesoporosa. En concret, la part mesoporosa de la sílice està funcionalitzada amb cadenes d'oligo(etilen glicol) unides mitjançant un pont disulfur, mentre que la part de l'or s'utilitza per a pegar l'enzim acetilcolinesterasa. Com a par substrat-enzim model s'utilitza acetiltiocolina-acetilcolinesterasa, ja que en aquest cas la reacció enzimàtica produeix tiocolina com a espècie que indueix l'apertura de la porta molecular. A

més, es demostra que la unitat enzimàtica pot detectar la presencia d'inhibidors i com a resultat s'obté un modulació de l'alliberació. Els estudis en cèl·lules mostren que el dispositiu es biocompatible quan està carregat amb safranina O. Per altra banda, el nanodispositiu mostra una major eficàcia per a alliberar el citotòxic doxorubicina en cèl·lules canceroses en presència d'acetiltiocolina.

El cinquè capítol mostra un sistema de comunicació química entre dos nanopartícules Janus distintes que imita el model de comunicació interactiva. En concret, la primera partícula ($S1_{gal}$) està funcionaliztada amb l'enzim β-galactosidasa en la part de l'or, i la part mesoporosa està carregada amb un colorant i tapada amb β-ciclodextrina unida a la sílice mitjançant ponts disulfur. En el segon tipus de nanopartícula ($S2_{gox}$), la part mesoporosa està carregada amb un agent reductor (*N*-acetil-L-cisteïna) i tapada amb una nanovàlvula supramolecular (β-ciclodextrina:benzimidazol). El procés de comunicació es dispara en presència de lactosa. La lactosa es hidrolitzada per la β-galactosidasa sobre la primera partícula ($S1_{gal}$) y la glucosa generada (primer missatger químic) difon cap a la segona nanopartícula ($S2_{gox}$), on la glucosa oxidasa la transforma en àcid glucònic. Açò resulta en la baixada local del pH, el que indueix l'apertura de la nanovàlvula supramolecular i l' alliberació de *N*-acetil-L-cisteïna (segon missatger químic), que difon de tornada cap a la primera nanopartícula ($S1_{gal}$). La *N*-acetil-L-cisteïna indueix la ruptura dels ponts disulfur que tapen la part mesoporosa de $S1_{gal}$ y açò resulta en l'alliberació del colorant encapsulat.

En el sisè capítol es presenta el disseny de nanodispositius capaços de llegir la presència simultània de varies biomolècules de l'ambient i actuar mitjançant el processament de funcions lògiques que resulten en l'alliberació programada de la càrrega. En concret, es preparen nanopartícules Janus d'or-sílice mesoporosa funcionalitzades amb l'enzim glucosa deshidrogenasa en la superfície de l'or i nanovàlcules supramoleculars (β-ciclodextrina:benzimidazol) com a portes sobre la superfície de la sílice. El nanodispositiu actua com una porta lògica AND i es capaç de llegir la presència simultània de glucosa i NAD^+ per a disparar l'alliberació de la càrrega. A més, es mostra que es poden coimmobilitzar glucosa deshidrogenasa i l'enzim ureasa per a imitar la funció lògica INHIBIT, de forma que la funció AND es desconnecta en presència d'urea. Finalment, es mostra que aquestes nanopartícules poden alliberar un fàrmac citotòxic en cèl·lules canceroses al detectar la presència simultània de glucosa i NAD^+ intracel·lular.

En el sèptim capítol, es proposa una nova aproximació per al disseny de nanosensors òptics basats en el desancoratge mediat enzimàticament d'espècies indicadores. Com a proba de concepte, es presenta un nanosensor per a la detecció d'urea basat en el desanclatge d'un oligonucleòtid fluorescent des de nanopartícules Janus d'or-sílice mesoporosa. En concret, les nanopartícules es funcionalitzen sobre la sílice amb grups amino (carregats positivament a pH neutre) als quals es pega l'oligonucleòtid fluorescent per interaccions electrostàtiques, mentre que la part de l'or s'utilitza per a pegar l'enzim ureasa. El mecanisme de detecció es basa en el reconeixement de la urea per la unitat enzimàtica i la seua transformació en amoníac (missatger químic), que produeix la desprotonació dels grups amino sobre la superfície silícia i l'alliberació de l'oligonucleòtid fluorescent al medi. El nanodispositiu s'ha aplicat per a la detecció d'urea en sang i per a la identificació de llet adulterada.

Com a conclusió general, els estudis realitzats mostren que la incorporació d'enzims sobre nanopartícules permeten introduir funcions de reconeixement amb alta especificitat i dissenyar nanodispositius avançats per a distintes finalitats. La combinació de nanopartícules híbrides amb grups orgànics com portes moleculars, efectors enzimàtics i espècies cromo-fluorogèniques o fàrmacs pot resultar molt versàtil; i s'espera que els resultats obsessos inspiren el desenvolupament de nous materials intel·ligents amb aplicació en distintes àrees com la nanomedicina i la detecció de molècules d'interés.

Abstract

This PhD thesis entitled "Enzyme-functionalized hybrid mesoporous nanodevices for sensing, controlled release and molecular communication" is focused on the design, synthesis, characterization and evaluation of several hybrid organic-inorganic nanodevices using Janus gold-mesoporous silica nanoparticles as scaffolds, equipped with enzymes, fluorescent species and molecular gates.

The first chapter gives an overview about the conceptual framework in which are located the studies presented which combine tools and concepts related with nanotechnology, supramolecular chemistry, the field of mesoporous materials and molecular gates, as well as Janus particles and enzymes. Next, there is the presentation of the general objectives that are addressed in the following experimental chapters.

The third chapter shows a nanodevice for controlled release in response to the neurotransmitter acetylcholine. In particular, it is based on Janus gold-mesoporous silica nanoparticles functionalized with the enzyme acetylcholinesterase on the gold face and with supramolecular inclusion complexes between β-cyclodextrin and benzimidazole on the silica surface. The supramolecular complex acts as a cap or nanovalve blocking the exit of the cargo from the silica pores. The selective release in response to acetylcholine is produced due to the hydrolysis of this neurotransmitter by the enzyme, which induces the formation of acetic acid and opening of the supramolecular nanovalve via benzimidazole protonation.

The forth chapter presents an enzyme-controlled delivery system based on the opening of a thiol-responsive molecular gate using Janus gold-mesoporous silica nanoparticles as support. Specifically, the mesoporous is functionalized with oligo(ethylene glycol) chains linked through disulfide bonds, whereas the gold face is used for anchoring acetylcholinesterase. Acetylthiocholine-acetylcholinesterase are employed as model substrate-enzyme pair, since in this case the enzymatic reaction produces thiocholine which is able to induce the opening of the molecular gate. Furthermore, it is shown that the enzymatic unit can detect the presence of inhibitors and adjust the release accordingly.

Experiments with cells show that the system is biocompatible when it is loaded with safranin O. Moreover, the nanodevice shows an enhanced release of the cytotoxic doxorubicin in cancer cells in the presence of acetylthiocholine.

The fifth chapter shows a chemical communication system between two different Janus nanoparticles that mimics the interactive model of communication. In particular, the first particle ($S1_{gal}$) is functionalized with the enzyme β-galactosidase on the gold face, whereas the mesoporous face is loaded with a dye and capped with β-cyclodextrin linked to the silica surface by disulfide bonds. In the second type of nanoparticle ($S2_{gox}$), the mesoporous face is loaded with a reducing agent (*N*-aceytl-L-cysteine) and capped with a pH-sensitive supramolecular nanovalve (β-cyclodextrin:benzimidazole). The communication is triggered in the presence of lactose. Lactose is hydrolyzed by β-galactosidase on the first nanoparticle ($S1_{gal}$) and the generated glucose (first chemical messenger) diffuses to the second nanoparticle ($S2_{gox}$), where glucose oxidase transforms it into gluconic acid. This results in lowering the local pH, which produces the uncapping of the supramolecular nanovalve delivering the entrapped cargo *N*-acetyl-L-cysteine (the second chemical messenger), which difusses as a feedback toward the first nanoparticle ($S1_{gal}$). *N*-acetyl-L-cysteine induces the rupture of the disulfide linkages on the mesoporous face of $S1_{gal}$ and this results in the release of the entrapped dye.

The sixth chapter presents the design of nanocarriers capable of reading the simultaneous presence of several biomolecules from the environment and act accordingly by processing logic tasks which results in a programmed cargo release. In particular, Janus gold-mesoporous silica nanoparticles are functionalized with the enzyme glucose dehydrogenase on the gold surface and with supramolecular nanovalves (β-cyclodextrin:benzimidazole) as caps on the silica surface. The nanodevice acts as an AND logic gate and is able to detect the simultaneous presence of glucose and NAD^+, which results in cargo release. Additionally, it is shown that is possible to coimmobilize glucose dehydrogenase and the enzyme urease on nanoparticles to mimic an INHIBIT logic gate, in which the AND gate is switched off by the presence of urea. Finally, it is shown that such nanodevices can deliver cytotoxic drugs in cancer cells by recognizing the simultaneous presence of glucose and intracellular NAD$^+$.

In the seventh chapter, we propose a new approach for the design of optical nanosensors based on enzyme-mediated detachment of labelled reporters. As a proof of concept, a urea nanosensor based on the detachment of a fluorescent oligonucleotide from Janus nanoparticles is presented. Specifically, nanoparticles are functionalized on the silica surface with amino moieties (positively charged at neutral pH) to which oligonucleotide strands attach by electrostatic interactions, whereas the gold face is used for immobilizing the enzyme urease. The sensing mechanism is based on the recognition of urea by the enzymatic unit and its transformation into ammonia (chemical messenger), which induces the deprotonation of the amino moieties on the silica surface and the release of the fluorescent oligonucleotide to the solution. This nanodevice has been applied for the detection of urea in human blood and for the identification of adulterated milk.

In conclusion, these studies show that the incorporation of enzymes on nanoparticles allows to introduce recognition capabilities with high specificity and to design advanced nanodevices for different purposes. The combination of hybrid nanoparticles with organic groups such as molecular gates, enzymatic effectors and chromo-fluorogenic species or drugs can be very versatile; and we hope that the obtained results inspire the development of new smart materials with application in different areas such as nanomedice and sensing.

Publications

Results of this PhD Thesis and other contributions have resulted in the following scientific publications:

- L. E. Santos-Figueroa, **A. Llopis-Lorente,** S. Royo, F. Sancenón, R. Martínez-Máñez, A. M. Costero, S. Gil, M. Parra. “A Chalcone-Based Highly Selective and Sensitive Chromofluorogenic Probe for Trivalent Metal Cations”. *ChemPlusChem* **2015**, *80*, 800-804.

- **A. Llopis-Lorente**, P. Díez, C. de la Torre, A. Sánchez, F. Sancenón, E. Aznar, M. D. Marcos, P. Martínez-Ruíz, R. Martínez-Máñez, R. Villalonga. “Enzyme-Controlled Nanodevice for Acetylcholine-Triggered Cargo Delivery Based on Janus Au-Mesoporous Silica Nanoparticles”. *Chemistry – A European Journal*, **2017**, *23*, 4276-4281.

- **A. Llopis-Lorente**, B. Lozano-Torres, A. Bernardos, R. Martínez-Máñez, F. Sancenón. “Mesoporous Silica Materials for Controlled Delivery Based on Enzymes”. *Journal of Materials Chemistry B*, **2017**, *5*, 3069-3083.

- A. Casula, **A. Llopis-Lorente**, A. Garau, F. Isaia, M. Kubicki, V. Lippolis, F. Sancenón, R. Martínez-Máñez, A. Owczarzak, C. Santi, M. A. Scorciapino, C. Caltagirone. “A New Class of Silica-Supported Chromo-Fluorogenic Chemosensors for Anion Recognition Based on a Selenourea Scaffold”. *Chemical Communications*, **2017**, *53*, 3729-3732.

- **A. Llopis-Lorente**, P. Díez, A. Sánchez, M. D. Marcos, F. Sancenón, P. Martínez-Ruiz, R. Villalonga, R. Martínez-Máñez. “Interactive Models of Communication at the Nanoscale Using Nanoparticles that Talk to One Another”. *Nature Communications*, **2017**, *8*, 15511.

- **A. Llopis-Lorente**, B. de Luis, A. García-Férnandez, P. Díez, A. Sánchez, M. D. Marcos, F. Sancenón, R. Villalonga, R. Martínez-Máñez, F. Sancenón. “Au-Mesoporous Silica Nanoparticles Gated with Disulfide-Linked Oligo(Ethylene Glycol) Chains for Tunable Cargo Delivery Mediated by an Integrated Enzymatic Control Unit”. *Journal of Materials Chemistry B*, **2017**, *5*, 6734-6739.

- **A. Llopis-Lorente**, P. Díez, A. Sánchez, M. D. Marcos, F. Sancenón, P. Martínez-Ruiz, R. Villalonga, R. Martínez-Máñez. “Toward Chemical Communication Between Nanodevices”. *NanoToday*, **2018**, *18*, 8-11.

- T. M. Godoy-Reyes, **A. Llopis-Lorente**, A. M. Costero, F. Sanecón, P. Gaviña, R. Martínez-Máñez. “Selective and Sensitive Detection of the Neurotransmitter Serotonin Based on the Aggregation of Bifunctionalized Gold Nanoparticles”. *Sensors and Actuators B*, **2018**, *1*, 829-835.

- **A. Llopis-Lorente**, B. de Luis, A. García-Férnandez, S. Jimenez-Falcao, M. Orzáez, F. Sancenón, R. Villalonga, R. Martínez-Máñez. “Hybrid Nanocarriers Act by Processing Logic Tasks: Toward the Design of Nanobots Capable of Reading Information from the Environment”. *ACS Applied Materials & Interfaces,* **2018**, *10*, 26494-26500.

- **A. Llopis-Lorente**, R. Villalonga, M. D. Marcos, R. Martínez-Máñez, F. Sancenón. “Versatile New Paradigm for the Design of Optical Nanosensors based on Enzyme-Mediated Detachment of Labelled-Reporters: The Example of Urea Detection”. *Chemistry – A European Journal,* **2018**, DOI 10.1002/chem.201804706.

Abbreviations and Acronyms

ACh	Acetylcholine
ABTS	2,2′-Azino-bis(3-ethylbenzothiazoline-6-sulfonic acid)
AMF	Alternating magnetic field
ATCh	Acetylthiocholine
ATP	Adenosine triphosphate
Au	Gold
AuNPs	Gold nanoparticles
APTES	3-aminopropyltriethoxysilane
BET	Brunauer-Emmet-Teller
BJH	Barret-Joyner-Halenda
BZI	Benzimidazole
CTAB	Cetyltrimethylamonium bromide
CBPQT^{4+}	Cyclobis(paraquat-*p*-phenylene)
C3	Caspase 3
^{13}***C-NMR***	Carbon-13 nuclear magnetic resonance
DCNP	Diethyl cyanophosphonate
DCP	Diethyl chlorophosphate
DMEM	Dulbecco’s Modified Eagle’s Medium
DFP	Diisopropyl fluorophosphate
DLS	Dynamic light scattering
DNP	Dioxynaphthalene
DOX	Doxorubicin
Doxo	Doxorubicin
DTNB	5,5’-dithiobis(2-nitrobenzoic acid)
DTT	Dithiotheritol
EA	Elemental analysis
EDC	*N*-(3-dimethylaminopropyl)-*N*$^{\prime}$-ethylcarbodiimide
EDX	Energy dispersive X-ray spectroscopy
FBS	Fetal bovine serum

FDA	Food and Drug Administration
FTIR	Fourier-transform infrared spectroscopy
Gox	Glucose oxidase
IR	Infrared
IUPAC	International Union of Pure and Applied Chemistry
HRP	Horseadish peroxidase
LOD	Limit of detection
MCM	Mobile Composition of Matter
ME	Mercaptoethanol
MS	Mesoporous silica
MSNPs	Mesoporous silica nanoparticles
NAC	*N*-acetyl-cysteine
NAD^+	Nicotinamide adenine dinucleotide
NADH	Nicotinamide adenine dinucleotide reduced
$NADP^+$	Nicotinamide adenine phosphate dinucleotide
NADPH	Nicotinamide adenine phosphate dinucleotide reduced
NHS	*N*-hydroxysuccinimide
NIR	Near-infrared
NMR	Nuclear magnetic resonance
OEG	Oligo(ethylene glycol)
PBS	Phosphate buffer saline
PD	Parkinson’s disease
PNIPAM	Poly(*N*-isopropylacrylamide)
PXRD	Powder x-ray diffraction
Rh	Rhodamine
$[Ru(bpy)_3]Cl_2$	Tris(2,2′-bipyridyl)dichlororuthenium(II)
$[Ru(bpy)_3]^{2+}$	Tris(2,2′-bipyridyl)ruthenium(II)
SBA	Santa Barbara Amorphous
SERS	Surface enhanced Raman Spectroscopy
SEM	Scanning electron microscopy
SMS	Silica mesoporous supports

SS-OEG	Disulfide-linked oligo(ethylene glycol)
STEM	Scanning transmission electron microscopy
TEM	Transmission electron microscopy
TEOS	Tetraethyl orthosilicate
TGA	Thermogravimetric analysis
TMOS	Tetramethyl orthosilicate
TNB^{2-}	2-nitro-5-thiobenzoate
TTF	Tetrathiafulvalene
U	Enzymatic units
UV-vis	Ultraviolet-visible
WST-1	Water Soluble Tetrazolium-1 (cell proliferation reagent)
β-*CD*	β-cylodextrin
β-*gal*	β-galactosidase
λ_{exc}	Excitation wavelength

Table of Contents

Chapter 1: General introduction

1.1 Nanotechnology

Nanotechnology is an exciting area of research which deals with the study, design, synthesis, and application of materials and devices with dimensions from one to a few hundred nanometers. It is a relatively new and highly multidisciplinary field which encompasses disciplines like chemistry, physics, biology, material science, engineering and electronics and therefore requires the collaboration of scientists from different backgrounds. At the nanoscale, dimensions are so small that are difficult to understand from our everyday life human perspective. A nanometer (nm, 10^{-9} m) is equivalent to a distance 100000 times smaller than the diameter of a human hair (Figure 1). For instance, a fullerene (a molecule formed by 60 carbon atoms) has a diameter of 1 nm and a shape similar to a football. To convert a football into a fullerene, we would need to reduce the football as many times as we would need to convert the Earth into a football: a hundred million times.[1]

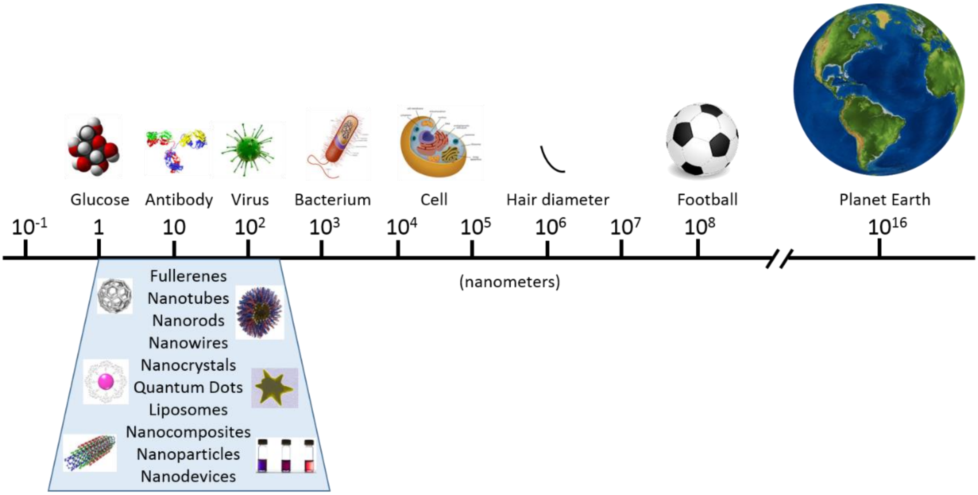

Figure 1. Scheme to compare the range of sizes of nanomaterials, cells and other items.

Ever since in 1959 the physicist Richard Feynman gave his famous lecture "There's plenty of Room at the Bottom" and envisioned the manipulation of matter at the nanoscale,[2] significant advancements in the nanotechnology area have been made. There have been several key factors that have contributed to push forward nanotechnology, a term first used in 1974 by professor Norio Taniguchi from Tokyo Science University.[3] One of them has been the frenetic race to reduce dimensions of electronic transistors, from 100 µm in the 70s to its actual sub-100 nm size. Another key factor has been the development and improvement of electronic microscopes and the invention in 1981 of the scanning tunnelling microscope by Nobel laureates Gerd Binnig and Heinrich Rohrer,[4] and the atomic force microscope in 1985.[5] Furthermore, the discovery of nanomaterials such as the fullerenes in 1985,[6] carbon nanotubes in 1991,[7] or graphene in 2004[8] (among others) with unexpected and advantageous properties for a variety of applications has attracted the attention from the scientific community. Nowadays, examples of nanoparticles with different compositions, sizes, and properties and more complex nanodevices such as nanomemories,[9] nanobatteries,[10] nanocarriers[11] and nanomotors[12] have already been developed with application in a number of different areas.

Materials behave differently when they have nanoscale dimensions and therefore they have different properties compared to their bulk counterparts. For example, there is the popular thought that gold always exhibits its yellow shinning colour. However, gold nanoparticles can be red or blue due to the so-called surface plasmon resonance which is produced by the interaction of its conducting electrons with the light. In general, a common characteristic property of nanomaterials is their high surface-to-volume ratio since as their volume decreases, their surface-to-volume ratio increases. This can be an advantageous for some applications such as to catalyze reactions on their surface or for functionalization with a high percentage of biomolecules in order to develop more sensitive biosensors. In addition, due to their small size, nanoparticles can penetrate inside cells to perform certain functions such as the delivery of a drug or a localized heating upon application of an external light. Nanomaterials, such as graphene or carbon nanotubes, exhibit highly efficient conductivity and also extraordinary mechanical properties. Notwithstanding, a nanomaterial does not necessarily have to be studied and used alone, and an appealing area of research is the development of combinations of nanomaterials (nanocomposites) with synergistic and advantageous properties.[13]

The main areas of research and application of nanotechnology include medicine, electronics, the design of new materials, and energy production among others.[14] Regarding nanomedicine, one of the main interests rely on the development of delivery systems able to release drugs at specific regions or cells, increasing the efficacy of treatments and avoiding therapy-derived side-effects. Another key point is to develop sensitive and specific sensors for the early diagnostic of disease with characteristics such as easy usage, cost-effectiveness and portability. Although there are already more than 50 nanomedicines approved by the FDA,[15] it is important to be aware that introduction of nanotechnology in the actual medical practice will be slow due to the complexities and regulations involved. In electronics, the challenge is to reduce the size of electronic elements as well as increase their efficiency and power. Nanomaterials with improved mechanical, optical and electronic properties are being developed for technological applications. Furthermore, nanotechnology holds also great potential in the development of solar cells and more efficient catalysts for the removal of toxic emissions. Nanomaterials are already applied in a number of commercial products such as tennis rackets and bicycles with improved lightness and resistance thanks to carbon nanotubes, sun creams with titanium dioxide nanoparticles able to filter the UV-radiation, paints and deodorants with antibacterial nanoparticles, television screen with quantum dots, car bodyworks with nanocomposites, and so on.

Nanotechnology is an ongoing field of research and although remarkable advancements has been made in the last decades, there is still much progress to be made. For many experts, nanotechnology is called to be the revolution of the 21st century. A better understanding of the properties of nanomaterials, the improvement of the preparation processes, the development of more advanced nanodevices, and collaboration between researchers from different fields and between academics and industry will be crucial to translate nanotechnology from the lab bench to our daily life.

1.2 Supramolecular Chemistry

Supramolecular chemistry plays an important role in the design and synthesis of nanostructured materials and nanoparticles and in the development of hybrid nanomaterials with advanced functionalities.[16] According to Nobel Laureate Jean-Marie Lehn (who received this prize in 1987 together with Donald J. Cram and Charles J. Pedersen for their contributions that led to the establishment of this branch of chemistry), supramolecular chemistry can be defined as “chemistry beyond the molecule”.[17] Whereas molecular chemistry is related to the study of molecules and the molecular structures that originate from the formation of covalent bonds between atoms; supramolecular chemistry is related to the study of molecular assemblies that originate from interactions between different molecules through non-covalent intermolecular forces (Figure 2).[18] This difference may also be explained using the following comparison: molecules are like individuals (people), so molecular chemistry studies individuals and supramolecular chemistry studies society or (molecular) interactions between them.

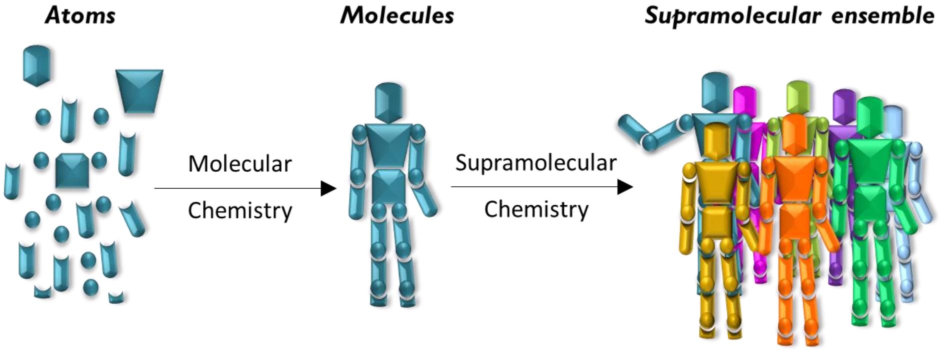

Figure 2. Schematic representation that illustrates the difference between molecular and supramolecular chemistry.

The kind of supramolecular or non-covalent interactions that can exist between molecules include:

a) electrostatics (ion-ion, ion-dipole and dipole-dipole).
b) hydrogen bonding.
c) metal-ligand coordination.
d) π-π interactions.
e) induced dipole-induced dipole interactions (van der Waals forces).
f) hydrophobic or solvatophobic effects.

Numerous examples of supramolecular interactions can be found in nature. For instance, water properties such as the boiling and freezing points, or volume expansion after unfreezing, are due to hydrogen bonding interactions between water molecules. Supramolecular interactions determine also the structure and function of proteins or the attachment of virus to cell surfaces. Perhaps, one of the most beautiful examples is the DNA double helix. Single DNA strands are composed of pyrimidine (cytosine and thymine) and purine (adenine and guanine) bases linked to backbone of phosphorylated sugars. In the DNA double helix, two complementary strands are held together by supramolecular interactions: (i) hydrogen bonds between complementary bases in different strands and (ii) π-π interactions between the aromatic rings of the bases. In particular, adenine complement with thymine with the formation of two hydrogen bonds, whereas guanine forms three hydrogen bonds with cytosine.

Molecular recognition and **molecular self-assembly** are two key concepts in this area.[19] Regarding molecular recognition, the design and synthesis of receptor groups able to interact through supramolecular interactions with target molecules has been very fruitful over the last decades. Molecular recognition can be defined as the specific binding of a guest molecule to a host compound to form a supramolecular complex. A subarea of this field is the concept of molecular sensors or probes. Typical molecular sensors consist of a recognition subunit capable of interacting with the target and a signaling subunit (a flurogenic or chromogenic group) that translates the recognition event into a measurable optical signal.[20] As host groups capable of forming supramolecular complexes with guest molecules, diverse structural families have been studied such as crown ethers, cyclodextrins, cucurbiturils, cavitands, calixarenes and pillarenes. These knowledge has been transferred to the nanotechnology field, for instance, using these supramolecular receptors as functional components of nanoparticles.[21]

On the other hand, self-assembly can be defined as a process in which molecules spontaneously adopt a defined arrangement due to its chemical properties without management from an outside source. Molecular self-assembly allows the construction of large structures such as micelles, membranes, vesicles, liquid crystal phases, and Langmuir monolayers.[22] In fact, molecular self-assembly is a recurrent tool in nanotechnology for the construction of nanomaterials. Compared to top-down methods in which the material is first synthesized in a macroscopic scale and later nanostructured (for example, in the case of electronic chips using photolithography), self-assembly is a bottom-up approach that offers several advantages for the rapid and efficient fabrication of nanostructures. It can be pointed out that the nanostructure is directly and spontaneously built from the assembly of its molecular entities, and thus it avoids the use of sophisticated equipment and overcomes steps of manipulation at the atomic level that can not be attained by top-down methods. Furthermore, scientists can draw inspiration from the examples of self-assembly found in nature and use interactions between biological components to assembly nanodevices. For instance, Willner and co-workers constructed a hybrid nanosystem in which self-assembled DNA nanostructures with predetermined architectures serve as scaffolds to assemble enzymatic cascades with tunable properties.[23] Another positive point of self-assembly is that it allows to incorporate biological components on the final abiotic system using mild conditions that preserve their functionality. Additionally, self-assembly gives the most thermodynamically stable structures (under the pre-established conditions) and therefore the process of formation of the nanostructure is usually self-healing and produces homogeneous structures.

The importance of self-assembly, supramolecular interactions, and molecular recognition chemistry in relation to the preparation and design of mesoporous materials, nanoparticles, and gated materials is remarkable. For instance, it is worth to mention the following examples which are related with some of the concepts developed in this thesis:

- self-organization of surfactant molecules into predetermined structures in the synthesis of porous materials.
- condensation of inorganic precursors around surfactant micelles due to supramolecular interactions in the synthesis of porous materials.
- in the synthesis of gold nanoparticles, citrate ions assemble on the gold nanocrystal surface, govern the nucleation process and its concentration determine the nanoparticle size.
- self-assembly of nanoparticles at water-oil interfaces.
- creation of hydrophobic “binding pockets” in porous materials by functionalization with alkyl chain in order to locate hydrophobic guests.
- attachment of oligonucleotides to silica surfaces by electrostatic interactions.

- use of DNA hybridization as a trigger that induces uncapping of gated solids and cargo release.
- design of capping agents or molecular gates based on supramolecular (host-guest) ensembles like those based on cyclodextrins, cucurbiturils, crown ethers, and so on.
- repulsive forces between the gating molecules (for example, due to protonation of capping polymer branches) can control the controlled-release process from a gated solid.

1.3 Mesoporous silica materials

Porous materials are classified according to their pore diameter as defined by the IUPAC in microporous (< 2 nm), mesoporous (2-50 nm) and macroporous (> 50 nm) materials.[24] Due to their large specific surface area, porous materials have attracted considerable attention for applications such as catalysis,[25] adsorption of gasses and chemicals,[26] filtration and separation,[27] enzyme immobilization,[28] tissue regeneration,[29] and drug delivery.[30]

One of the most known examples of porous materials are zeolites. These are microporous aluminosilicates that are used for applications like catalytic preparation of pharmaceuticals, in petroleum production processes and for water purification.[31] Depending on the zeolite composition, they can act as molecular "sieves" allowing selected molecules to diffuse through their porous and favor the formation of specific products with high yields and minimum waste. However, the pore size of zeolites is usually between 3 to 10 Å which makes them not suitable for applications involving chemicals with a larger size.

In the search of porous materials with larger pore sizes for catalytic applications, researchers from Mobil oil company developed, patented and reported in 1992 the synthesis of a family of mesoporous silica materials known as the M41S phases.[32] These include three main structure types (Figure 3): MCM-41 with a hexagonal arrangement of mesopores (like a honeycomb), MCM-48 with a cubic arrangement of mesopores and MCM-50 with a lamellar structure, where MCM stands for Mobile Composition of Matter.[33] These phases typically exhibit a pore diameter from 2 to 5 nm, although it can be further increased using different strategies. Among these phases, the MCM-41 is the most studied and used due to the relative simplicity of its synthesis and its particular honeycomb-like structure. Furthermore, in 1998 researchers from Santa Barbara University reported the so-called SBA-15 which have a hexagonal arrangement of pores with a tunable size from 5-30 nm.[34]

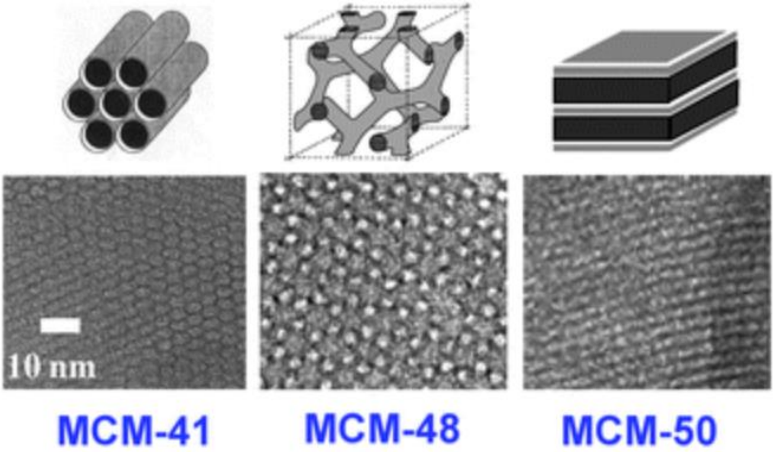

Figure 3. The M41S family of mesoporous silica materials. Schematic 3-D structures on top and corresponding TEM images of the pore network at the bottom. *Reprinted with permission from Chem. Soc. Rev. 2013, 42, 3663. Copyright © 2013 The Royal Society of Chemistry.*

Since the first studies, mesoporous silica materials have been object of considerable attention and research efforts in different areas due to their unique properties. The main appealing features of mesoporous silica materials are:

- Large specific surface area (500-1000 m^2/g).
- High specific pore volume and loading capacity.
- Ordered and uniform pore distribution.
- Tunable pore size from 2-30 nm.

- Preparation in the form of micrometric particles or nanoparticles with tunable size depending on the synthetic parameters.
- Their synthesis requires inexpensive and non-hazardous chemicals and can be produced in large scales.
- Thermal stability, chemical inertness and easy handling.
- Easy functionalization with trialcoxysilane derivatives.
- Biocompatibility.[35]

❖ ***Synthesis of mesoporous silica materials***

In general, the synthesis of mesoporous silica materials is based on the condensation of a silica precursor (tetraethyl orthosilicate, sodium silicate or tetramethylammonium silicate) in the presence of cationic surfactants under basic conditions.[36] It is considered a sol-gel process which means that involves the conversion of monomers in solution (sol) into an integrated solid network (gel), similar to the method described by Stöber in 1968 for obtaining silica nanoparticles, but performed in the presence of surfactants.

In particular, the role of the surfactant molecules is to act as a template or structure directing agent by forming supermicelles (supramolecular self-assemblies of individual micelles) over which the precursors molecules condensate. The structure of supermicelles depends on the selected conditions such as temperature, pH, ionic force and surfactant nature and concentration. Once the supermicelles are formed, the silica precursors are added. In this step, the molecules of the silica precursor are hydrolyzed and form silanol groups (Si-OH) which polymerize by condensation creating a network of siloxane bonds (Si-O-Si) as depicted in Figure 4. At this point, the presence of the supermicelles is crucial to produce the assembly of the silica on its surroundings and the formation of the pores. The structure of the pores in the final material (hexagonal in the case of MCM-41) is the result of the arrangement of the surfactant's micelles. The progressive formation of the silica material can be observed with the naked eyed by the appearance of a white turbidity. Later, the surfactant is removed by an extraction process under reflux in acidic media or by calcination (heating of the solid in a muffle furnace at high temperatures for several hours).

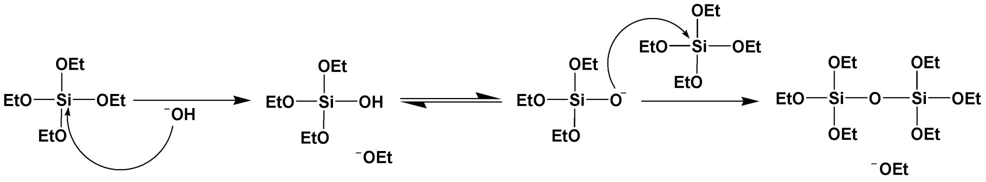

Figure 4. Mechanism of TEOS hydrolysis and condensation.

The size, shape and regularity of the resulting particles depends on different parameters such as temperature, time and amount, proportion and nature of reagents added. In the particular case of 100 nm MCM-41 mesoporous silica nanoparticles, a typical synthetic procedure involves the addition of tetraethyl orthosilicate (TEOS) (silica precursor) over a cetyltrimethylamonium bromide (CTAB) micellar solution at 80 °C and at basic pH (adjusted with NaOH) (Figure 5). The mixture is let to stir during 2 hours and afterwards the solid is collected by centrifugation or filtration. Other conditions can be used for obtaining microparticles or nanoparticles with larger or smaller size. Typically, the final MCM-41 mesoporous scaffold presents cylindrical unidirectional channels of pores with a diameter of ca. 2.5 nm. Notwithstanding, the pore size can also be modulated using suitable swelling organic molecules, by post-synthesis treatment or by adjusting the reaction parameters. In the case of SBA-15 materials, the synthesis involves the use of triblock copolymer templates under acidic conditions.

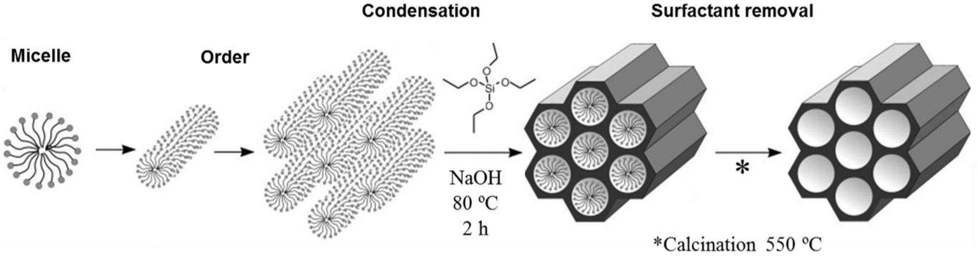

Figure 5. Schematic of synthetic procedure for preparing MCM-41-type mesoporous silica nanoparticles. *Adapted from Angew. Chem. Int. Ed. 2006, 45, 3216. Copyright © 2006 Wiley-VCH.*

❖ ***Functionalization of mesoporous silica materials***

Functionalization (of inorganic materials) is a term used by researchers working in this field which usually refers to the incorporation of organic groups on the materials surface. Functionalization of materials leads to the production of hybrid organic-inorganic materials. Hybrid organic-inorganic materials are highly interesting for a wide range of applications (e.g. chromatography, sensing, catalysis, etc.) since they combine the high surface area, stability and easy handling of the inorganic scaffold with a high number of localized functional organic moieties.

Two main strategies are used for the synthesis of porous hybrid materials based on: (i) grafting, which is the post-synthetic modification of the surface of an inorganic silica material; and (ii) co-condensation, which is the simultaneous condensation of silica and organosilica precursors.[37] Whatever the functionalization procedure, the incorporated organic group can have a function by itself (like increasing the surface hydrophobicity/hydrophilicity, stabilization, etc.) or be used as reacting groups to further anchor other molecules by the formation of covalent bonds (using for instance click reactions, formation of amides or urea) or by electrostatic or supramolecular interactions.

▪ **Functionalization by grafting:**

In this method, the inorganic mesoporous silica material is first synthesized and, in a posterior step, it is functionalized with the selected organic groups. It is based on the fact that the surface of silica materials has a high concentration of silanol groups (Si-OH) which act as a reactive point to anchor organosilanes containing the desired organic moiety. There are a wide range of commercially available organosilanes, being trialkoxysilanes with structures $(R'O)_3$-Si-R (where R is an organic group) the most common and widely used, and less frequently silazanes $HN(SiR_3)_2$ or chlorosilanes $ClSiR_3$. The reaction of superficial silanol groups with trialkoxysilanes can be considered as a simple condensation reaction or nucleophilic substitution (Figure 6). Using this method, organosilanes are preferentially placed on the external silica surface due to its more impaired diffusion towards the internal pores.

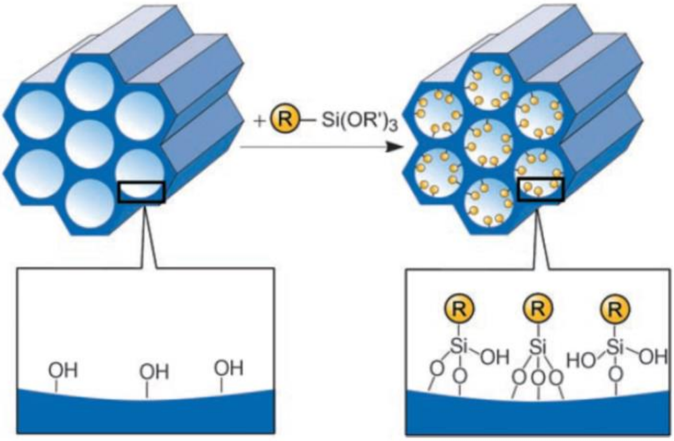

Figure 6. Schematic of the grafting procedure for functionalization of mesoporous pure silica materials with organotryalkoxysilanes of the type $(R'O)_3$-Si-R where R represents and organic functional group. *Adapted from Angew. Chem. Int. Ed. 2006, 45, 3216. Copyright © 2006 Wiley-VCH.*

This method has two main advantages. One is that the mesoporous silica support can be synthesized using well-known standard procedures in large scales and later modified with the selected organosilanes. The second is that the mesostructure of the silica phase as well as the morphology of the particles are usually retained after the functionalization process.

Furthermore, it is possible to achieve a regioselective functionalization of the mesoporous materials by anchoring different groups on the external and internal surface. For this, an appealing strategy is to use the as-synthesised mesoporous scaffold (with pores filled by the surfactant molecules) and treat it with an organosilane that will be attached to the outer surface. Then, the surfactant is removed by extraction (with a refluxing solution of HCl in ethanol) and the resulting surfactant-free scaffold is further functionalized in its internal surface with a different organosilane. For instance, we used this strategy in a collaboration with the group of Prof. Claudia Caltagirone to prepare mesoporous silica nanoparticles with hydrophobic pore cavities (functionalized with trimethylsilyl, in order to locate a hydrophobic molecular sensor) that were previously functionalized on their external surface with hydrophilic polyethylene glycol chains (that improve the stability of nanoparticle suspensions) as depicted in Figure 7.[38]

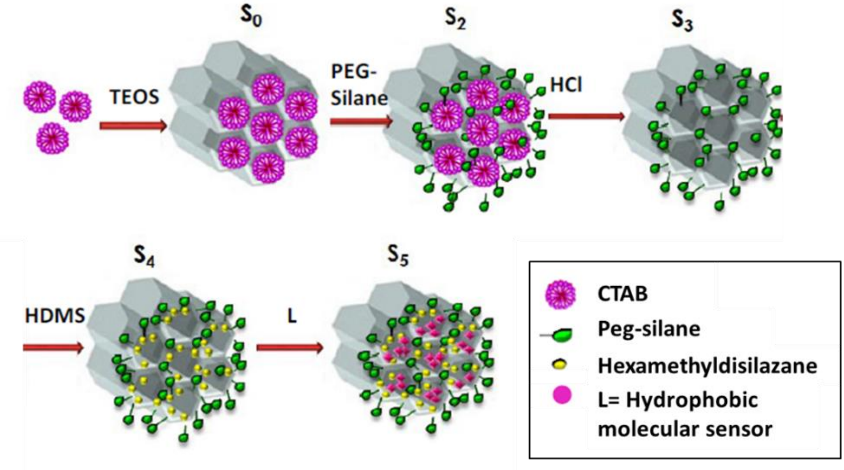

Figure 7. Example of regioselective functionalization strategy used in ref. 38, to yield hydrophobic pores and a hydrophilic external surface.

- **Functionalization by co-condensation:**

This is an alternative procedure to prepare organically functionalized mesoporous silica phases in which the main silica precursor (eg. TEOS or TMOS) and the functional organosilane are incorporated in the synthetic mixture at the same time and condensate in the presence of a structure-directing agent (Figure 8). It is a one-pot synthesis or also called direct synthesis.

The resulting silica matrix contains alkoxy functional groups intercalated in the main silica skeleton and distributed homogenously both on the external and internal surfaces. In this case, the surfactant must be removed by extraction since calcination would spoil the organic functional groups. It is also important to point out that the introduction of functional groups will affect the interactions with the surfactant as well as the structure stability and the particle morphology. In some cases, if the amount of added organosilane is too high, it can even prevent the formation of the mesoporous structure. Therefore, although some procedures for incorporating specific and common tryalkosylanes like APTES can be found in the literature, this method is less versatile since the procedure should be optimized in each particular case.

There is also the possibility to use silsesquioxane precursors that have a molecular structure of the type $(R'O)_3Si\text{-}R\text{-}Si(OR')_3$, being R the organic functional group to be introduced on the material. They are also called "single-source" precursors since they act as the precursor of the inorganic network and, at the same time, incorporate the organic functionality. The materials produced using this approach are called periodic mesoporous organosilicas (PMOs).[39] However, the variety of commercially available silsesquioxanes is smaller compared to the wide variety of tryalkoxysilanes and this strategy has been less employed.

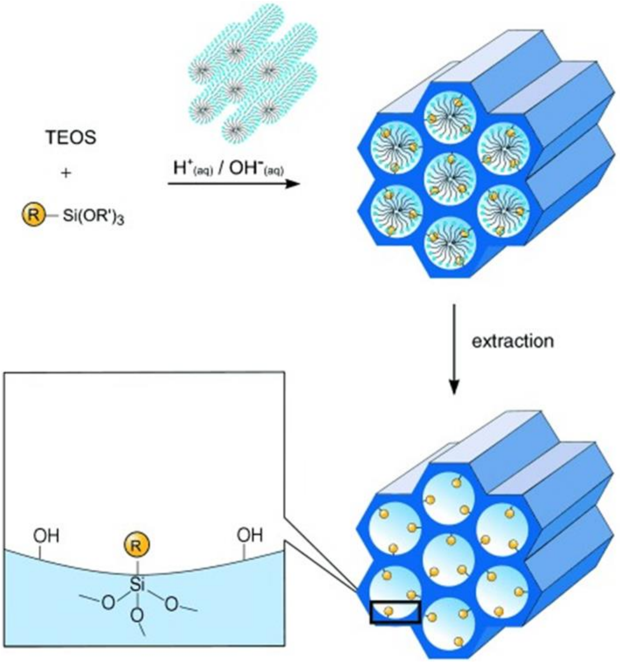

Figure 8. Schematic of the co-condensation method for organic functionalization of mesoporous silica materials. *Adapted from Angew. Chem. Int. Ed. 2006, 45, 3216. Copyright © 2006 Wiley-VCH.*

❖ *Characterization of mesoporous silica materials*

A series of common characterization techniques are used with the aim of checking (or elucidating) the formation of the mesoporous structure, its preservation along the different modification steps, and the incorporation of the different components.

Powder X-Ray Diffraction (PXRD) is a non-destructive technique that allows to study periodically ordered structures at atomic scales. In a typical experiment, the sample is placed in a holder at the center between the source and the detector. The source emits X-ray radiation with a variant incident angle, and the diffracted light is collected by the detector. PXRD patterns are plots of intensity (of diffracted light) as a function of the angle of the incident beam. According to Brag's law (Figure 9), the angles at which there are intensity peaks (reflections, due to constructive interferences) are determined by the distance between atomic planes in the ordered structure.

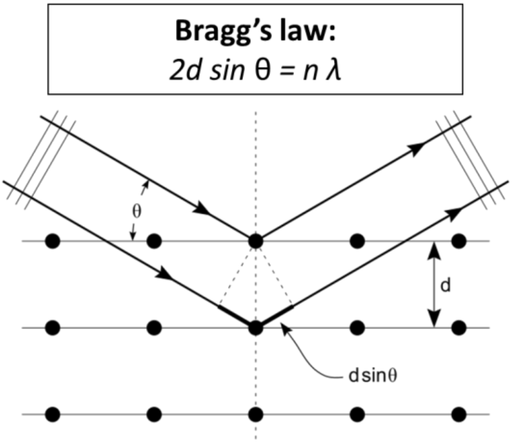

Figure 9. Illustration of Bragg's law which determines that there is a constructive interference (refraction peak) when *2d sin* θ = *n λ* (where *d* is the spacing between diffracting planes, θ is the incident angle, n is any whole number and *λ* is the wavelength of the incident beam).

In the case of the mesoporous silica materials, the arrangement of Si and O atoms in the silica phase is amorphous, but there are characteristic peaks on the

PXRD pattern due to the periodic arrangement of the pores. The peaks appear at low angles since the distance between planes of pores is large (compared to atomic planes distances in other kind of materials like for example metallic particles). Therefore, PXRD gives information about the arrangement of the pores in the mesoporous material. This technique is especially useful to verify the integrity of mesoporous scaffold after the modification steps that can potentially damage the structure. For instance, the diffractogram of mesoporous nanoparticles with an MCM-41 structure (Figure 10) shows a main characteristic peak at around 2.4° that is indexed as the (100) Bragg peak, and three other secondary peaks are higher angles indexed as the (100), (200) and (210) Bragg peaks.

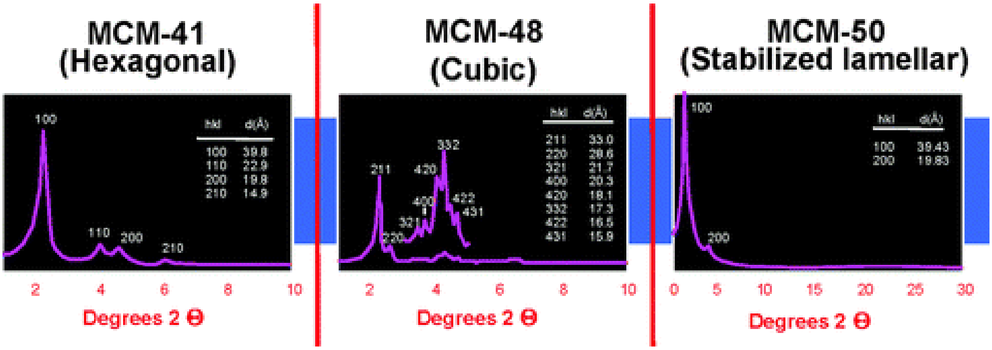

Figure 10. Characteristic PXRD patterns of the M41S family of mesoporous silica materials. *Adapted from Chem. Soc. Rev. 2013, 42, 3663. Copyright © 2013 The Royal Society of Chemistry.*

On the other hand, **nitrogen adsorption-desorption** isotherms is a fundamental technique in the characterization of mesoporous materials. It gives information about the specific surface area, pore size and specific pore volume. These isotherms are plots of quantity of nitrogen adsorbed per gram of material as a function of the relative pressure. When the mesoporous scaffold has empty pores the quantity of nitrogen adsorbed is high due to its adsorption inside the pore channels. On the contrary, when the pores are filled with a cargo or have not been properly formed, the quantity of adsorbed nitrogen is significantly lower.

Furthermore, there is a correlation between the shape of the isotherm plot (that can be grouped into 6 types) and the structure of the material (porous materials have isotherms of type IV and V).[40] The absence of hysteresis loops indicates the homogeneity of the pore network. Typically, the specific surface area of mesoporous materials is determined by applying the Brunauer-Emmet-Teller (BET) method on the adsorption branch of the isotherm.[41] The pore size and specific pore volumes are calculated by applying the Barret-Joyner-Halenda (BJH) model also in the adsorption branch of the isotherm.[42]

Transmission electron microscopy (TEM) allows to visualize the size and morphology of the materials with high resolution. Using TEM, the presence of pores on the material and their periodicity can be usually discerned. In addition, **scanning electron microscopy** (SEM) can also be used to study the particle size and morphology. Whereas TEM produces images by detecting primary electrons transmitted through the sample, SEM produces images by detecting secondary electrons which are emitted from the material surface due to excitation by the incident electron beam. Scanning Transmission Electron Microscopy coupled with energy dispersive X-ray spectroscopy (**STEM-EDX**) is used in some cases to map the presence of certain elements in the material. STEM-EDX is based on the fact that under excitation with a high-energy beam, a certain element will emit X-ray at specific wavelengths due to the excitation-relaxation of its electrons.

There are several techniques that can be used to evaluate qualitatively and/or quantitatively the functionalization with organic molecules. **Elemental analysis** (EA) is performed (using a special analyzer) by combustion of a small amount of sample (1-2 mg) and gives information about the percentage in weight of carbon, hydrogen, nitrogen and Sulphur. Thus, the results can be related with the amount of organic functional molecules. **Thermogravimetric analysis** (TGA) register the loss in weight of the material as a function of the temperature so the overall percentage of organic matter can be calculated. **Solid-state nuclear magnetic resonance** (NMR) allows to obtain the NMR spectra of the solid and therefore confirm the presence of different functional organic molecules by showing its characteristic NMR peaks. Although it can give very useful information, it requires a large amount of sample (more than 100 mg) and long accumulation times (several hours). Moreover, the signal tends to appear broader and with less resolution compared to conventional NMR of organic molecules in solution. By Fourier-transform infrared spectroscopy (**FT-IR**), the specific IR absorption peaks of organic groups are sometimes discernible depending on the amount of functionalization, the groups and the absence of overlapping signals.

Other technique used in the characterisation of nanoparticles is **Dynamic Light Scattering** (DLS). It is based on measuring the fluctuation in scattered light due to the Brownian motion of the particles in solution while it is irradiated with a laser beam. The particles move faster the smaller they are and thus the fluctuations can be related with the size of the particles. It serves for estimating the hydrodynamic diameter of the particles which is usually higher than the diameter determined by TEM. Also by DLS, the zeta potential (charge on the surface of the material) of the nanoparticles can be determined by using a special cuvette with two electrodes. When an alternating electric field is applied between the two electrodes, particles move at a velocity that is related its zeta potential.

Finally, it is important to not forget two general and well-known techniques that are very useful when working with mesoporous materials: **UV-visible spectrophotometry** and **fluorescence**. They can be used, for instance, for monitoring the release of a fluorescent or colored cargo from the nanoparticles, checking nanoparticle fluorescence due to the incorporation of a certain component, for conducting enzymatic assays, quantifying the amount of encapsulated cargo, and so on.

1.4 Stimuli-responsive gated materials

The functionalization of inorganic materials with molecular or supramolecular assemblies has recently led to the preparation of hybrid materials with advanced functionalities.[21,43] In fact, grafting organic (bio)molecules or supramolecules onto selected inorganic solids (with different natures, sizes and shapes) has promoted the development of smart nanodevices with applications in several scientific fields.[44]

Within the realm of functional nanodevices, one appealing concept is related with the design of stimuli-responsive gated materials. These systems are constructed for the purpose of finely tuning the release of chemical species from the voids of porous supports to a solution in response to an external stimulus.[45] These nanodevices are generally composed of two subunits: (i) a porous inorganic support, on which a cargo is entrapped; and (ii) selected molecular and/or supramolecular entities (the so-called molecular gates), grafted onto the external surface, which control mass transport from the pores to the solution in response to a certain stimulus (Figure 11).

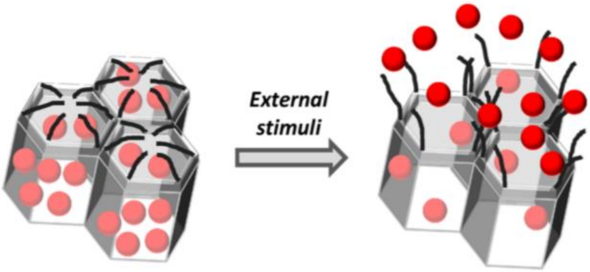

Figure 11. Schematic representation of the operation of a gated material**.**

Since Fujiwara and coworkers reported in 2003 the first example of a molecular gate,[46] gated materials have attracted great attention due to their potential applications for the controlled release of chemicals, which is highly appealing in the biomedical field,[47] and also in the development of new sensing/recognition paradigms.[48] Multidisciplinary researchers working on this topic have reported a variety of gated materials that respond to different stimuli such us light, temperature, magnetic fields, redox species, ions and biomolecules.[45a] In this regard, one of the most widely used inorganic supports has been mesoporous silica nanoparticles (MSNPs). Additionally, others employed supports include mesoporous silica microparticles,[49] core-shell nanoparticles with different cores (such as gold, magnetite (Fe_2O_3), platinum and upconversion particles) surrounded by a mesoporous silica shell,[50] anodic alumina[51] and bioactive glasses.[52] The gating mechanisms usually take advantage of electrostatic or supramolecular interactions, the rupture/formation of covalent bonds, or changes in the physical properties of molecules or macromolecules. Different kind of gatekeepers have been used such as polymers, supramolecular ensembles, inorganic nanoparticles, and biomacromolecules.

Extensive reviews about gated materials have been published in recent years and give a comprehensive landscape of the work done so far.[35,45,53] As examples, some designs of gated materials classified according to the triggering stimuli are showed below.

❖ ***Light driven molecular gates***

Light-responsive delivery systems are appealing for biomedical applications since the release can be externally triggered at will by choosing the time and area of irradiation. Light-driven molecular gates, reported so far, can be classified into three main paradigms: (i) photodimerization or cis-trans photoconversions; (ii) photocleavage of chemical bonds directly or assisted by photosensitizers and (iii) photoinduced heating of gold nanostructures.

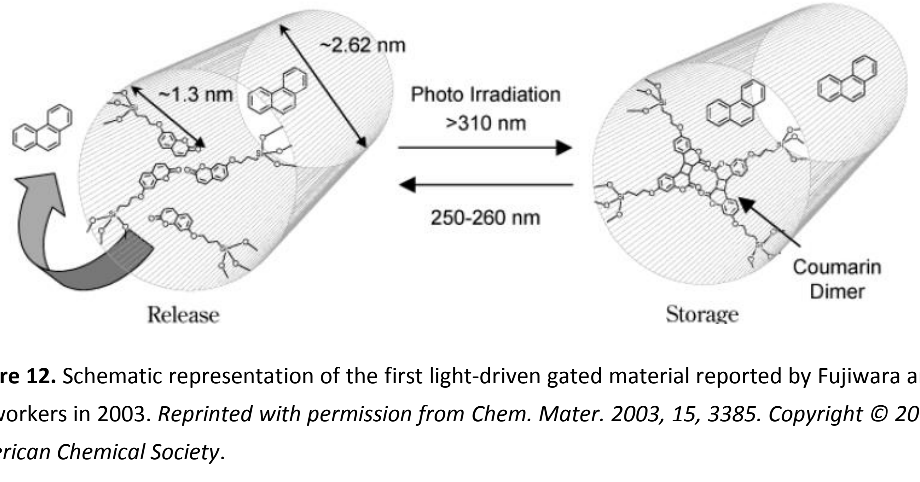

Figure 12. Schematic representation of the first light-driven gated material reported by Fujiwara and co-workers in 2003. *Reprinted with permission from Chem. Mater. 2003, 15, 3385. Copyright © 2013 American Chemical Society*.

In the first example of a molecular gate, Fujiwara and co-workers used light as the triggering stimulus.[46] In this work (Figure 12), the MCM-41-type mesoporous support was functionalized with 7-[(3-triethoxysilyl)propoxy]coumarin (a coumarin derivative) on the external surface, loaded with selected cargos (phenantracene, cholestane, and progesterone) and capped by irradiation with light at λ > 310 nm which induce the formation of dimers between adjacent coumarin molecules. Upon irradiation using a 250 nm light source, the pores were uncapped due to the photo-rupture of coumarin dimers and cargo release was observed in organic media.

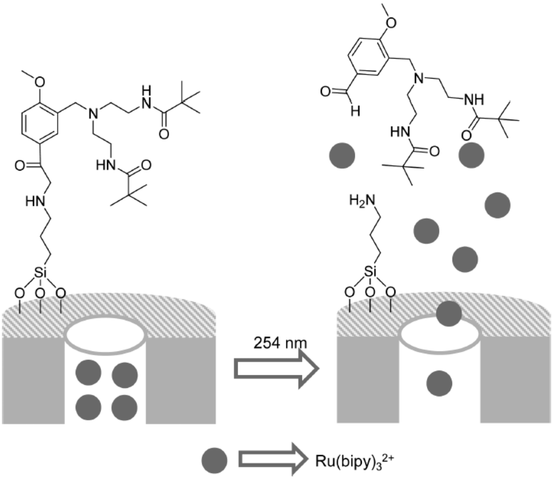

Figure 13. Schematic representation of a UV-light-driven gated material based on MSNPs loaded with $[Ru(bpy)_3]Cl_2$ and capped with photo-cleavable *o*-methoxybenzylamine derivative. *Reprinted with permission from Chem. Rev. 2016, 116, 516. Copyright © 2016 American Chemical Society*.

A simple and illustrative example of a light-driven molecular gate is depicted in Figure 13. The authors prepared MSNPs loaded with $[Ru(bpy)_3]Cl_2$ and capped with a photo-cleavable bulky *o*-methoxybenzylamine derivative that contained two *t*-butyl moieties and triethoxysilane in its structure. The bulky *t*-butyl subunits of the o-methoxybenzylamine derivative impeded the release of the entrapped cargo in aqueous media. In contrast, upon irradiation with UV light (250 nm), the bulky group was cleaved which decreased the steric hindrance at the pores outlets and allowed the diffusion of the dye to the solution.[54]

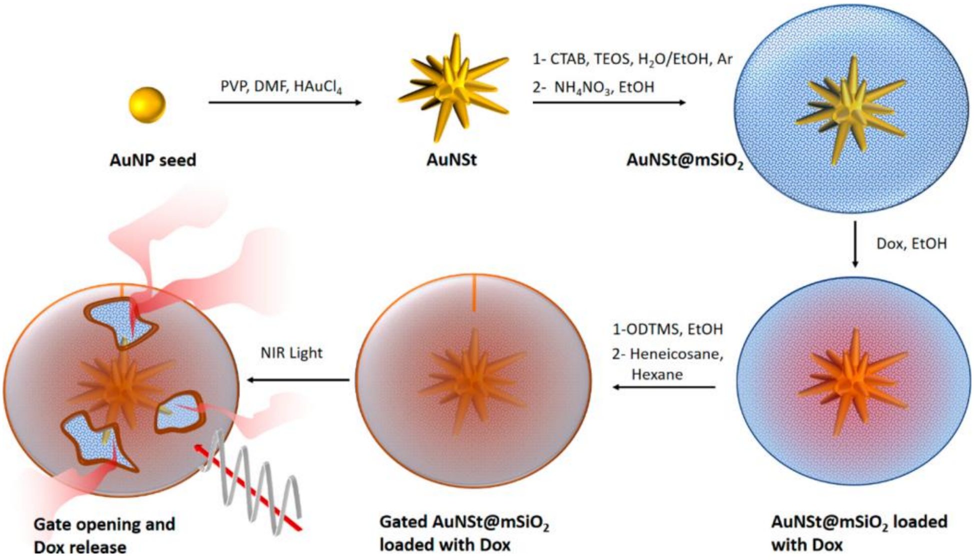

Figure 14. Schematic representation of the preparation and operating paradigm of a NIR-light-driven nanodevice based on AuNSts coated with a mesoporous silica shell and paraffin. *Reprinted with permission from ACS Appl. Mater. Interfaces, 2018, 33, 27644. Copyright © 2018 American Chemical Society*.

In a very recent work, Hernández-Montoto and co-workers have reported a near infrared (NIR)-light responsive system based on gold nanostars (AuNSts) coated with a mesoporous silica shell.[55] NIR light (λ=700-1000 nm) has deeper tissue penetration compared to UV-light and produces minimal cell damage. The mesoporous shell was loaded with doxorubicin (DOX), functionalized on the outer surface with octacedyltrimethoxysilane and capped with the paraffin heneicosane (Figure 14). The paraffin molecules formed a hydrophobic layer that blocked the pores and prevented cargo leakage. Upon irradiation with NIR laser at low powers, the AuNSts absorbed light and transformed it into a local temperature increase that resulted in the melting of the paraffin and cargo release. The nanodevice displayed no cytotoxicity towards HeLa cells, until cargo release was triggered upon 808 nm laser irradiation.

❖ ***Temperature-driven molecular gates***

Three main strategies have been employed for developing gated materials for temperature-triggered cargo release: (i) the use of thermosensitive polymers, (ii) uncapping of the pores due to temperature-induced dehybridization of DNA sequences, and (iii) melting of organic caps such as paraffin.

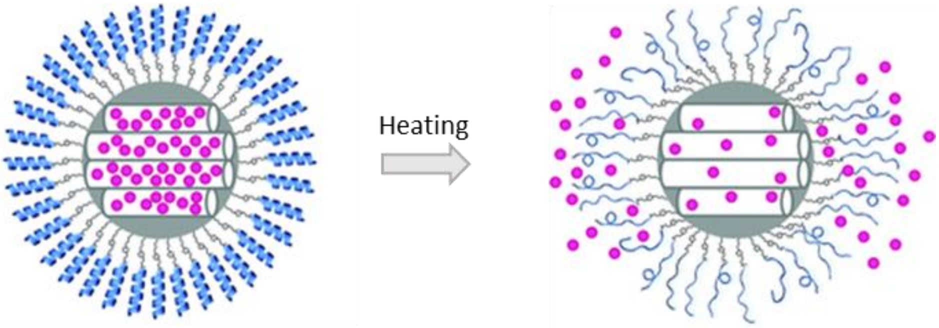

Figure 15. Schematic representation of a temperature-responsive gated material capped with a thermo-sensitive peptide. *Adapted with permission from Chem. Commun. 2014, 50, 3184. Copyright © 2014 The Royal Society of Chemistry.*

A temperature-driven gated material was designed by de la Torre and co-workers in 2014 that was based in the conformational transformation of peptide sequences from α-helix to a disordered conformation induced by an increase in temperature (Figure 15).[56] MSNPs were loaded with safranin O and functionalized on the external surface with (azidopropyl)triethoxysilane. Then, a peptide of 17 aminoacids with a terminal pentynoic group was linked to azide groups on the silica surface by click reaction. The peptide was specifically designed to adopt an α-helix conformation at room temperature. This self-aggregation of the peptide in the form of α-helix bundles inhibited cargo release until the temperature was increased. When temperature increased above 50 °C, the peptide structure change to a disordered conformation which reduced the steric crowding around the pores outlets and resulted in cargo release.

Another system for cargo delivery induced by temperature changes was recently reported by Yu and co-workers based on the use of thermo-responsive polymer poly(*N*-isopropylacrylamide) (PNIPAM) as a capping agent.[57] Core-shell nanoparticles comprised of Fe_3O_4 cores and a MCM-41 mesoporous silica shell were prepared and further treated for 3 days for pore expansion to around 6.1 nm. The particles were loaded with $[Ru(bpy)_3]Cl_2$ or lysozyme and later capped with PNIPAM for blocking the pore outlets. At room temperature (25 °C), the PNIPAM brushes were hydrated and expanded blocking the pores as depicted in Figure 16. At a physiological temperature (37 °C), an abrupt cargo release was observed due to the collapse of the brushes and the exposure of the expanded pores to the medium. The material was applied as an antibacterial agent and a significant reduction in bacterial growth was observed due to the successful release of lysozyme.

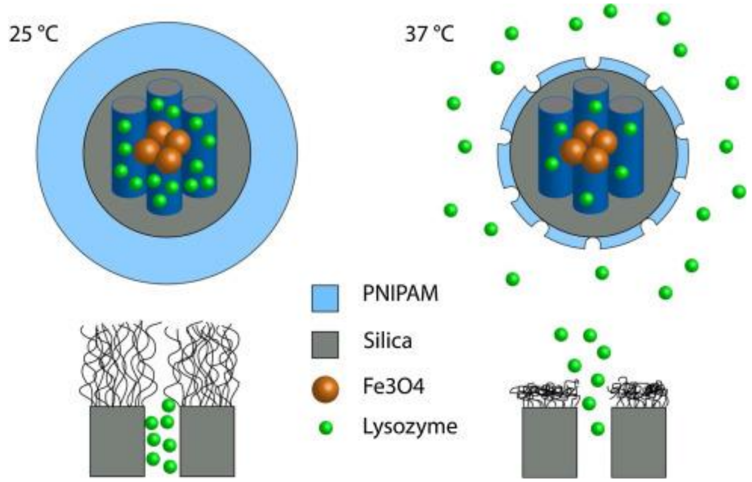

Figure 16. Schematic drawing of the temperature-responsive system based on core-shell nanoparticles loaded with lysozyme and capped with PNIPAM. *Reprinted with permission from Colloids Surf. B, 2015, 135, 652. Copyright © 2015 Elsevier B.V.*

❖ *Magnetically-driven molecular gates*

Several systems for controlled release using alternating magnetic fields (AMF) as external stimulus have been reported. These systems are based on the use of core-shell nanoparticles having a magnetic core (Fe_2O_3) surrounded by a mesoporous silica shell. The application of an alternating magnetic field leads to a local heating of the nanoparticles which induces the commutation of the molecular gate (from close to open) and cargo release. Importantly, the incorporation of a magnetic core is interesting for biomedical application since it offers the possibility of guiding the materials and enhancing its accumulation in certain tissues with external magnets.

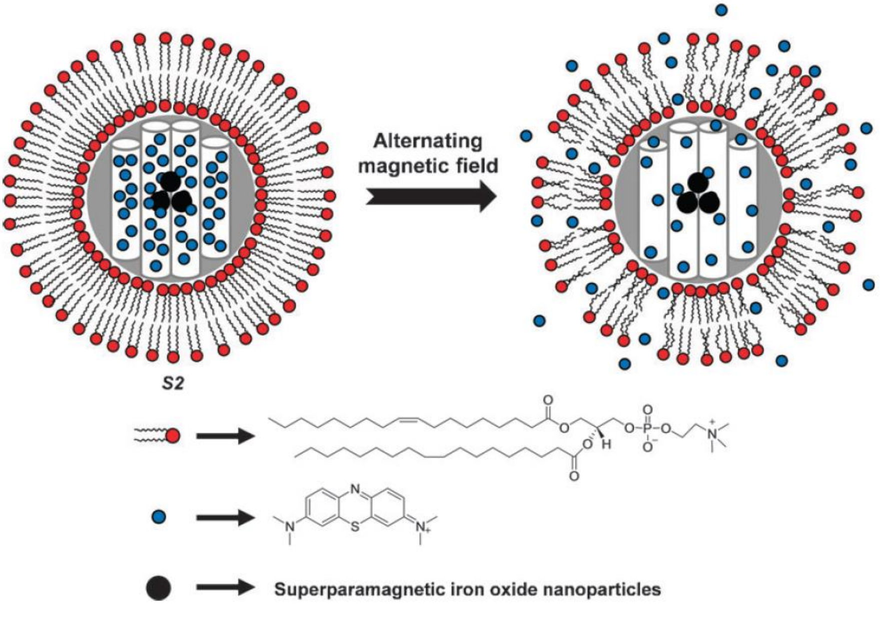

Figure 17. Schematic drawing of the core-shell nanoparticles capped with a lipid bilayer for controlled delivery triggered by an external magnetic field. *Reprinted with permission from Chem. Commun. 2012, 48, 5647. Copyright © 2012 The Royal Society of Chemistry.*

As an illustrative example, Stroeve's and Martínez-Máñez's groups developed the magnetic-responsive delivery system depicted in Figure 17.[58] MSNPs with supermagnetic iron oxide cores were loaded with methylene blue (MB) and capped with 1,2-dioleoyl-*sn*-glycero-3-phosphocholine (DOPC) by the formation of lipid bilayers around the nanoparticles. Cargo release was observed when aqueous suspensions of the nanoparticles were exposed to an alternating magnetic field (50 Hz, 1570 G), whereas payload delivery was negligible in the absence of it. The response was ascribed to an increase in the permeability of the lipid bilayer due to the vibration of the particles upon application of the AMF as well as to an increase of the nanoparticles temperature that partially disrupted the bilayer. This was confirmed by studying the release of nanoparticles suspensions at 50 °C, which resulted in a massive delivery at short times. Additionally, the nanodevice was non-toxic for several human cell lines tested such as human nerve (A172), liver (Hep G2), heart (HCM), lung (A549), kidney (293T), colon (SW480), brain (BE(2)-C) and skin (A431) in concentrations below 0.5 mg mL^{-1}.

❖ ***pH-driven molecular gates***

In these systems, the addition or abstraction of protons induces a change in the gating ensemble (such as a change of conformation, its rupture or attraction/repulsion interactions between its components) that controls the open/close mechanism. A large number of pH-responsive gated materials have been developed. As capping agents, researchers have reported the use of polyamines, different polymers, supramolecular ensembles, layer-by-layer coatings, biomolecules like DNA or proteins, lipid bilayers and inorganic nanoparticles, among others.

For instance, Lee and co-workers prepared pH-responsive MSNPs capped with a calcium phosphate layer (Figure 18).[59] First, MSNPs were functionalised with aminopropyl moieties, which were further reacted with glutaraldehyde to yield aldehyde groups on the external silica surface. Afterward, the authors linked the enzyme urease to the aldehyde groups through the formation of imine bonds. DOX was loaded into the pores and the system was closed by the enzyme-mediated formation of a calcium phosphate coating using hydroxyapatite and urea. At pH 7.4, the system remained capped, but DOX delivery was remarkable at pH 4.5 due to the dissolution of the calcium phosphate layer and hydrolysis of imine bonds under acidic conditions. The DOX-loaded nanoparticles were tested in MCF-7 cancer cells and induced cell death was observed due to the gradual release of DOX at the lysosomal pH.

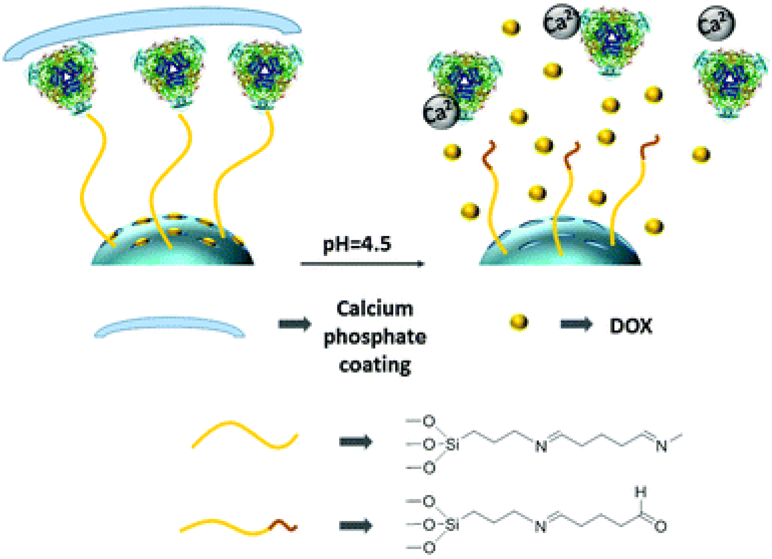

Figure 18. Schematic representation of a pH-responsive delivery system based on the dissolution of calcium phosphate coating at acidic pH. *Reprinted with permission from J. Mater. Chem. B 2017, 5, 3069. Copyright © 2017 The Royal Society of Chemistry.*

Recently, pH-responsive capped MSNPs were reported by Yang and co-workers.[60] In this case, MSNPs were first functionalized with 2-bromoisobutyryl bromide (BIBB) in order to later attach poly(2-dimethylaminoethyl methacrylate) brushes (PDMAEMA) by peroxidase mimetic catalytic atom transfer radical polymerization (ATRP). The system was then loaded with rhodamine (Rh) 6G. PBS suspensions of the nanoparticles at pH 7.4 showed a moderate Rh 6G release. However, marked dye delivery was observed upon lowering the solution pH to 2.0. The release was ascribed to electrostatic repulsions between the positively charged polymer chains that adopted an extended conformation with subsequent pore opening (Figure 19).

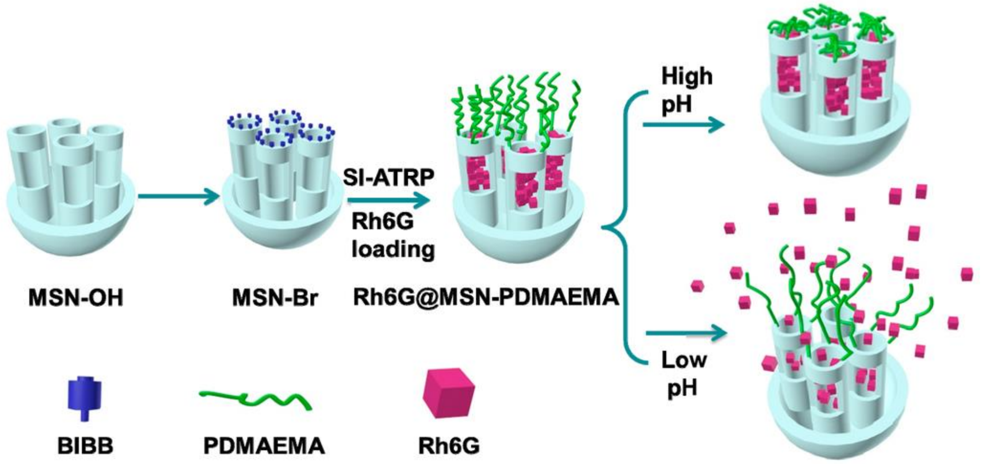

Figure 19. Schematic representation of a pH-driven gated solid based on the protonation of polymer brushes. *Reprinted with permission from Polymers 2016, 8, 277. Copyright © 2016 MDPI AG.*

❖ ***Redox-driven molecular gates***

The development of redox driven molecular gates have been widely explored, mainly due to the biological relevance of redox agents and redox reactions. Most of the reported systems can be classified into two main categories: (i) those based on rotaxanes and pseudorotaxes where supramolecular ensembles between macrocycles (like cyclophanes, curcubiturils or cyclodextrins) and an organic chain anchored to the external surface of the porous scaffold control the open/close state of the gate; and (ii) those based on disulphide-linked capping agents (eg. polymers or inorganic nanoparticles) that are detached by reducing agents like glutathione or DTT. Interestingly, some of these systems are reversible which means that the gate can be opened and closed repeatedly by changing the redox conditions of the environment.

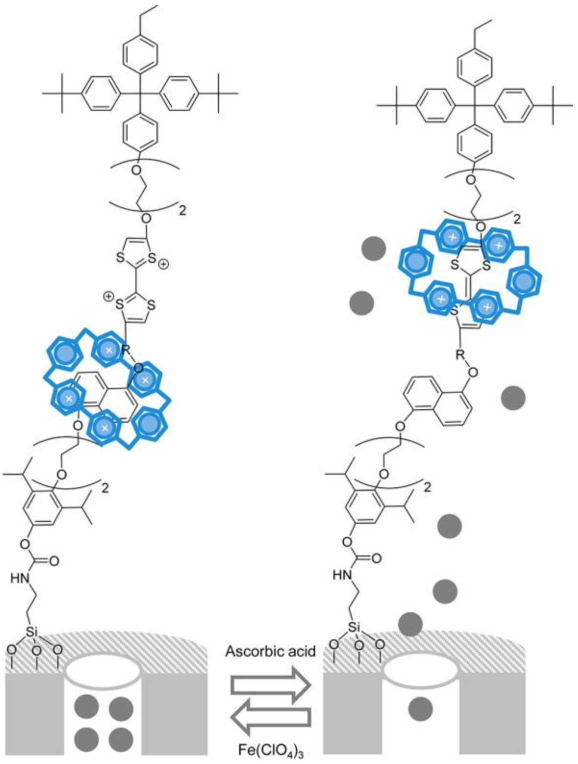

Figure 20. Reversible redox-driven molecular gate. *Reprinted with permission from Chem. Rev. 2016, 116, 516. Copyright © 2016 American Chemical Society*.

Nobel Laureate James Fraser Stoddart and co-workers reported one of the first examples of a reversible redox-driven molecular gate in 2004 (Figure 20).[61] They synthesized a bistable[2]rotaxane that consisted of the macrocycle cyclobis(paraquat-*p*-phenylene) ($CBPQT^{4+}$), a tetrathiafulvalene (TTF) and a dioxynaphthalene (DNP) stations separated by an oligoethylene glycol chain, and a terminal rigid terphenylene as the stopper. The material was loaded with an iridium complex or Rh B and the rotaxane was anchored via the formation of a carbamate bond with isocyanate moieties on the silica surface. In this supramolecular ensemble, the oxidation of TTF, using $Fe(ClO_4)_3$, to give a TTF^{2+} promoted the movement of the $CBPQT^{4+}$ ring to the DNP station and resulted in the blocking of the pores. Upon addition of ascorbic acid, the TTF^{2+} unit was reduced back to the neutral TTF which induced the movement of the macrocycle ring to the TTF station (due to its higher affinity compared to the complex with DNP). Since the TTF station was farther away from the silica surface, the movement of the macrocycle unblocked the pores and resulted in the release of the cargo. The release experiments were conducted in organic solvent due to the properties of the gating ensemble.

Similar systems have also been reported by the same group and also by others.[45] One of the challenges in this kind of systems is the multiple and complex steps required for synthesis the gating ensemble.

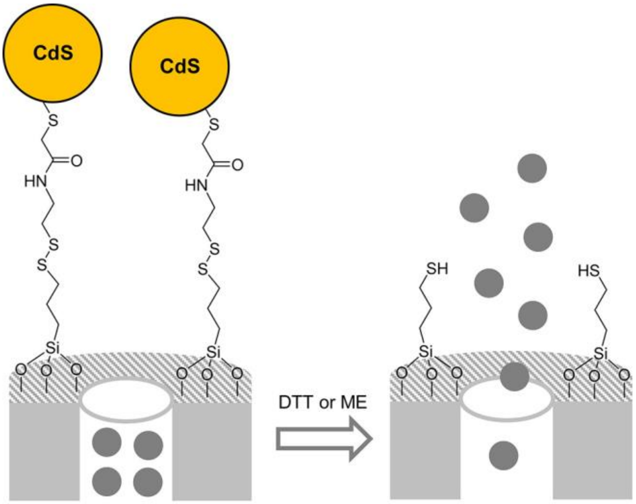

Figure 21. Schematic representation of a redox-driven molecular gate based on the rupture of disulfide bonds, reported by Lin and co-workers in 2003. *Reprinted with permission from Chem. Rev. 2016, 116, 516. Copyright © 2016 American Chemical Society*.

On the other hand, one of the first examples of redox-driven materials based on the reduction of disulfide bonds was reported by Lin and co-workers in 2003 (Figure 21).[62] The authors used CdS nanoparticles as a capping agent anchored through a disulfide linker to MSNPs. Mercaptopropyl-modified MSNPs were synthesized via a co-condensation method and then the external mercapto moieties were reacted with (2-pyridyldisulfanyl)ethylamine to yield (2-propyldisulfanyl)ethylamine groups. Afterward, the resulting MSNPs were loaded with vancomycin or adenosine triphosphate (ATP) and capped via an amidation reaction with 2 nm CdS nanoparticles functionalized with mercaptoacetic acid. The resulting gated materials showed a release of less than 1% in PBS after 12 hours. On the contrary, in the presence of the reducing agents dithiotheritol (DTT) or mercaptoethanol (ME), the disulfide bridges that linked the CdS were broken and this resulted in a fast delivery of the entrapped cargo. The system was tested in a culture of neuroglial cells. Upon perfusion of ME, ATP was released from the MSNPs and bind to its corresponding receptor in the cell surface which triggered a rapid increase in intracellular Ca^{2+}.

❖ ***Molecule- and biomolecule-driven molecular gates***

Gated materials can also be designed to respond to specific molecules or biomolecules. In these cases, the gating mechanism is based on supramolecular interactions or chemical reactions between the capping ensemble and the target molecule or biomolecule. Examples of gated materials that respond to anions, cations, neutral molecules, and biomolecules have been reported.[48] Although these materials are diverse, three main categories of gating ensembles have been used: (i) oligonucleotides for recognizing complementary strands or certain analytes (using aptamers and DNAzymes), (ii) supramolecular ensembles responsive to small molecules (mainly anions and cations), (iii) peptide sequences or organic groups that are hydrolyzed by certain enzymes. Designing molecular gates for recognition of small molecules is not a trivial task and less examples have been reported compared to other stimuli.

The first example of an oligonucleotide-gated material was reported by Martínez-Máñez's group in 2013 (Figure 22).[63] In this work, 100 nm MSNPs were loaded with a fluorescent cargo (fluorescein) and then the external surface was functionalized with 3-aminopropyltriethoxysilane (APTES). Aminopropyl groups are positively charge at neutral pH and its interaction with a 21-bases oligonucleotide (negatively charged) resulted in the capping of the porous material. The opening mechanism was based in the displacement of the capping oligonucleotide by hybridization with its complementary strand. The same researchers reported later the use a similar system for the detection of *Mycoplasma* genomic DNA.[64] Additionally, other examples of oligonucleotide-capped materials include, for instance, the use of specific aptamers for detection of selected analytes such as thrombin,[65] ochratoxine,[66] and As(III).[67]

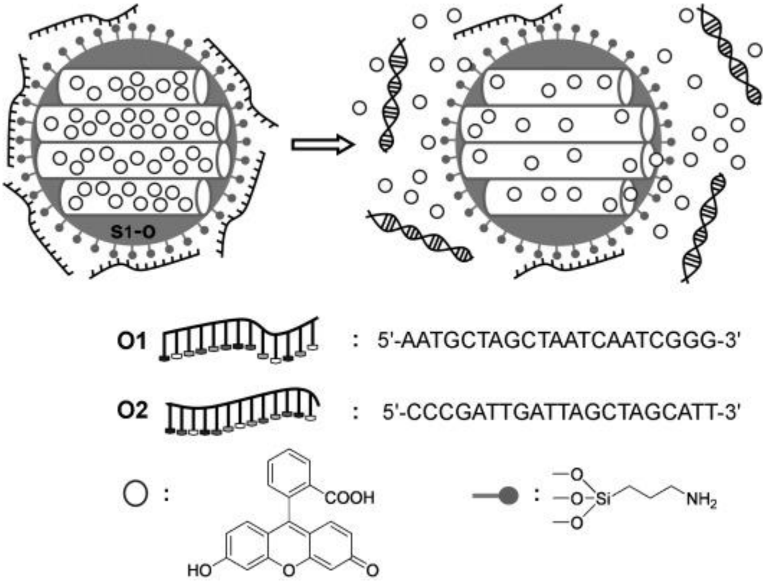

Figure 22. Representation of a gated material functionalized with APTES and capped with single-sranded oligonucleotide O1 for cargo release triggered by the complementary strand O2. *Reprinted with permission from Angew. Chem. Int. Ed. 2010, 49,7281. Copyright © 2010 Wiley-VCH.*

Recently, S. El Sayed and co-workers reported an illustrative example of MSNPs capped with a supramolecular complex for detection of cyanide (Figure 22).[68] MSNPs were loaded with $[Ru(bpy)_3]Cl_2$ and functionalized with a macrocyclic nickel (II) complex subunits, and capped with a sterically hindering anion (hexametaphosphate) by electrostatic interactions with the nickel complex. In the absence of cyanide, the release was negligible due to the blockage of the pore oultets by the bulky supramolecular ensemble. In contrast, addition of cyanide induced demetallation of nickel(II) complexes and the removal of the capping hexametaphosphate from the silica surface, allowing the release of the dye with the consequent increase in fluorescence signal. The system was selective toward cyanide with a limit of detection of 2 μM.

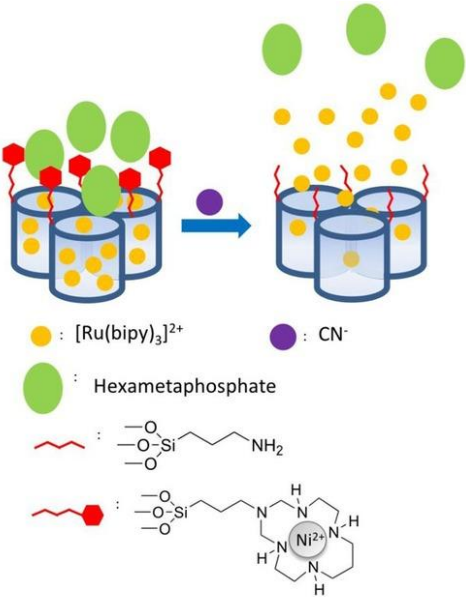

Figure 23. Schematic representation of a gated material for cyanide recognition using a supramolecular complex as the gating ensemble. *Reprinted with permission from Chem. Asian J. 2017, 18, 2670. Copyright © 2017 Wiley-VCH*.

Using enzyme-inhibitor interactions, Martínez-Máñez and co-workers have very recently prepared acetylcholinesterase-capped nanoparticles capable of delivering Rh B selectively in the presence of the nerve agent simulant diisopropyl fluorophosphate (DFP) (Figure 24).[69] MSNPs were loaded with Rh B and the external surface was functionalised with a pyridostigmine derivative. Pyridostigmine is a well-known acetylcholinesterase reversible inhibitor. Finally, pores were capped by the interaction between the acetylcholinesterase active-site and the anchored pyridostigmine derivative. DFP is a stronger inhibitor than pyridostigmine and was able to displace acetylcholinesterase from the silica surface, which resulted in cargo delivery. The detection system responded selectively to DFP compared to other nerve agent simulants and organophosphorus derivatives.

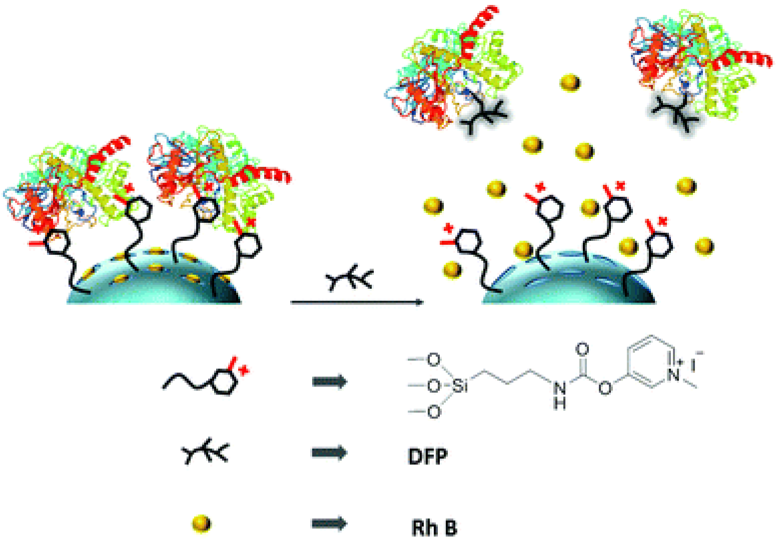

Figure 24. Schematic representation of a DFP-recognition system based on enzyme-inhibitor interactions. *Reprinted with permission from J. Mater. Chem. B 2017, 5, 3069. Copyright © 2017 The Royal Society of Chemistry.*

Furthermore, an example of a glucose-responsive delivery system was reported by Lu and co-workers. The external silica surface of the MSNPs was functionalised with prop-2-yn-1-yl(3-(triethoxysilyl)propyl) carbamate. Then, D-(+)-glucosamine was grafted through a click chemistry reaction. Rh B was loaded into the pores and glucose oxidase (GOx) was used as capping agent via the formation of a complex with the grafted inhibitor (D-(+)-glucosamine) In the presence of glucose, GOx was displaced from the nanoparticles and a proportional dye release was observed. Other tested monosaccharides (i.e., fructose, mannose and galactose) did not induce payload release.[70]

On the other hand, Villalonga, Martínez-Máñez and co-workers demonstrated that gating ensembles and enzymatic effectors can be integrated in a single nanodevice via the use of Janus-type nanoparticles with opposing gold and mesoporous silica faces (Figure 25).[71] First, the authors developed the synthesis of this kind of Janus nanoparticles based on a masking method. Afterward, the mesoporous silica matrix was loaded with $[Ru(bpy)_3]Cl_2$ and functionalized on the external surface with 3-(2-aminoethylamino)propyl trimethoxysilane that acted as the molecular gate. Aside from this, the gold side was functionalized with thiol-modified urease enzyme. In acetate buffer at pH 5.0, the nanoparticles showed a negligible release due to blockage of the pores produced by the protonation of polyamines. In the presence of urea, a clear delivery of the entrapped ruthenium complex took place. The opening mechanism was based on the urease-mediated transformation of urea into CO_2 and NH_3, which induced a rise in pH and the subsequent deprotonation of polyamines leading to cargo release.

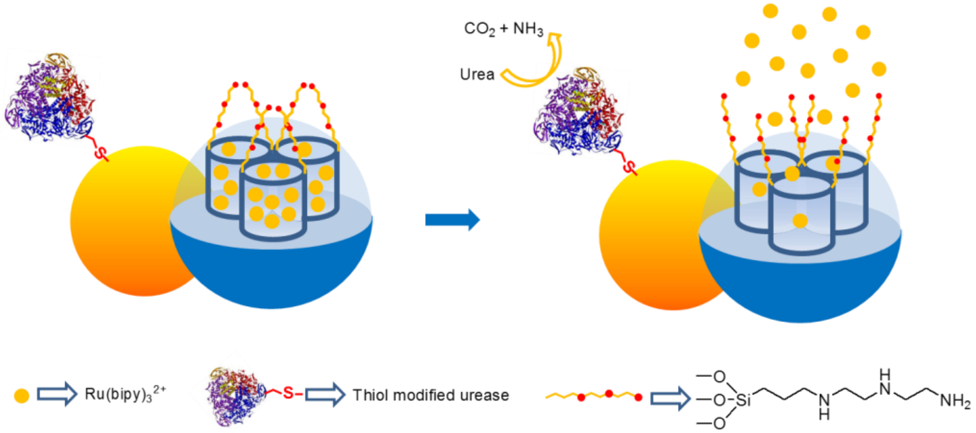

Figure 25. Representation of a urea-responsive delivery system based on gold-mesoporous silica nanoparticles capped with polyamines.

Regarding the design of enzyme-responsive delivery system, the strategy is usually based on capping the particles with organic groups that are hydrolyzed by the target enzyme.[72] As an example, Martínez-Máñez and co-workers prepared peptide-capped MSNPs loaded with a safranin O for cargo delivery triggered by the enzyme caspase 3 (C3) (Figure 26).[73] The peptide (KKGDEVDKKARDEVDK) contained two repeats of a target sequence that is hydrolyzed by C3 (DEVD). First, MSNPs were functionalized with 3-(azido-propyl)triethoxysilane, loaded with the dye and then the alkyne-containing peptidic sequence was attached by "click" reaction with the azide groups on the silica surface. In the absence of C3, the system showed negligible release whereas in the presence of the enzyme a remarkable cargo release was observed due to hydrolysis of the peptidic sequence. The prepared MSNPs were introduced in HeLa cells by electroporation in order to avoid endocytosis taking into account the cytoplasmic location of C3. Cells were treated or not with staurosporin which induces apoptosis with the subsequent activation of C3 in the cytosol. Safranin delivery in cells was observed only when C3 was activated.

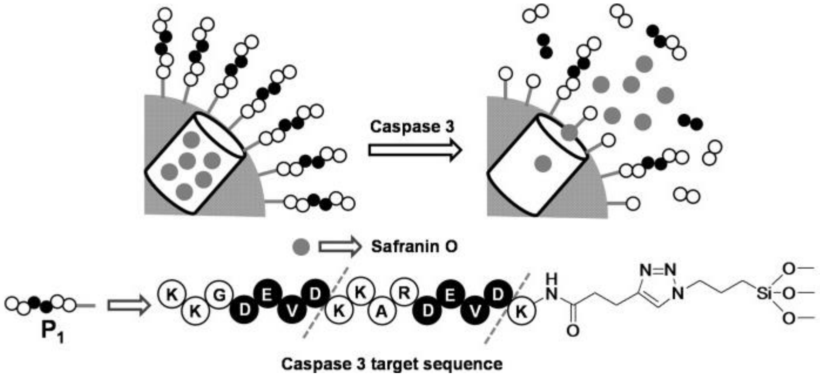

Figure 26. Example of a peptide-capped gated material for controlled delivery triggered by the enzyme caspase 3. *Adapted with permission from Chem. Eur. J.* 2015, *21*, 15506. Copyright © 2015 Wiley-VCH.

1.5 Janus particles

Janus is a god of the ancient Roman religion and mythology. It is the god of beginnings and endings, transitions, gates, passages and duality. It was honoured in the beginning and ending of a conflict, and hence before war and after peace proclamation. It is usually represented with two faces, one looks to the future and the other to the past, and the month January is thought to be named for Janus.

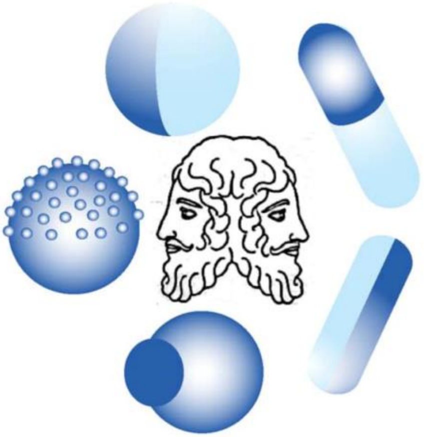

Figure 27. Schematic illustration of the two-faced Roman god Janus (middle) and Janus particles of different morphologies and shapes. *Reprinted with permission from Analyst 2016, 141*, 3526. *Copyright ©2016 The Royal Society of Chemistry.*

In the scientific literature, the term Janus is used to define particles that have two (or more) surfaces with different chemical and physical properties.[74] This term Janus was first used in 1988 in an article by C. Casagrande and M. Veyssie in which they reported the preparation of glass beads that were hydrophobic on one side and hydrophilic on the other.[75] Three years later, Pierre-Gilles de Gennes in his speech as Nobel Laurate (for his outstanding contributions in the study of soft materials, crystal liquids and polymers) introduced the term Janus particles to the scientific society.[76] He envisioned that that Janus particles with anisotropic surfaces would have interesting properties and applications not possible for particles of uniform composition.

Over the last decade, a diverse variety of Janus architectures for different applications have been reported. As depicted in Figure 27, Janus particles with different morphologies and shapes have been designed like half-and-half hemispheres, rods and dumbbell-, acorn- and snowman-shaped particles.[77] Although many of the reported examples of Janus particles are in the microscale, the development of nanosized Janus particles has also been recently explored.[74,77] One of the main appeals of Janus particles is that they allow two different types of chemistry to happen on the same particle. Another advantage is that one of its surfaces can have certain magnetic, electrical or optical properties.

Due to its diverse nature, applications of Janus particles range from catalysis and emulsion stabilization to sensing, drug delivery and theranostics.[78] For instance, She and co-workers prepared Janus-like Au-TiO_2 nanoparticles that were applied for the photocatalytic generation of hydrogen (under visible-light irradiation thanks to TiO_2 particles) and subsequent reduction of 4-nitrophenol to 4-aminophenol catalyzed on the gold surface.[79] In another work, spherical amphiphilic Janus polymeric nanoparticles were applied as stabilizers in the emulsion polymerization of styrene and *n*-butylacrylate.[80]

On the other hand, chemically-propelled Janus micro- and nano-motors have been build based on the incorporation of platinum or other catalysts into one or more building blocks of the Janus particle.[81] Such micro and nano-motors exhibit self-propulsion due to the decomposition of H_2O_2 catalysed by the platinum side (Figure 28). Regarding biomedical applications, an interesting example was reported by Jiang and co-workers in which one side of the Janus Fe_3O_4-Ag nanoparticle was magnetic and the other fluorescent, thus enabling simultaneous magnetic hyperthermia and imaging.[82] In another example, Hsieh and co-workers prepared Janus nanoparticles consisting on roughened gold coating on one side and polystyrene on the other that was employed for targeting (thanks to anti-HER-2 antibodies on the polystyrene surface) of cancer cells, SERS imaging (thanks to the gold surface) and intracellular drug delivery (previously anchored through the gold surface by disulphide linkages).[83]

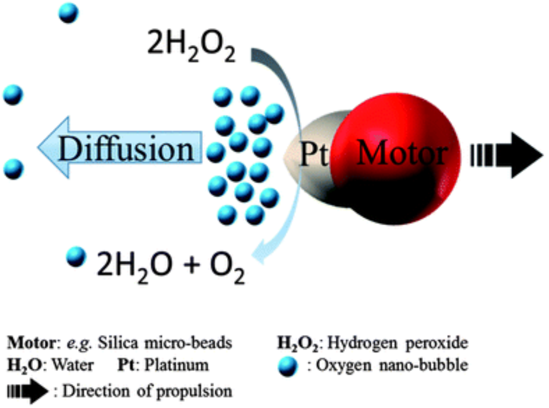

Figure 28. Schematic illustration of a Janus micro-motor fueled by hydrogen peroxide which is catalytically transformed to oxygen on the platinum surface. *Reprinted with permission J. Mater. Chem. B 2014, 2, 2395. Copyright © 2014 The Royal Society of Chemistry.*

The Janus Au-mesoporous silica nanoparticles that are object of this thesis have also been employed (by Villalonga, Pingarrón and co-workers) as functional elements to design an H_2O_2 electrochemical sensing system (Figure 29).[84] In that study, the starting Au-MSNPs were functionalized on the silica face with horseradish peroxidase (HRP) and with streptavidin on the gold surface in consecutive steps. Methoxypoly(ethylene glycol) thiol (PEG-SH) was also attached to the gold face in order to improve nanoparticle dispersion in water. Then, the resulting nanoparticles were immobilized on biotin-functionalized gold electrodes using biotin-streptavidin recognition and the performance of the electrochemical system was evaluated. The sensing paradigm was based on the cathodic current increase produced in the presence of H_2O_2 due to its electrocatalyzed transformation mediated by HRP. The system showed improved performance thanks to the biotin-streptavidin recognition, compared to immobilization of particles by simple deposition-adsorption.

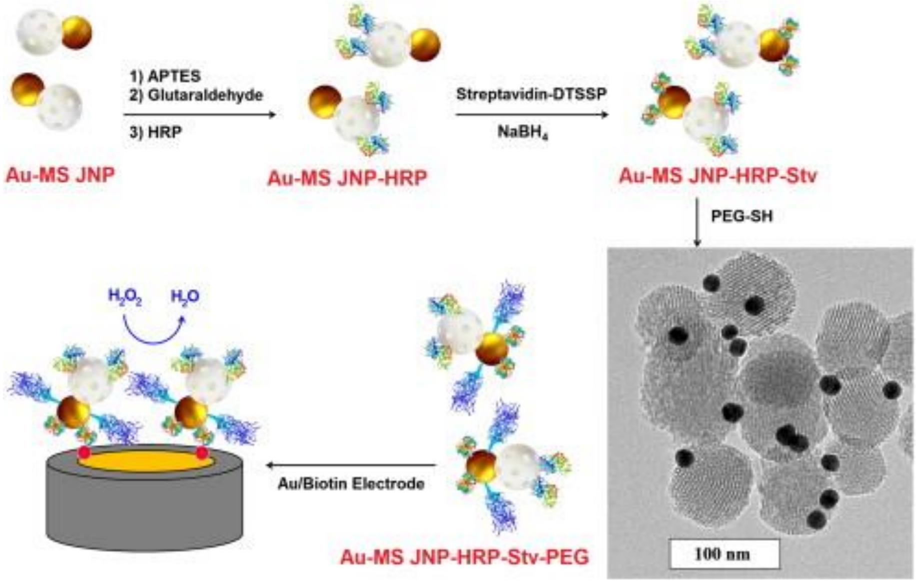

Figure 29. Schematic representation of the preparation of the Janus nanoparticle-based biorecognition-signalling system. *Reprinted with permission from Electrochem. Commun.* **2013**, *30*, 51. *Copyright © 2013 Elsevier B.V.*

Combining different material surfaces on a single particle opens a wide myriad of possibilities, so special effort has been put in the development of synthetic strategies. Although the synthetic conditions strongly vary on each case (depending on the composition, size, shape and properties of the final Janus particle), two main methods can be pointed out: vapour deposition on particle monolayers and functionalization at a Pickering emulsion. Notwithstanding, for preparing polymeric Janus particles other techniques like photopolymerization in microfluidic devices or self-assembly and cross-linking of block copolymers has also been reported.[74,77,85]

In the process of vapor deposition, the first step is to create a monolayer of particles on a glass slide or other kind of flat substrate. In a typical procedure, particles are dispersed in an appropriate solvent and an aliquot of a few microliters is manually added over the glass. Then, the solvent it let to evaporate, so ideally a closely packed monolayer of particles is obtained. Once dried, the top of the hemispheres is coated with metal films by electron-beam evaporation under high vacuum and low temperatures (Figure 30a). Thickness of the coating is controlled by the deposition time and can be between a few to a hundred nanometers. Afterward, the glass is scratched to separate the Janus particles in the form of a tiny powder. The major drawback of this method is that the amount of particles obtained is extremely limited.[77] Additionally, it can be challenging to obtain monolayers and if multilayers are obtained, only the external one will yield Janus particles. Moreover, if the particles are smaller than a few hundred nanometres, they can be bridged by the coating.

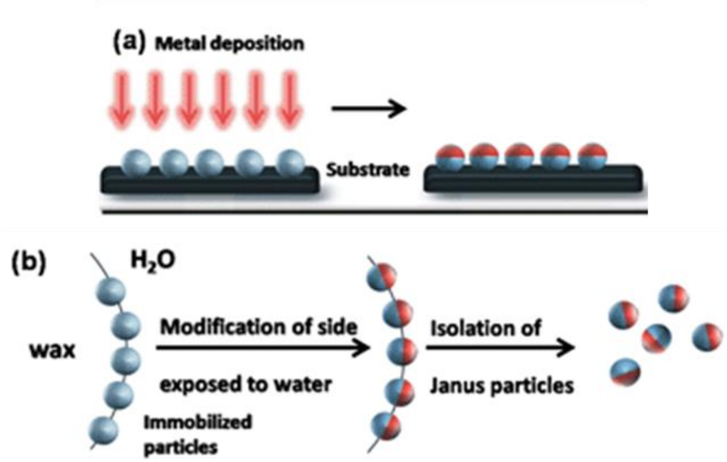

Figure 30. Overview of approaches for the preparation of Janus particles. (a) Vapor deposition technique involving immobilization of nanoparticles on a solid substrate. (b) Pickering emulsion route based on the functionalization at a water-liquid interfaces. *Adapted with permission from Soft Matter, 2008, 4, 663. Copyright © 2008 The Royal Society of Chemistry.*

The masking strategy based on creating a Pickering emulsion was first reported by Granick and coworkers.[86] Solid particles tend to adsorb onto the interface between two liquid immiscible phases to give a Pickering emulsion (Figure 30b). When the mixture is conveniently emulsified, wax droplets are formed so the total interface is highly increased and it can locate a large number of particles. In Granick’s work, they created a Pickering emulsion of water and wax at high temperature using silica microparticles as stabilizers. After cooling down, the wax was solidified and the microparticles were immobilized at the interface suppressing their rotational diffusion. Then, the particles were filtered and transfer into methanol so one part of the particle was exposed to the liquid phase whereas the other was embedded in the wax. Janus particles were then obtained by functionalizing the exposed side (with APTES and fluorescein) and later removing the wax by dissolving it in organic solvents like hexane or chloroform. The main advantage of this method is that it allows to obtain larger quantities of particles and that it avoids the use of a vapour deposition system. The Pickering emulsion route was later adapted by Villalonga, Martínez-Máñez and co-workers to develop the synthesis of Janus Au-mesoporous silica nanoparticles that are used in this thesis.[71] In particular, as shown in Figure 31, the synthesis of Janus Au-MSNPs is based on the partial functionalization of silica with thiolated silane derivative (by confinement at the water-wax interface) and the posterior attachment of Au-nanoparticles by the formation of Au-S bonds.

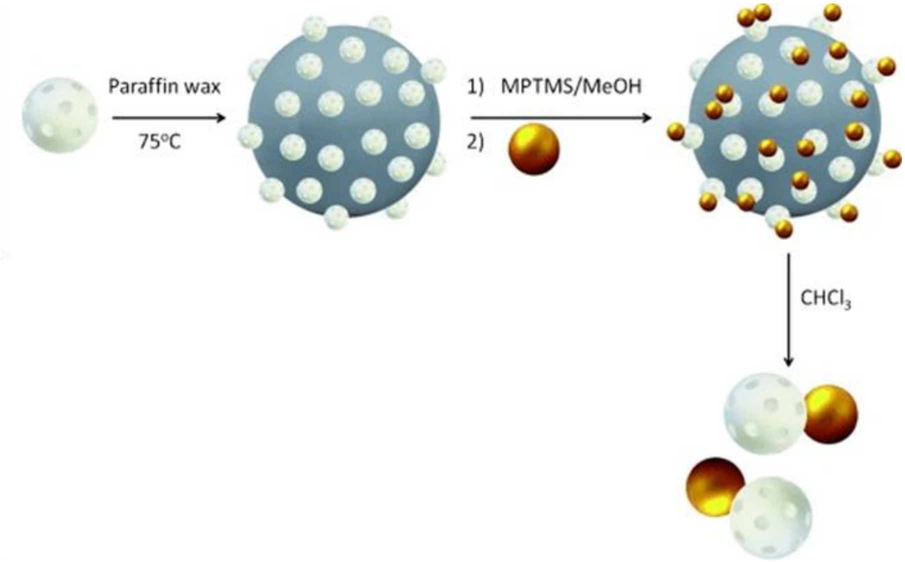

Figure 31. Schematic representation of preparation process of Janus Au-MSNPs developed by Villalonga and co-workers. *Adapted with permission from Chem. Eur. J. 2013, 19, 7889. Copyright © 2013 Wiley-VCH.*

1.6 Enzymes

Enzymes are the catalysts of life and nature. Thanks to enzymes, thousands of chemical reactions happen in our bodies every second. Enzymes accelerate the velocity of reactions that otherwise would take too long (or would not take place at all) and make them possible in a time short enough to be compatible with life. They are involved in vital processes such as reactions needed to digest food, send nerve signals, contract muscles and many others.

The information encoded in our DNA is translated into enzymes and other proteins. Each 3 nucleotides in DNA determine one amino acid in the sequence of enzymes and proteins. That is why some defects in a certain gene can result in enzyme-related diseases.[87] For instance, phenylketonuria is a hereditary disease caused by a defect in the gene for the hepatic enzyme phenylalanine hydroxylase. People affected of phenylketonuria are not able to digest the amino acid phenylalanine and need to follow a special diet.

There are around 75000 total enzymes in the human body, whereas smaller organisms like bacteria *E. Coli* have almost 3000.[88] According to the type of reaction catalyzed, enzymes are classified into 6 main categories:

1. Oxidoreductases: catalyze oxidation-reduction reactions.
2. Transferases: transfer a functional group from one molecule to another (e.g. a methyl or phosphate group).
3. Hydrolases: rupture of a substrate into two products by hydrolysis.
4. Lyases: catalyze elimination reactions or non-hydrolytic addition of a substrate to double bond.
5. Isomerases: catalyze isomerization changes within a single molecule.
6. Ligases: join two molecules with covalent bonds with consumption of ATP.

Every known enzyme is identified with an Enzyme commission number (EC number) according to the type of reaction they catalyse. This is a system of enzyme nomenclature that is internationally accepted and used by the most important enzyme databases like BRENDA (The Comprehensive Enzyme Information System).[89] More than 5000 types of enzymes are registered. The enzyme code consists of the letters “EC” follow by four numbers separated by dots. For example, for tripeptide aminopeptidase (also called tripeptidase) the code is EC 3.4.11.4, where each number specifies the following:

- EC 3 → belongs to the category of hydrolases
- EC 3.4 → belongs to the subcategory of hydrolases that act on peptide bonds
- EC 3.4.11 → are those hydrolases that cleave off the amino-terminal amino acid from a polypeptide
- EC 3.4.11.4 → are those EC 3.4.11 that act on tripeptide.

Enzymes are highly specific and efficient. They are able to accelerate chemical reactions 10^4-10^{15} times and in some cases the increase is even higher. For instance, the velocity constant for the hydrolysis of methyl phosphate is 10^{-20} M^{-1} s^{-1} without enzyme and $1.2 \cdot 10^6$ M^{-1} s^{-1} in the presence of alkaline phosphatase, that is a 10^{26}-fold increase and means that instead of taking a billion of years, the hydrolysis only takes milliseconds.[87]

The extraordinary efficiency and specificity of enzymes comes from the reduction of the reaction activation energy via interaction of substrates with the enzyme's active site. The enzyme's active site is composed of only a few amino acids (around 2-12), whereas the rest of the amino acids (between 62 to 2500) act as a scaffold that provides structural stability to the biomolecule. Substrate molecules bind to the active site by non-covalent interactions like electrostatic interactions, hydrogen bonding, metal-ligand interactions, hydrophobic interactions, π- π interactions and van der Waal forces.

The "lock and key" model was proposed in 1894 by Emil Fischer to explain enzyme specificity.[90] According to this model, the enzyme's active site and its substrate fit complementarily like a specific key fits in its lock (Figure 32). Later in 1958, Daniel Koshland (1920-2007) suggested a modification of the lock and key model and proposed the "induced fit model", also known as the "glove and hand model".[91] It takes into account that enzymes are flexible structures and once the substrate interacts with the active site, there is a molding effect that enables the enzyme to perform its catalytic function.

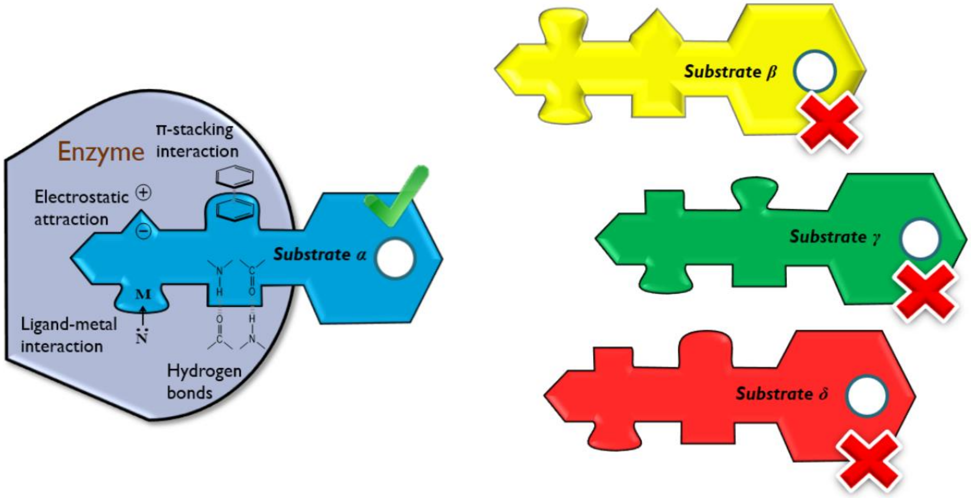

Figure 32. Schematic illustration of the "lock and key" model proposed by Fisher for explaining enzyme-substrate specificity.

Nowadays, enzymes are widely used in different industries as a unit of the production process or as a component of the final product (see Table 1). In this regard, enzyme technology can be defined as the interdisciplinary field that deals with the application of enzymes in the production of goods and services.[92] Its applications range from standardized industrial processes (e.g. in food, chemical, pharmaceutical, textile, paper and other industries) to synthesis and discovery of new drugs and products. Since the first protease for detergent formulation was launched to the market in 1963, the industrial and commercial use of enzymes has been in continuous increase.[93]

Hundreds of enzymes are currently commercially available thanks to the progress in large-scale enzyme production.[94] There are two main methods for the obtention of enzymes. First, some enzymes can be directly extracted from certain plants, animals or microorganisms that produce them in large quantities. This is the case of urease and acetylcholinesterase that are extracted from jack beans and electric eel respectively. Another method is the production of enzymes by means of genetic engineering using genetically modified organism of plants. The gene that encodes the enzyme is inserted in a host microorganism like yeast, bacteria or fungi that is then cultured under the appropriate conditions. These organisms can reproduce very fast yielding a large amount of the desired enzyme that in many cases is simply released in extracellular vesicles. Depending on the applications, if required, the enzyme is purified using chromatographic techniques.

Table 1. Some examples of enzyme industrial applications.

Industry	Enzyme	Technical benefits / Application
Biofuel	Cellulases, ligninases	Breakdown of cellulose and biomass for production of ethanol and other biofuels
Detergent	Proteases, amylases, lipases	Removing protein, starch, and fat stains and residues
Dairy	Chymosin, lipases, lysozymes	Cheese manufacturing
	Lactases	Breakdown of lactose in milk processing to avoid lactose intolerance
Juice	Pectinases, cellulases	Clarify fruit juices and lowering viscosity
Starch	Amylases	Obtainment of glucose and syrups from starch
Brewing	Pullululanases	Adjust fermentation and hydrolyzing starch
Cosmetic	Oxidases and peroxidases	Hair dyeing, toothpastes and mouthwashes
Textile and paper	Laccases	Bleaching to improve whiteness
	Cellulases	Soother and glossier appearance by hydrolyzing cellulose fibbers
Pharmaceutical	Hydrolases, oxygenases, dehydrogenases	Synthesis of chiral compounds, antibiotics and drugs
	Proteases	Remove proteins on contact lenses

Although it has been scarcely explored, combining the extraordinary properties of enzymes and nanomaterials holds great potential for the construction of smart devices with advanced capabilities. Incorporation of enzymes on micro- or nanosystems can introduce certain functions (based on specific substrate recognition and transformation) that would be very difficult to achieve by means of artificial chemical components. For example, Sánchez and co-workers reported the use of enzymes (catalase, glucose oxidase or urease) for the construction of silica nanomotors fueled by their respective substrates (H_2O_2, glucose and urea).[95] In those cases, the transformation of the substrate by the enzyme anchored on one side of the nanoparticle produces a propelling force that induces the movement of the nanodevice. In another example, Wilson, van Hest and co-workers created polymeric stomatocytes that allowed the entrapment of multiple enzymes and conferred the system sustained autonomous movement based on an out-of-equilibrium enzymatic cascade.[96] On the other hand, A. Sen and co-workers have developed enzyme-powered micropumps which are fluidic systems with enzymes anchored to their surface (catalase, urease, glucose oxidase or lipase) that induce the pumping of solutions containing their substrates.[97] Recently, W. Yang and coworkers developed a catalyst nanoarchitecture in which graphene oxide nanosheets are functionalized with closely-arranged enzymes and the substrate is efficiently channeled between active centers speeding the reaction kinetics.[98] Additionally, several examples of glucose-responsive insulin-delivery systems have been developed based on the incorporation of glucose oxidase in hydrogels, MOFs, inorganic nanomaterials or polymers[99]. In other studies, Walther and co-workers combined esterase and urease on a pH-responsive DNA hydrogel to modulate the sol-gel state according to substrates (ethyl acetate/urea) presence,[100] and van Hest's group developed urease-containing polymeric particles that change their diameter according to urea concentrations.[101]

The development of enzyme-based micro and nanodevices is receiving growing attention in recent years, as showed in the above cited studies. However, the field is still in its infancy and offers a broad range of possibilities to advance towards the design of smart devices with application in a number of different areas such as sensing, drug delivery and switchable materials. In this context, this PhD thesis has aimed to explore the possibilities offered by enzyme incorporation on nanomaterials and to develop several examples of hybrid nanodevices using enzymes as functional components.

1.7 References

1. J. A. Martín-Gago, C. Briones, E. Casero, P. A. Serena, *El nanomundo en tus manos: Las claves de la nanociencia y la nanotecnología*, Editorial Critica, **2014**.
2. R.P. Feynman, *Caltech Eng. Sci.* **1960**, *23*, 22-36.
3. N. Taniguchi, *Proc. Intl. Conf. Prod. Eng. Tokyo, Part II, Japan Society of Precision Engineering*, **1974**.
4. G. Binnig, H. Rohrer, *Surf. Sci.* **1983**, *126*, 236-244.
5. G. Binnig, C. Quate, C. Gerber, *Phys. Rev. Lett.* **1986**, *56*, 930-934.
6. K. S. Novoselov, A. K. Geim, S. V. Morozov, D. Jiang, Y. Zhang, S. V. Dubonos, I. V. Grigorieva, A. A. Firsov, *Science* **2004**, *306*, 666-669.
7. H. W. Kroto, J. R. Heath, S. C. O'Brien, R. F. Curl, R. E. Smalley, *Nature* **1985**, *318*, 162-163.
8. S. Iijima, *Nature* **1991**, *354*, 56-58.
9. R. Tseng, J. Huang, J. Ouyang, R. Kaner, Y. Yang, *Nano Lett.* **2005**, *5*, 1077–1080.
10. I. Valov, E. Linn, S. Tappertzhofen, S. Schmelzer, J. van den Hurk, F. Lentz, R. Waser, *Nat. Commun.* **2013**, *4*, 1771.
11. D. Tarn, C. E. Ashley, M. Xue, E. C. Carnes, J. I. Zink, C. J. Brinker, *Acc. Chem. Res.* **2013**, *46*, 792-801.
12. S. Sánchez, L. Soler, J. Katuri, *Angew. Chem. Int. Ed.* **2015**, *54*, 1414-1444.
13. R. Bott, *Springer Handbook of Nanotechnology*, Springer, **2014**.
14. K. Narendra, S. Kumbhat, *Essentials in Nanoscience and Nanotechnology,* John Wiley & Sons, **2016**.
15. D. Bobo, K. J. Robinson, J. Islam, K. Thurecht, S. R. Corrie, *Pharm. Res.* **2016**, *33*, 2373-2387.
16. a) K Rurack, R. Martínez-Máñez, *The Supramolecular Chemistry of Organic-Inorganic Hybrid Materials*, John Wiley & Sons, **2010;** b) X. Y. Ling, D. N. Reinhoudt, J. Huskens, *Pure Appl. Chem.* **2009**, *81*, 2225-2233.
17. a) J. M. Lehn, *Nobel Lectures: Chemistry 1981-1990*, World Scientific Publishing Co., **1992**, 444-491; b) G. R. Desiraju, *Nature* **2001**, *412*, 397-400.
18. J. M. Lehn, *Supramolecular chemistry: Concepts and Perspectives*, Wiley-VCH, **1995**.
19. a) K. Ariga, T. Kunitake, *Supramolecular Chemistry-Fundamentals and applications*, Springer, **2006**; b) J. W. Steed, J. L. Atwood, *Supramolecular Chemistry*, John Wiley & Sons, **2009**.
20. a) R. Martínez-Máñez, F. Sancenón, *Chem. Rev.* **2003**, *103*, 4419-4476; b) L. E. Santos-Figueroa, M. E. Moragues, E. Climent, A. Agostini, R. Martínez-Máñez, F. Sancenón, *Chem. Soc. Rev.* **2013**, *42*, 3489-3613.
21. a) A. B. Descalzo, R. Martínez-Máñez, F. Sancenón, K. Hoffmann, K. Rurack, *Angew. Chem. Int. Ed.* **2006**, *45*, 5924-5948: b) M.-V. Salvia, G. Salassa, F. Rastrelli, F. Mancin, *J. Am. Chem. Soc.* **2015**, *137*, 11399-11406; c) Y.-W. Yang, Y.-L. Sun, N. Song, *Acc. Chem. Res.*, **2014**, *47*, 1950-1960.
22. K. Ariga, J. P. Hill, M. V. Lee, A. Vinu, R. Charvet, S. Acharya, *Sci. Technol. Adv. Mater.* **2008**, *9*, 014109.
23. O. I. Willner, Y. Weizmann, R. Gill, O. Lioubashevsky, R. Freeman, I. Willner, *Nat. Nanotechnol.* **2009**, *4*, 249-254.
24. a) IUPAC, *Pure appl. Chem.* **1972**, *31*, 578; b) X. S. Zhao, *J. Mater. Chem.* **2006**, *16*, 623-625.
25. C. Perego, R. Millini, *Chem. Soc. Rev.* **2013**, *42*, 3956-3976.
26. K. M. Thomas, *Catal. Today*, **2007**, *120*, 389-398.

27. X. Liu, Y. Du, Z. Guo, S. Gunasekaran, C.-B. Ching, Y. Chen, S. S. J. Leong, Y. Yang, *Micropor. Mesopor. Mater.* **2009**, *122*, 114-120.
28. C. Ispas, I. Sokolov, S. Andreescu, *Anal. Bioanal. Chem*. **2009**, *393*, 543-554.
29. M. Vallet-Regi, M. Colilla, I. J. Izquierdo-Barba, *J. Biomed. Nanotechnol.* **2008**, *4*, 1-15.
30. I. I. Slowing, B. G. Trewyn, S. Giri, V. S.-Y. Lin, *Adv. Funct. Mater*. **2007**,*17*, 1225-1236.
31. M. J. Climent, A. Corma, S. Iborra, J. Primo, *J. Catalysis* **1995**, *151*, 60-66.
32. J. S. Beck, J. C. Vartuli, W. J. Roth, M. E. Leonowicz, C. T. Kresge, K. D. Schmitt, C. T. W. Chu, D. H. Olson, E. W. Sheppard, S. B. McCullen, J. B. Higgins, J. L. Schlenker, *J. Am. Chem. Soc.* **1992**, *114*, 10834-10843.
33. C. T. Kresge, W. J. Roth, *Chem. Soc. Rev.* **2013**, *42*, 3663-3670.
34. D. Zhao, J. Feng, Q. Huo, N. Melosh, G. H. Fredrickson, B. F. Chmelka, G. D. Stucky, *Science* **1998**, *279*, 548-*552.*
35. J. G. Croissant, Y. Fatieiev, A. Almalik, N. M. Khashab, *Adv. Healthcare Mater.* **2018**, *7*, 1700831.
36. M. C. Llinàs, D. Sánchez-García, *Afinidad LXXI* **2014**, *565*, 20-31.
37. F. Hoffmann, M. Cornelius, J. Morell, M. Fröba, *Angew. Chem. Int. Ed.* **2006**, *45*, 3216-3251.
38. A. Casula, A. Llopis-Lorente, A. Garau, F. Isaia, M. Kubicki, V. Lippolis, F. Sancenón, R. Martínez-Máñez, A. Owzarzak, C. Santi, M. A. Scorciapino, C. Caltagirone, *Chem. Commun.* **2017**, *53*, 3729-3732.
39. B. Hatton, K. Landskron, W. Whitnall, D. Perovic, G. A. Ozin, *Acc. Chem. Res.* **2005**, *38*, 305-312.
40. K. S. W. Sing, D. H. Everett, R. A. W. Haul, L. Moscou, R. A. Pierotti, J. Rouquerol, T. Siemieniewska, *Pure Appl. Chem.* **1985**, *57* ,603-619.
41. S. Brunauer, P. H. Emmett, T. Teller, *J. Am. Chem. Soc.* **1938**, *60*, 309-319.
42. E. P. Barrett, L. G. Joyner, P. P. Halenda, *J. Am. Chem. Soc.* **1951**, *73*, 373-380.
43. a) L. Nicole, C. Laberty-Robert, L. Rozesa, C. Sanchez, *Nanoscale* **2014**, *12*, 6267-6292; b) M. Faustini, L. Nicole, E. Ruiz-Hitzky, C. Sanchez, *Adv. Funct. Mater.* **2018**, *28*, 1704158.
44. a) Q. Zhang, E. Uchaker, S. L. Candelariaza, G. Gao, *Chem. Soc. Rev.* **2013**, *42*, 3127-3171; b) N. Linares, A. M. Silvestre-Albero, E. Serrano, J. Silvestre-Albero, J. García-Martínez, *Chem. Soc. Rev.*, **2014**, *43*, 7681-7717; c) T. Wagner, S. Haffer, C. Weinberger, D. Klaus, M. Tiemann, *Chem. Soc. Rev*. **2013**, *42*, 4036-4053; d) A. E. Garcia-Bennett, *Nanomedicine*, **2011**, *6*, 867-877; e) A. P. Wight and M. E. Davis, *Chem. Rev.* **2002**, *102*, 3589-3614.
45. a) E. Aznar, M. Oroval, L. Pascual, J. R. Murguía, R. Martínez-Máñez, F. Sancenón, *Chem. Rev.* **2016**, *116*, 561-718; b) C. Coll, A. Bernardos, R. Martínez-Máñez, F. Sancenón, *Acc. Chem. Res.* **2013**, *46*, 339-349.
46. a) N. K. Mal, M. Fujiwara, Y. Tanaka, *Nature* **2003**, *421*, 350-353; N. K. Mal, M. Fujiwara, Y. Tanaka, T. Taguchi, M. Matsukata, *Chem. Mater.* **2003**, *15*, 3385-3394.
47. a) Z. Li, J. C. Barnes, A. Bosoy, J. F. Stoddart, J. I. Zink, *Chem. Soc. Rev.* **2012**, *41*, 2590-2605; b) Y. Wang, Q. Zhao, N. Han, L. Bai, J. Li, J. Liu, E. Che, L. Hu, Q. Zhang, T. Jiang, S. Wang, *Nanomedicine* **2015**, *11*, 313-327; c) R. R. Castillo, M. Colilla, M. Vallet-Regí, *Expert. Opin. Drug Deliv.* **2017**, *14*, 229-243.
48. F. Sancenón, L. Pascual, M. Oroval, E. Aznar, R. Martínez-Máñez, *ChemistryOpen* **2015**, *4*, 418-437.
49. a) A. Bernardos, A. Aznar, C. Coll, R. Martínez-Máñez, J. M. Barat, M. D. Marcos, F. Sancenón, A. Benito, J. Soto, *J. Control. Release* **2008**, *131,* 181-189; b) *E.* Aznar, M. Dolores Marcos, R. Martínez-Máñez, F. Sancenón, J. Soto, P. Amorós, C. Guillem, *J. Am. Chem. Soc.* **2009**, *131*,

6833-6843; c) A. H. Teruel, C. Coll, A. M. Costero, D. Ferri, M. Parra, P. Gaviña, M. González-Álvarez, V. Merino, M. D. Marcos, R. Martínez-Máñez, F. Sancenón, *Molecules* **2018**, *23*, 375-377.

50. a) S. F. Lee, X. M. Zhu, Y. X. J. Wang, S. H. Xuan, Q. H. You, W. H. Chan, C. H. Wong, F. Wang, J. C. Yu, C. H. Cheng, K. C. Leung, *ACS Appl. Mater. Interfaces* **2013**, *5*, 1566-1574; b) W.-P. Li, P.-Y. Liao, C.-H. Su, C.-S. Yeh, *J. Am. Chem. Soc.* **2014**, *136*, 10062-10075; c) Z. F. Wang, X. Yang, J. Feng, Y. J. Tang, Y. Y. Jiang, N. Y. He, *Analyst* **2014**, *139*, 6088-6091; d) M. L. Yin, E. G. Ju, Z. W. Chen, Z. H. Li, J. S. Ren, X. G. Qu, *Chem. Eur. J.* **2014**, *20*, 14012-14017.
51. a) A. Ribes, E. Xifré-Pérez, E. Aznar, F. Sancenón, T. Pardo, L. F. Marsal, R. Martínez-Máñez, *Sci. Rep.* **2016**, *6*, 38649; b) L. Pla, E. Xifré-Pérez, A. Ribes, E. Aznar, M. D. Marcos, L. F. Marsal, R. Martínez-Máñez, F. Sancenón, *ChemPlusChem* **2017**, *82*, 337-341.
52. L. Polo, N. Gómez-Cerezo, E. Aznar, J.-L. Vivancos, F. Sancenón, D. Arcos, M. Vallet-Regí, R. Martínez-Máñez, *Acta Biomater.* **2017**, *50*, 114-126.
53. a) N. Song, Y.-W. Yang, *Chem. Soc. Rev.* **2015**, *44*, 3474-3504; b) J. Wen, K. Yang, F. Liu, Y. Xiu, S. Sun, *Chem. Soc. Rev.* **2017**, *46*, 6024-6045; c) J. Zhu, Y. Niu, Y. Li, Y. Gong, H. Shi, Q. Huo, Y. Liu, Q. Xu, *J. Mater. Chem. B.* **2017**, *5*, 1339-1352.
54. A. Agostini, F. Sancenón, R. Martínez-Máñez, M. D. Marcos, J. Soto, P. Amorós, *Chem*. Eur. *J.* **2012**, *18*, 12218-12221.
55. A. Hernández-Montoto, R. Montes, A. Samadi, M. Gorbe, J. M. Terrés, R. Cao-Milán, E. Aznar, J. Ibáñez, R. Masot, M. D. Marcos, M. Orzáez, F. Sancenón, L. B. Oddershede, R. Martínez-Máñez, *ACS Appl. Mater. Interfaces* **2018**, *33*, 27644-27656.
56. C. de la Torre, A. Agostini, L. Mondragón, M. Orzáez, F. Sancenón, R. Martínez-Máñez, M. D. Marcos, P Amorós, E. Pérez-Payá, *Chem. Commun.* **2014**, *50*, 3184-3186.
57. E. Yu, I. Galiana, R. Martínez-Máñez, P. Stroeve, M. D. Marcos, E. Aznar, F. Sancenón, J. R. Murguía, P. Amorós, *Colloids Surf. B* **2015**, *135*, 652-660.
58. E. Bringas, O. Koysuren, D. V. Quach, M. Mahmoudi, E. Aznar, J. D. Roehling, M. D. Marcos, R. Martínez-Máñez, P. Stroeve, *Chem. Commun.* **2012**, *48*, 5647-5649.
59. H. P. Rim, K. H. Min, H. J. Lee, S. Y. Jeong, S. C. Lee, *Angew. Chem. Int. Ed.* **2011**, *50*, 8853-8857.
60. H. Zhou, X. Wang, J. Tang, Y.-W. Yang, *Polymers* **2016**, *8*, 277.
61. T. D. Nguyen, H. R. Tseng, P. C. Celestre, A. H. Flood, Y. Liu, J. F. Stoddart, J. I. Zink, *Proc. Natl. Acad. Sci. U. S. A.* **2005**, *102*, 10029-10034.
62. C. Y. Lai, B. G. Trewyn, M. D. Jeftinija, K. Jeftinija, S. Xu, S. Jeftinija, V. S. Y. Lin, *J. Am. Chem. Soc.* **2003**, *125*, 4451-4459.
63. E. Climent, R. Martínez-Máñez, F. Sancenón, M. D. Marcos, J. Soto, A. Maquieira, P. Amorós, *Angew. Chem. Int. Ed.* **2010**, *49*, 7281-7283.
64. E. Climent, L. Mondragón, R. Martínez-Máñez, F. Sancenón, M. D. Marcos, J. R. Murgía, P. Amorós, K. Rurack, E. Pérez-Payá, *Angew. Chem. Int. Ed.* **2013**, *52*, 8938-8942.
65. M. Oroval, E. Climent, C. Coll, R. Eritja, A. Aviñó, M. D. Marcos, F. Sancenón, R. Martínez-Máñez, P. Amorós, *Chem. Commun.* **2013**, *49*, 5480-5482.
66. A. Ribes, S. Santiago-Felipe, A. Bernardos, M. D. Marcos, T. Pardo, F. Sancenón, R. Martínez-Máñez, E. Aznar, *ChemistryOpen* **2017**, *6*, 653-659.
67. M. Oroval, C. Coll, A. Bernardos, M. D. Marcos, R. Martínez-Máñez, D. G. Shchukin, F. Sancenón, *ACS Appl. Mater. Inerfaces* **2017**, *9*, 11332-11336.
68. S. Elsayed, M. Licchelli, R. Martínez-Máñez, F. Sancenón, *Chem. Asian J.* **2017**, *18*, 2670-2674.

69. L. Pascual, S. El Sayed, R. Martínez-Máñez, A. M. Costero, S. Gil, P. Gaviña, F. Sancenón, *Org. Lett.* **2016**, *18*, 5548-5551.
70. M. Chen, C. Huang, C. He, W. Zhu, Y. Xu, Y. Lu, *Chem. Commun.* **2012**, *48*, 9522-9524.
71. R. Villalonga, P. Díez, A. Sánchez, E. Aznar, R. Martínez-Máñez, J. M. Pingarrón, *Chem. Eur. J.* **2013**, *19*, 7889-7894.
72. A. Llopis-Lorente, B. Lozano, A. Bernardos, R. Martínez-Máñez, F. Sancenón, *J. Mater. Chem. B* **2017**, *5*, 3069-3083.
73. C. de la Torre, L. Mondragón, C. Coll, A. García-Fernández, F. Sancenón, R. Martínez-Máñez, P. Amorós, E. Pérez-Payá, M. Orzáez, *Chem. Eur. J.* **2015**, *21*, 15506-15510.
74. Y. Yi, L. Sanchez, Y. Gao, Y. Yu, *Analyst* **2016**, *141*, 3526-3539.
75. C. Casagrande, M. Veyssie, *C. R. Acad. Sci. Ser. II* **1988**, *306*, 1423-1425.
76. P. G. D. Gennes, *Science* **1992**, *256*, 495-497.
77. a) A. Walther, A. H. Müller, *Chem. Rev.* **2013**, *113*, 5194-5261; b) A. Walther, A. H. Müller, *Soft Matter* **2008**, *4*, 663-668.
78. Y. Song, S. Chen, *Chem. Asian J.* **2014**, *9*, 418-430.
79. Z. W. Seh, S. Liu, S. -Y. Zhang, M. S. Bharathi, H. Ramanarayan, M. Low, K. W. Shah, Y. -W. Zhang, M. -Y. Han, *Angew. Chem. Int. Ed.* **2011**, *50*, 10140-10143.
80. A. Walther, M. Hoffmann, A. H. Müller, *Angew. Chem. Int. Ed*. **2008**, *47*, 711-714.
81. a) X. Ma, K. Hahn, S. Sánchez, *J. Am. Chem. Soc.* **2015**, *137*, 4976-4979; b) L. K. E. A. Abdelmohsen, F. Peng, Y. Tu, D. A. Wilson, *J. Mater. Chem. B* **2014**, *2*, 2395-2408.
82. J. Jiang, H. Gu, H. Shao, E. Devlin, G. C. Papaefthymiou, J. Y. Ying, *Adv. Mater.* **2008**, *20*, 4403-4407.
83. H. -Y. Hsieh, T. -W. Huang, J. -L. Xiao, C. -S. Yang, C. -C. Chang, C. -C. Chu, L. -W. Lo, S. -H. Wang, P. -C. Wang, C. -C. Chieng, C. -H. Lee, F. -G. Tseng, *J. Mater. Chem.* **2012**, *22*, 20918-20928.
84. A. Sánchez, P. Díez, P. Martínez-Ruiz, R. Villalonga, J. M Pingarrón, *Electrochem. Commun.* **2013**, *30*, 51-54.
85. J. Zhang, B. A. Grzybowski, S. Granick, *Langmuir* **2017**, *33*, 6964-6977.
86. L. Song, S. Jiang, S. Granick, *Langmuir* **2006**, *22*, 9495-9499.
87. F. J. Plou, *Las enzimas*, CSIC, **2016**.
88. P. Barnes-Svarney, T. E. Svarney, *The Handy Biology Answer Book,* Visible Ink Press, **2015**.
89. I. Schomburg, A. Chang, S. Placzek, C. Söhngen, M. Rother, M. Lang, C. Munaretto, S. Ulas, M. Stelzer, A. Grote, M. Scheer, D. Schomburg, *Nucleic Acids Res.* ***2013***, *41*, 764-772.
90. E. Fischer, *Ber. Dtsch. Chem. Ges*. **1895**, 28, 1429-1438.
91. D. E. Koshland, *Proc. Natl. Acad. Sci.*, **1958**, *44*, 98-104.
92. J. B. van Beilen, Z. Li, *Curr. Opin. Biotech.* **2002**, *13*, 338-344.
93. S. Li, X. Yang, S. Yang, M. Zhu, X. Wang, *Comput. Struct. Biotech. J.* **2012**, *2*, e20120917.
94. A. Wolfgang, *Enzymes in Industry*: *Production and Applications*, 3rd Ed, Wiley-VCH, **2007**.
95. a) X. Ma, A. Jannasch, U. -R. Albrecht, K. Hahn, A. Miguel-López, E. Schäffer, S. Sánchez, *Nano Lett.* **2015**, *15*, 7043−7050; b) A. Hortelão, T. Patiño, A. Pérez-Jiménez, A. Blanco, S. Sánchez, *Adv. Funct. Mater.* **2017**, 1705086.
96. a) M. Nijemeisland, L. K. E. A. Abdelmohsen, W. T. S. Huck, D. Wilson, J. C. M. van Hest, *ACS Cent. Sci.* **2016**, *2*, 843-849; b) L. K. E. A. Abdelmohsen, M. Nijemeisland, G. M. Pawar, G.-J. A. Janssen, R. J. M. Nolte, J. C. M. van Hest, D. A. Wilson, *ACS Nano* **2016**, *10*, 2652−2660.
97. a) S. Sengupta, D. Patra, I. Ortiz-Rivera, A. Agrawal, S. Shklyaev, K. D. Dey, U. Córdova-Figueroa, T. E. Mallouk, A. Sen, *Nat. Chem.* **2014**, *6*, 415-416; b) I. Ortiz-Rivera, H. Shum, A. Agrawal, A.

Sen, A. C. Balazs, *Proc. Natl. Acad. Sci. U. S. A.* **2016**, *113*, 2585-2590; c) I. Ortiz-Rivera, T. M. Courtney, A. Sen, *Adv. Funct. Mater.* **2016**, *26*, 2135-2142.

98. M. Mathesh, J. Liu, C. J. Barrow, W. Yang, *Chem. Eur. J.* **2017**, *23*, 304-311.
99. Y. Duan, F. Ye, Y. Huang, Y. Qin, C. He, S. Zhao, *Chem. Commun.* **2018**, *54*, 5377-5380.
100. L. Heinen, T. Heuser, A. Steinschulte, A. Walther, *Nano Lett.* **2017**, *17*, 4989-4995.
101. H. Che, B. C. Buddingh, J. C. M. van Hest, *Angew. Chem. Int. Ed.* **2017**, *56*, 12581-12585.

Chapter 2: Objectives

Taking into account the growing interest in the development of smart nanodevices and materials, this PhD thesis has aimed to contribute to the field of nanotechnology and to develop several enzyme-functionalized hybrid nanodevices for sensing, controlled release and molecular communication at the nanoscale.

In particular, we have focused on the design, preparation, characterization and evaluation of nanodevices based on Janus gold-mesoporous silica nanoparticles equipped with enzymatic effectors, molecular gates and chromo-fluorogenic species or drugs.

The specific objectives have been:

- To develop a delivery system responsive to the neurotransmitter acetylcholine.

- To prepare an enzyme-controlled delivery system based on the commutation of a disulfide-linked molecular gate and evaluate the possibility to detect the presence of enzyme inhibitors.

- To design a system of communication between different nanodevices based on the interchange of chemical messengers mediated by enzymes and molecular gates.

- To design nanocarriers that respond to specific combinations of certain biomolecules mimicking Boolean logic functions and evaluate their performance to deliver drugs in cancer cells.

- To present a novel paradigm for preparing optical nanosensors based on the enzyme-mediated detachment of labelled-reporters from silica surfaces, and show its feasibility by developing a urea nanosensor.

3. Enzyme-Controlled Nanodevice for Acetylcholine-Triggered Cargo Delivery Based on Janus Au-Mesoporous Silica Nanoparticles

Enzyme-Controlled Nanodevice for Acetylcholine-Triggered Cargo Delivery Based on Janus Au-Mesoporous Silica Nanoparticles

A. Llopis-Lorente,[a,b,c] P. Díez,[d] C. de La Torre,[a,b,c] A. Sánchez,[d,e] F. Sancenón,[a,b,c] E. Aznar,[a,b,c] M. D. Marcos,[a,b,c] P. Martínez-Ruíz,[f] R. Martínez-Máñez*[a,b,c] and R. Villalonga*[d,e]

[a] Instituto Interuniversitario de Investigación de Reconocimiento Molecular y Desarrollo Tecnológico (IDM), Universitat Politècnica de València-Universitat de València (Spain).

[b] Departamento de Química, Universitat Politècnica de València, Camino de Vera s/n, 46022 Valencia (Spain). E-mail: rmaez@quim.upv.es

[c] CIBER de Bioingeniería, Biomateriales y Nanomedicina (CIBER-BBN).

[d] Department of Analytical Chemistry, Faculty of Chemistry, Complutense University of Madrid, 28040 Madrid (Spain). E-mail: rvillalonga@quim.ucm.es

[e] IMDEA Nanoscience, Cantoblanco University City, 28049 Madrid (Spain).

[f] Department of Organic Chemistry I, Faculty of Chemistry, Complutense University of Madrid, 28040 Madrid (Spain).

(Reprinted with permission from ***Chem. Eur. J.*** **2017, *23*, 4276-4281**.

3.1 Abstract

This work reports a new gated nanodevice for acetylcholine-triggered cargo delivery. We prepared and characterized Janus Au–mesoporous silica nanoparticles functionalized with acetylcholinesterase on the Au face and with supramolecular β-cyclodextrin:benzimidazole inclusion complexes as caps on the mesoporous silica face. The nanodevice is able to selectively deliver the cargo in the presence of acetylcholine (ACh) via enzyme-mediated acetylcholine hydrolysis, locally lowering the pH and opening the supramolecular gate. Given the key role played by ACh and its relation with Parkinson's disease and other nervous system diseases, we believe that these findings could help design new therapeutic strategies.

3.2 Introduction

Acetylcholine (ACh) is an essential neurotransmitter that operates in the central and peripheral nervous system.[1] It acts as a messenger from neurons to muscle cells producing muscle contraction, and is involved in attention, memory and learning.[2] Research has related ACh abnormal levels with neurodegenerative disorders, such as Parkinson's disease (PD), Alzheimer's disease, multiple sclerosis and Huntington's disease.[3] In PD, diminished striatal dopaminergic activity leads to increased ACh release by interneurons.[4] In this context, disruption of the acetylcholine–dopamine balance leads to PD symptoms, which include tremors, hypokinesia, muscular rigidity, and neuropsychiatric disorders, including depression, fatigue, and speech and memory problems.[5] Drug therapy in PD aims to correct the imbalance between dopamine and ACh,[6] as accomplished by oral administration of: (i) levodopa, a dopamine precursor,[7] (ii) dopamine agonists that activate dopamine receptors,[8] and (iii) anticholinergics, used to lower ACh levels.[9] However, many adverse side effects (e.g. dyskinesia, motor fluctuations, psychosis and drug resistance) are associated with these drugs and impact PD patients' quality of life.[10] In order to find new ways to treat PD, an appealing approach is to design nanocarriers able to deliver a certain drug in regions with high ACh levels.

From another point of view, much interest has been shown in recent years in the development of stimuli-responsive nanomaterials for drug delivery given their potential application in nanomedicine.[11] Among the various potential nanocarriers, silica mesoporous supports (SMS) are especially appealing because of their unique properties, such as high loading capacity, easy functionalization, low cost and biocompatibility.[12] In addition, one interesting characteristic of SMS is the possibility of functionalizing the external surface with molecular and/or supramolecular ensembles that act as molecular gates. These gated solids show no cargo release, but can deliver the payload in response to certain external stimuli, thus minimizing therapy-derived side effects. In line with this, SMS that are responsive to different stimuli, for example, light, temperature, magnetic fields, enzymes, DNA, redox reactions and pH, have been developed.[13] However, very few examples of gated SMS that can deliver their cargo in the presence of target small molecules of biological importance have been reported.[13b]

In this area of gated chemistry, we recently reported the design of more sophisticated nanodevices for delivery applications based on Janus nanoparticles with Au and mesoporous silica (MS) on opposite faces.[14] This allows the inclusion of responsive ensembles anchored to the pore outlets of the mesoporous face, and also a “control unit” on the Au face that directs the operation (cargo delivery) of the gated material.

3.3 Results and discussion

Given the importance of ACh in nervous system diseases such as PD, the need for developing better therapies, and given our interest in designing gated hybrid materials,[15] we report herein the preparation of an acetylcholinesterase-controlled nanodevice based on Janus-type Au–mesoporous silica nanoparticles. Scheme 1 illustrates the design of the system. Enzyme acetylcholinesterase is immobilized on the Au face of the Janus support, which acts as the “control unit”. The MS face is loaded with the cargo (e.g., $[Ru(bpy)_3]Cl_2$ (bpy=2,2’-bipyridine)) and is functionalized with a pH-responsive β-cyclodextrin (β-CD):benzimidazole supramolecular nanovalve. The β-CD:benzimidazole nanovalve has been proved to operate well in other delivery systems.[16] The Au side acts as an “effector” in which acetylcholinesterase monitors the presence of over-expressed ACh and induces cargo delivery. In particular, it is expected that the hydrolysis of ACh by the enzyme to give choline and acetic acid will induce a local decrease in pH, which will result in the protonation of benzimidazole, the rupture of β-CD:benzimidazole ensemble and cargo release. Such a nanodevice may play a double role when reaching regions with high ACh concentrations, such as neuromuscular junctions or the striatum in PD patients: (i) local cargo delivery that would reduce side effects and (ii) lowering ACh levels, thus acting as anticholinergic agents.

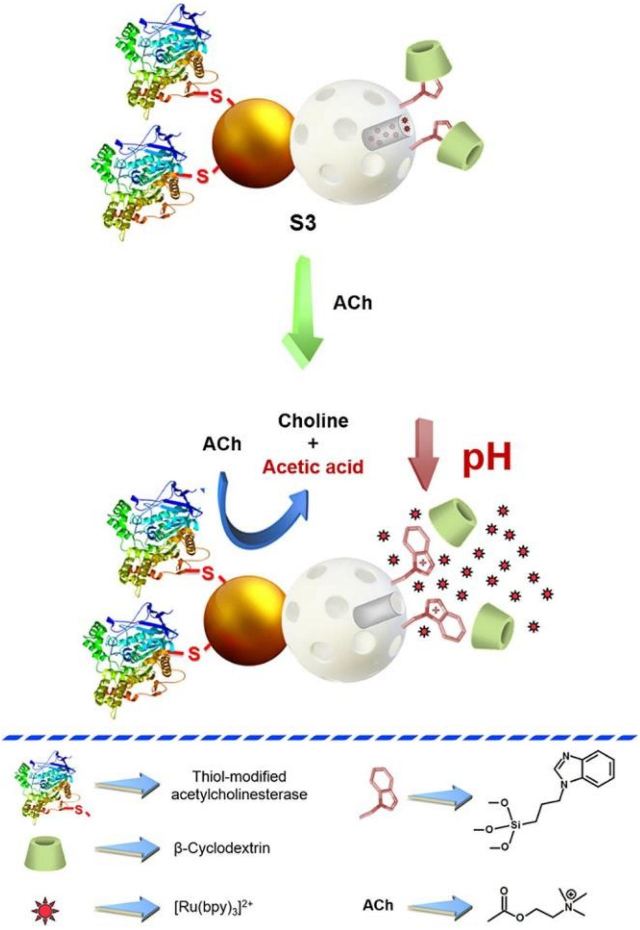

Scheme 1. Representation of the performance of nanodevice **S3**. The "control unit" (Au face) is functionalized with acetylcholinesterase, which directs the cargo delivery from the mesoporous face in the presence of ACh.

In order to prepare the nanodevice, we first synthesized MS nanoparticles by hydrolysis and condensation of tetraethyl orthosilicate in basic media using *n*-cetyltrimethylammonium bromide as a template. Surfactant removal by calcination yielded the starting mesoporous support (**MCM-41**). Gold nanoparticles were synthesized by reduction of Au^{III} with sodium citrate, according to the Turkevich–Frens method.[17] Then **MCM-41** nanoparticles were confined at a Pickering emulsion using paraffin wax to achieve its partial functionalization with

(3-mercaptopropyl)triethoxysilane, to which Au nanoparticles were attached. Next, we dissolved paraffin wax in $CHCl_3$ to obtain Janus Au–MS nanoparticles (**S1**). Afterward, mesoporous scaffold pores were loaded with $[Ru(bpy)_3]Cl_2$ and the external surface was functionalized with (3-iodopropyl)trimethoxysilane. Then a nucleophilic substitution reaction between the grafted iodopropyl moieties and benzimidazole yielded solid **S2**. The pores of the **S2** nanoparticles were capped with a pH-sensitive supramolecular nanovalve by stirring the solid with β-CD in water, which led to the formation of inclusion complexes between the benzimidazole groups and β-CD (solid **S2-CD**). Finally, acetylcholinesterase, previously modified on its glycosylation chains with thiol groups,[18] was covalently immobilized on the Au face by incubation in 50 mm sodium phosphate buffer (pH 7.5) at 0 °C, which resulted in the final nanodevice **S3** (see Supporting Information for further details).

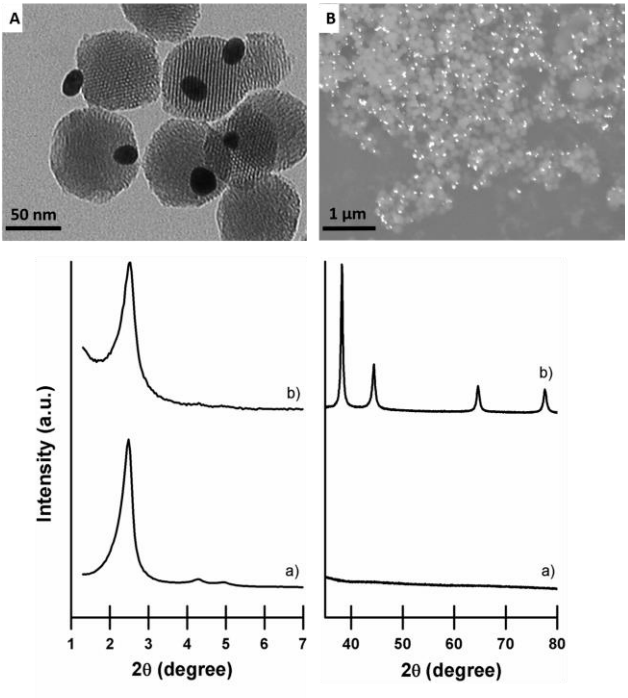

Figure 1. Top: Representative (A) TEM and (B) SEM images of Janus Au–MS nanoparticles (**S1**) Down: PXRD of (a) calcined **MCM-41** and (b) final nanodevice **S3** at low (left) and high (right) angles.

We followed standard procedures to characterize the prepared solids (see Supporting Information). Transmission electron microscopy (TEM) confirmed both the mesoporous morphology of the **MCM-41** nanoparticles (average diameter: 70 ± 15 nm) and the presence of Au nanoparticles (average diameter: 21 ± 4 nm) in Janus colloids (**S1**, see Figure 1A). Statistical analysis of TEM images (see Supporting Information Figure SI-3) of the as-made Janus colloids shown that around 80% were Au-Si nanoparticles (56% with a 1:1 Au-Si ratio, 15% with a 2:1 ratio and 9% with a higher ratio). Additionally, SEM images of the colloids were also acquired in which gold nanoparticles clearly appear as bright dots (see Figure 1B). Powder X-ray diffraction (PXRD), carried out on the starting **MCM-41** nanoparticles, showed the (100) low-angle reflection peak that is characteristic of these mesoporous materials. Preservation of the (100) peak in the solids **S1**, **S2**, and **S3** (see Supporting Information Figure SI-4) clearly confirmed that the dye loading and chemical modifications processes did not damage the 3D mesoporous structure. The diffraction pattern at a high angle for all the Janus colloids showed the cubic gold characteristic (111), (200), (220), and (311) peaks, which confirmed the presence of gold nanocrystals.[19] From thermogravimetric and elemental analyses, we determined the contents of $[Ru(bpy)_3]Cl_2$ and benzimidazole on **S2** to be 0.162 and 0.105 g per gram of nanoparticles, respectively. For nanodevice **S3**, we determined the amount of immobilized acetylcholinesterase as 93 $U \cdot g^{-1}$, that corresponds to 3.4 $mg \cdot g^{-1}$ of **S3** (see Supporting Information Figure SI-10). The correct operation of the proton-responsive nanovalve was verified by monitoring the cargo release from the capped **S2-CD** in water solutions at different pH (see Supporting Information Figure SI-7). Additionally, the assembly of the different components on the Janus support was confirmed by ^{13}C-NMR (Supporting Information Figure SI-8). We also calculated the Brunauer–Emmett–Teller (BET) specific surface values, pore volumes, and pore sizes from the N_2 adsorption–desorption isotherms (summarized in Supporting Information Table SI-1). The solids were also characterized by FT-IR analysis (see Supporting Information Figure SI-9). Furthermore, dynamic light scattering (DLS) studies under physiological conditions (PBS, pH 7.5) were carried out on the materials (see Supporting

Information Table SI-2). Functionalization with benzimidazole moieties reduced the zeta potential of the nanoparticles **S2** (-6.6 mV) compared to calcined **MCM-41** (-21.5 mV) and Janus colloids **S1** (-12.5 mV). For the final nanodevice **S3**, the surface charge increased (-14.9) compared to **S2** as a consequence of enzyme functionalization and β-cyclodextrin capping. This increase in negative charge after enzyme attachment is in agreement with the zeta potential determined for the acetylcholinesterase (-15.6 mV, see Supporting Information for measurement details). In addition, the hydrodynamic diameter for each material was also determined. An increase after each functionalization step was observed which resulted in a hydrodynamic diameter of 195 nm for the final **S3** nanodevice (hydrodynamic diameter for **MCM-41**, **S1**, **S2** and acetylcholinesterase was 91.2, 141.8, 164.2, and 6.0 nm, respectively).

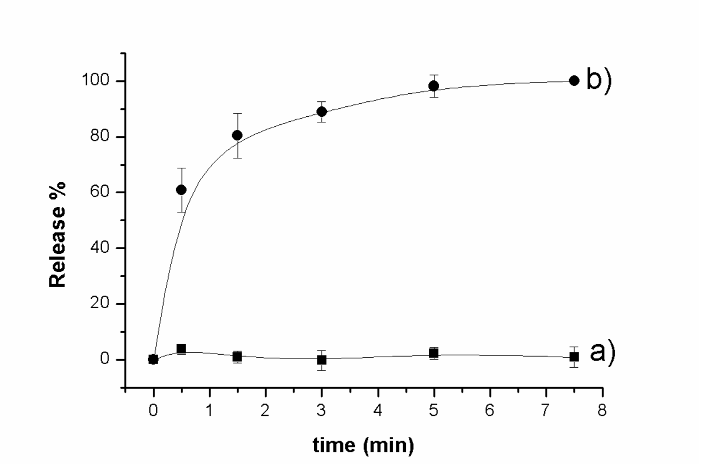

Figure 2. Normalized cargo release from **S3** determined by measuring $[Ru(bpy)_3]Cl_2$ fluorescence at 595 nm (λ_{exc}=453 nm) versus time in water at pH 7.5 (20 mM Na_2SO_4) in the absence (curve a) and presence (curve b) of ACh 1 mM. Error bars from three independent experiments.

In order to test the capacity of the capped Janus nanoparticles to deliver the cargo, we brought **S3** to a concentration of 0.9 mg·mL^{-1} in water at pH 7.5 (20 mM Na_2SO_4) in the absence and presence of ACh (1 mM). We took aliquots at scheduled times, removed the nanoparticles by centrifugation, and evaluated cargo release by measuring the emission band of $[Ru(bpy)_3]Cl_2$ at 595 nm (λ_{exc} =453 nm). Figure 2 shows the payload delivery kinetics. In the absence of ACh, **S3** is tightly capped and dye release is negligible. However, presence of ACh induced pore opening and a subsequent remarkable cargo delivery in under 5 minutes. We attributed the response in the presence of ACh to the “detection” of this neurotransmitter by acetylcholinesterase (effector) in the “control unit”, which triggered cargo release from the MS nanocarrier. Acetylcholinesterase catalyzed the hydrolysis of ACh to choline and acetic acid (pK_a =4.75). Acetic acid induced the protonation of benzimidazole groups (pK_a =5.55)[20] on the MS face and the dethreading of the supramolecular nanovalve, which finally resulted in cargo delivery. We determined the pH of the aqueous suspensions of the nanoparticles before and after addition of acetylcholine and no pH changes were observed. This could be ascribed to the fact that the generated protons reacted with the benzimidazole moieties (that protonate). Taking into account the experimental conditions in a typical experiment it is expected to obtain 6.3×10^{-4} moles of acetic acid by hydrolysis of ACh, and this acetic acid is able to protonate the benzimidazole groups (7.99×10^{-4} moles) in **S3**. Testing the response of the β-cyclodextrin-capped solid without enzyme (solid **S2-CD**) in the presence of ACh demonstrated the crucial role played by the enzyme in the “control unit”. In this case, no payload delivery took place.

The second step tested the response of solid **S3** in the presence of other important neurotransmitters, such as serotonin (5-HT), dopamine (DA), norepinephrine (NE), glycine (Gly), ɣ-aminobutyric acid (GABA), aspartic acid (Asp), and glutamic acid (Glu). Figure 3a shows the release of ruthenium dye upon the addition of these neurotransmitters (1 mM) to suspensions of **S3** (0.9 mg·mL^{-1}). These chemicals were unable to trigger cargo release in **S3**, which opened selectively in the presence of ACh.

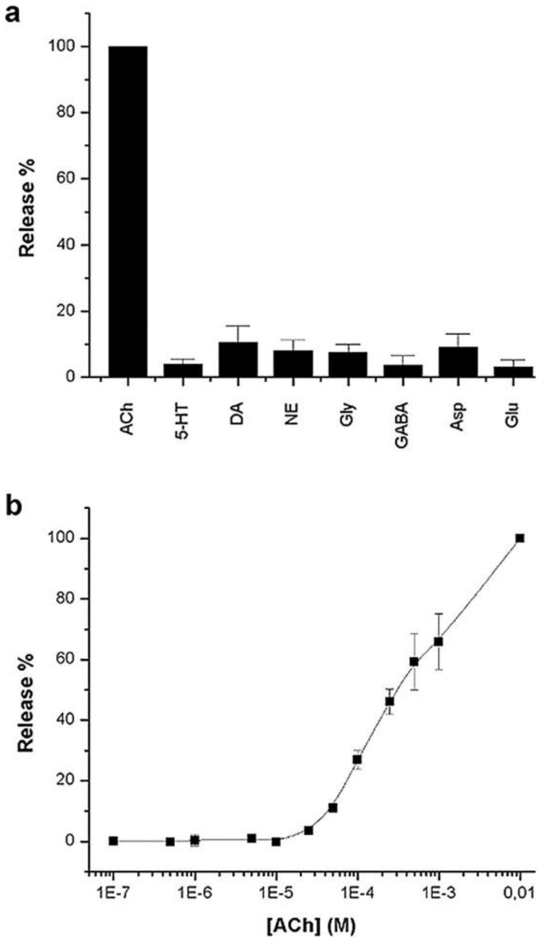

Figure 3. a) Normalized cargo release from **S3** in the presence of different neurotransmitters at 1 mm. b) Normalized cargo release after 5 min according to ACh concentration. Error bars from three independent experiments.

In another step we studied the response of **S3** according to ACh concentration (see the results in Figure 3b). A linear dye release occurred within the 10^{-5}-10^{-2} mol·L^{-1} ACh concentration range. From the calibration curve, we calculated a limit of detection (LOD) to be 1.5×10^{-5} mol·L^{-1}. It is noteworthy that **S3** did not respond to concentrations lower than 10 µM. When compared this data with the ACh concentrations found in the body and reported in the literature (see Supporting

Information Table SI-5), this suggested that **S3** would remain capped at ACh levels found in human blood (9 nM),[21] but would release its cargo at regions with higher ACh concentrations. For instance, ACh concentration in synaptic vesicles is estimated to be 100 mM[22] and in neuromuscular junctions and synaptic clefts ACh levels have been reported to be 3–0.5 µM[22] under normal conditions and might increase in PD patients.[4] Although, the ACh concentration reached just upon presynaptic release is not precisely known, several studies have reported ACh concentrations in the striatum (which is the target region for levodopa and other PD drugs) to be 30–50 µM.[23] In other brain regions such as the hippocampus and frontal cortex, ACh levels are also higher (ca. 7 and 3.75 mM respectively)[24] suggesting that **S3** would also deliver the cargo in these regions. Despite the fact that the road from these results to the *in vivo* use of similar nanodevices remains long and uncertain, these results suggested that **S3** or similar nanodevices could be suitable drug release systems for the treatment of diseases such as PD.

We ultimately aimed to demonstrate that the Janus capped system can be used to deliver cargo in the presence of ACh in a biological complex medium. In particular for these experiments, we prepared similar nanoparticles to **S3**, but loaded with cytotoxic doxorubicin (Doxo) (solid **S4**, see Supporting Information). We did spectrophotometric studies to calculate the amount of Doxo loaded on **S4** that was found to be 0.035 g per gram of solid. The release in vitro experiments showed that **S4** (0.9 $mg \cdot mL^{-1}$) remained capped for at least 24 h, but Doxo release was substantial in the presence of ACh (see Figure 4A).

Next as proof of concept, we added 100 $mg \cdot mL^{-1}$ of **S4** to the culture media of human cervix adenocarcinoma (HeLa) cells, further incubated alone or in the presence of ACh (thus simulating a biological region with overexpressed ACh). We studied Doxo delivery from **S4** by means of cell viability WST1 assays and confocal microscopy by tracking Doxo-associated fluorescence. Figure 4B shows the cell viability results after 24 h. These experiments clearly indicated the reduction in viability of the HeLa cells treated with **S4** in a medium that contained ACh (50% of cells were dead after 24 h). We ascribed this effect to the ACh-induced opening of **S4** nanoparticles with the subsequent Doxo release. In contrast, the cells treated with **S4** in an ACh-free medium remained alive, which indicated that **S4** nanoparticles were not toxic for HeLa cells in the absence of ACh. We also observed a clear **S4** concentration-dependent decrease of living cells in the presence of ACh (see Supporting Information Figure SI-13).

Furthermore, the confocal microscopy images of the HeLa cells (Figure 4C) incubated with **S4** showed clear Doxo-related fluorescence (green) in the cellular cytosolic compartment. In contrast, we observed negligible fluorescence in the cells incubated with **S4** in ACh-free media. This meant that the nanocarrier was unable to release its cargo under these conditions. Remarkably, despite the presence of a large amount of cellular metabolites and proteins in the cell media, which could have compromised the performance of **S4**, the results indicated optimal functional behavior for the nanoparticles that delivered the cargo in the presence of ACh.

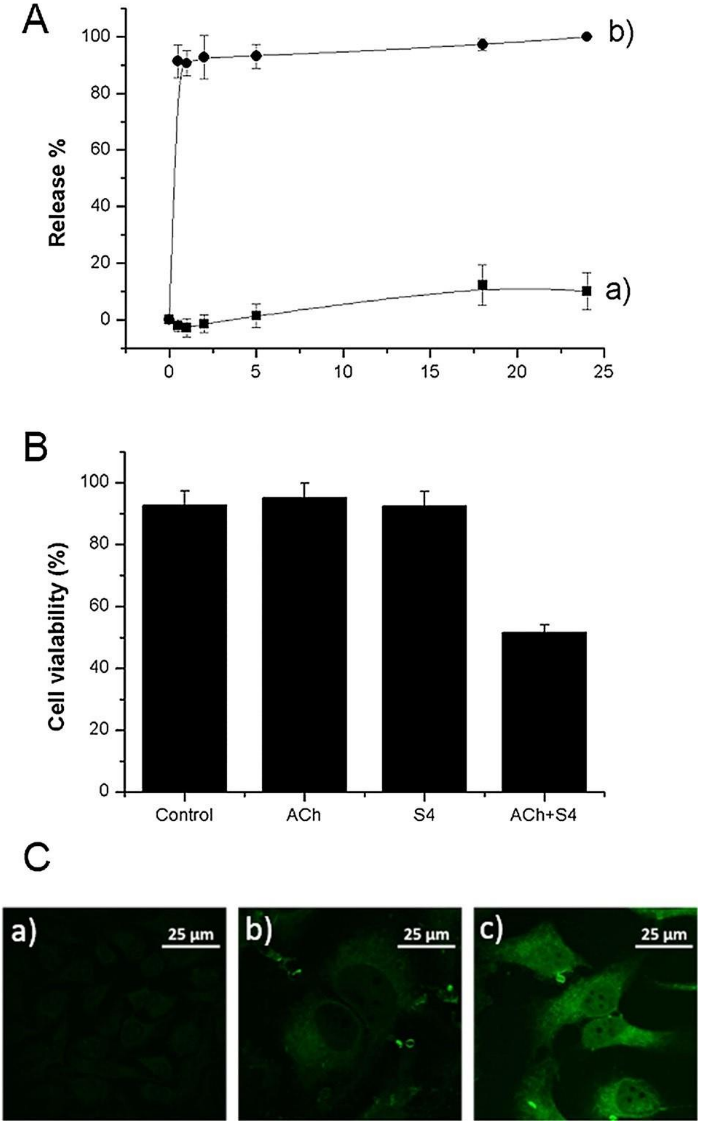

Figure 4. A) Kinetics of Doxo release from **S4** (0.9 mg·mL^{-1}) in water at pH 7.5 (20 mM Na_sSO_4) in the absence (a) and presence (b) of ACh (10 mM), estimated by measuring fluorescence at 557 nm (λ_{exc}=495 nm). B) Cell viability test for **S4**. Results plotted from left to right for the control experiment, incubation with ACh (40 mm), incubation with **S4** (100 mg·mL^{-1}), and incubation with both ACh (40 mM) and **S4** 100 (mg·mL^{-1}). Error bars for three independent experiments. C) Controlled release of Doxo from **S4** (100 mg·mL^{-1}) in HeLa cells culture media examined by confocal microscopy for (a) the control experiment, (b) incubation with **S4**, and (c) incubation with **S4** and ACh.

3.4 Conclusions

In conclusion, we have designed, synthesized and characterized a new enzyme-controlled nanocarrier for ACh-triggered cargo delivery. In particular, the functional capped solid is based on Janus-type nanoparticles functionalized with acetylcholinesterase on the Au-face and a supramolecular pH-responsive nanovalve on the MS surface. In the presence of ACh, the acetylcholinesterase enzyme hydrolyses the neurotransmitter and induces the dethreading of the nanovalve and cargo release. We observed fast cargo delivery kinetics (less than 5 min) and a selective response to ACh among other neurotransmitters tested. The nanocarrier responded to ACh concentrations higher than 10 µM, which is below the ACh blood levels and within the range of concentrations found in neuromuscular junctions and in the striatum, the target region for PD drugs. The capped Janus nanoparticles displayed selective ACh-dependent cargo delivery even in a biological complex medium (HeLa cells). If we bear in mind the key role played by ACh and its relation with PD and other nervous system diseases, we believe that these findings could help design new therapeutic strategies. We also expect the possibility of combining different molecular gates on the MS face with distinct enzyme based effectors on the Au surface to inspire the development of new advanced delivery systems that could selectively deliver their cargo in the presence of target small molecules of biological importance.

Acknowledgements

A. L. L. is grateful to “La Caixa” Banking Foundation for his PhD fellowship. The authors are grateful to the Spanish Government (MINECO Projects MAT2012-38429-C04-01, MAT201564139-C4-1, CTQ2014-58989-P and CTQ2015-71936-REDT) and the Generalitat Valencia (Project PROMETEOII/2014/047) for support. The Comunidad de Madrid (S2013/MIT-3029, Programme NANOAVANSENS) is also gratefully acknowledged.

3.5 References

1. a) C. Gotti, F. Clementi, *Prog. Neurobiol.* **2004**, *74*, 363–396; b) J. Lindstrom, *Mol. Neurobiol.* **1997**, *15*, 193–222; c) L. Descarries, V. Gisiger, M. Steriade, *Prog. Neurobiol.* **1997**, *53*, 603–625.
2. a) L. Leblond, C. Beaufort, F. Delerue, T. P. Durkin, *Behav. Brain Res.* **2002**, *128*, 91–102; b) C. L. Nelson, J. A. Burk, J. P. Bruno, M. Sarter, *Psychopharmacology (Berl)* **2002**, *161*, 168–79; c) M. E. Hasselmo, J. M. Bower, *Trends Neurosci.* **1993**, *16*, 218–22; d) G. Pepeu, M. G. Giovannini, *Learn. Mem.* **2004**. *11*, 21–27.
3. a) P. Calabresi, B. Picconi, L. Parnetti, M. Di Filippo, *Lancet Neurol.* **2006**, *5*, 974–983; b) G. Ehrenstein, Z. Galdzicki, G. D. Lange, *Biophys. J.* **1997**, *73*, 1276–1280; c) M. Reale, F. de Angelis, M. di Nicola, E. Capello, M. di Ioia, G. de Luca, A. Lugaresi, A. M. Tata, *Int. J. Mol. Sci.* **2012**, *13*, 12656–12664; d) R. S. Brett, J. H. Schmidt, J. S. Cage, S. A. Schartel, P. J. Poppers, *J. Am. Soc. Anesthesiol.* **1987**, *66*, 837–838; e) B. Picconi, E. Passino, C. Sgobio, P. Bonsi, I. Barone, V. Ghiglieri, A. Pisani, G. Bernardi, M. Ammassari-Teule, P. Calabresi, *Neurobiol. Dis.* **2006**, *22*, 143–52.
4. a) A. Pisani, G. Bernardi, J. Ding, D. J. Surmeier, *Trends Neurosci.* **2007**, *30*, 545–553; b) T. Aosaki, M. Miura, T. Suzuki, K. Nishimura, M. Masuda, *Geriatr. Gerontol. Int.* **2010**, *10*, S148-S157.
5. a) A. D. Mosley, D. S. Romaine, *The A to Z of Parkinson's Disease*, Checkmark Books, **2007**; b) M. Guttman, S. J. Kish, Y. Furukawa, *Can. Med. Assoc. J.* **2003**, *168*, 293–301.
6. B. S. Connolly, A. E. Lang, *JAMA* **2014**, *311*, 1670–1683.
7. S. Fahn, D. Oakes, I. Shoulson, K. Kieburtz, A. Rudolph, A. Lang, C. W. Olanow, C. Tanner, K. Marek, P. S. Group, *N. Engl. J. Med.* **2004**, *351*, 2498–2508.
8. a) P. Jenner, *Neurology* **2002**, *58*, S1–S8; b) F. Stocchi, *CNS Drugs* **1998**, *10*, 159–170.
9. S. Takahashi, H. Tohgi, H. Yonezawa, S. Obara, E. Yamazaki, *J. Neurol. Sci.* **1999**, *167*, 56–61.
10. a) C. W. Olanow, Y. Agid, Y. Mizuno, *Mov. Disord.* **2005**, *20*, 643–644; b) O. Rascol, P. Payoux, F. Ory, J. J. Ferreira, C. Brefel-Courbon, J.-L. Montastruc, *Ann. Neurol.* **2003**, *53(S3),* S3–S15; c) E. Melamed, D. Offen, A. Shirvan, I. Ziv, *J. Neurol.* **2000**, *247*, 135–139; d) T. Muller, H. Hefter, R. Hueber, W. Jost, K. Leenders, P. Odin, J. Schwarz, *J. Neurol.* **2004**, *251*, 44-46; e) T. López, J. L. Bata-García, D. Esquivel, E. Ortiz-Islas, R. Gonzalez, J. Ascencio, P. Quintana, G. Oskam, F. J. Álvarez-Cervera, F. J. Heredia-López, et al., *Int. J. Nanomedicine* **2011**, *6*, 19–31.; f) T. López, D. Esquivel, G. Mendoza-Díaz, E. Ortiz-Islas, R. D. González, O. Novaro, *Mater. Lett.* **2015**, *161*, 160–163.
11. a) E. Aznar, M. Oroval, L. Pascual, J. R. Murguía, R. Martínez-Máñez, F. Sancenón, *Chem. Rev.* **2016**, *116*, 561–718; b) S. Giret, M. Wong Chi Man, C. Carcel, *Chem. Eur. J.* **2015**, *21*, 13850-13865; c) M. Vallet-Regí, F. Balas, D. Arcos, *Angew. Chem. Int. Ed.* **2007**, *46*, 7548–7558; d) K. T. Kim, S. A. Meeuwissen, R. J. M. Nolte, J. C. M. van Hest, *Nanoscale* **2010**, *2*, 844−858; e) G. Bao, S. Mitragotri, S. Tong, *Annu. Rev. Biomed. Eng.* **2013**, *15*, 253−282; f) S. Mura, J. Nicolas, P. Couvreur, *Nat. Mater.* **2013**, *12*, 991−1003; g) S.-H. Wu, Y. Hung, C.-Y. Mou, *Chem. Commun*. **2011**, *47*, 9972−9985.
12. a) F. Tang, L. Li, D. Chen, *Adv. Mater.* **2012**, *24*, 1504–34; b) Z. Li, J. C. Barnes, A. Bosoy, J. F. Stoddart, J. I. Zink, *Chem. Soc. Rev.* **2012**, *41*, 2590–2605; c) D. Tarn, C. E. Ashley, M. Xue, E. C. Carnes, J. I. Zink, C. J. Brinker, *Acc. Chem. Res.* **2013**, *46*, 792–801; d) Y. Zhao, J. L. Vivero-Escoto, I. I. Slowing, B.G. Trewyn, V. S.-Y. Lin, *Expert Opin. Drug Deliv.* **2010**, *7*, 1013−1029; e)

C. Argyo, V. Weiss, C. Bräuchle, T. Bein, *Chem. Mater.* **2014**, *26*, 435−451; f) Y.-W Yang, Y.-L. Sun, N. Song, *Acc. Chem. Res.* **2014**, *47*, 1950−1960; g) A. Popat, S. B. Hartono, F. Stahr, J. Liu, S. Z. Qiao, G. Qing Lu, *Nanoscale* **2011**, *3*, 2801−2818.

13. a) T. M. Guardado-Alvarez, L. Sudha Devi, M. M. Russell, B. J. Schwartz, J. I. Zink, *J. Am. Chem. Soc.* **2013**, *135*, 14000–14003; b) F. Sancenón, L. Pascual, M. Oroval, E. Aznar, R. Martínez-Máñez, *ChemistryOpen*, **2015**, *4*, 418-437; c) E. Yu, I. Galiana, R. Martínez-Máñez, P. Stroeve, M. D. Marcos, E. Aznar, F. Sancenón, J. R. Murguía, P. Amorós, *Colloids Surf. B.* **2015**, *135*, 652–660; d) A. Baeza, E. Guisasola, E. Ruiz-Hernández, M. Vallet-Regí, *Chem. Mater.* **2012**, *24*, 517–524; e) A. Bernardos, E. Aznar, M. D. Marcos, R. Martínez-Máñez, F. Sancenón, J. Soto, J. M. Barat, P. Amorós, *Angew. Chem. Int. Ed.* **2009**, *121*, 5998–6001; f) Z. Zhang, D. Balogh, F. Wang, S. Y. Sung, R. Nechushtai, I. Willner, E. Sciences, *ACS nano* **2013**, *7*, 8455–8468; g) S. El Sayed, C. Giménez, E. Aznar, R. Martínez-Máñez, F. Sancenón, M. Licchelli, *Org. Biomol. Chem.* **2015**, *13*, 1017–1021; h) A. Bansal, Y. Zhang, *Acc. Chem. Res.* **2014**, *47*, 3052−3060; i) V. Z. Ozalp, F. Eyidogan, H. A. Oktem, *Pharmaceuticals* **2011**, *4*, 1137−1157; j) R. de la Rica, D. Aili, M. M. Stevens, *Adv. Drug Delivery Rev.* **2012**, *64*, 967−978, k) K. C.-F. Leung, C. P. Chak, C.-M. Lo, W.-Y. Wong, S. Xuan, C. H. K. Cheng, *Chem.-Asian J.* **2009**, *4*, 364−381.
14. a) R. Villalonga, P. Díez, A. Sánchez, E. Aznar, R. Martínez-Máñez, J. M. Pingarrón, *Chem. Eur. J.* **2013**, *19*, 7889–7894; b) P. Díez, A. Sánchez, M. Gamella, P. Martínez-Ruíz, E. Aznar, C. De La Torre, J. R. Murguía, R. Martínez-Máñez, R. Villalonga, J. M. Pingarrón, *J. Am. Chem. Soc.* **2014**, *136*, 9116–9123.
15. a) C. Coll, A. Bernardos, R. Martínez-Máñez, F. Sancenón, *Acc. Chem. Res.* **2013**, *46*, 339–349; b) E. Aznar, R. Martinez-Manez, F. Sancenon, *Expert Opin. Drug Deliv.* **2009**, *6*, 643–655; c) A. Ultimo, C. Giménez, P. Bartovsky, E. Aznar, F. Sancenón, M. D. Marcos, P. Amorós, A. R. Bernardo, R. Martínez-Máñez, A. M. Jiménez-Lara, J. R. Murguía, *Chem. Eur. J.* **2016**, *22*, 1582–1586; d) L. Pascual, I. Baroja, E. Aznar, F. Sancenón, M. D. Marcos, J. R. Murguía, P. Amorós, K. Rurack, R. Martínez-Máñez, *Chem. Commun.* **2015**, *51*, 1414–1416; e) C. Giménez, E. Climent, E. Aznar, R. Martínez-Máñez, F. Sancenón, M. D. Marcos, P. Amorós, K. Rurack, *Angew. Chem. Int. Ed.* **2014**, *53*, 12629–12633.
16. a) H. Meng, M. Xue, T. Xia, Y.-L. Zhao, F. Tamanoi, J. F. Stoddart, J. I. Zink, A. E. Nel, *J. Am. Chem. Soc.* **2010**, *132*, 12690–12697; b) M. Xue, X. Zhong, Z. Shaposhnik, Y. Qu, Fuyuhiko Tamanoi, Xiangfeng Duan, J. I. Zink, *J. Am. Chem. Soc.* **2011**, *133*, 8798–8801; c) T. Wang, M. Wang, C. Ding, J. Fu, *Chem. Commun.* **2014**, *50*, 12469–12472; d) S. Angelos, N. M. Khashab, Y. W. Yang, A. Trabolsi, H. A. Khatib, J. F. Stoddart, J. I. Zink., *J. Am. Chem. Soc.* **2009**, *131*, 12912–12914.
17. a) J.A. Turkevich, *Discuss. Faraday Soc.* **1951**, *11*, 55-75; b) G.Frens, *Nature* **1973**, *241*, 20-22.
18. a) L. Gómez, H.L. Ramírez, M.L. Villalonga, J. Hernández, R. Villalonga, *Enzyme Microb. Technol.* **2006**, *38*, 22-27; b) B. Chico, C. Camacho, M. Pérez, M.A. Longo, M.A. Sanromán, J.M. Pingarrón, R. Villalonga, *J. Electroanal. Chem.* **2009**, *629*, 126-132.
19. A. Sánchez, P. Díez, P. Martínez-Ruíz, R. Villalonga, J. M. Pingarrón, *Electrochem. Commun.* **2013**, *30*, 51–54.
20. G. Jerez, G. Kaufman, M. Prystai, S. Schenkeveld, K. K. Donkor, *J. Sep. Sci.* **2009**, *32*, 1087–1095.
21. S. Lin, C.-C. Liu, T.-C. Chou, *Biosens. Bioelectron.* **2004**, *20*, 9–14.
22. a) E. S. Vizi, A. Fekete, R. Karoly, A. Mike, *Br. J. Pharmacol.* **2010**, *160*, 785–809; b) A. Schena, K. Johnsson, *Angew. Chem. Int. Ed.* **2014**, *53*, 1302–1305; c) Y. Zhou, L.-L.Tan, Q.-L. Li, X-L. Qiu, A.-D. Qi, Y. Tao, Y.-W. Yang, *Chem. Eur. J.* **2014**, *20*, 2998–3004.

23. a) R. Hassler, P. Haug, C. Nitsch, J. S. Kim, K. Paik, *J. Neurochem.* **1982**, *38*, 1087–1098; b) M. H. Sethy, V. H.; Van Woert, *Nature* **1974**, *251*, 529–530.
24. Z. Batool, S. Sadir, L. Liaquat, S. Tabassum, S. Madiha, S. Rafiq, S. Tariq, T. S. Batool, S, Saleem, Fizza Naqvi et. al., *Brain Res. Bull.* **2016**, *120*, 63–74.

3.6 Supporting Information

Chemicals

The chemicals tetraethyl orthosilicate (TEOS), *n*-cetyltrimethylammonium bromide (CTABr), sodium hydroxide (NaOH), tris(2,2′-bipyridyl)dichlororuthenium(II) hexahydrate ($[Ru(bpy)_3]Cl_2$), (3-iodopropyl)trimethoxysilane, benzimidazole, triethylamine, (3-mercaptopropyl)-triethoxysilane, hydrogen tetrachloroaurate(III) ($HAuCl_4·3H_2O$), sodium citrate tribasic dihydrate, paraffin wax, acetylcholinesterase from *Electrophorus electricus*, acetylcholine chloride, dopamine hydrochloride, serotonin hydrochloride, glycine, aspartic acid, glutamic acid, γ-aminobutyric acid, L-norepinephrine hydrochloride, sodium periodate, cystamine hydrochloride, $NaCNBH_3$, $NaBH_4$, β-cyclodextrin and acetylthiocholine iodide were purchased from Sigma-Aldrich. Sodium dihydrogen phosphate monohydrate, disodium hydrogen phosphate heptahydrate, sodium sulfate anhydrous and solvents were provided by Scharlau. Doxorubicin hydrochloride was purchased from Sequoia Research Products. For cell experiments, HeLa human cervix adenocarcinoma cells were purchased from the German Resource Centre for Biological Materials (DSMZ), Dulbecco's Modified Eagle's Medium (DMEM) was acquired from Life technologies (Grand Island, NY), and cell proliferation reagent WST-1 was purchased from Roche Applied science.

General Methods

Powder X-ray diffraction (PXRD), transmission electron microscopy (TEM), scanning electron microscopy (SEM), N_2 adsorption-desorption isotherms, UV-visible and fluorescence spectrophotometry, FT-IR, dynamic light scattering (DLS), thermogravimetric and elemental analysis, techniques were employed for materials characterization. PXRD measurements were performed on a Seifert 3000TT diffractometer using CuK_α radiation. TEM images were acquired using a JEOL TEM-1010 Electron microscope working at 100 kV. SEM images were acquired with a JEOL JSM 7600 F. DLS studies were performed using a ZetaSizer

Nano ZS (Malvern). N_2 adsorption-desorption isotherms were recorded on a Micromeritics TriStar II Plus automated analyzer. UV-visible spectra were recorded with a JASCO V-650 Spectrophotometer. Fluorescence measurements were carried out in a JASCO FP-8500 Spectrophotometer. FT-IR were performed with a Bruker Platinum ATR. Thermogravimetric analysis were carried out on a TGA/SDTA 851e Mettler Toledo equipment, using an oxidant atmosphere (Air, 80 mL/min) with a heating program consisting on a heating ramp of 10 °C per minute from 393 K to 1273 K and an isothermal heating step at this temperature for 30 minutes. Elemental analysis was performed in a CE Instrument EA-1110 CHN Elemental Analyzer. Confocal microscopy imaging was performed employing a Leica TCS SPE (Leica Microsystems Heidelberg GmbH) inverted laser scanning confocal microscope using oil objective HC PL APO 40x. Cell viability measurements were carried out with a Wallac 1420 workstation. Solid State ^{13}C-NMR was carried out on a Bruker AV 400 WB Spectrometer.

Synthesis of the MCM-41 mesoporous silica nanoparticles

1.00 g (2.74 mmol) of *n*-cetyltrimethylammonium bromide (CTABr) was dissolved in 480 mL of deionized water. Then, the pH was basified by adding 3.5 mL of a 2 mol·L^{-1} NaOH solution and the temperature was increased to 80 °C. Then, TEOS (5.00 mL, 22.4 mmol) was then added dropwise to this solution. Magnetic stirring was kept for 2 hours to give a white precipitate. Finally, the solid was isolated by centrifugation, washed several times with water and dried at 70 °C overnight (as-synthesized MCM-41). To obtain the final mesoporous nanoparticles (**MCM-41**), the as-synthesized solid was calcined at 550 ^{o}C using an oxidant atmosphere for 5 hours in order to remove the surfactant.

Synthesis of gold nanoparticles

Gold nanoparticles were synthesized based on the Turkevich-Frens method.[1] Briefly, 300 mL of a 0.3 mM $HAuCl_4 \cdot 3H_2O$ solution was brought to 100 °C under stirring and refluxing. Then, 4.5 mL of a 1% sodium citrate solution was added to synthesize 20 nm gold nanoparticles. The initially faint yellow colour turned to blue-black and finally red wine in 10 min. After this, the colloidal suspension was let to cool at room temperature.

Preparation of Janus Au-MS nanoparticles (S1)

Janus nanoparticles were synthesized by adapting a method previously reported in the literature.[2] MCM-41 mesoporous silica nanoparticles (180 mg) were dispersed in 9 mL of aqueous solution (6.7% ethanol) and *n*-cetyltrimethylammonium bromide (CTABr) was added for a 1 µM final concentration. The mixture was heated at 75 °C, and then 1 g of paraffin wax was added. Once the paraffin was melted, the mixture was vigorously stirred for 15 minutes using an Ultra-Turrax T-8 homogenizer (IKA). Afterward, the mixture was further stirred for 1 h at 1500 rpm and 75 °C using a magnetic stirrer. The resulting Pickering emulsion was then cooled to room temperature, diluted with 9 mL of methanol and reacted with 180 µL of (3-mercaptopropyl)triethoxysilane for 3 hours. The solid was collected by centrifugation and washed with methanol. For gold attachment, the partially mercapto-functionalized MCM-41 nanoparticles were dispersed in 75 mL of methanol and added over 300 mL of the as-synthesized gold nanoparticles. The mixture was stirred overnight. Then, the solid was isolated by filtration and exhaustively washed with ethanol and with chloroform. The solid was dried and ground. This process finally yielded the Janus Au-MS nanoparticles (**S1**).

Preparation of S2

To prepare **S2**, first 140 mg of **S1** and 80 mg of tris(2,2'-bipyridyl)dichlororuthenium(II) hexahydrate were suspended in 7 mL of acetonitrile and stirred for 24 h in order to load the MS-face pores. Afterward, an excess of (3-iodopropyl)trimethoxysilane (70 µL) was added and the suspension was stirred overnight. This solid (**S1-I**) was isolated by centrifugation and dried at 70 °C overnight. Then, 140 mg of **S1-I** were suspended in 11 mL of a saturated solution of benzimidazole in toluene at 80 °C and 33 mL of triethylamine were added (1:3 v/v toluene-triethylamine ratio). The suspension was stirred and heated at 80 °C for three days. After this, the resulting solid was isolated by centrifugation and dried at 70 °C overnight. This protocol finally yielded solid **S2**.

Enzyme derivatization

In order to attach acetylcholinesterase to the gold face on Janus colloids, the enzyme was first thiolated. For this process, we took into account that acetylcholinesterase is a glycoprotein that contains oligosaccharide chains covalently attached to polypeptide side-chains that can be modified.[3] First, 1 mg of enzyme was treated with sodium periodate (21.3 mg) in 50 mM sodium phosphate buffer (pH 7.5) in an ice bath for 30 min. Afterward, the solution was centrifuged to removed undissolved periodate. Then, cystamine (2 mg) and 400 µL of $NaCNBH_3$ solution (100 µM) were added and the mixture further was stirred at 0 °C. After 2 hours under magnetic stirring, 250 µL of $NaBH_4$ solution (100 mM) was added, and the mixture was stirred for 30 min at 0 °C. Afterward, the solution was exhaustively dialyzed using Amicon Ultra-05 centrifugal filters units with Ultracel-10 membranes (Millipore) and cold 50 mM sodium phosphate buffer at pH 7.5. The modified enzyme was finally brought to a concentration of 2 mg/mL (0.5 ml) and kept in the refrigerator until use.

Preparation of S3

To prepare **S3**, 100 mg of **S2** were suspended in 25 mL of 50 mM sodium phosphate buffer at pH 7.5 containing β-cyclodextrin (1.6 $mg\cdot mL^{-1}$) and tris(2,2'-bipyridyl)dichlororuthenium(II) hexahydrate (0.06 mmol, in order to avoid the delivery of the previously loaded complex from the pores to the bulk solution during the synthesis of the final solid). The suspension was stirred for 12 h at room temperature, then washed with 50 mM sodium phosphate buffer (pH 7.5) and dried under vacuum. Then, 250 µL of the modified enzyme solution was added to a suspension of 8 mg this solid (**S2-CD**) in 4 mL of 50 mM sodium phosphate buffer (pH 7.5) at 0 °C and stirred overnight. Afterward, the solid was isolated by centrifugation, washed several times with a cold solution of 50 mM sodium phosphate buffer (pH 7.5) and kept in a refrigeration until use. This protocol finally yielded the nanodevice **S3**.

Preparation of S4

A material similar to **S3** but loaded with doxorubicin (Doxo) instead of tris(2,2’-bipyridyl)dichlororuthenium(II) was also prepared (solid **S4**). For this purpose, and in a first step, 50 mg of **S1** were suspended in 2.5 mL of anhydrous acetonitrile under stirring and treated with an excess of (3-iodopropyl)trimethoxysilane (25 µL, 0.12 mmol). The suspension was stirred overnight and then the solid was isolated by centrifugation, washed with acetonitrile and dried at 70 °C overnight. Afterward, the resulting solid was ground and suspended in 4 mL of a saturated solution of benzimidazole in toluene at 80 °C and 12 mL of triethylamine (1:3 v/v toluene-triethylamine ratio). The mixture was stirred and heated at 80 °C for three days. After this, the resulting solid was centrifuged, washed with acetonitrile and dried at 70 °C overnight. 15 mg of this solid was suspended in 4 mL of 50 mM sodium phosphate buffer (pH 7.5) and 10 µmol of Doxo were added. The suspension was stirred overnight and then 10 mg of β-cyclodextrin were added followed by further stirring for 12 hours at room temperature. Afterward, the resulting capped solid was washed with 50 mM sodium phosphate buffer and dried. To functionalize these nanoparticles with the enzyme, the solid was suspended in 7.5 mL of 50 mM sodium phosphate buffer (pH 7.5) at 0 °C and then 375 µL of thiolated enzyme (2 $mg \cdot mL^{-1}$) was added. The mixture was stirred overnight and the resulting solid **S4** was isolated by centrifugation, exhaustively washed with cold 50 mM sodium phosphate buffer (pH 7.5), centrifuged and kept in the refrigerator until use. The quantity of Doxo entrapped within nanoparticles was calculated by the difference between the total amount used to prepare the material and the amount present in the aqueous phase after capping with β-cyclodextrin and attachment of the enzyme.[4]

Materials Characterization

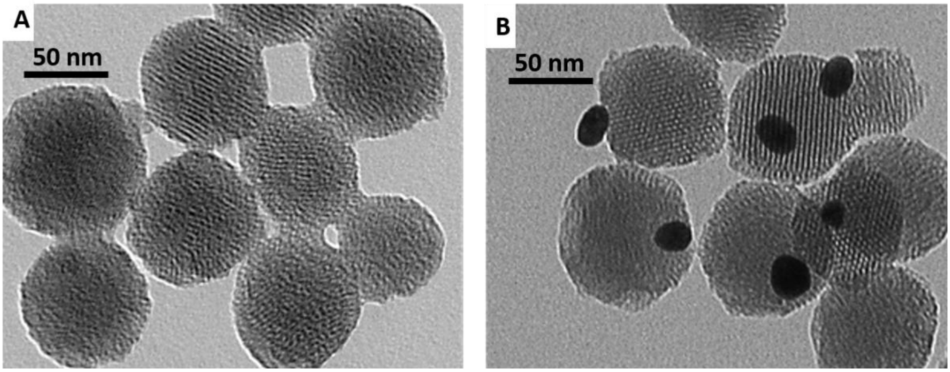

Figure SI-1. Representative TEM images of: (A) calcined **MCM-41** and (B) Janus Au-MS nanoparticles (**S1**).

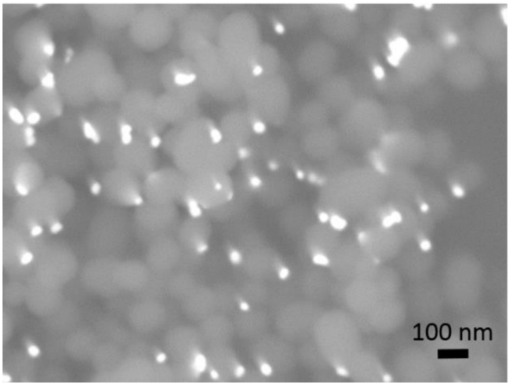

Figure SI-2. Representative SEM image of the Janus Au-mesoporous silica nanoparticles (**S1**).

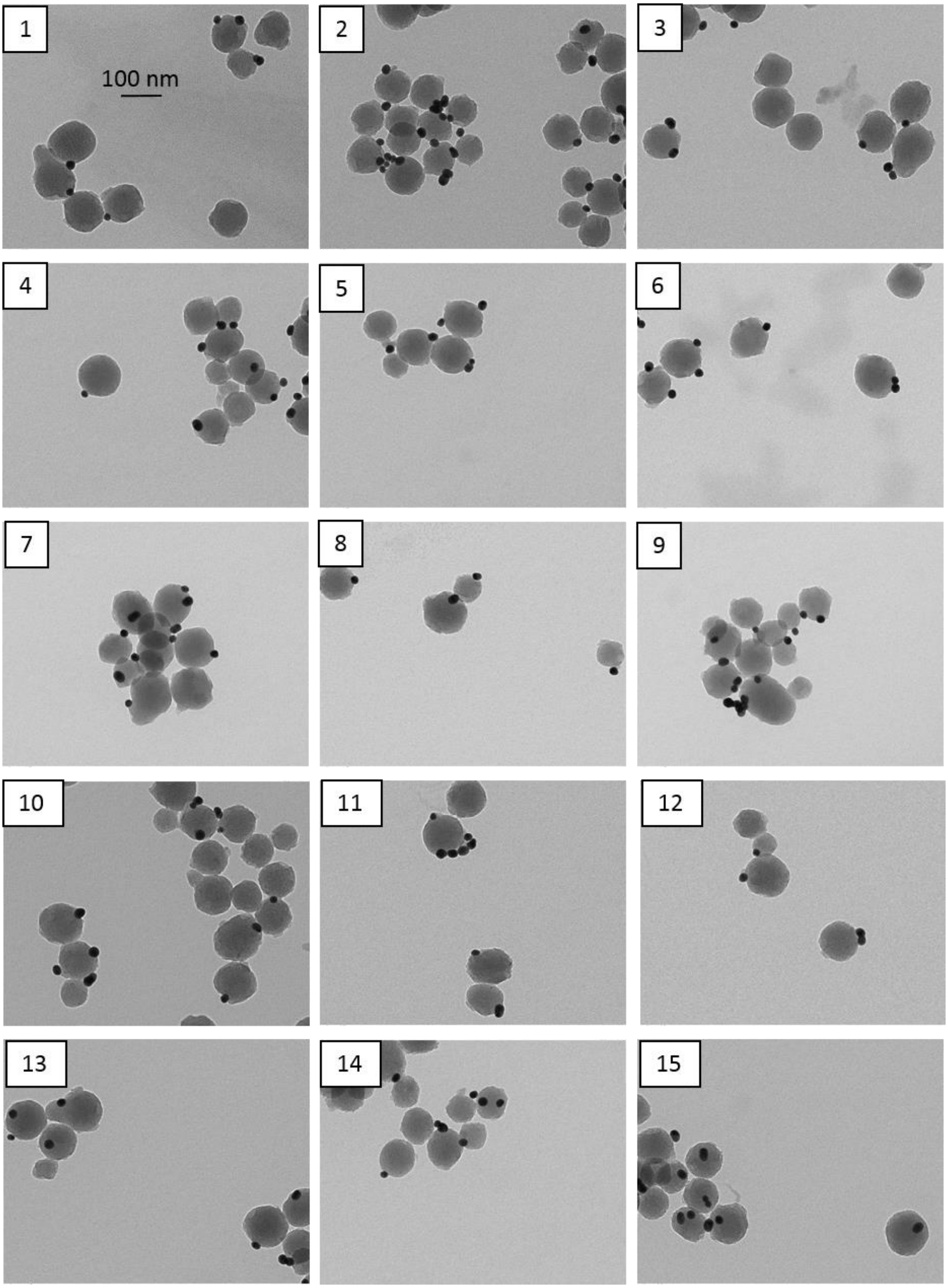

Figure SI-3. Additional TEM images of the Janus Au-mesoporous silica nanoparticles.

Table SI-1. Statistical analysis of TEM pictures.

	Au-Si Ratio					
Sample	0:1	1:1	2:1	3:1	>3:1	Total NPs
1	3	4	1	0	0	8
2	2	11	0	1	5	19
3	3	4	2	0	0	9
4	2	6	2	0	0	10
5	1	2	2	0	0	5
6	1	1	3	0	0	5
7	2	7	1	0	0	10
8	0	4	0	0	0	4
9	2	5	1	1	1	10
10	6	5	1	2	0	14
11	1	2	0	0	1	4
12	1	2	1	0	0	4
13	1	4	2	0	0	7
14	2	6	1	1	0	10
15	2	5	1	0	0	8
Total	29	68	18	4	7	127
%	22.8	53.5	14.2	3.1	5.5	100

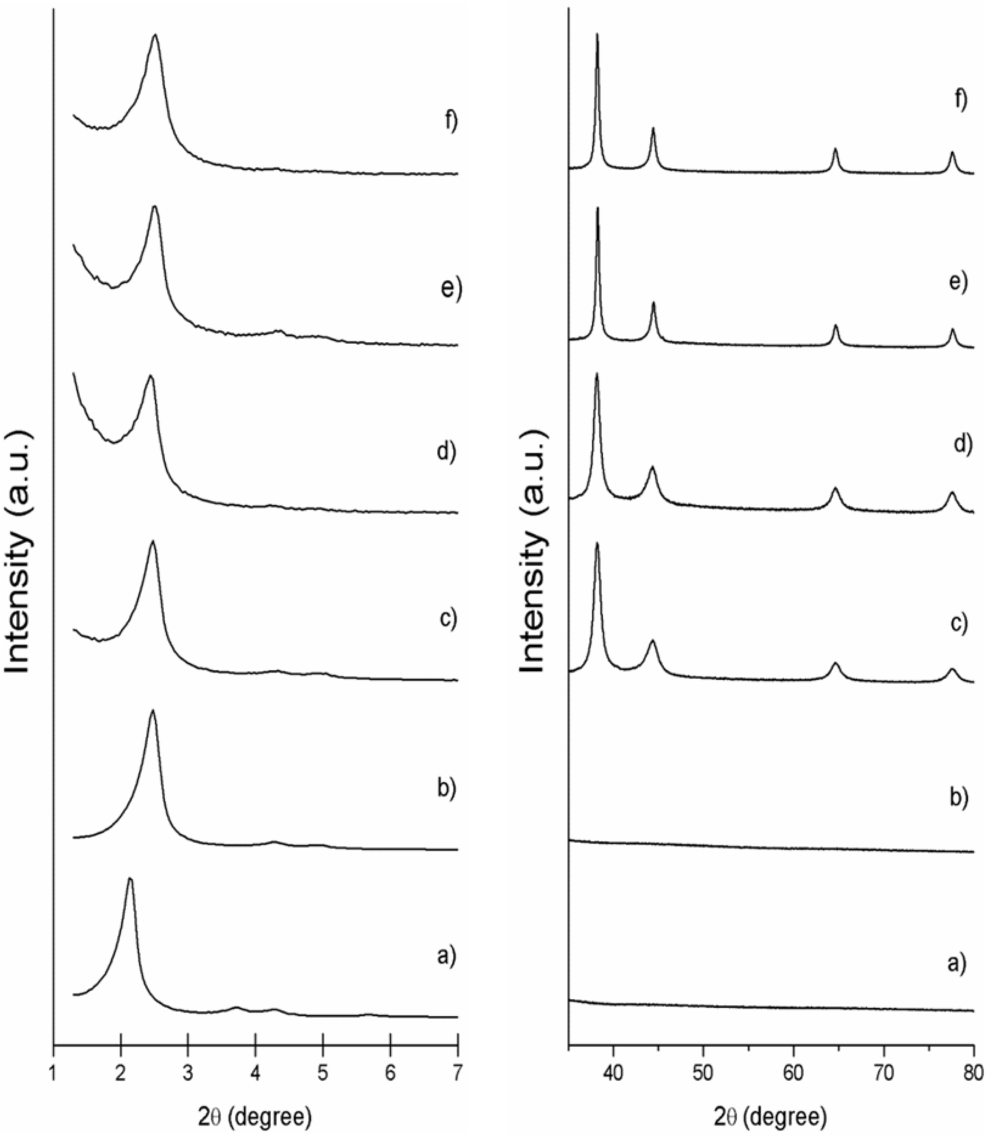

Figure SI-4. Powder X-Ray patterns at low (left) and high (right) angles of: (a) as-synthesised **MCM-41**, (b) calcined **MCM-41**, (c) **S1** nanoparticles, (d) **S1-I** nanoparticles, (e) solid **S2** and final nanodevice **S3**.

PXRD profile of the as-made **MCM-41** mesoporous silica nanoparticles in the 1.5 < 2θ < 7 range (Figure SI-4, a) shows the typical low-angle reflections that can be indexed as (100), (110) and (200) Bragg peaks. A slight displacement of the peaks in the PXRD of the calcined **MCM-41** is related to the condensation of silanol groups during the calcination process. These typical peaks are also observed for **S1** (Figure SI-4, c) which indicates that the mesoporous structure is preserved in the Janus Au-MS nanoparticles. The presence of the (100) peak in the PXRD patterns of the other solids indicates that the different chemical modifications, functionalization and cargo loading had not damage the mesoporous structure. Moreover, the high-angle diffraction pattern of the Janus Au-mesoporous silica colloids showed the cubic gold characteristic (111), (200), (220) and (331) diffraction peaks, confirming the presence of gold nanocrystals and the Janus Au-MS architecture.

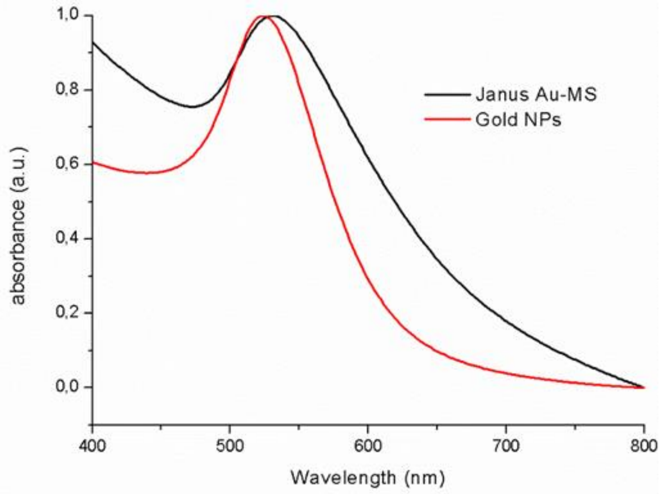

Figure SI-5. Normalized UV-Visible spectra of the gold nanoparticles (red) and Janus Au-MS **S1** (black).

UV/vis measurements in aqueous solution were performed on the as-synthesized gold nanoparticles and on Janus Au-MS nanoparticles **S1** (by suspending 0.5 mg of solid in 2 mL of water). The starting gold colloid shows a single absorption band at 524 nm, characteristic of the surface plasmon resonance of spherically shaped nanospheres with an approximately 20 nm diameter (Figure SI-5). In the **S1** spectrum, there is a redshift of the absorbance maximum (531 nm) and a broadening of the band. These two facts can be ascribed to the increase in the refractive index around the gold nanospheres due to the MS attachment and to light refraction produced by silica.[5]

The N_2 adsorption-desorption isotherms of the calcined **MCM-41** and Janus nanoparticles **S1** show the typical curve for mesoporous solid; i.e. an adsorption step at intermediate P/P_0 value 0.3 (see figure SI-6, curves a and b). This step is related to the nitrogen condensation inside the mesopores by capillarity. The absence of a hysteresis loop in this interval and the narrow BJH pore distribution suggest the existence of uniform cylindrical mesopores. The application of the BET model results in a value for the total specific surface of 893.63 $m^2 \cdot g^{-1}$ for calcined **MCM-41** and 721.01 $m^2 \cdot g^{-1}$ for **S1**. N_2 adsorption-desorption isotherms for the loaded and functionalized solid **S2** show a significant decrease in N_2 volume adsorbed and they are flat when compared (at the same scale) to parent **MCM-41** and **S1** curves. This indicates that there is a significant pore blocking for **S2** as a consequence of cargo loading. Additionally, the curve for **S2** shows a N_2 adsorption at high relative pressure similar to the calcined **MCM-41**, confirming that the textural porosity is preserved. The pore size was estimated by using the BJH model applied on the adsorption band of the isotherm for $P/P_0 < 0.6$. Pore size for calcined **MCM-41** and **S1** are 2.34 and 2.33 nm respectively, which are in agreement with the typical values for these materials and can associated to the surfactant generated mesopores. Total pore volume was also calculated according to BJH model. BET specific values, pore volumes and pore sizes calculated from N_2 adsorption-desorption isotherms for selected materials are listed in Table SI-2.

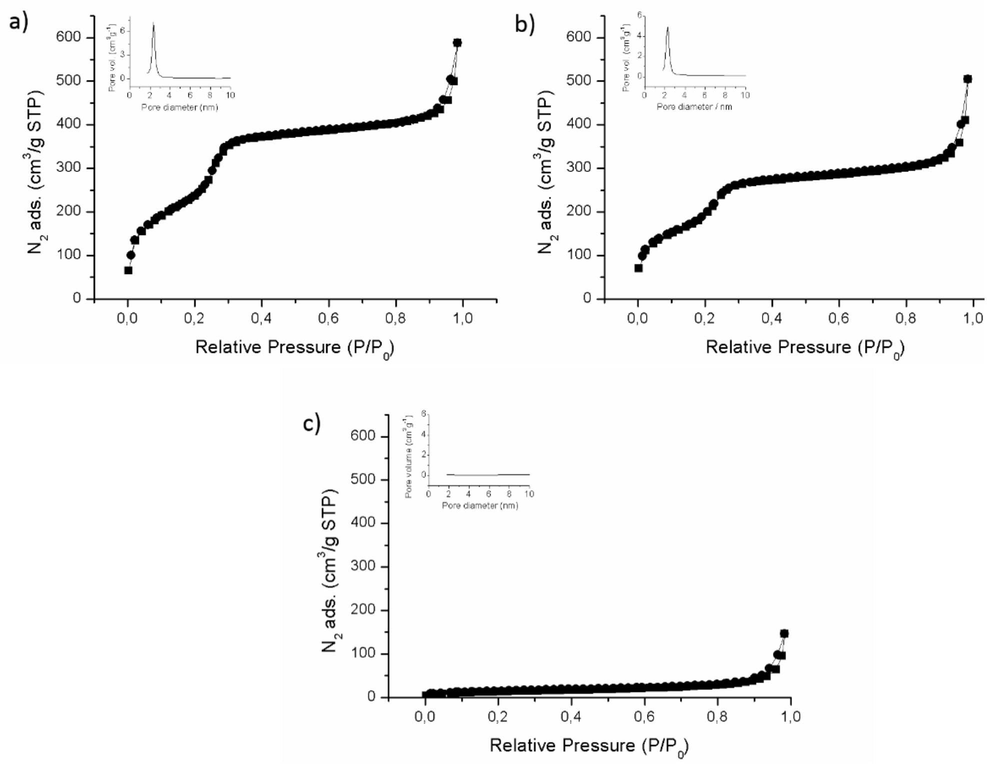

Figure SI-6. The N$_2$ adsorption-desorption isotherms for (a) the calcined **MCM-41** mesoporous material, (b) Janus Au-MS nanoparticles **S1** and (c) **S2** loaded solid. Inset: Pore size distribution.

Table SI-2. BET specific surface values, pore volumes and pore sizes calculated from N$_2$ adsorption-desorption isotherms for selected materials.

Sample	S_{BET} [m^2 g^{-1}]	Pore Volume [cm^{3}g^{-1}]	Pore size [nm]
MCM-41	893.63	0.68	2.34
S1	721.00	0.51	2.33
S2	49.12	0.037	--

In order to assess the correct operation of the proton-responsive nanovalve, the release from the capped solid **S2-CD** (0.9 mg·mL^{-1}) as a function of time was monitored in solutions at different pHs. As can be seen in Figure SI-7, the release increased when the pH was reduced.

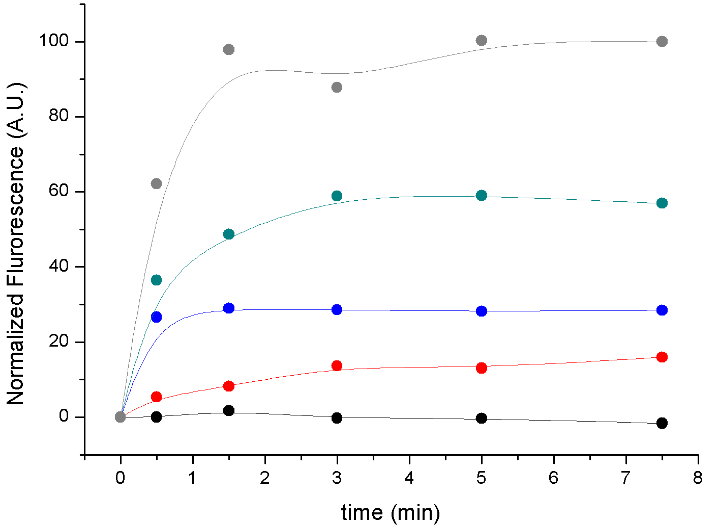

Figure SI-7. Normalized cargo release from **S2-CD** determined by measuring [Ru(bpy)$_3$]Cl$_2$ fluorescence at 595 nm (λ_{exc} = 453 nm) versus time in water at pH 7.5 (black curve), pH 6.8 (red curve), pH 6 (blue curve), pH 5 (green curve) and pH 4 (grey curve).

In order to directly confirm the assembly of all the organic components on the Au-Si support we have carried out solid state ^{13}C-NMR. As can be seen in Figure SI-8, the loaded solid (**S1-l**) spectrum shows four main aromatic signals corresponding to the bipyridine from [Ru(bpy)$_3$]Cl$_2$ cargo that appear between 160-120 ppm. After functionalization with benzimidazole, new aromatic signals appear between 120-115 ppm and at 135 ppm which correspond to the reported values for benzimidazole.[6] Moreover, the capped solid spectrum also shows a main aliphatic signal at 75 corresponding to the C-atoms linked to O-atoms of β-cyclodextrin.

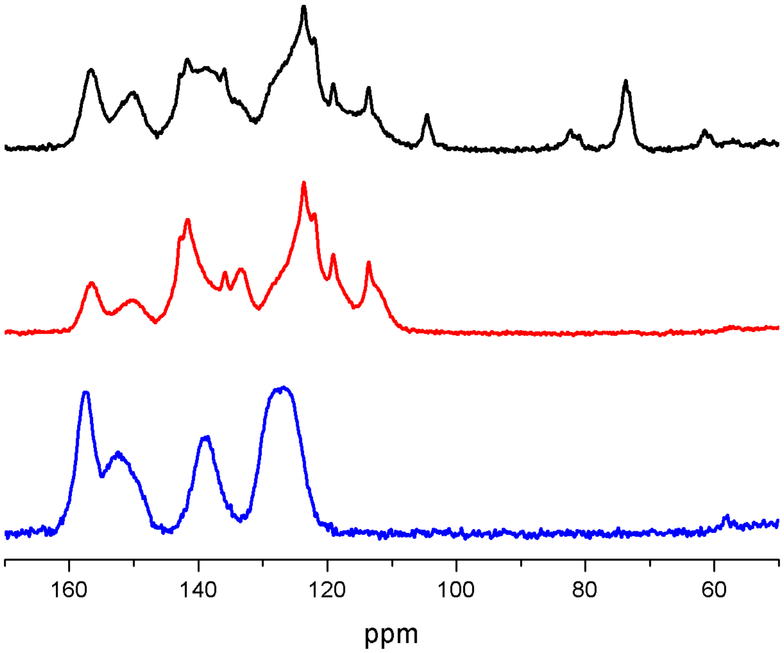

Figure SI-8. ^{13}C-NMR spectra for the loaded solid **S1-I** (blue line), solid **S2** (functionalized with benzimidazole, red line) and nanoparticles capped with β-cyclodextrin **S2-CD** (black line).

Figure SI-9 shows the Fourier transform infrared (FT-IR) spectra for all synthesized solids. **MCM-41** and **S1** had spectra similar to those previously reported for MS and Janus Au-MS nanoparticles. The band at 1080 cm^{-1} with a shoulder at 1200 cm^{-1} can be ascribed to the bond stretching vibrations of Si-O-Si. The spectrum of the Janus nanoparticles **S1** shows antisymmetric and symmetric stretching vibrations of the CH_2 groups at 2927 and 2851 cm^{-1}, confirming the modification of the mesoporous silica with (3-mercaptopropyl)triethoxysilane. The spectrum of **S2** showed the presence of characteristic IR adsorption bands of benzimidazole groups.[7] The spectrum of **S3** showed the typical β-cyclodextrin bands at 1060 cm^{-1} and the amide I band of proteins at 1642 cm^{-1}. The presence of both bands confirmed the successful immobilization of acetylcholinesterase. In addition, the broad band at 3700-3000 cm^{-1} can be attributed to the O-H bonding vibration of adsorbed water.

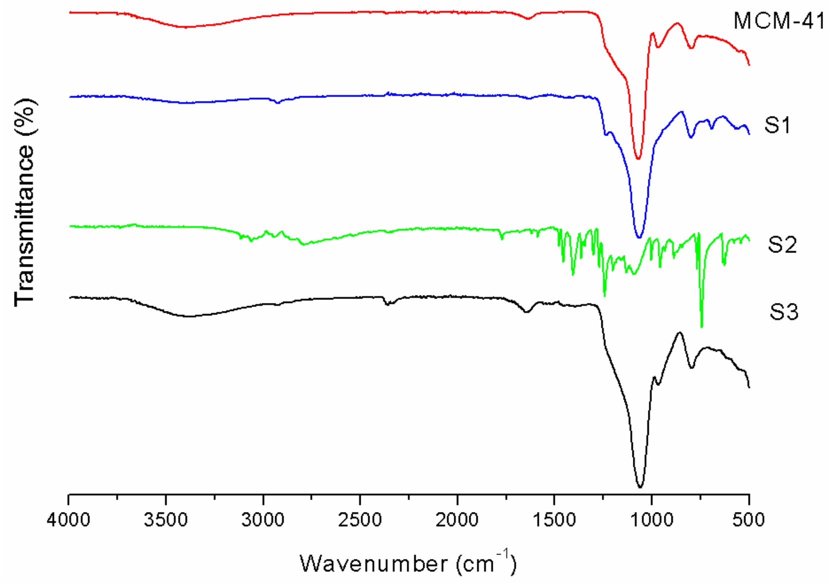

Figure SI-9. FT-IR analysis for the solids **MCM-41**, **S1**, **S2** and final nanodevice.

We determined the hydrodynamic diameter and zeta potential of each material and also of the enzyme acetylcholinesterase. For carrying out the experiments, 1 mg of the corresponding material was suspended in 1 mL of PBS. For experiments with the enzyme, we prepared 100 µL of enzyme solution in PBS (4 mg·mL^{-1}) and measured it by using the diffusion barrier technique.[8] The diffusion barrier technique allows to introduce a small plug of sample (100-20 µL) in the middle of the cuvette and separated from the electrodes by the same buffer that the enzyme is dissolved in. This allows to use a low amount of protein (that might be very expensive) and to obtain reliable measurements. We determined a zeta potential of -15.6 mV for the enzyme which is in agreement with the increase seen after the enzyme attachment to the nanoparticles (from -6.6 mV for **S2** to -14.9 for **S3**). For the hydrodynamic light scattering, we determined a value of 6.0 nm for the enzyme which is in the range of the Stokes radii previously reported for acetylcholinesterases.[9]

Table SI-3. Hydrodynamic diameter (nm) and zeta potential (mV) for each material and the enzyme under physiological conditions (PBS).

Sample	Hydrodynamic diameter (nm)	Zeta potential (mV)
MCM-41	91.2	-21.5
S1	141.8	-12.6
S2	164.2	-6.6
S3	195.3	-14.9
Acetylcholinesterase	6.0	-15.6

Table SI-4. Elemental analysis contents for the different materials.

Solid	% C	% H	% N	% S
S1	3.14	2.32	0.11	0.29
S1-I	20.76	3.63	2.23	0.11
S2	21.23	2.75	4.75	0.12

From elemental analysis data, first we determined the content of [(Ru(bpy)$_3$]Cl$_2$ taking into account that 2.13% increase in N content from **S1** to **S1-I** corresponded to the N atoms of the loaded dye (0.131 g of N per g of [Ru(bpy)$_3$]Cl$_2$). For calculating, benzimidazole content on **S2**, we took into account that [Ru(bpy)$_3$]Cl$_2$ is not soluble in toluene (it would remain inside the solid), and therefore the 2.52 % increase in N content can be ascribed to the anchored benzimidazole groups. The contents of $[Ru(bpy)_3]Cl_2$ and benzimidazole were determined as follows:

$$\text{dye content} = \frac{2.12\ g\ of\ N}{100\ g\ of\ solid} * \frac{1\ g\ of\ [Ru(bpy)_3]Cl_2}{0.131\ g\ of\ N} = 0.162\ \frac{g\ [Ru(bpy)_3]Cl_2}{g\ of\ solid}$$

$$\text{benzim. content} = \frac{2.52\ g\ of\ N}{100\ g\ of\ solid} * \frac{1\ g\ of\ benzim.}{0.239\ g\ of\ N} = 0.105\ \frac{g\ of\ benz.}{g\ of\ solid}$$

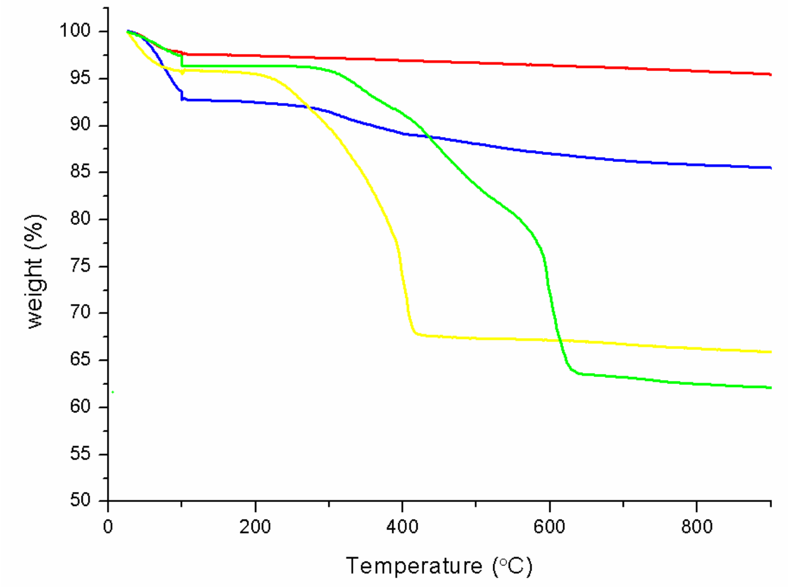

Figure SI-10. Termogravimetric analysis (TG) for calcined **MCM-41** (red), **S1** nanoparticles (blue), **S1-I** nanoparticles (yellow) and solid **S2** (green).

Enzyme activity assay

Acetylcholinesterase activity on **S3** was checked by the Ellman's assay.[10] The test is based on the fact that thiols react with Ellman's reagent (5,5'-dithiobis(2-nitrobenzoic acid), DTNB), cleaving the disulfide bond to give 2-nitro-5-thiobenzoate (TNB^{2-}). This TNB^{2-} has a characteristic yellow colour that can be monitored by UV-visible spectrophotometry. Acetylthiocholine is used as the enzyme substrate which when hydrolysed produces the resulting thiocholine as the thiol containing molecule.

In a typical assay, 900 µL of 100 mM sodium phosphate buffer (pH 7.5), 30 µL 10 mM DTNB solution and 12 µL of acetylthiocholine (75 mM) where placed in a quartz cuvette. Then, 6 µL of either buffer (for blank) or modified-acetylcholinesterase (2 mg·mL^{-1}) or **S3** (2.7 mg·mL^{-1}) were added. The mixture was shaken and absorbance at 412 nm was monitored. When the modified-enzyme or **S3** were added, the solution turned yellow quickly as a consequence of TNB^{2-} formation due to the acetylcholinesterase activity (Figure SI-11 and 12).

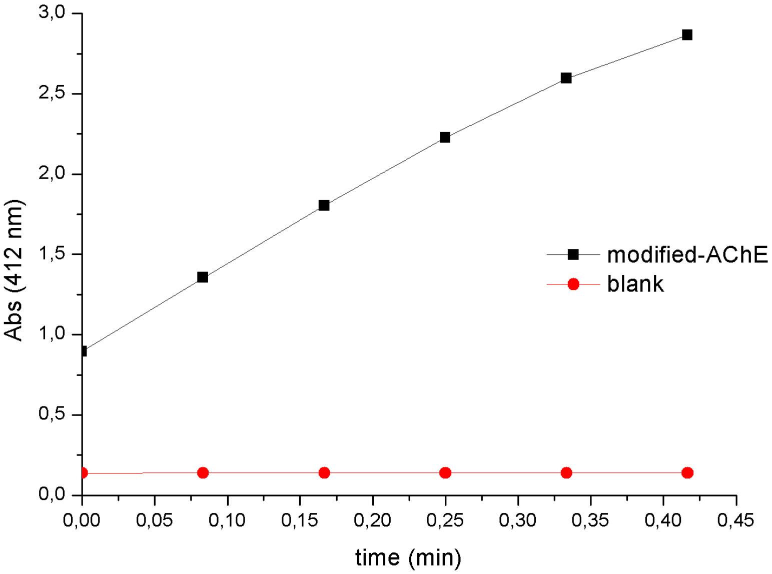

Figure SI-11. Monitoring of TNB^{2-} formation due to acetylcholinesterase activity of the modified-enzyme.

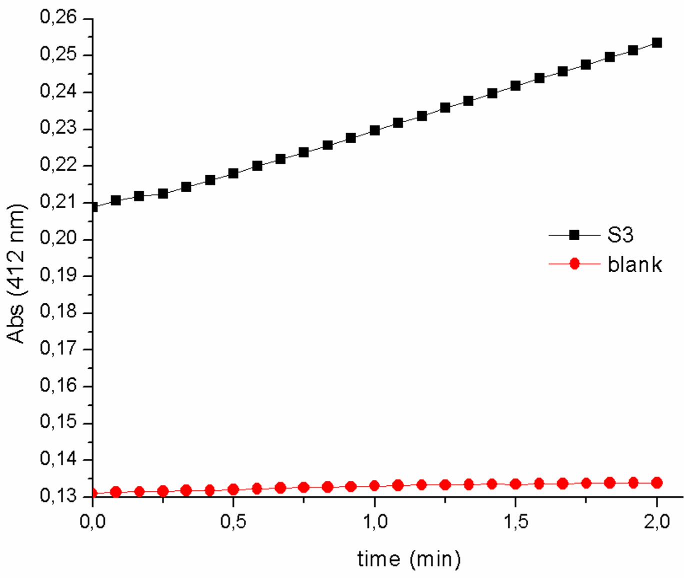

Figure SI-12. Monitoring of TNB^{2-} formation due to acetylcholinesterase activity on **S3**.

The acetylcholinesterase activity on **S3** was estimated to be 93 U·g^{-1}, by applying the following formula:

$$\frac{\text{Enzyme Units}}{\text{g}} = \frac{(\Delta - \Delta_{\text{blank}}) * \text{V}_{\text{T}} * \text{F}_{\text{D}}}{\varepsilon_{TNB} * \text{l} * \text{V}_{NPs} * C_{NPs}}$$

Where,

Δ is the slope of the graph (min^{-1})

Δ_{blank} is the slope of the graph for the blank (min^{-1})

V_T is the total volume in the cuvette

ε_{TNB} is the molar extinction of TNB^{2-} at 412 nm (13,700 $M^{-1} \cdot cm^{-1}$)

L is the optical path in the cuvette (1 cm)

V_{NPs} is the volume of nanoparticles added (mL)

C_{NPs} is the concentration of nanoparticles suspension added (g/mL).

Acetylcholine concentrations in the body

Table SI-5. Acetylcholine concentrations in the body.

Region	Acetylcholine concentration	Reference
Blood	9 nM	11
Synaptic vesicles	100 mM	12,13
Neuromuscular junction/Synaptic Cleft	1-0.5 mM	13,14
Extrasynaptic space	3-0.01 µM	13
Striatum	30-50 µM	15
Hippocampus	7 mM	16
Frontal Cortex	3.75 mM	16

Release experiments

In a typical release experiment, refrigerated solutions of **S3** where aliquoted and suspended in 1.5 mL of aqueous solution (20 mM Na_2SO_4, pH 7.5). Nanoparticles were washed, divided in two fractions and finally brought to a concentration of 0.9 mg·mL^{-1}. Then, the corresponding input was introduced to one of the suspensions and shaken over time. Aliquots were taken at scheduled time and centrifuged to remove the nanoparticles. Then, the fluorescence at 595 nm of the $[Ru(bpy)_3]Cl_2$ dye released was measured (λ_{exc} = 453 nm). For **S4** (loaded with Doxo), the procedure was the same but in this case Doxo emission was registered at 557 nm (λ_{exc} = 495 nm).

Cell experiments

Cell culture conditions

The HeLa human cervix adenocarcinoma cells were grown in Dulbecco's Modified Eagle's Medium (DMEM) supplemented with 10% fetal bovine serum and 1% antibiotic-antimycotic. Cells were maintained at 37 °C and 5% CO_2 with 95% humidity. Cells underwent passage twice in a week.

Confocal microscopy

HeLa cells were seeded in 24 mm glass coverslips in 6-well microtiter plates at a seeding density of 10^5 cells/well. After 24 hours, cells were treated with **S4** nanoparticles at a final concentration of 100 µg/mL. Then, acetylcholine in DMEM was added at a final concentration of 40 mM and cells were incubated during 1 hour at 37 °C. After that, slides were washed twice with PBS. For fixed cell imaging, the cells were treated with 1 ml of 4% PFA PBS solution for 15 min at room temperature and then slides were visualized under a confocal.

The images were acquired under a confocal microscope employing Leica TCS SPE inverted laser scanning confocal microscope using oil objective HC PL APO 40x. The images were acquired with an excitation wavelength of 480 nm for Doxorubicin. Two-dimensional pseudo-colour images (255 colour levels) were gathered with a size of 1024x1024 pixels and Airy 1 pinhole diameter. Three fields of each condition in two independent experiments were performed obtaining similar results.

Cell viability assays

Cells were cultured in sterile 24–well microtiter plates at a seeding density of 2 x 10^4 cells/well for HeLa and were allowed to settle for 24h. Then acetylcholine, **S4**, or both were added to the cells at different final concentrations. After 1 hour of incubation cells were washed and incubated for 22 h, then WST-1 was added to each well. Cells were further incubated for 1 h (a total of 24 h of incubation was therefore studied). Afterward, cells were shaken thoroughly for 1 minute on a shaker and the absorbance was measured at 450 nm against a background control as blank using a microplate ELISA reader. The reference wavelength was 690 nm.

Cells were treated with **S4** at final concentrations of 25, 50, 75 and 100 µg/ml with or without acetylcholine at a final concentration of 40 mM. Furthermore, the toxicity of acetylcholine was assessed showing no toxicity up to 40 mM for 24 hours (see Figure SI-13).

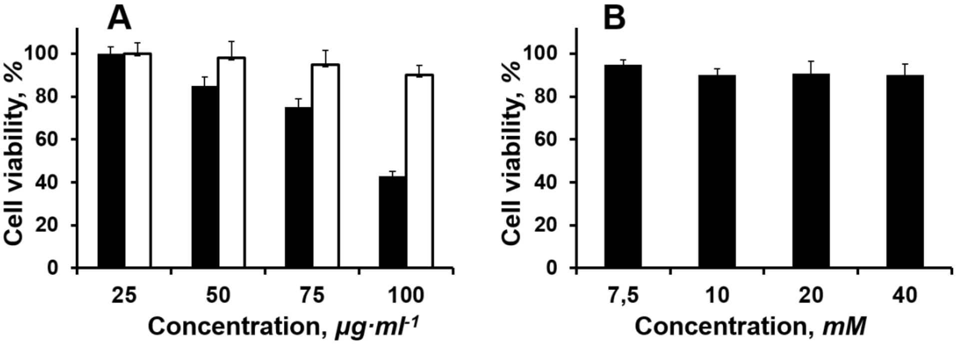

Figure SI-13. WST-1 Cell viability assay. (A) **S4** nanoparticles in the presence of acetylcholine (40 mM) (black bars) or in the absence (white bars). (B) Cell viability of HeLa cells treated with different amounts of acetylcholine for 24 hours.

---

1. J. A. Turkevich, *Discuss. Faraday Soc.* **1951**, *11*, 55-75; b) G. Frens, *Nature* **1973**, *241*, 20-22.
2. a) R. Villalonga, P. Díez, A. Sánchez, E. Aznar, R. Martínez-Máñez, J. M. Pingarrón, *Chem. Eur. J.* **2013**, *19*, 7889–7894; b) P. Díez, A. Sánchez, M. Gamella, P. Martínez-Ruíz, E. Aznar, C. De La Torre, J. R. Murguía, R. Martínez-Máñez, R. Villalonga, J. M. Pingarrón, *J. Am. Chem. Soc.* **2014**, *136*, 9116–9123.
3. a) L. Gómez, H.L. Ramírez, M.L. Villalonga, J. Hernández, R. Villalonga, *Enzyme Microb. Technol.* **2006**, *38*, 22-27; b) B. Chico, C. Camacho, M. Pérez, M.A. Longo, M.A. Sanromán, J.M. Pingarrón, R. Villalonga, *J. Electroanal. Chem.* **2009**, *629*, 126-132.
4. S. Moktan, E. Perkins, F. Kratz, D. Raucher, *Mol. Cancer Ther.* **2012**, *11*, 1547-1556.
5. K. L. Kelly, E. Coronado, L.L. Zhao, G.C. Schatz, *J. Phys. Chem. B* **2003**, *107*, 668-677.
6. K. J. Morgan, *J. Chem. Soc.* **1961**, 2343-2347.
7. J. C. Corbett, M. Connah, K. Mattison, *Electrophoresis* **2011**, *32*, 1787-1794.
8. S. Bon, M. Vigny, J. Massoulié, *PNAS* **1979**, *76*, 2546-2550.
9. T. Wang, M. Wang, C. Ding, J. Fu, *Chem. Commun.* **2014**, *50*, 12469-12472.
10. G. L. Ellman, K. D. Courtney, V. Andres, R. Featherstone, *Biochem. Pharm.* **1961**, *7*, 88-95.

11. S. Lin, C.-C. Liu, T.-C. Chou, *Biosens. Bioelectron.* **2004**, *20*, 9–14.
12. A. Schena, K. Johnsson, *Angew. Chem. Int. Ed.* **2014**, *53*, 1302-1305.
13. E. S. Vizi, A. Fekete, R. Karoly, A. Mike, *Br. J. Pharmacol.* **2010**, *160*, 785-809.
14. Y. Zhou, L.-L. Tan, Q.-L. Li, X-L. Qiu, A.-D. Qi, Y. Tao, Y.-W. Yang, *Chem. Eur. J.* **2014**, *20*, 2998-3004.
15. a) R. Hassler, P. Haug, C. Nitsch, J. S. Kim, K. Paik, *J. Neurochem.* **1982**, *38*, 1087-1098; b) M. H. Sethy, V. H.; Van Woert, *Nature* **1974**, *251*, 529-530.
16. Z. Batool, S. Sadir, L. Liaquat, S. Tabassum, S. Madiha, S. Rafiq, S. Tariq, T. S. Batool, S. Saleem, F. Naqvi *et al.*, *Brain Res. Bull.* **2016**, *120*, 63-74.

4. Au-Mesoporous Silica Nanoparticles Gated with Disulfide-Linked Oligo(Ethylene Glycol) Chains for Tunable Cargo Delivery Mediated by an Integrated Enzymatic Control Unit

Au-Mesoporous Silica Nanoparticles Gated with Disulfide-Linked Oligo(ethylene glycol) Chains for Tunable Cargo Delivery Mediated by an Integrated Enzymatic Control Unit

A. Llopis-Lorente,[a,b,c] B. de Luis,[a,b,c] A. García-Fernández,[a,b,c] P. Díez,[d] A. Sánchez,[d] M. D. Marcos,[a,b,c] R. Villalonga,*[d] R. Martínez-Máñez,*[a,b,c] and F. Sancenón[a,b,c]

[a] Instituto Interuniversitario de Investigación de Reconocimiento Molecular y Desarrollo Tecnológico (IDM), Universitat Politècnica de València-Universitat de València (Spain).

[b] Departamento de Química, Universitat Politècnica de València, Camino de Vera s/n, 46022 Valencia (Spain). E-mail: rmaez@quim.upv.es

[c] CIBER de Bioingeniería, Biomateriales y Nanomedicina (CIBER-BBN).

[d] Department of Analytical Chemistry, Faculty of Chemistry, Complutense University of Madrid, 28040 Madrid (Spain). E-mail: rvillalonga@quim.ucm.es

(Reprinted with permission from ***J. Mater. Chem. B* 2017, *5*, 6734-6739**.

4.1 Abstract

We report a delivery system based on Au–mesoporous silica (MS) nanoparticles functionalized with acetylcholinesterase on the Au face as a control unit and with disulfide-containing oligo(ethylene glycol) chains on the MS face as caps. The control unit handles the chemical information in the environment (the presence of acetylthiocholine or enzyme inhibitors) that results in a tuned cargo delivery from the nanocarrier. The nanodevice displayed an enhanced cargo delivery in cancer cells (safranin O and doxorubicin) in the presence of acetylthiocholine.

4.2 Introduction

In recent years, the development of smart delivery systems able to release their cargo upon application of specific stimuli has attracted much attention due to their potential application in the biomedical and sensing fields.[1] Systems based on liposomes, inorganic scaffolds and polymeric nanoparticles having different size, structure, surface and delivery properties have been reported.[2] In addition, researchers are currently developing active nanomotors using enzymes as future nanovehicles, and some examples are already available.[3] Among potential drug nanocarriers, mesoporous silica (MS) supports are especially appealing because of their unique properties, such as chemical stability, high loading capacity, low cost and biocompatibility.[4] Gated MS supports for cargo delivery usually contain two subunits: (i) a porous scaffold in which a cargo is loaded and (ii) molecular, supramolecular or biomolecular ensembles, placed on the external surface of the loaded solid, capable of being ‘‘opened’’ or ‘‘closed’’ on-command in order to control payload delivery from pores. In line with this concept, examples of gated MS supports responsive to physical (light, temperature, magnetic fields, ultrasounds), chemical (anions, cations, neutral molecules, redox-active species and pH) and biochemical (such as enzymes, DNA and antibodies) stimuli have been reported.[5]

Inside this area of gated materials, we have recently reported the design of more sophisticated nanodevices for delivery applications based on Janus nanoparticles with Au and MS on opposite faces.[6] This allows the immobilization of enzymes on the Au face (control unit) and molecular/supramolecular gates on the MS face. The role of the ‘‘control unit’’ is to handle chemical information (input) of the environment and transform it into new molecules that control the state of the gate (open or closed) (see Scheme 1). Such systems have been used in complex communication networks.[5b,6c] Moreover, this expands the possibilities for the construction of smart delivery systems since enzymes can be chosen to recognize a large number of different specific substrates and produce a certain stimulus, through an enzyme mediated process, able to open the gated ensemble. As far as we know, very few examples of gated Janus Au–MS nanoparticles have been reported and both are based on enzyme-mediated commutation of pH-responsive molecular gates.[6]

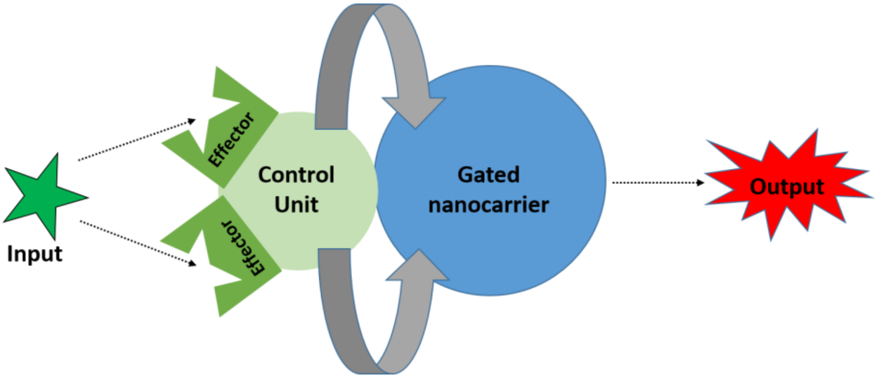

Scheme 1. Representation of a Janus Au–MS nanodevice containing a control unit that regulates delivery in the gated MS face.

4.3 Results and discussion

With the aim of opening new directions towards the construction of smart delivery systems, we report herein the first example of an enzyme-controlled Janus Au–MS nanodevice in which delivery is driven by a thiol-exchange redox mechanism. Additionally, we also show that cargo release can be modulated by the presence of certain substances. Usually gated nanodevices exhibited a simple delivery upon application of a triggering stimulus. However, in our designed system, the control unit is able to detect the presence of certain chemicals in the solution (enzyme inhibitors) and tune cargo delivery accordingly.

Scheme 2 illustrates the design and operation of the system. The enzyme acetylcholinesterase was immobilized on the Au face of the of the Janus Au–MS nanoparticles. The MS face was loaded with a suitable cargo (safranin O) and its external surface was functionalized with disulfide-containing oligo(ethylene glycol) chains (SS-OEG) which act as molecular gates. The Au side (control unit) was functionalized with acetylcholinesterase that is able to detect the presence of acetylthiocholine, a derivative of the neurotransmitter acetylcholine.[7] In particular, the hydrolysis of acetylthiocholine[8] by the enzyme produces thiocholine that cleavages the disulfide bond on the MS face resulting in pore opening and payload release. Moreover, the nanodevice is also sensitive to the presence of diisopropyl fluorophosphate (DFP) which regulates enzyme activity and consequently also cargo delivery from the MS face.

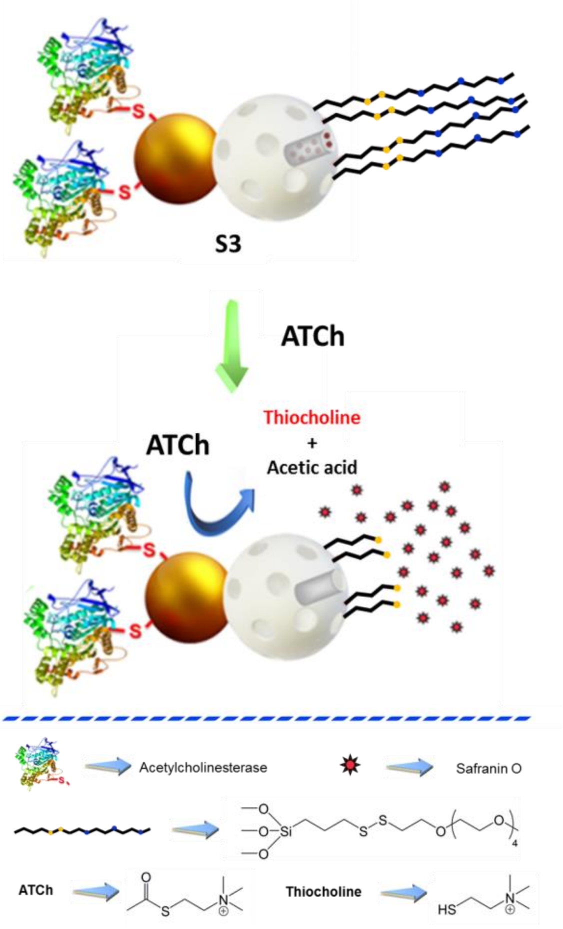

Scheme 2. Representation of the performance of the nanodevice **S3**. The ‘’control unit’’ (Au face) is functionalized with acetylcholinesterase, which directs the cargo delivery form the mesoporous face in the presence of acetylthiocholine (ATCh).

In order to prepare the nanodevice, first MS nanoparticles were obtained by hydrolysis and condensation of tetraethyl orthosilicate in basic media using cetyltrimethylammonium bromide as a template. The surfactant was then removed by calcination in air at high temperature which yield the starting mesoporous support. In a second step, gold nanoparticles were synthesised by reduction of Au(III) with sodium citrate based on the Turkevich–Frens method.[9] Next, MS nanoparticles were confined at the interface of a Pickering emulsion between paraffin and an aqueous face in order to achieve its partial functionalization with (3-mercaptopropyl)trimethoxysilane on which Au nanoparticles were attached by the formation of S–Au bonds. The paraffin wax was removed by washing with $CHCl_3$ which yield the initial Janus Au–MS nanoparticles (**S1**). In a further step, the pores of the MS face were loaded with safranin O by stirring overnight at room temperature a suspension of the nanoparticles in an aqueous solution of the dye. Next, the Au surface was functionalized with 3-mercaptopropionic acid, which was attached by the formation of Au–S bonds. Afterward, an excess of (3-mercaptopropyl)trimethoxysilane was added to functionalize the mesoporous surface and the thiol-functionalized solid was further reacted with 2,2-dipyridyl disulfide. Then, substitution of dipyridyl groups by reaction with O-(2-mercaptoethyl)-O-methyl-hexa(ethylene glycol) (SS-OEG) allowed the capping of the mesoporous scaffold yielding the nanoparticles **S2**. Finally, the enzyme acetylcholinesterase was immobilized by coupling lysine residues in the enzyme with the carboxylic groups on the gold surface via the use of *N*-hydroxysuccinimide (NHS) and ethyl(dimethylaminopropyl)carbodiimide (EDC).[10] This process finally yielded **S3** nanoparticles (see Scheme 3) which were kept wet in the refrigerator until use. Nanoparticles similar to **S3**, but loaded with the cytotoxic agent doxorubicin, were also prepared (**S3**$_{\mathbf{DOX}}$, see Supporting Information for details).

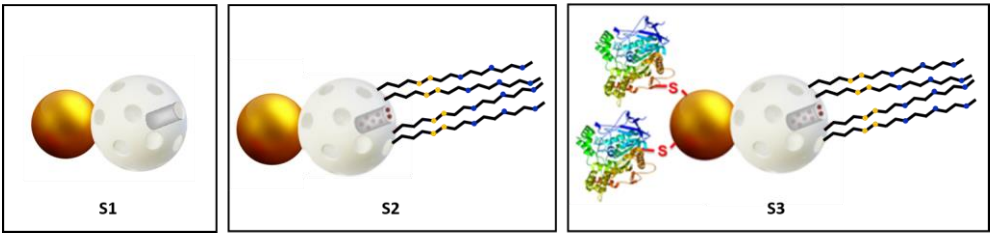

Scheme 3. Representation of the Janus Au–MS nanoparticles (**S1**), capped nanoparticles (**S2**) and enzyme-functionalized nanodevice (**S3**).

Solids were characterized using standard procedures (see Supporting Information). The mesoporous morphology of the MS nanoparticles (diameter of ca. 70–100 nm) as well as the presence of the Au nanoparticles (diameter of ca. 20–25 nm) in Au–MS colloids was confirmed by transmission electron microscopy (TEM) analysis (see Figure 1 and Figure SI-1 for additional images). The powder X-ray diffraction (PXRD) pattern of the starting MS nanoparticles showed the mesoporous characteristic reflection peak (100) around 2.41° (see Figure 1). The preservation of this typical peak in **S1** and **S2** clearly confirms that the surface functionalization and cargo loading processes did not damage the mesoporous scaffolding. Moreover, the diffraction pattern at high angles for Janus colloids showed the cubic gold nanocrystals characteristic (111), (200), (220), and (311) peaks,[11] confirming the Au–MS architecture observed by TEM (see also Figure 1). N_2 adsorption–desorption isotherms of starting MS and **S1** showed an adsorption step at intermediate P/P_0 values (0.1–0.3) which indicates the presence of empty pores (see Figure SI-2). BET specific surface area,[12] BJH pore volumes[13] and pore sizes were calculated and are summarized in Table SI-1. Moreover, contents of safranin O and SS-OEG groups in **S2** were determined by elemental analysis (see Table SI-2), giving values of 52.6 and 137 mg per gram of solid, respectively. Furthermore, the activity of immobilized enzyme on the final nanodevice **S3** was determined to be 797 U g^{-1}, that corresponds to 3.5 mg g^{-1} (see Figure SI-3). Moreover, TEM-EDX mapping of the gold side of the nanodevice shows that this area was rich in sulphur atoms (see Figure SI-4), thus confirming the preferential localization of the enzyme in the gold face.

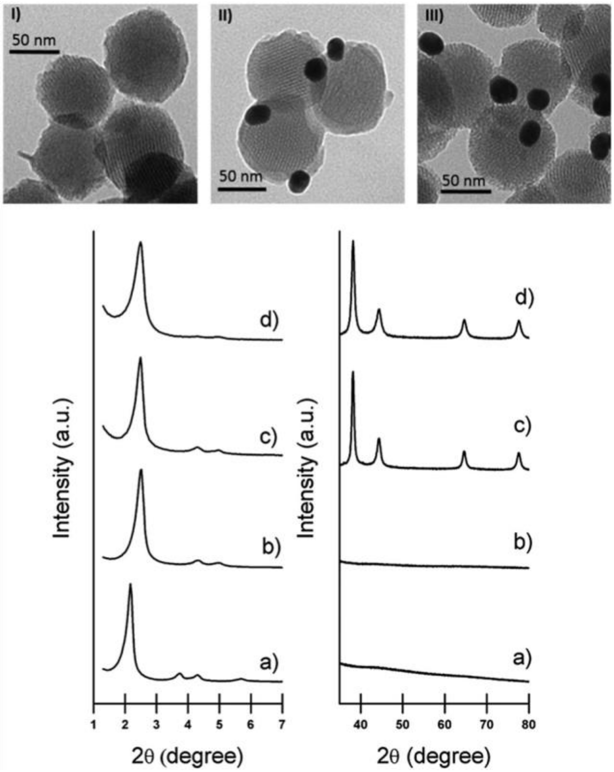

Figure 1. Top: TEM images of (I) calcined mesoporous silica, (II) Janus Au–MS nanoparticles (**S1**) and (III) capped nanoparticles (**S2**). Down: PXRD of (a) as-made mesoporous silica, (b) calcined mesoporous silica, (c) Janus Au–MS nanoparticles (**S1**) and (d) capped nanoparticles (**S2**) at low (left) and high (right) angles.

In order to test the ability of the nanodevice to recognize acetylthiocholine, we brought **S3** to a concentration of 0.9 mg mL^{-1} in aqueous solution at pH 7.5 (50 mM sodium phosphate buffer) in the absence and presence of acetylthiocholine (1 mM). Aliquots were taken at scheduled times, centrifuged to remove nanoparticles, and cargo release was evaluated by measuring the emission band of safranin O at 585 nm (λ_{exc} = 520 nm). Figure 2 shows payload delivery kinetics. In the absence of acetylchiocholine, dye release from **S3** was negligible. However, presence of acetylthiocholine induced pore opening and a subsequent remarkable cargo delivery in less than one hour. In addition, we also carried out experiments in 50 mM sodium phosphate buffer at different relevant pHs, in simulated blood plasma and in PBS (see Supporting Information for details) and in all these cases a similar behaviour was observed (see Figure 3). The observed payload release is attributed to the ‘‘detection’’ of acetylthiocholine by acetylcholinesterase in the control unit. The enzyme transforms acetylthiocholine into thiocholine, which induced cleavage of disulfide bonds in SS-OEG on the MS face, finally resulting in uncapping of the pores and cargo delivery. Thiocholine is able to break disulphide bonds via a thiol–disulfide interchange reaction.[14] This reaction consists on a nucleophilic substitution of a thiol in disulfides with another thiol from a different molecule and plays an important role in biochemistry.

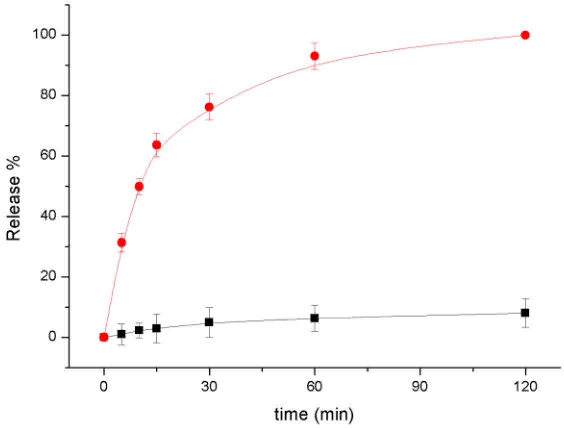

Figure 2. Normalized cargo release from **S3** determined by measuring safranin O fluorescence at 585 nm (λ_{exc} = 520 nm) *versus* time in aqueous solution (50 mM sodium phosphate buffer, pH 7.5) in the absence (black) and presence (red) of acetylthiocholine 1 mM. Error bars from three independent experiments.

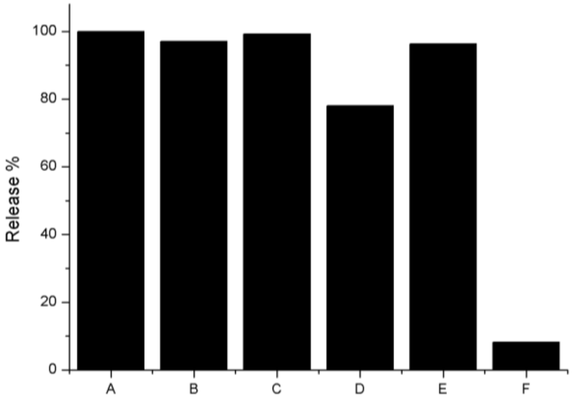

Figure 3. Normalized cargo release from **S3** determined by measuring safranin O fluorescence at 585 nm (λ_{exc} = 520 nm) under different conditions after 120 min. From left to right: in the presence of ATCh 1 mM in 50 mM sodium phosphate buffer at pH 7.5 (A), pH 8.5 (B) and pH 6.5 (C); in the presence of ATCh 1 mM in simulated body plasma (D) and PBS (E) and in the absence of ATCh in PBS (F).

In order to validate the proposed gating mechanism, we carried out additional control experiments. First, the response of **S3** in the presence of acetylcholine was studied. Acetylcholine is also hydrolyzed by the enzyme resulting in the formation of choline and acetic acid.[8] In this case, the release from **S3** in the presence of acetylcholine was negligible since the enzymatic process does not yield thiocholine and therefore the MS face remained capped (Figure 4). Release experiments in the presence of sodium iodide showed that the anion iodide (we used acetylthiocholine iodide for the release experiments in Figure 2) had no effect in the response of **S3** (Figure 4). Moreover, the response of the capped solid **S2** (without enzyme) in the presence of acetylthiocholine resulted in no delivery demonstrating the key role played by the enzyme in the ‘‘control unit’’. The fact that **S3** is able to deliver the cargo in the presence of acetylthiocholine and not with acetylcholine points out how enzymes and molecular gates can be assembled on Janus nanoparticles to operate synergistically and recognize small differences on molecular structure.

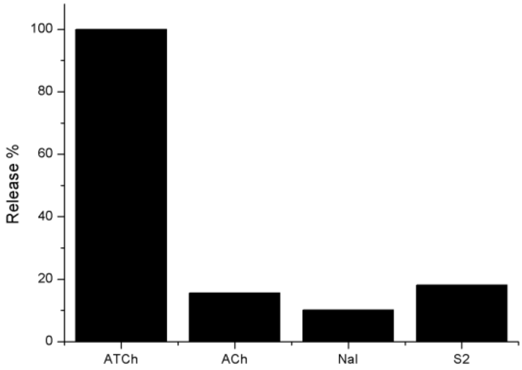

Figure 4. Normalized cargo release from **S3** in aqueous solution (50 mM sodium phosphate buffer, pH 7.5) in the presence of acetylthiocholine (ATCh), acetylcholine (ACh), and sodium iodide and from **S2** (without enzyme) in the presence of ATCh after 120 min.

Encouraged by these findings, we tested in a further step if delivery from **S3** could also be tuned by the presence of enzyme inhibitors. Diisopropyl fluorophosphate (DFP) is a known acetylcholinesterase inhibitor which is used in neuromedicine, also as a pesticide and as a nerve agent simulant.[15] In the presence of DFP, acetylcholinesterase is phosphorylated at the active site, and accordingly, it was expected that acetylthiocholine could not be hydrolyzed.[16] In a typical experiment, **S3** suspensions were incubated with a certain concentration of DFP and acetylthiocholine (1 mM). As shown in Figure 5, cargo delivery from the MS support can be finely tuned depending on DFP concentration. This result stresses again the role of the enzyme-based ʹʹcontrol unitʹʹ, which is able to ʹʹrecognizeʹʹ the presence of the inhibitor and consequently modulate the cargo delivered. Cargo delivery from **S3** can be modulated using concentrations of DFP as low as 5 µM. We also observed a similar response (payload release inhibition) with diethyl cyanophosphonate (DCNP), another acetylcholinesterase inhibitor (see Figure SI-5) and in a less extent with diethyl chlorophosphate (DCP) which indicated that cargo delivery can not only be regulated based on the amount of inhibitor but also on the inhibitor structure.

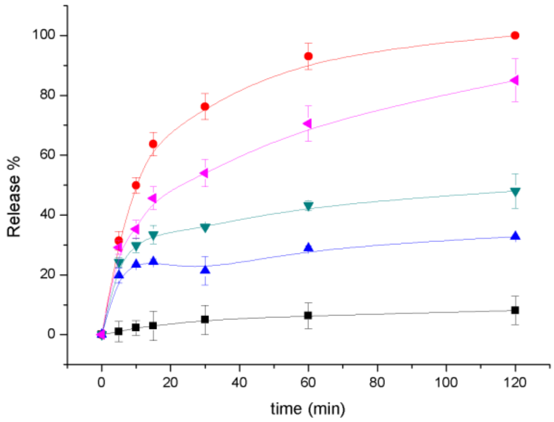

Figure 5. Normalized cargo release from **S3** determined by measuring safranin O fluorescence at 585 nm (λ_{exc} = 520 nm) versus time in aqueous solution (50 mM sodium phosphate buffer, pH 7.5) in the absence (black) and in the presence of acetylthiocholine 1 mM previously incubated with DFP 0.5 mM (blue), 0.05 mM (green), 0.005 mM (magenta) and without DFP (red).

Finally, we evaluated the performance of the nanodevice at cellular level. For this purpose, the human cervix adenocarcinoma (HeLa) cell line was used. First, in order to assess the biocompatibility of **S3** and discard any toxicity associated with the Janus scaffold or the coating shell, cell viability assays were carried out. Cells were incubated with different **S3** concentrations and evaluated by WST-1 cell viability assays after 24 h of exposure. The results demonstrated that **S3** nanoparticles were well-tolerated by HeLa cells at concentrations as high as 200 mg mL^{-1} (see Figure SI-6). Next, the intracellular delivery of the cytotoxic agent doxorubicin using **S3$_{DOX}$** was studied. Doxorubicin is used in cancer therapy in order to kill cancer cells by DNA intercalation and oxidative stress. Cell were treated with 50 and 100 mg mL^{-1} **S3$_{DOX}$** for 30 min, washed to remove noninternalized nanoparticles and further incubated with and without acetylthiocholine for 24 h. At lower **S3$_{DOX}$** dosage (50 mg mL^{-1}), no reduction in cell viability was observed in the absence of acetylthiocoline whereas 20% cell death was induced in the presence of the stimulus (see Figure 6). At higher **S3$_{DOX}$** dosage

(100 mg mL^{-1}), cell viability decreased to around 65% in the absence of acetylthiocholine and it was further decreased to a remarkable 15% in the presence of acetylthiocholine (see also Figure 6). A more efficient elimination of cancer cells was achieved when **S3$_{DOX}$** and acetylthiocholine were co-administered. We also checked that acetylthiocholine did not have any toxic effect by itself. These results demonstrated that cargo release from the Janus nanodevice triggered by acetylthiocholine also works in cells which is a complex high competitive medium.

Additionally, we carried out confocal microscopy experiments to directly image the payload release from the nanodevice in HeLa cells. For this experiments, HeLa cells were incubated with **S3** (100 mg mL^{-1}) in the presence or in the absence of acetylthiocholine. For visualization, cells were stained with DNA-associated dye Hoeschst 3342 and intracellular release of **S3** was monitored by measuring safranin-associated fluorescence. As shown in Figure 6, a strong safranin-associated fluorescence was observed upon addition of acetylthiocholine due to the enzyme mediated uncapping of the particles. On the other hand, only a slight safranin-fluorescence was observed in the absence of acetylthiocholine due to a partial rupture of the disulphide bond by the reductive environment inside the cells. These results were in agreement with WST-1 cell viability assays, thus confirming a much more efficient delivery of the cargo into cancer cells using the nanodevice in combination with acetythiocholine.

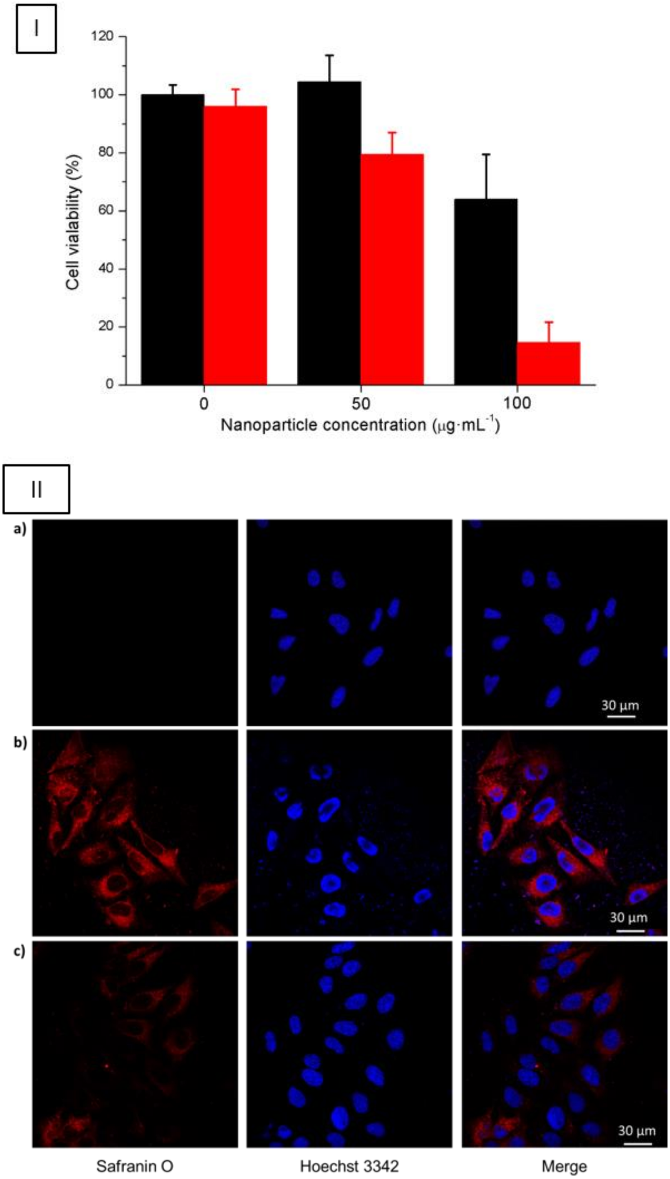

Figure 6. Cell experiments. Top (I): cell viability assays of HeLa cells treated with different concentration of **S3**$_{\mathbf{DOX}}$ (0, 50 and 100 µg mL^{-1}) in the absence (black bars or in the presence (red bars)) of acetylthiocholine (40 mM). Three independent experiments were done. Data are expressed as mean±σ. Down (II): Controlled release from **S3** (100 µg mL^{-1}) in HeLa cells examined by confocal microscopy for (a) control experiment, (b) incubation with **S3** and acetylthiocholine (40 mM) and (c) incubation with **S3**. From left to right: cargo (safranin O) fluorescence, DNA-marker (Hoechst 3342) fluorescence and combined (merge).

Regarding redox-responsive systems, various examples have been designed in the past years with the aim of improving the delivery of drugs into cancer cells. In fact, it has been shown that the incorporation of redox-sensitive moieties in the structure of doxorubicin-loaded biodegradable micelles improved tumour growth inhibition *in vivo*.[17] Other authors have developed glutathione-sensitive bowl-shaped polymeric nanomotors by introducing a disulphide bridge between hydrophilic poly(ethylene glycol) and hydrophobic polystyrene blocks and showed the intracellular delivery of doxorubicin in HeLa cells.[18] Also recently, polymeric nanoparticles containing disulphide bonds between their network have been developed and tested in cells and tumour models.[19] Inorganic materials containing disulphide bridges in their structure or capped with redox-responsive moieties able to realize controlled release of drugs have also been reported.[20] These recent studies point out the current interest in developing redox-sensitive delivery systems with optimized design in order to achieve a better efficiency in drug delivery. As we have shown here, the incorporation of enzymes in combination with redox-responsive systems is a suitable strategy to modulate the delivery of gated nanodevices. In addition, the presence of gold nanoparticles could be of interest for future applications in which drug delivery is combined with optical hyperthermia.[21]

4.4 Conclusions

In summary, we reported here the design, synthesis and characterization of a new enzyme-controlled SS-OEG-gated nanodevice based on Janus Au–MS nanoparticles for cargo delivery. In particular, the Au–MS nanoparticles were functionalized with acetylcholinesterase enzyme on the Au-face and with disulfide -containing oligo(ethylene-glycol) chains on the MS face. Hydrolysis of acetylthiocholine by the enzyme resulted in the formation of thiocholine that induced cleavage of the disulfide bond in SS-OEG, uncapping of the pores and cargo delivery. The nanodevice was opened in the presence of acetylthiocholine but not acetylcholine, which demonstrates how the assembly of enzymes and molecular gates can synergically recognise small differences between molecules. Additionally, we found that the kinetics and amount of payload delivered can be finely tuned by the presence of enzyme inhibitors. Finally, the nanodevice, tested in cancer cells, displayed an enhanced cargo delivery (safranin O and doxorubicin) upon addition to the culture media of acetylthiocholine. Given the number of enzyme-mediated redox processes[22] and gated ensembles that can be brought together in Janus Au–MS supports, we believe our findings could help in the development of new advanced delivery systems.

Acknowledgements

A. Llopis-Lorente thanks ''La Caixa'' Banking Foundation for his PhD fellowship. A. García-Fernández is grateful to the Spanish government for an FPU grant. The authors are grateful to the Spanish Government (MINECO Projects MAT2015-64139-C4-1, CTQ2014-58989-P and CTQ2015-71936-REDT) and the Generalitat Valencia (Project PROMETEOII/2014/047) for support. The Comunidad de Madrid (S2013/MIT-3029, Programme NANOAVANSENS) is also gratefully acknowledged.

4.5 References

1. a) E. Aznar, M. Oroval, L. Pascual, J. R. Murguía, R. Martínez-Máñez and F. Sancenón, *Chem. Rev.*, 2016, **116**, 561; b) S. Giret, M. Wong Chi Man and C. Carcel, *Chem. Eur. J.*, 2015, **21**, 13850; c) M. Vallet-Regí, F. Balas and D. Arcos, *Angew. Chem. Int. Ed.* 2007, **46**, 7548; d) K. T. Kim, S. A. Meeuwissen, R. J. M. Nolte and J. C. M. van Hest, *Nanoscale*, 2010, **2**, 844; e) G. Bao, S. Mitragotri and S. Tong, *Annu. Rev. Biomed. Eng.* 2013, **15**, 253; f) S. Mura, J. Nicolas and P. Couvreur, *Nat. Mater.*, 2013, **12**, 991; g) S.-H. Wu, Y. Hung and C.-Y. Mou, *Chem. Commun.*, 2011, **47**, 9972.
2. a) N. Kamaly, B. Yameen, J. Wu and O. C. Farokhzad, *Chem. Rev.*, 2016, **116**, 2602; b) Y. Li, G. Liu, X. Wang, J. Hu and S. Liu, *Angew. Chem. Int. Ed.*, 2016, **55**, 1760; c) N. K. Sharma, K. Neeraj and V. Kumar, *Drug Delivery Lett.*, 2014, **4**, 12; d) I. K. Yazdi, A. Ziemys, M. Evangelopoulos, J. O. Martinez, M. Kojic and E. Tasciotti, *Nanomedicine*, 2015, **10**, 3057; e) N. Z. Knežević and J.-O. Durand, *Nanoscale*, 2015, **7**, 2199.

3. a) L. K. E. A. Abdelmohsen, M. Nijemeisland, G. M. Pawar, G.-J. A. Janssem, R. J. M. Nolte, J. C. M. van Hest and D. A. Wilson, *ACS Nano*, 2016, **10**, 2652; b) M. Nijemeisland, L. K. E. A. Abdelmohsen, W. T. S. Huck, D. A. Wilson and J. C. M. van Hest, *ACS Cent. Sci.*, 2016, **2**, 843; c) X. Ma, A. Jannasch, U.-R. Albrecht, K. Hahn, A. Miguel-López, E. Schäffer and S. Sánchez, *Nano Lett.*, 2015, **15**, 7043; d) X. Ma, Ana C. Hortelao, A. Miguel-López and S. Sánchez, *J. Am. Chem. Soc.*, 2016, **138**, 13782; e) S. Sengupta, K. K. Dey, H. S. Muddana, T. Tabouillot, M. E. Ibele and P. J. Butler, A. Sen, *J. Am. Chem. Soc.*, 2013, **135**, 1406.
4. a) F. Tang, L. Li and D. Chen, *Adv. Mater.* 2012, **24**, 1504; b) Z. Li, J. C. Barnes, A. Bosoy, J. F. Stoddart and J. I. Zink, *Chem. Soc. Rev.*, 2012, **41**, 2590; c) D. Tarn, C. E. Ashley, M. Xue, E. C. Carnes, J. I. Zink and C. J. Brinker, *Acc. Chem. Res.*, 2013, **46**, 792; d) Y. Zhao, J. L. Vivero-Escoto, I. I. Slowing, B.G. Trewyn and V. S.-Y. Lin, *Expert Opin. Drug Deliv.*, 2010, **7**, 1013; e) C. Argyo, V. Weiss, C. Bräuchle and T. Bein, *Chem. Mater.*, 2014, **26**, 435; f) Y.-W Yang, Y.-L. Sun and N. Song, *Acc. Chem. Res.*, 2014, **47**, 1950; g) A. Popat, S. B. Hartono, F. Stahr, J. Liu, S. Z. Qiao and G. Qing Lu, *Nanoscale*, 2011, **3**, 2801.
5. a) T. M. Guardado-Alvarez, L. Sudha Devi, M. M. Russell, B. J. Schwartz and J. I. Zink, *J. Am. Chem. Soc.*, 2013, **135**, 14000; b) F. Sancenón, L. Pascual, M. Oroval, E. Aznar and R. Martínez-Máñez, *ChemistryOpen*, 2015, **4**, 418; c) A. Baeza, E. Guisasola, E. Ruiz-Hernández and M. Vallet-Regí, *Chem. Mater.* 2012, **24**, 517; d) Z. Zhang, D. Balogh, F. Wang, S. Y. Sung, R. Nechushtai and I. Willner, *ACS nano*, 2013, **7**, 8455; e) A. Bansal and Y. Zhang, *Acc. Chem. Res.*, 2014, **47**, 3052; f) C. Coll, A. Bernardos, R. Martínez-Máñez and F. Sancenón, *Acc. Chem. Res.*, 2013, **46**, 339; g) Y. Chen, H. Zhang, X. Cai, J. Ji, S. He and G. Zha, *RSC Adv.*, 2016, **6**, 92073.
6. a) P. Díez, A. Sánchez, M. Gamella, P. Martínez-Ruíz, E. Aznar, C. De La Torre, J. R. Murguía, R. Martínez-Máñez, R. Villalonga and J. M. Pingarrón, *J. Am. Chem. Soc.*, 2014, **136**, 9116. b) R. Villalonga, P. Díez, A. Sánchez, E. Aznar, R. Martínez-Máñez and J. M. Pingarrón, *Chem. Eur. J.*, 2013, **19**, 7889.
7. a) C. Gotti and F. Clementi, *Prog. Neurobiol.*, 2004, **74**, 363; b) J. Lindstrom, *Mol. Neurobiol.*, 1997, **15**, 193; c) L. Descarries, V. Gisiger and M. Steriade, *Prog. Neurobiol.*, 1997, **53**, 603.
8. H. C. Froede and I. B. Wilson, *J. Biol. Chem.*, 1984, **259**, 11010.
9. a) J. A. Turkevich, *Discuss. Faraday Soc.*, 1951, **11**, 55; b) G. Frens, *Nature*, 1973, **241**, 20.
10. P. Tengvall, E. Jansson, A. Askendal, P. Thomsen and C. Gretzer, *Colloids Surf. B*, 2003., **28**, 261.
11. A. Sánchez, P. Díez, P. Martínez-Ruíz, R. Villalonga and J. M. Pingarrón, *Electrochem. commun.*, 2013, **30**, 51.
12. S. Brunauer, P. H. Emmett and E. Teller, *J. Am. Chem. Soc*., 1938, **60**, 309.
13. E. P. Barrett, L. G. Joyner and P. P. Halenda, *J. Am. Chem. Soc.*, 1951, **73**, 373.
14. a) G. L. Ellman, K. D. Courtney, V. Andres and R. M. Featherstone, *Biochem. Pharmacol*., 1961, **7**, 88; b) P. Nagy, *Antioxid. Redox Signal.*, 2013, **18**, 1623; c) P. C. Jocelyn, *Methods Enzymol.*, 1987, **143**, 246.
15. a) R. A. Westsmith and R. E. Abernethy, *AMA Arch. Ophthalmol.*, 1954, **52**, 779; b) K. Kim, O.G. Tsay, D.A. Atwood and D.G. Churchill, *Chem. Rev.*, 2011, **111**,5345.
16. a) T.M. Shit, R.K. Kan and J.H. McDonough, *Chem. Biol. Interact.,* 2005, **157**, 293; b) C. H. Gunderson, C. R. Lehmann, F. R. Sidell and B. Jabbari, *Neurology*, 1992, **42**, 946; c) A. Silver, The Biology of Cholinesterases, *Elsevier*, New York, 1974, 449-488.
17. Y. Zhu, J. Zhang, F. Meng, C. Deng, R. Cheng, J. Feijem and Z. Zhong, *J. Control. Release*, 2016, **233**, 29.
18. Y. Tu, F. Peng, P. B. White and D. A. Wilson*, Angew. Chem. Int. Ed.*, 2017, **56**, 7620.

19. a) J. Sun, Y. Liu, Y. Chen, W. Zhao, Q. Zhai, S. Rathod, Y. Huang, S. Tang, Y. Tae Kwon, C. Fernandez, R. Venkataramanan and S. Li, *J. Control. Release*, 2017, **258**, 43; b) W. C. de Vries, D. Grill, M. Tesch, A. Ricker, H. Nüsse, J. Klingauf, A. Studer, V. Gerke and B. J. Ravoo, *Angew. Chem. Int. Ed.*, 2017, DOI: 10.1002/anie.201702620.
20. a) J.T. Lin, Z.-K. Liu, Q.-Lin Zhu, X.-H. Rong, C.-L. Liang, J. Wang, D. Ma, J. Sun, and G.-H. Wang, *Colloids Surf. B*, 2017, **155**, 41; b) L. Han, X.-Y. Zhang, Y.L. Wang, X. Li, X.-H. Yang, M. Huang, K. Hu, L.-H. Li and Y. Wei, *J. Control. Release*, 2017, DOI: 10.1016/j.jconrel.2017.03.018; c) Q. Zhang, C. Shen, N. Zhao and F.-J. Xu, *Adv. Funct. Mater.*, 2017, **27**, 1606229; d) S. Zhao, M. Xu, C. Cao, Q. Yu, Y. Zhou and J. Liu, *J. Mater. Chem. B.*, 2017, DOI:10.1039/C7TB00613F.
21. J. F. Hainfeld, L. Lin, D. N. Slatkin, F. A. Dilmanian, T. Vadas and H. M. Smilowitz, *Nanomedicine*, 2014, **10**, 1609.
22. D. Gamenara, G. Seoane, P. Saenz Mendez and P. Dominguez de Maria, Redox Biocatalysis: Fundamentals and Applications, *John Wiley & Sons*, 2012.

4.6 Supporting Information

Chemicals

Tetraethyl orthosilicate (TEOS), *n*-cetyltrimethylammonium bromide (CTABr), sodium hydroxide (NaOH), (3-mercaptopropyl)trimethoxysilane, hydrogen tetrachloroaurate(III) ($HAuCl_4 \cdot 3H_2O$), sodium citrate tribasic dihydrate, paraffin wax, safranin O, 3-mercaptopropionic acid, 2,2'-dipyridyl disulfide, *O*-(2-mercaptoethyl)-*O'*-methyl-hexa(ethylene glycol), acetylcholinesterase from *Electrophorus electricus*, acetylcholine chloride, acetylthiocholine iodide, diisopropylfluorophosphate (DFP), diethyl cyanophosphonate (DCNP), diethyl chlorophosphate (DCP), *N*-(3-dimethylaminopropyl)-*N*^{I}-ethylcarbodiimide hydrochloride (EDC) and *N*-hydroxysuccinimide (NHS) were purchased from Sigma-Aldrich. Sodium dihydrogen phosphate monohydrate, disodium hydrogen phosphate heptahydrate, ethanol, chloroform and acetonitrile were provided by Scharlau. For cell culture, Dulbecco's Phosphate Buffered Saline (PBS), Dulbecco's Modified Eagle's Medium (DMEM) - high glucose, Fetal Bovine Serum (FBS) and Hoechst 33342 were purchased from Sigma-Aldrich. Cell proliferation reagent WST-1 was obtained from Roche Applied Science. HeLa human cervix adenocarcinoma cells were purchased from the German Resource Centre for Biological Materials (DSMZ). The rest of chemicals were commercially available and used without further purification.

General methods

Powder X-ray diffraction (PXRD), transmission electron microscopy (TEM), N_2 adsorption-desorption isotherms, elemental analysis and UV-visible and fluorescence spectrophotometry techniques were employed for materials characterization. PXRD measurements were performed on a Seifert 3000TT diffractometer using CuK_α radiation. TEM images were acquired using a JEOL TEM-1010 Electron microscope. N_2 adsorption-desorption isotherms were recorded on a Micromeritics TriStar II Plus automated analyzer. UV-visible spectra were recorded with a JASCO V-650 Spectrophotometer. Fluorescence measurements were carried out in a JASCO FP-8500 Spectrophotometer. Elemental analysis was performed in a CE Instrument EA-1110 CHN Elemental Analyzer. Furthermore, TEM coupled with energy dispersive X-ray spectroscopy (TEM-EDX) was used for element mapping using a JEOL TEM-2100F microscope. Cell viability measurements were taken with a Wallac 1420 workstation. Confocal microscopy imaging was performed with a Leica TCS SP2 AOBS (Leica Microsystems Heidelberg GmbH) inverted laser scanning confocal microscope.

Synthesis of mesoporous silica nanoparticles

1.00 g (2.74 mmol) of *n*-cetyltrimethylammonium bromide (CTABr) was dissolved in 480 mL of deionized water. Then, the pH was basified by adding 3.5 mL of a 2 mol·L^{-1} NaOH solution and the temperature was increased to 80 °C. Then, TEOS (5.00 mL, 22.4 mmol) was then added dropwise to this solution. Magnetic stirring was kept for 2 hours to give a white precipitate. Finally, the solid was isolated by centrifugation, washed several times with water and dried at 70 °C overnight (as-synthesized MCM-41). To obtain the final mesoporous nanoparticles, the as-synthesized solid was calcined at 550 °C using an oxidant atmosphere for 5 hours in order to remove the surfactant.

Synthesis of gold nanoparticles

Gold nanoparticles were synthesized based on the Turkevich-Frens method.[1] Briefly, 360 mL of a 0.3 mM $HAuCl_4 \cdot 3H_2O$ solution was brought to 100 °C under stirring and refluxing. Then, 5.4 mL of a 1% sodium citrate solution was added to synthesize 20 nm gold nanoparticles. The initially faint yellow colour turned to blue-black and finally to red wine in 10 min. After this, the colloidal suspension was let to cool at room temperature.

Synthesis of Janus Au-MS nanoparticles (S1)

Janus nanoparticles were synthesized by adapting a method previously reported in the literature.[2] MCM-41 mesoporous silica nanoparticles (180 mg) were dispersed in 9 mL of aqueous solution (6.7 % ethanol) and *n*-

cetyltrimethylammonium bromide (CTABr) was added for a 1 µM final concentration. The mixture was heated at 75 °C, and then 1 g of paraffin wax was added. Once the paraffin was melted, the mixture was vigorously stirred for 15 minutes using an Ultra-Turrax T-8 homogenizer (IKA). Afterward, the mixture was further stirred for 1 hour at 1500 rpm and 75 °C using a magnetic stirrer. The resulting Pickering emulsion was then cooled to room temperature, diluted with 9 mL of methanol and reacted with 180 µL of (3-mercaptopropyl)trimethoxysilane for 3 hours. The solid was collected by centrifugation and washed with methanol. For gold attachment, the partially mercapto-functionalized MCM-41 nanoparticles were dispersed in 75 mL of methanol and added over 360 mL of the as-synthesized gold nanoparticles. The mixture was stirred overnight. Then, the solid was isolated by filtration and exhaustively washed with ethanol and with chloroform. The solid was dried and ground. This process finally yielded the Janus Au-MS nanoparticles (**S1**).

Synthesis of S2

For the preparation of **S2**, 80 mg of **S1** and safranin O dye (24 mg, 0.07 mmol) were suspended in distilled water (5 mL) in a round-bottomed flask. The mixture was stirred for 24 hours at room temperature, filtered off and dried under vacuum. Afterwards, in order to protect the gold face, this loaded solid was re-suspended in ethanol (8 mL) and treated with 100 µL of 3-mercaptopropionic acid for 1 hour. The solid was isolated by centrifugation, washed twice ethanol and allowed to air dry. Next, 50 mg of this solid was re-suspended in acetonitrile (1.7 mL) and (3-mercaptopropyl)trimethoxysilane (93 µL, 0.5 mmol) was added. The suspension was stirred for 5.5 hours at room temperature and then, 2,2'-dipyridyl disulfide (110 mg, 0.5 mmol) was added to the reaction mixture. After stirring overnight at room temperature, the resulting solid was centrifuged, washed once with acetonitrile and dried under vacuum. Finally, a mixture of this prepared solid and O-(2-mercaptoethyl)-O’-methyl-hexa(ethylene glycol) (50 µL, 0,14 mmol) were suspended in acetonitrile (3.33 mL) in the presence of an excess of safranin O. The mixture was stirred for overnight and the final capped Janus nanoparticles

S2 were isolated by centrifugation and washed with abundant acetonitrile and dried under vacuum.

Preparation of S3

8 mg of **S2** were suspended in 4 mL of 50 mM sodium phosphate buffer at pH 7.5. Then, 2.5 mg of EDC, 2.5 mg of NHS and 1 mg of commercial acetylcholinesterase were added and the suspension was stirred overnight in an ice bath. The solid was isolated by centrifugation and washed several times with cold 50 mM sodium phosphate buffer (pH 7.5). The resulting **S3** was kept wet in refrigerator until use.

Preparation of S3$_{DOX}$

For the preparation of **S3$_{DOX}$**, the procedure was similar to that used for **S3** but using doxorubicin as the cargo. Briefly, 50 mg of **S1** and 24 mg of doxorubicin were suspended in 3.2 mL of water and stirred overnight. The particles were then collected by filtration and dried at 36 °C overnight. Next, the solid was suspended in 5 mL of ethanol and treated with 70 µL of 3-mercaptopropionic acid for 1 hour, in order to functionalize the Au face. The sample was then collected by centrifugation, washed twice with ethanol and dried at room temperature. Afterwards, the particles were suspended in acetonitrile and further functionalize with (3-mercaptopropyl)trimethoxysilane (93 µL for 5.5 hours at room temperature). Then, 110 mg of 2,2'-dipyridyl disulfide (110 mg, 0.5 mmol) were added and the mixture was stirred overnight. The resulting solid was centrifuged, washed once with ethanol and dried under vacuum overnight. Finally, the prepared solid, 50 µL of O-(2-mercaptoethyl)-O’-methyl-hexa(ethylene glycol) and 5 mg of doxorubicin were suspended in acetonitrile (3.33 mL). The doxorubicin loaded solid was washed with acetonitrile 4 times and dried overnight. 8 mg of this solid was functionalized with acetylcholinesterase as described above.

Characterization

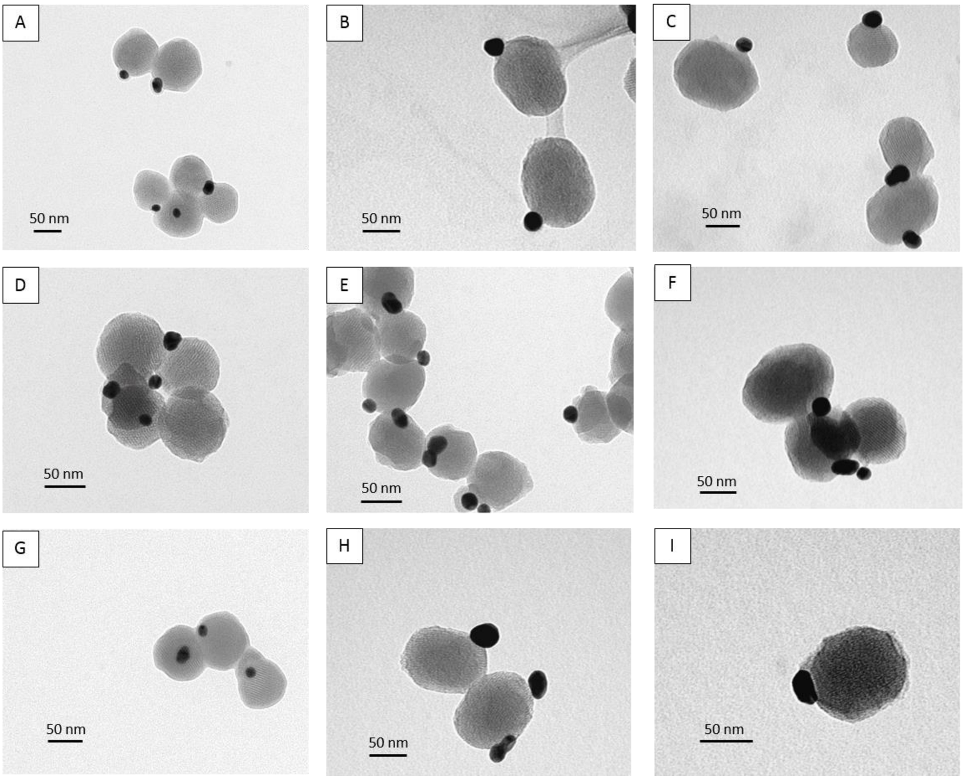

Figure SI-1. Additional TEM images of the Janus Au-mesoporous silica nanoparticles.

The N_2 adsorption-desorption isotherms of the calcined mesoporous nanoparticles and Janus nanoparticles **S1** show the typical curve for mesoporous solid; i.e. an adsorption step at intermediate P/P_0 value 0.25 (see Figure SI-2). This step is related to the nitrogen condensation inside the mesopores by capillarity. The absence of a hysteresis loop in this interval and the narrow BJH pore distribution suggest the existence of uniform cylindrical mesopores. The application of the BET model results in a value for the total specific surface of 1075.90 $m^2 \cdot g^{-1}$ for calcined mesoporous nanoparticles and 907.73 $m^2 \cdot g^{-1}$ for **S1**. The pore size was estimated by using the BJH model applied on the adsorption band of the isotherm for $P/P_0 < 0.5$. Pore size for calcined mesoporous nanoparticles and **S1** are 2.30 and 2.28 nm respectively, which are in agreement with the typical values for these materials and can be associated to the surfactant generated mesopores. Total pore volume was also calculated according to BJH model. BET specific values, pore volumes and pore sizes calculated from N_2 adsorption-desorption isotherms for selected materials are listed in Table SI-1.

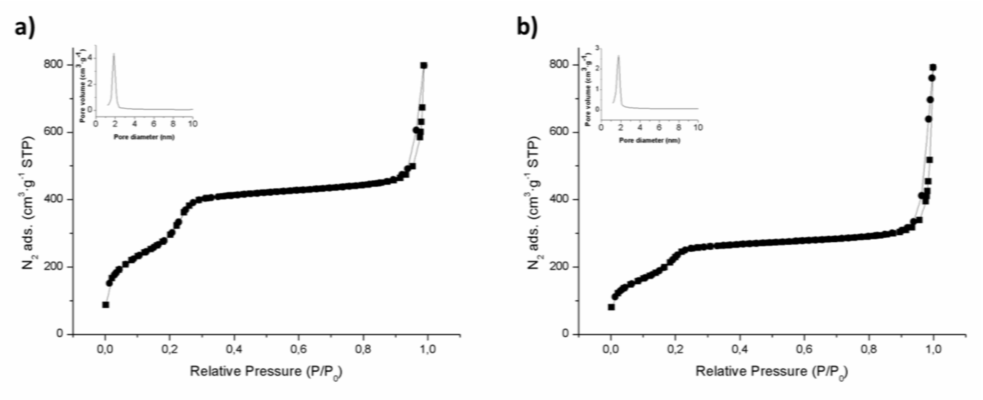

Figure SI-2. The N_2 adsorption-desorption isotherms for (a) the calcined **MCM-41** mesoporous material and (b) Janus Au-MS nanoparticles **S1**. Inset: Pore size distribution.

Table SI-1. BET specific surface values, pore volumes and pore sizes calculated from N_2 adsorption-desorption isotherms for selected materials.

Solid	S_{BET} [m^2 g^{-1}]	Pore Volume [cm^3g^{-1}]	Pore size [nm]
Calcined **MCM-41**	1075.90	0.76	2.30
S1	907.73	0.52	2.28

Table SI-2. Elemental analysis for MCM-41, **S1** and **S2**.

Solid	% C	% H	% N	% S
Calcined **MCM-41**	0.13	0.60	0.14	0.01
S1	3.14	2.32	0.11	0.29
S2	5.22	1.63	0.53	1.52

From elemental analysis measurements (Table SI-2), the amount of safranin O loaded in **S2** was estimated to be 52.6 mg·g^{-1}. Besides, the amount of oligo(ethylene glycol) grafted onto the MS face was estimated to be 137.0 mg·g^{-1}.

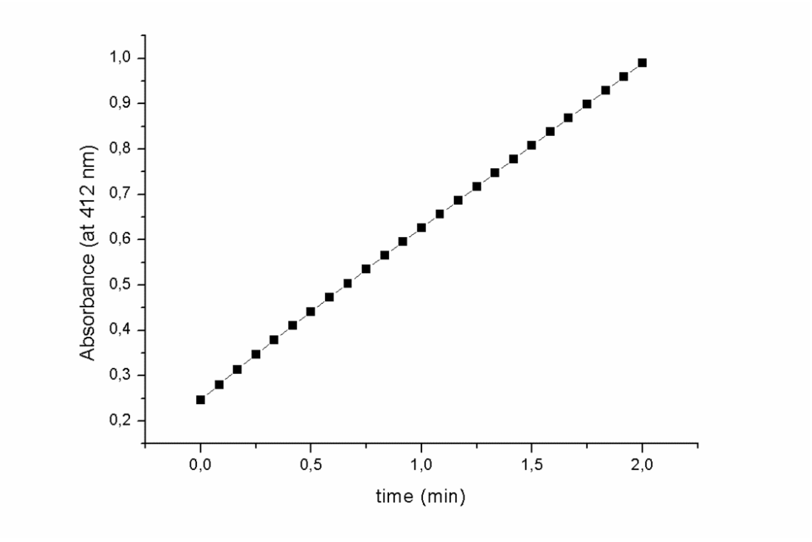

Figure SI-3. Monitoring of TNB^{2-} formation due to acetylcholinesterase activity on **S3**.

Acetylcholinesterase activity on **S3** was checked by the Ellman's assay.[3] The test is based on the fact that thiols react with Ellman's reagent (5,5'-dithiobis(2-nitrobenzoic acid), DTNB), cleaving the disulfide bond to give 2-nitro-5-thiobenzoate (TNB^{2-}). This TNB^{2-} has a characteristic yellow colour that can be monitored by UV-visible spectrophotometry. Acetylthiocholine is used as the enzyme substrate which when hydrolysed produces the resulting thiocholine as the thiol containing molecule. In a typical assay, 900 µL of 100 mM sodium phosphate buffer (pH 7.5), 30 µL 10 mM DTNB solution and 12 µL of acetylthiocholine (75 mM) where placed in a quartz cuvette. Then, 6 µL of either buffer (for blank), **S3** (5.3 $mg \cdot mL^{-1}$) or commercial enzyme (0.1 $mg \cdot mL^{-1}$) were added. The mixture was shaken and absorbance at 412 nm was monitored. When **S3** was added, the solution turned yellow quickly as a consequence of TNB^{2-} formation due to the acetylcholinesterase activity. The acetylcholinesterase activity on **S3** was estimated to be 797 $U \cdot g^{-1}$, by applying the following formula:

$$\frac{\text{Enzyme Units}}{\text{g}} = \frac{(\Delta - \Delta_{\text{blank}}) * \text{V}_{\text{T}} * \text{F}_{\text{D}}}{\varepsilon_{TNB} * \text{l} * \text{V}_{NPs} * C_{NPs}}$$

Where,

Δ is the slope of the graph (min^{-1})

Δ_{Blank} is the slope of the graph for the blank (min^{-1})

V_T is the total volume in the cuvette

ε_{TNB} is the molar extinction of TNB^{2-} at 412 nm (13,700 $M^{-1} \cdot cm^{-1}$)

L is the optical path in the cuvette (1 cm)

V_{NPs} is the volume of nanoparticles added (mL)

C_{NPs} is the concentration of nanoparticles suspension added (g/mL).

Taking into account that the activity for the commercial acetylcholinesterase was determined to be 217 U/mg, the amount of enzyme immobilized on **S3** can be estimated as 3.51 $mg \cdot g^{-1}$.

TEM-EDX mapping of the gold side of the nanodevice shows that this area was rich in sulphur atoms (see Supporting Information), thus strongly suggesting the preferential localization of the enzyme in the gold face (see Figure SI-4).

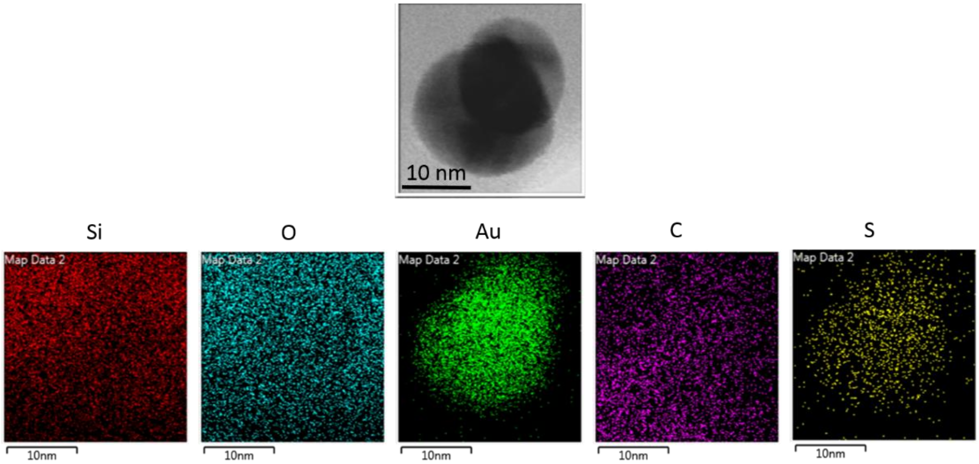

Figure SI-4. TEM-EDX element mapping of the gold region in the final nanodevice **S3**. Top: mapped area. Bottom: mapping of different atoms.

Release Experiments

In a typical release experiment, refrigerated solutions of **S3** where aliquoted and suspended in 1.5 mL of aqueous solution (50 mM sodium phosphate buffer, pH 7.5). Nanoparticles were washed and brought to a concentration of 0.9 mg·mL^{-1} for each release experiment. For inhibition experiments, the corresponding amount of inhibitor was added to the suspension. Samples were incubated for 75 min and then 15 µL of acetyltiocholine were added for a total concentration of 1 mM. Aliquots were taken at scheduled times and centrifuged to remove the nanoparticles. Then, the fluorescence at 585 nm of the safranin O dye released was measured (λ_{exc} = 520 nm). For release experiments in different media, 50 mM sodium phosphate buffer at pH 6.5 and 8.5, phosphate buffered saline 1x (PBS 1x) and simulated body plasma were prepared. PBS 1x consisted of 137 mM NaCl, 1.47 mM KH_2PO_4, 7.85 mM Na_2HPO_4, 2.68 mM KCl (pH 7.5) and simulated body plasma (SBP) consisted of NaCl 137 mM, $NaHCO_3$ 27 mM, KCl 3 mM, $K_2HPO_4 \cdot 3H2O$ 1 mM, $MgCl_2 \cdot 6H_2O$ 1.5 mM, $CaCl_2$ 2.5 mM, Na_2SO_4 0.5 mM, $NH_2C(CH_2OH)_3$ 50 mM and HCl 45 mM (final pH 7.25).

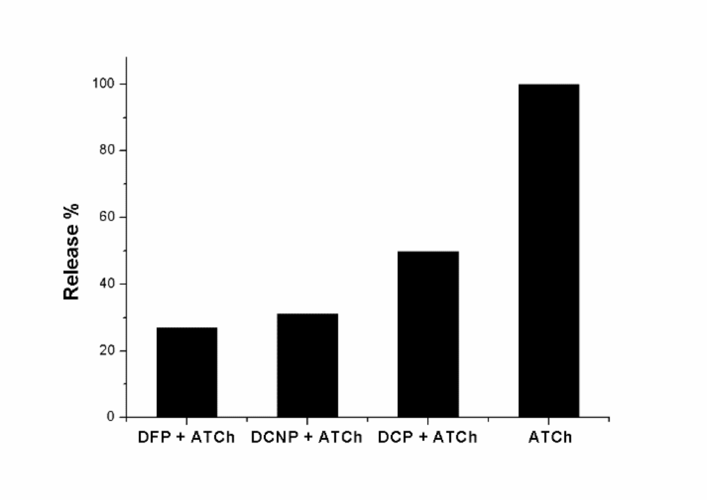

Figure SI-5. Normalized cargo release after 60 min from **S3** in the presence of 1 mM acetylthiocholine (ATCh) determined by measuring safranin O fluorescence at 585 nm (λ_{exc} = 520 nm) in aqueous solution (50 mM sodium phosphate buffer, pH 7.5) previously incubated (75 min, 5 mM) with DFP, DCNP, DCP and without inhibitor.

Cell Experiments

Cell culture conditions

HeLa human cervix adenocarcinoma cells were and were grown in Dulbecco's Modified Eagle's Medium (DMEM) supplemented with 10% fetal bovine serum (FBS). Cells were incubated at 37 °C in an atmosphere of 5% carbon dioxide and 95% air and underwent passage twice a week.

Cell viability studies with S3

To discard any intrinsic toxicity of the nanodevice, the toxicological profile of the safranin-loaded nanodevice **S3** was tested *in vitro* in Hela cells. For this purpose, Hela cells were seeded in a 96-well plate at 50000 cells/well and treated at different solid concentrations (0, 25, 50, 100 and 200 µg·mL^{-1} in PBS). Cells were incubated for 24 h and the viability was determined by the WST-1 cell proliferation assay. Finally, the cell viability was measured at 595 nm in the Wallac Workstation. Three independent experiments containing triplicates were carried out. The results demonstrated that **S3** nanoparticles were well-tolerated by HeLa cells at concentrations up to 200 µg·mL^{-1} after 24 h of exposure.

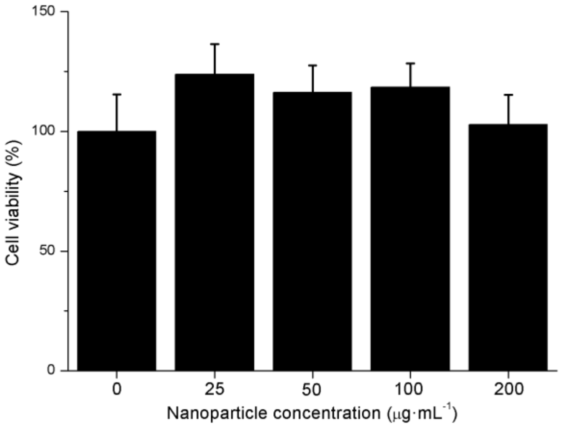

Figure SI-6. Cell viability studies in the presence of **S3** at different concentrations (0, 25, 50, 100 and 200 µg·mL^{-1}) after 24 h of incubation. WST-1 reagent was added and cell viability was measured. Data are expressed as mean±σ.

Delivery of doxorubicin in HeLa cells

The performance of the nanodevice **S3$_{DOX}$** to deliver the cytotoxic agent doxorubicin in HeLa cells was tested. For this purpose, Hela cells were seeded in a 24-well plate at 50000 cells/well and incubated at 37 °C for 24 h. **S3$_{DOX}$** was added at a concentration of 50 and 100 µg/mL and after 30 min of incubation, cells were washed with PBS in order to remove non-internalized nanoparticles and new media was added. The nanoparticles were incubated for 24 h in the absence or in the presence of 40 mM of acetylthiocholine for 24 h. Finally, doxorubicin delivery was evaluated by incubation with the cell proliferation WST-1 reagent for 1 h and measuring the absorbance at 595 nm.

*Confocal microscopy studies of controlled release from **S3** in HeLa cells*

Internalization and cargo delivery of **S3** in HeLa cells was studied by confocal microscopy. For this purpose, Hela cells were seeded over glass coverslips at 300.000 cells/ml in 6-well culture plates and incubated at 37 °C for 24 h. Then, **S3** was added to HeLa cells at 100 $\mu g \cdot mL^{-1}$ and cells were incubated at 37 °C for 30 min. Afterwards, cells were washed several times with PBS to remove non-internalized nanoparticles and incubated in fresh media for 2 h in the absence or presence of 40 mM of acetylthiocholine. After 2 h, cells were washed several times with PBS and DNA marker Hoechst 33342 was added at 2 $\mu g \cdot ml^{-1}$. Finally, slides were visualized using a confocal microscope Leica TCS SP2 AOBS.

---

1. a) J. A. Turkevich, *Discuss. Faraday Soc.*, 1951, **11**, 55; b) G. Frens, *Nature*, 1973, **241**, 20.
2. a) R. Villalonga, P. Díez, A. Sánchez, E. Aznar; R. Martínez-Máñez and J. M. Pingarrón, *Chem. Eur. J.*, 2013, **19**, 7889; b) P. Díez, A. Sánchez, M. Gamella, P. Martínez-Ruíz, E. Aznar, C. de la Torre, J. R. Murguía, R. Martínez-Máñez, R. Villalonga and J. M. Pingarrón, *J. Am. Chem. Soc.*, 2014, **136**, 9116.
3. G. L. Ellman, K. D. Courtney, V. Andres and R. M. Featherstone, *Biochem. Pharmacol.*, 1961, **7**, 88.

5. Interactive Models of Communication at the Nanoscale Using Nanoparticles that Talk to One Another

Interactive Models of Communication at the Nanoscale Using Nanoparticles that Talk to One Another

A. Llopis-Lorente,[a,b,c] P. Díez,[d] A. Sánchez,[d,e] M. D. Marcos,[a,b,c] F. Sancenón,[a,b,c] P. Martínez-Ruíz,[e] R. Villalonga*[d] and R. Martínez-Máñez*[a,b,c]

[a] Instituto Interuniversitario de Investigación de Reconocimiento Molecular y Desarrollo Tecnológico (IDM), Universidad Politècnica de València-Universitat de València (Spain).

[b] Departamento de Química, Universitat Politècnica de València, Camino de Vera s/n, 46022 Valencia (Spain). E-mail: rmaez@quim.upv.es

[c] CIBER de Bioingeniería, Biomateriales y Nanomedicina (CIBER-BBN).

[d] Department of Analytical Chemistry, Faculty of Chemistry, Complutense University of Madrid, 28040 Madrid (Spain). E-mail: rvillalonga@quim.ucm.es

[e] Department of Organic Chemistry I, Faculty of Chemistry, Complutense University of Madrid, 28040 Madrid (Spain).

(Reprinted with permission from ***Nat. Commun.*** **2017, *8*, 15511**.

5.1 Abstract

'Communication' between abiotic nanoscale chemical systems is an almost-unexplored field with enormous potential. Here we show the design and preparation of a chemical communication system based on enzyme-powered Janus nanoparticles, which mimics an interactive model of communication. Cargo delivery from one nanoparticle is governed by the biunivocal communication with another nanoparticle, which involves two enzymatic processes and the interchange of chemical messengers. The conceptual idea of establishing communication between nanodevices opens the opportunity to develop complex nanoscale systems capable of sharing information and cooperating.

5.2 Introduction

Nanotechnology has undergone a remarkable growth in recent years, and a large number of nanodevices such as nanomemories,[1] nanobatteries,[2,3] nanocontainers[4] and nanomotors[5] have already been developed. Nevertheless, communication between human-made nanodevices remains almost unexplored. Experts in telecommunication and computer engineering have already envisioned the interconnection of nanodevices in 'nanonetworks' and their virtually-unlimited applications in different fields.[6-8] At the nanoscale, traditional communication technologies are not applicable given the large size and power requirements of classical transceivers, receivers and other components.[9] In this context, an interesting approach for establishing communication at the nanometric level is to mimic how nature communicates. Chemical or molecular communication,[10] based on transmitting and receiving information by means of molecules (chemical messengers), is the communication form used by living organisms. For instance, cells communicate with neighbours by exchanging chemicals;[11-13] neurons propagate, share and process information by using neurotransmitters;[14-15] and insects, bacteria and many mammals use pheromones to communicate with members of their same species. Inspired by biological organisms and cells, scientists have reported, for instance, the use of DNA systems and enzymatic cascades as a tool for information processing and computing.[16,17] Moreover, chemical logic systems based on individual molecules[18,19] and bio-molecular networks[20-22] have also been developed.[23-26]

However, despite these interesting advances, communication between nanoparticles has barely been explored. In this scenario, there are many unanswered questions about the construction of nanonetworks that integrate nanoparticles and molecules, such as: Which molecules should be used to encode information? How will these molecules be recognized? How can recognition be converted into propagation of information, and how can this information be reported? Addressing these questions is no trivial matter, and the experimental realization of these systems is still to come.

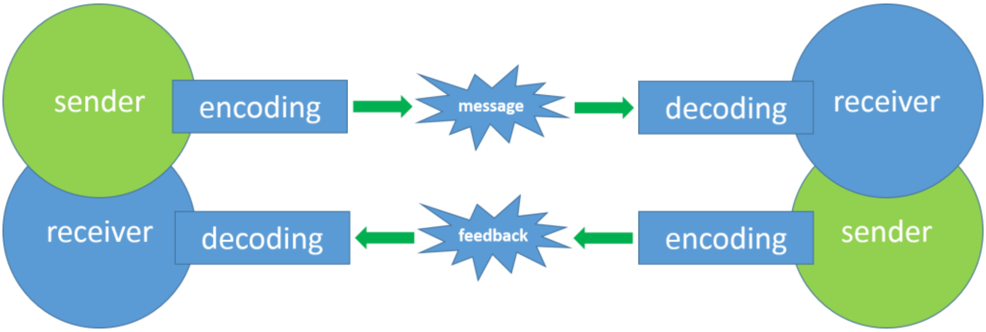

Figure 1. Illustration of an interactive model of communication. The sender receives a stimulus and encodes a message for the receiver. The receiver interprets the message and returns feedback to the first point.

In communication theory terms, communication can be defined as the process of establishing a connection between two points for information exchange.[27] At one point of the communication process, there is the sender of information, which receives a stimulus to send a message across. The sender converts information into a code and transmits the message through an appropriate medium. The receiver perceives the message and decodes it. Communication models are systematic representations of the process that helps to understand how communication can be done. For example, in the linear model of communication, the message flows in a straight line from the sender to the receiver, and there is no feedback concept. In the more complex interactive model, the sender channels a message to the receiver and the receiver then sends feedback and channels a message to the original sender.[28] In this context, the interactive model is like two linear models piled on top of each other (Fig. 1). Communication is considered effective if it receives the desired result, response or reaction.

To design human-made nanodevices capable of communicating on the nanoscale, here we show a chemical communication process between gated nanoparticles, which mimics the interactive communication model shown in Fig. 1. It employs Janus Au-mesoporous silica gated nanoparticles containing a mesoporous face, loaded with a cargo and capped with stoppers that can be opened in the presence of a specific stimulus;[29-35] and an Au face that is functionalized with different bio-molecules.[36,37] Cargo delivery from one nanoparticle only occurs after biunivocal communication with the second nanoparticle through two enzymatic processes and the exchange of two chemical messengers.

5.3 Results and discussion

Communication system design and operation

A representation of the communication process we report herein is depicted in Fig. 2. The first nanomachine (**S1$_{gal}$**) is loaded with $(Ru(bpy)_3)^{2+}$, capped with β-cyclodextrin (β-CD) attached through disulfide bonds to the mesoporous face and functionalized with enzyme β-galactosidase on the Au face. The second nanomachine (**S2$_{gox}$**) is loaded with *N*-acetyl-L-cysteine, capped with a pH-responsive β-CD:benzimidazole supramolecular nanovalve on the mesoporous face and functionalized with glucose oxidase (GOx) on the Au face. When **S1**$_{gal}$ and **S2**$_{gox}$ are placed together in an aqueous medium, addition of lactose triggers the communication process. First, lactose is hydrolysed by β-galactosidase into galactose and glucose. The produced glucose is transmitted through the aqueous medium towards the Au face of **S2**$_{gox}$, where it is recognized by glucose oxidase and hydrolysed into gluconic acid (pK_a=3.6). The generation of gluconic acid induces a local drop in pH that causes the protonation of benzimidazole groups (pK_a=5.55)[38] on the mesoporous face of **S2**$_{gox}$ and the dethreading of the supramolecular nanovalve. **S2**$_{gox}$ uncapping results in the delivery of entrapped *N*-acetyl-L-cysteine, which diffuses as feedback toward **S1**$_{gal}$. Finally, *N*-acetyl-L-cysteine induces the rupture of the disulphide linkages[39] on the mesoporous face of **S1**$_{gal}$, and $(Ru(bpy)_3)^{2+}$ is released into the medium. Delivery of $(Ru(bpy)_3)^{2+}$ (output) is expected to occur only when the two nanoparticles communicate.

In terms of the interactive model of communication shown in Fig. 1, **S1**$_{gal}$ nanoparticles (the sender) receive a stimulus (lactose) and transmit information to the receiver (**S2**$_{gox}$) via a messenger (glucose). At this point the receiver (**S2**$_{gox}$) perceives the message and operates as a new sender by channelling the message to the original sender (**S1**$_{gal}$) by using a second chemical messenger (*N*-acetyl-L-cysteine). Finally, the new receiver (**S1**$_{gal}$) interprets the message, which results in a final desired response (that is, delivery of $(Ru(bpy)_3)^{2+}$).

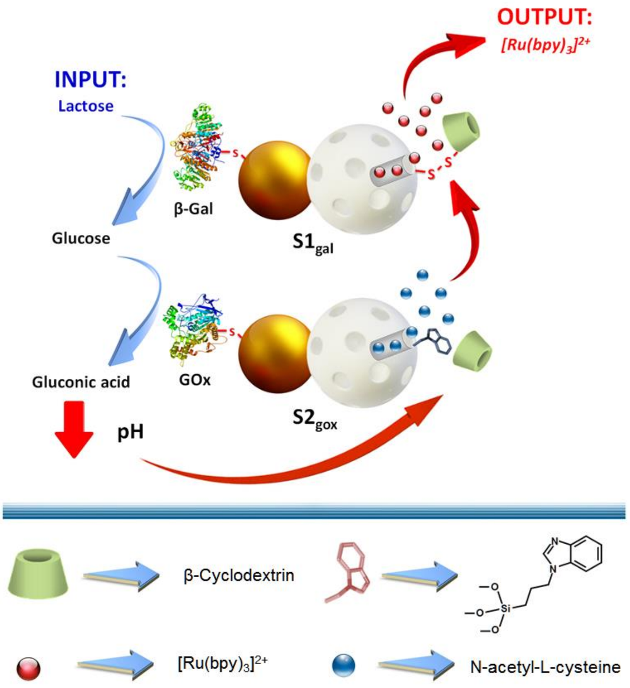

Figure 2. Representation of the interactive communication process between two Janus gated nanodevices. Chemical input (lactose) is hydrolysed by β-galactosidase on $\mathbf{S1_{gal}}$ to glucose (messenger 1), which is transformed into gluconic acid on $\mathbf{S2_{gox}}$. This induces a local drop in pH, which induces the dethreading of the β-CD:benzimidazole supramolecular nanovalve and cargo *N*-acetyl-L-cysteine release (messenger 2), which is the feedback that finally induces the delivery of the $(Ru(bpy)_3)^{2+}$ reporter from $\mathbf{S1_{gal}}$.

Synthesis of the nanodevices

In order to prepare $\mathbf{S1_{gal}}$ and $\mathbf{S2_{gox}}$, mesoporous silica (MS) nanoparticles were first obtained by the hydrolysis and condensation of tetraethyl orthosilicate in basic media using *n*-cetyltrimethylammonium bromide as a template. The surfactant was removed by calcination in air at a high temperature, which yielded the starting mesoporous support. In a second step, gold nanoparticles were prepared according to the Turkevich-Frens method.[40,41] Then, MS nanoparticles were confined at the interface of Pickering emulsion between paraffin and an aqueous face in order to achieve their partial functionalization with (3-

mercaptopropyl)trimethoxysilane, on which Au nanoparticles were attached by the formation of S-Au bonds. Paraffin wax was removed by washing the solid with $CHCl_3$, which yielded the initial Janus Au-MS nanoparticles (**S0**). To prepare **S1**$_{\mathbf{gal}}$, the mesoporous face of **S0** was loaded with $(Ru(bpy)_3)^{2+}$ and was first functionalized with 3-mercaptopropionic acid on the Au face, and later with (3-mercaptopropyl)trimethoxysilane on the mesoporous face. This solid was capped by the attachment of previously modified β-CDs through disulfide linkages, which yielded solid **S1**. Finally, the β-galactosidase enzyme was covalently immobilized by crosslinkng the primary amine groups in the enzyme with carboxylic acid moieties on the Au face, which yielded the final nanoparticles **S1**$_{\mathbf{gal}}$. To obtain **S2**$_{\mathbf{gox}}$, firstly a fraction of the **S0** was functionalized with (3-iodopropyl)trimethoxysilane on the mesoporous face. Then benzimidazole moieties were attached to the iodopropyl moieties through a nucleophilic substitution reaction and the Au face was functionalized with 3-mercaptopropionic acid. Next, pores were loaded with *N*-acetyl-L-cysteine and capped by the formation of inclusion complexes between benzimidazole groups and β-CDs (K_{11}=104 M^{-1}),[42] which resulted in solid **S2**. The glucose oxidase enzyme was then anchored to the Au face using a crosslinking reaction to yield **S2**$_{\mathbf{gox}}$. Furthermore, in order to demonstrate that **S1**$_{\mathbf{gal}}$ and **S2**$_{\mathbf{gox}}$ are essential for observing communication, **S2**$_{\mathbf{blank}}$ was synthesized, which contained the same components as **S2**$_{\mathbf{gox}}$, but lacked the cargo inside the pore voids. In order to assess the capping/uncapping performance of the second nanodevice, we synthesized **S2**$_{\mathbf{dye}}$, which contained the same components as **S2**$_{\mathbf{gox}}$ but was loaded with $(Ru(bpy)_3)^{2+}$ which facilitated cargo release monitoring by fluorometric techniques.

Characterization of the nanodevices

The different nanoparticles were characterized by standard methods (see Methods and Supplementary Methods for details). The mesoporous morphology of the MS nanoparticles (81 ± 18 nm) and the presence of the Au nanoparticles (19 ± 4 nm) in Janus colloids **S0** was confirmed by transmission electron microscopy (TEM) analysis (see Fig. 3a,b). The powder X-ray diffraction (PXRD) pattern of the starting MS nanoparticles showed the characteristic mesoporous reflection peak (100) at around 2.4°, which thus confirmed the ordered mesoporous structure (see Fig. 3c). The preservation of this typical peak in the following solids (**S0**, **S1**, **S2**, **S1$_{gal}$**, **S2$_{gox}$**) (Supplementary Fig. 1) clearly confirmed that the surface functionalization and cargo loading processes did not damage the mesoporous scaffolding. The diffraction pattern at high angles for all the Janus colloids showed the characteristic cubic gold nanocrystals (111), (200), (220) and (311) peaks,[43] which confirmed the Au-MS architecture observed by TEM. The starting gold colloid shows a single absorption band at 520 nm, whereas there is a redshift of the absorbance maximum (535 nm) for **S0** (Supplementary Fig. 2). Regarding the N_2 adsorption-desorption isotherms, starting MS and Janus nanoparticles **S0** showed an adsorption step at intermediate P/P_0 values (0.1-0.3), which indicates the presence of empty pores in the solid structure (Supplementary Fig. 3). As a result of cargo loading and capping the N_2 adsorption-desorption isotherms for the **S1** and **S2** nanoparticles led to a considerable reduction in the N_2 volume absorbed, and curves were flat compared to the parent solids (Supplementary Fig. 3). The Brunauer–Emmett–Teller (BET) total specific surface area, pore volumes and pore sizes were calculated are summarized in Table 1. From the thermogravimetric and elemental analysis studies, the contents of $(Ru(bpy)_3)^{2+}$ and β-CD on **S1** were determined as 119 and 78 mg per gram of solid, respectively (Supplementary Table 1, Supplementary Equations 1-5, and Supplementary Fig. 4). For **S2**, *N*-acetyl-L-cysteine and benzimidazole contents were determined as 31 and 58 mg per gram of solid, respectively. Furthermore, the presence of immobilized enzymes on **S1$_{gal}$** and **S2$_{gox}$** was confirmed by running specific glucose oxidase and β-galactosidase activity assays on each nanodevice (Supplementary Fig. 5 and Supplementary Equations 6-11).

To investigate the cooperative communication between **S1$_{gal}$** and **S2$_{dye}$**, we confirmed the optimal capping/uncapping behaviour of the molecular gates with the aid of dye-loaded nanoparticles **S1$_{gal}$** and **S2$_{dye}$** and ultraviolet-visible spectroscopy in the presence or absence of the corresponding messengers. The delivery studies with **S1**$_{gal}$ revealed that nanoparticles remained capped and displayed no dye release in aqueous solution, whereas the presence of the reducing agent *N*-acetyl-L-cysteine induced the opening of pores and dye release (Supplementary Fig. 6). With **S2**$_{dye}$, it was confirmed that the $(Ru(bpy)_3)^{2+}$ cargo was released only after adding glucose, whereas the solid remained capped in the absence of the messenger (Supplementary Fig. 7).

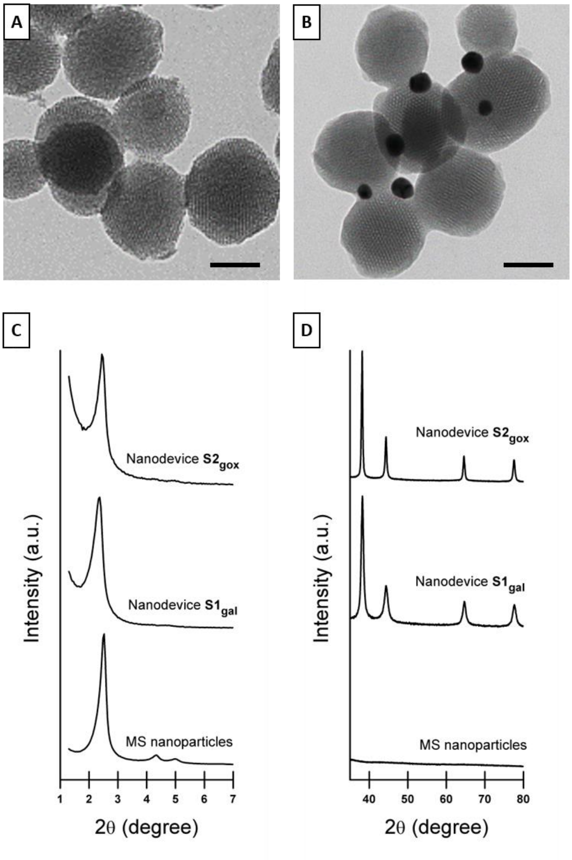

Figure 3. TEM images and PXRD of nanoparticles. TEM of (a) calcined MS nanoparticles and (b) Janus Au-MS nanoparticles (**S0**) showing the typical porosity of the MCM-41 matrix. Scale bars represent 50 nm. Powder X-ray diffraction pattern of calcined MS nanoparticles, **S1**$_{gal}$ and **S2**$_{gox}$ at low (c) and high (d) angles. Note the presence of the characteristic gold peaks for Janus colloids around 38°, 44°, 65° and 78°.

Table 1. The BET specific surface values, pore volumes and pore sizes calculated from the N_2 adsorption-desorption isotherms for the selected materials.

Sample	S_{BET} [$m^2 g^{-1}$]	Pore Volume[a] [$cm^3 g^{-1}$]	Pore size[b] [nm]
MCM-41	1093.9	0.72	2.52
S0	879.1	0.62	2.33
S1	95.12	0.10	--
S2	285.32	0.17	--

[a] Total pore volume according to the BJH model.

[b] Pore size estimated by using the BJH model applied to the adsorption branch of the isotherm, for $P/P_0 < 0.6$, which can be associated with the surfactant-generated mesopores.

Nanoparticles that talk to one another

Having characterized the single nanodevices, next we addressed the actual interactive communication process between them. In this complex system, the final release of the reporter $(Ru(bpy)_3)^{2+}$ from nanocarrier **S1**$_{\mathbf{gal}}$ was expected to be related with the information shared between **S1**$_{\mathbf{gal}}$ and **S2**$_{\mathbf{gox}}$ via the exchange of encoding molecules (glucose and *N*-acetyl-L-cysteine). In a typical experiment, **S1**$_{\mathbf{gal}}$ and **S2**$_{\mathbf{gox}}$ were suspended in aqueous solution at pH 7.5 and shaken over time at 25 °C in the presence or absence of 5 mM lactose, which acted as the input signal (see Methods for details). At scheduled times, aliquots were taken, centrifuged to remove nanoparticles, and the absorbance at 453 nm (maximum of the absorption band of $(Ru(bpy)_3)^{2+}$) was measured. Fig. 4 shows the time course of the$(Ru(bpy)_3)^{2+}$ delivery from **S1**$_{\mathbf{gal}}$ in the presence and absence of lactose. When there was no input (black curve), no communication between the nanodevices occurred and no output signal was observed. In contrast, when lactose was introduced into the system (red curve), the biunivocal communication in the nanonetwork was triggered, which resulted in the clear (Ru(bpy)$_3$)$^{2+}$ reporter release. In the presence of lactose, a total amount of 81 mM of (Ru(bpy)$_3$)$^{2+}$ was released after 210 min which corresponds to a 39% release efficiency (maximum theoretical release efficiency was calculated by dissolving of **S1$_{gal}$** in 20% NaOH solution). The final release of (Ru(bpy)$_3$)$^{2+}$ was ascribed to an effective interactive model of communication between **S1$_{gal}$** and **S2$_{gox}$,** as indicated in Fig. 2.

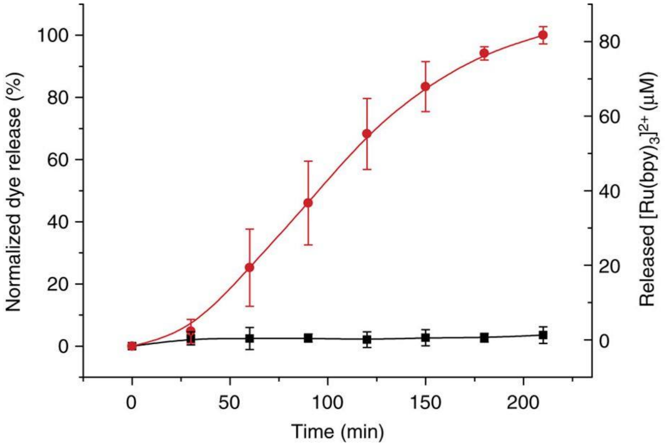

Figure 4. Cargo release from the interactive communication between nanoparticles. (Ru(bpy)$_3$)$^{2+}$ release in aqueous solution at pH 7.5 that contained **S1$_{gal}$** and **S2$_{gox}$** in the absence (black curve) and presence (red curve) of lactose (5 mM). Error bars correspond to the s.d. from five independent experiments.

For communication to take place, all the individual nanocomponents act together and cooperatively to produce collective behaviour. To demonstrate the crucial role played by the messengers and enzymes in the nanonetwork, additional experiments were carried out with **S1** (lacking β-galactosidase), **S2** (lacking glucose oxidase) and **S2$_{blank}$** (lacking the *N*-acetyl-L-cysteine messenger). If in the community **S1$_{gal}$/S2$_{gox}$** the information was shared and the final desired response (that is, delivery of (Ru(bpy)$_3$)$^{2+}$ was observed, mixtures **S1/S2$_{gox}$, S1$_{gal}$/S2** and **S1$_{gal}$/S2$_{blank}$** should not be able to communicate, which would result in no dye release occurring. The delivery experiments with **S1**/**S2$_{gox}$**, **S1$_{gal}$**/**S2** and **S1$_{gal}$**/**S2$_{blank}$** were performed by suspending nanoparticles in an aqueous solution at pH 7.5 in the presence of lactose. In the three uncompleted communities, communication was broken at a certain stage, and the information loop could not close. Therefore, no output signal ($(Ru(bpy)_3)^{2+}$ delivery) was observed (see the release profiles shown in Fig. 5). These experiments clearly stress the essential role played by the different system components. Moreover, the operation in the presence of lactose of the community **S1$_{gal}$**/**S2$_{gox}$** was compared with the system **S1**/**S2**/free enzymes, in which enzymes are freely dissolved in the bulk solution. In these experiments, the enzyme-free solids **S1** and **S2** were placed in a solution containing β-galactosidase (2 U l^{-1}) and glucose oxidase (0.8 U ml^{-1}) (enzymes were dissolved in the bulk solution at an equivalent concentration to that found in the community **S1$_{gal}$**/**S2$_{gox}$**). As can be seen in Fig. 5 (purple curve), in the community **S1**/**S2**/free enzymes, the response (that is, delivery of the dye from **S1**) was very low and far from that found for the **S1$_{gal}$**/**S2$_{gox}$** system. This indicated that in order to have an effective communication, enzymes, in particular glucose oxidase, must be placed in the proximity of the β-CD:benzimidazole complex to be able to generate a local pH drop around the nanoparticle. If the enzymes are in the solution, communication was broken and dye delivery from **S1** was not observed.

A highly desirable characteristic for a communication system is to be selective to a certain input, and it should not respond to other similar inputs that may be in the surroundings. To demonstrate the specificity of the interactive communication between **S1$_{gal}$** and **S2$_{gox}$** triggered by lactose, the performance of aqueous suspensions of the **S1$_{gal}$**/**S2$_{gox}$** community in the presence of disaccharides maltose and lactulose was also studied. In these studies, no $(Ru(bpy)_3)^{2+}$ delivery was observed (see Fig. 6). Maltose is not recognized by β-galactosidase on **S1$_{gal}$**, whereas lactulose is hydrolysed by β-galactosidase into galactose and fructose, but these species are not recognized by glucose oxidase on **S2$_{gox}$**. In both cases, communication is disrupted and no output signal was found.

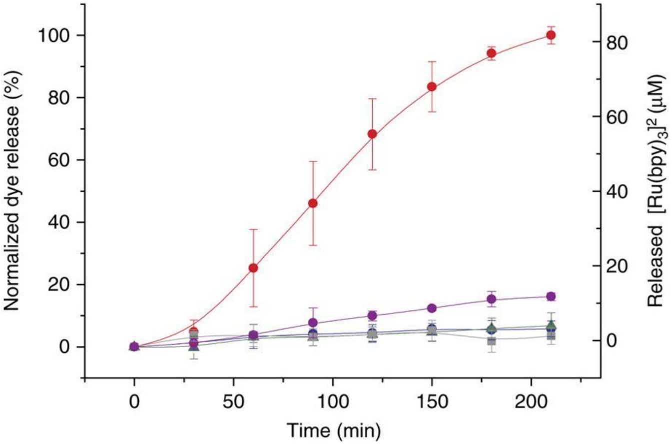

Figure 5. Cargo release from uncompleted communities of nanoparticles. $(Ru(bpy)_3)^{2+}$ release in aqueous solution at pH 7.5 in the presence of lactose (5mM) that contained communities of nanoparticles **S1**+**S2$_{gox}$** (lacking β-galactosidase, blue curve, circles), **S1$_{gal}$**+**S2** (lacking glucose oxidase, green curve, triangles), **S1$_{gal}$**+**S2$_{blank}$** (lacking the *N*-acetyl-L-cysteine messenger, grey curve, squares) and **S1**+**S2**+free enzymes (purple curve, circles), (error bars correspond to the s.d. from two independent experiments). Delivery from the full-equipped **S1$_{gal}$**+**S2$_{gox}$** system (red curve) is also displayed for comparative purposes. Error bars correspond to the s.d. from five independent experiments. Communication was achieved only when no component was lacking.

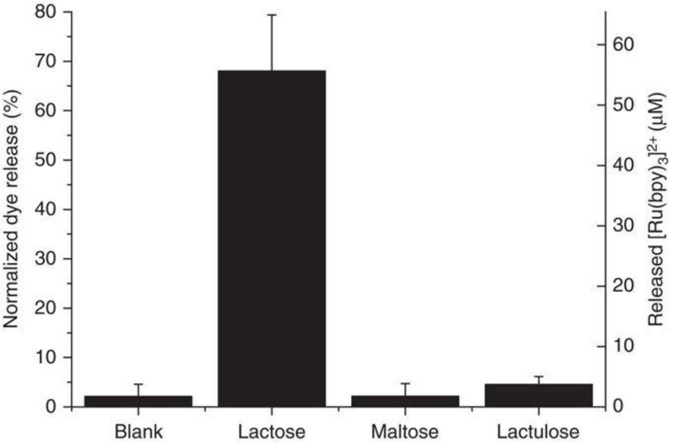

Figure 6. Specificity of the interactive communication. Release of dye in aqueous solution at pH 7.5 for the full-equipped nanonetwork **S1$_{gal}$**+**S2$_{gox}$** after 2 h in the presence of three different disaccharides: lactose, maltose and lactulose. Error bars correspond to the s.d. from two independent experiments.

Interactive communication is illustrated in Table 2 in a Boolean logic table that indicates how the final output (delivery of $(Ru(bpy)_3)^{2+}$ from **S1$_{gal}$**) is found only when using the complete community of gated nanoparticles (**S1$_{gal}$/S2$_{gox}$** mixture) in the presence of lactose, but not in its absence or when the sender/receiver is not complete (**S1**, **S2**, **S2$_{blank}$**, nanoparticles that lack β-galactosidase, glucose oxidase or *N*-acetyl-L-cysteine, respectively).

Table 2. Summary of the response of the communication system when using the full-equipped (**S1$_{gal}$** and **S2$_{gox}$**) or partially-equipped (**S1**, **S2**, **S2$_{blank}$**) nanoparticles and the presence or absence of input (lactose).

External Trigger[a] (lactose)	Presence of effector 1[a] (β-gal)	Presence of effector 2[a] (GOx)	Presence of messenger 3[a] (NAC)	Response ($[Ru(bpy)_3]^{2+}$)[b]
0	0	0	0	0
0	1	1	1	0
1	0	1	1	0
1	1	0	1	0
1	1	1	0	0
1	0	0	0	0
0	1	0	0	0
0	0	1	0	0
0	0	0	1	0
1	1	0	0	0
1	0	1	0	0
0	1	1	0	0
1	0	0	1	0
0	1	0	1	0
0	0	1	1	0
1	1	1	1	1

[a] The presence or absence of the trigger (lactose), enzymes (β-galactosidase and glucose oxidase) and *N*-acetyl-L-cysteine in the community of nanoparticles is represented by "1" and "0", respectively.

[b] Delivery or not of $(Ru(bpy)_3)^{2+}$ dye is represented by 0 = no release, 1 = release.

5.4 Conclusions

In conclusion, we have developed an example of communication between nanodevices based on Janus Au-mesoporous silica nanoparticles which mimics an interactive model of communication, in which a sender nanoparticle receives a stimulus and encodes a message for a receiver nanoparticle that interprets the message and returns feedback to the first nanoparticle. In our communication nanoscale system, delivery from one nanoparticle is governed by an interactive biunivocal communication with another nanoparticle, and involves two enzymatic processes and the use of two chemical messengers. We believe that, in communication terms on the nanoscale, the system we report herein would allow advances to be made in the knowledge of how the recognition of individual molecules (via simple chemical or biochemical reactions) can be used to encode information, and how to convert molecular recognition into information propagation. The idea of establishing communication between nanodevices embraces an enormous potential for the design of more advanced and complex nanoscale systems governed by communication between individual nanocomponents. Inspired by how biological and human communities communicate, the development of such nanodevice communities may open new directions in a number of different areas.[44-47]

5.5 Methods

Synthesis of MCM-41 mesoporous silica nanoparticles

Approximately 1.00 g (2.74 mmol) of *n*-cetyltrimethylammonium bromide (CTABr) was dissolved in 480 ml of deionized water. Then, the pH was basified by adding 3.5 ml of a 2 mol l^{-1} NaOH solution and the temperature was increased to 80 °C. Afterward, TEOS (5.00 ml, 22.4 mmol) was added dropwise to this solution. Magnetic stirring was kept for 2 h to give a white precipitate. Finally, the solid was isolated by centrifugation, washed several times with water and dried at 70 °C overnight (as-synthesized MCM-41). To obtain the final mesoporous nanoparticles (MCM-41), the as-synthesized solid was calcined at 550 °C using an oxidant atmosphere for 5 h in order to remove the surfactant.

Synthesis of gold nanoparticles

Gold nanoparticles were synthesized based on the Turkevich–Frens method.[40,41] Briefly, 100 ml of a 0.3 mM $HAuCl_4 \cdot 3H_2O$ solution was heated to boiling under stirring and refluxing. Then, 1.5 ml of a 3.9 mM trisodium citrate solution was added to synthesize 20 nm gold nanoparticles. The initially faint yellow colour turned to blue-black and finally red-wine in 10 min. After this, the colloidal suspension was let to cool at room temperature.

Synthesis of Janus Au-MS nanoparticles (S0)

Janus nanoparticles were synthesized following a method recently reported by us.[36,37] MCM-41 mesoporous silica nanoparticles (200 mg) were dispersed in 10 ml of aqueous solution (6.7% ethanol) and *n*-cetyltrimethylammonium bromide (CTABr) was added for a 1 mM final concentration. The mixture was heated at 75 °C, and then 1 g of paraffin wax was added. Once the paraffin was melted, the mixture was vigorously stirred at 25000 r.p.m. for 10 min using an Ultra-Turrax T-10 homogenizer (IKA, Germany). Afterward, the mixture was further stirred for 1 h at 4000 r.p.m. and 75 °C using a magnetic stirrer. The resulting Pickering emulsion was then cooled to room temperature, diluted with 10 ml of methanol and reacted with 200 ml of (3-mercaptopropyl) trimethoxysilane. After 3 h under magnetic stirring, the solid was collected by filtration and washed with methanol. For gold attachment, the partially mercapto-functionalized MCM-41 nanoparticles were dispersed in 75 ml of methanol and added over 400 ml of the as-synthesized gold nanoparticles. The mixture was stirred overnight. Then, the solid was isolated by filtration and exhaustively washed with ethanol and with chloroform. The solid was dried and ground. This process finally yielded the Janus Au-MS nanoparticles (**S0**).

Synthesis of β-CD-S-SO_2CH_3

$NaSSO_2CH_3$ (70 mg, 0.52 mmol) was added to a solution of mono 6-iodo-6-deoxy-β-cyclodextrin (0.5 g, 4.0x10^{-4} mmol) in anhydrous DMF (5 ml) under Argon and warmed to 50 °C while stirring.[48] After 18 h, the solution was cooled and the solvent evaporated. The residue was washed with EtOH (2x3 ml) and acetone (2x3 ml), yielding 470 mg of a white solid (94%).

Synthesis of S1

Around 50 mg of Janus Au-MS nanoparticles (**S0**) were suspended in a concentrated solution of $(Ru(bpy)_3)Cl_2$ (25 mg) in acetonitrile (5 ml), and stirred during 24 h in order to achieve the loading of the pores. Then, the suspension was treated with 50 ml of 3-mercaptopropionic acid for 1 h, filtered, and washed with toluene. Afterwards, this solid was suspended in 6 ml of toluene and reacted with an excess of (3-mercaptopropyl) trimethoxysilane (50 ml) for 24 h. The thiol-functionalized solid was treated with 100 mg of potassium tert-butoxide, isolated by centrifugation and washed with toluene and dimethylformamide (DMF). Finally, the solid was suspended with 50 mg of the as-synthesized β-CD-S-SO_2CH_3 in 10 ml of DMF under inert atmosphere for 24 h in order to cap the pores. Afterwards, the solid was isolated by centrifugation, washed with DMF and acetronitrile and dried under vacuum. This process resulted in the capped Janus solid **S1**.

Synthesis of $S1_{gal}$

Around 20 mg of Janus **S1** were suspended in 10 ml of 50 mM sodium phosphate buffer (pH 7.5) and then 5 mg of β-galactosidase, 5 mg of EDC and 5 mg of *N*-hydroxysuccinimide (NHS) were added. The mixture was stirred in an ice bath overnight. The immobilization is based on the coupling reaction between the amine primary groups of the enzyme and the carboxylic groups on the Au surface. The solid was isolated by centrifugation, washed several times with a cold solution of 50 mM sodium phosphate buffer (pH 7.5) and kept wet in the refrigerator until use. This process yielded the final nanomachine **$S1_{gal}$**.

Synthesis of S2

Around 100 mg of **S0** were first suspended in 10 ml of anhydrous acetonitrile under stirring, and then treated with an excess of (3-iodopropyl) trimethoxysilane (100 ml, 0.5 mmol). The suspension was stirred overnight and then the solid was isolated by centrifugation, washed with acetonitrile and dried at 70 °C overnight. To functionalize the surface with benzimidazole moieties, the resulting solid was ground and suspended in 8 ml of a saturated solution of benzimidazole in toluene at 80 °C and 24 ml of triethylamine were then added (toluene and triethylamine in 1:3 v/v ratio). The suspension was stirred and heated at 80 °C for three days. After this, the resulting solid was filtered off, washed with acetonitrile and dried at 70 °C overnight. To protect the gold face, 100 mg of the benzimizadole functionalized solid was suspended in 8 ml of EtOH and reacted with an excess of 3-mercaptopropionic acid (100 ml) for 1 h. The solid was centrifuged, rinsed with ethanol and with water and let to dry a room temperature for 1 day. 100 mg of this solid was suspended in 10 ml aqueous solution of *N*-acetyl-L-cysteine (0.5 g) at pH 7. After 12 h, 10 ml of 50 mM sodium phosphate buffer containing β-cyclodextrin (1.2 mg) and *N*-acetyl-L-cysteine (0.250 g) at pH 7.5 were added to the solid suspension and stirred overnight. Finally, the solid was filtered off, washed thoroughly with 50 mM phosphate buffer at pH 7.5 and dried under vacuum for 12 h. This process finally yielded solid **S2**.

Synthesis of S2$_{gox}$

Around 20 mg of **S2** were suspended in 10 ml of 50 mM sodium phosphate buffer at pH 7.5. Then, 5 mg of EDC, 5 mg of NHS and 5 mg of glucose oxidase were added and the suspension was stirred overnight at 0 °C. The solid was isolated by centrifugation and washed several times with cold 50 mM sodium phosphate buffer (pH 7.5). The resulting **S2$_{gox}$** was kept wet in refrigerator until use.

Synthesis of $S2_{blank}$

Solid **$S2_{blank}$** was prepared following the same procedure described for **$S2_{gox}$** but the mesoporous container was not loaded. First, the mesoporous surface on **S0** was modified with benzimidazole moieties and the gold surface was protected with 3-mercaptopropionic acid as described above. 10 mg of this solid was suspended in 5 ml of 50 mM sodium phosphate buffer at pH 7.5 containing β-cyclodextrin (1.2 mg ml^{-1}) and stirred overnight. Then, the solid was filtered off, washed with 50 mM phosphate buffer (pH 7.5) and dried under vacuum for 12 h. To functionalize this solid with the enzyme, we followed the same procedure, as described above. The solid was suspended in 5 ml of 50 mM sodium phosphate buffer (pH 7.5) and 2.5 mg of EDC, 2.5 mg of NHS and 2.5 mg of glucose oxidase were added. The mixture was stirred overnight at 0 °C. Finally, the nanoparticles were isolated by centrifugation and washed several times with cold 50 mM sodium phosphate buffer (pH 7.5). The resulting **$S2_{blank}$** was kept wet in the refrigerator until use.

Synthesis of $S2_{dye}$

Solid **$S2_{dye}$** was prepared following the same procedure described for **$S2_{gox}$** but the mesoporous container was loaded with $(Ru(bpy)_3)Cl_2$. First, the mesoporous surface on **S0** was modified with benzimidazole moieties and the gold surface was protected with 3-mercaptopropionic acid, as described above. 10 mg of this solid was suspended in 5 ml of aqueous solution of $(Ru(bpy)_3)Cl_2$ (5 mg). After 12 h, 10 ml of 50 mM sodium phosphate buffer at pH 7.5 containing β-cyclodextrin (1.2 mg ml^{-1}) were added to the solid suspension and stirred overnight. Then, the solid was filtered off, washed thoroughly with 50 mM phosphate buffer at pH 7.5 and dried under vacuum for 12 h. Finally, we follow the same procedure, as described above in order to attach the enzyme glucose oxidase to the Au face. This process finally yields the solid **$S2_{dye}$** that was kept wet in refrigerator until use.

Chemical communication studies

To demonstrate the performance of the nanonetwork, the refrigerated supensions of nanoparticles were aliquoted, washed separately with aqueous solution (20 mM Na_2SO_4) at pH 7.5 and placed together in the same recipient. In a typical experiment, $\mathbf{S1}_{\mathbf{gal}}$ and $\mathbf{S2}_{\mathbf{gox}}$ (4 mg ml^{-1} and 1 mg ml^{-1}, respectively) were suspended together and shaken overtime at 25 °C in the presence or absence of 5 mM lactose, which acts as the input signal. Aliquots were taken at scheduled times, centrifuged to remove the nanoparticles and the absorbance at 453 nm corresponding to the $(Ru(bpy)_3)Cl_2$ released was measured. In order to demonstrate the crucial role played by the components of the system, the same procedure was followed with suspensions of $\mathbf{S1}/\mathbf{S2}_{\mathbf{gox}}$, $\mathbf{S1}_{\mathbf{gal}}/\mathbf{S2}$ and $\mathbf{S1}_{\mathbf{gal}}/\mathbf{S2}_{\mathbf{blank}}$. For the release experiments with the community **S1**/**S2**/free enzymes, **S1** and **S2** (4 mg ml^{-1} and 1mg ml^{-1} respectively) were placed in a recipient with Gal (2 U l^{-1}) and GOx (0.8 U ml^{-1}). For specificity experiments, the procedure was the same but maltose (5 mM) and lactulose (5 mM), instead of lactose, were added as the inputs to suspensions of $\mathbf{S1}_{\mathbf{gal}}/\mathbf{S2}_{\mathbf{gox}}$.

5.6 References

1. Tseng, R., Huang, J., Ouyang, J., Kaner, R. & Yang, Y. Polyaniline nanofiber/gold nanoparticle nonvolatile memory. *Nano Lett.* **5**, 1077–1080 (2005).
2. Liu, R. & Sen, A. Autonomous nanomotor based on copper-platinum segmented nanobattery. *J. Am. Chem. Soc.* **133**, 20064–7 (2011).
3. Valov, I. et al. Nanobatteries in redox-based resistive switches require extension of memristor theory. *Nat. Commun*. **4**, 1771 (2013).
4. Tarn, D. et al. Mesoporous silica nanoparticle nanocarriers: Biofunctionality and biocompatibility. *Acc. Chem. Res.* **46**, 792–801 (2013).
5. Kline, T. & Paxton, W. Catalytic nanomotors: remote-controlled autonomous movement of striped metallic nanorods. *Angew. Chem. Int. Ed* **117**, 754–756 (2005).
6. Akyildiz, I. F., Brunetti, F. & Blázquez, C. Nanonetworks: A new communication paradigm. *Comput. Networks* **52**, 2260–2279 (2008).
7. Suda, T., Moore, M., Nakano, T., Egashira, R. & Enomoto, A. Exploratory Research on Molecular Communication between Nanomachines. Nat. Comput. 25, 1–30 (2005).
8. Malak, D. & Akan, O. B. Molecular communication nanonetworks inside human body. *Nano Commun. Netw.* **3**, 19–35 (2012).

9. Akyildiz, I. F., Jornet, J. M. & Pierobon, M. Nanonetworks. Commun. ACM 54, 84–89 (2011).
10. Nakano, T., Moore, M. J., Wei, F., Vasilakos, A. V. & Shuai, J. Molecular communication and networking: Opportunities and challenges. *IEEE Trans. Nanobioscience* **11**, 135–148 (2012).
11. Waters, C. M. & Bassler, B. L. Quorum sensing: cell-to-cell communication in bacteria. *Annu. Rev. Cell Dev. Biol.* **21**, 319–46 (2005).
12. Dickschat, J. S. Quorum sensing and bacterial biofilms. *Nat. Prod. Rep.* **27**, 343–69 (2010).
13. Kerényi, Á., Bihary, D., Venturi, V. & Pongor, S. Stability of multispecies bacterial communities: signaling networks may stabilize microbiomes. *PLoS One* **8**, e57947 (2013).
14. Gotti, C. & Clementi, F. Neuronal nicotinic receptors: from structure to pathology. *Prog. Neurobiol*. **74**, 363–396 (2004).
15. Betke, K. M., Wells, C. A. & Hamm, H. E. *GPCR* mediated regulation of synaptic transmission*. Prog. Neurobiol.* **96**, 304–21 (2012).
16. Qian, L., Winfree, E. & Bruck, J. Neural network computation with DNA strand displacement cascades. *Nature* **475**, 368–372 (2011).
17. Benenson, Y. Biomolecular computing systems: principles, progress and potential. *Nat. Rev. Genet.* **13**, 455-468 (2012).
18. Ball, P. Chemistry meets computing. *Nature* **406**, 118–120 (2000).
19. de Silva, A. P. & McClenaghan, N. D. Molecular-Scale Logic Gates. *Chem. Eur. J.* **10**, 574–586 (2004).
20. Condon, A. Automata make antisense. *Nature* **429**, 351–352 (2004).
21. Seelig, G., Soloveichik, D., Zhang, D. Y., & Winfree, E. Enzyme-free nucleic acid logic circuits. *Science* **314**, 1585–1588 (2006).
22. Douglas, S. M., Bachelet, I., & Church, G. M. A logic-gated nanorobot for targeted transport of molecular payloads. *Science* **335**, 831–834 (2012).
23. Angelos, S., Yang, Y. W., Khashab, N. M., Stoddart, J. F., & Zink, J. I. Dual-controlled nanoparticles exhibiting AND logic. *J. Am. Chem. Soc.* **131**, 11344–11346 (2009).
24. Liu, H., Li, Y., Sun, K., Fan, J., Zhang, P., Meng, J., Wang, S. & Jiang, L. Dual-responsive surfaces modified with phenylboronic acid-containing polymer brush to reversibly capture and release cancer cells. *J. Am. Chem. Soc.* **135**, 7603–7609 (2013).
25. Lee, J. W. & Klajn, R. Dual-responsive nanoparticles that aggregate under the simultaneous action of light and CO_2. *Chem. Commun.* **51**, 2036–2039 (2015).
26. Liu, D., Chen, W., Sun, K., Deng, K., Zhang, W., Wang, Z., & Jiang, X. Resettable, multi-readout logic gates based on controllably reversible aggregation of gold nanoparticles. *Angew. Chem. Int. Ed.* **50**, 4103–4107 (2011).
27. Chitode, J. S. *Communication Theory*. (Technical Publications, Pune, 2010).
28. Wood, J. T. *Communication in our lives*. (Wadsworth, Boston, 2009).
29. Guardado-Alvarez, T. M., Sudha Devi, L., Russell, M. M., Schwartz, B. J. & Zink, J. I. Activation of snap-top capped mesoporous silica nanocontainers using two near-infrared photons. *J. Am. Chem. Soc.* **135**, 14000–14003 (2013).
30. Baeza, A., Guisasola, E., Ruiz-Hernández, E. & Vallet-Regí, M. Magnetically Triggered Multidrug Release by Hybrid Mesoporous Silica Nanoparticles. *Chem. Mater.* **24**, 517–524 (2012).
31. Zhang, Z., Balogh, D., Wang, F., Yung, S. Y., Nechushtai, R., Willner, I. Biocatalytic Release of an Anticancer Drug from Nucleic-Acids-Capped Mesoporous SiO2 Using DNA or Molecular Biomarkers as Triggering Stimuli. *ACS Nano* **7**, 8455–8468 (2013).

32. Tang, F., Li, L. & Chen, D. Mesoporous silica nanoparticles: synthesis, biocompatibility and drug delivery. *Adv. Mater.* **24**, 1504–34 (2012).
33. Li, Z., Barnes, J. C., Bosoy, A., Stoddart, J. F. & Zink, J. I. Mesoporous silica nanoparticles in biomedical applications. *Chem. Soc. Rev*. **41**, 2590–605 (2012).
34. Coll, C., Bernardos, A., Martínez-Máñez, R. & Sancenón, F. Gated silica mesoporous supports for controlled release and signaling applications. *Acc. Chem. Res.* **46**, 339–49 (2013).
35. Aznar, E. et al. Gated Materials for On-Command Release of Guest Molecules. *Chem. Rev.* **116**, 561–718 (2016).
36. Díez, P. et al. Toward the design of smart delivery systems controlled by integrated enzyme-based biocomputing ensembles. *J. Am. Chem. Soc.* **136**, 9116–9123 (2014).
37. Villalonga, R. et al. Enzyme-controlled sensing-actuating nanomachine based on janus Au-mesoporous silica nanoparticles. *Chem. - A Eur. J.* **19**, 7889–7894 (2013).
38. Jerez, G., Kaufman, G., Prystai, M., Schenkeveld, S., & Donkor, K. K. Determination of thermodynamic pKa values of benzimidazole and benzimidazole derivatives by capillary electrophoresis. *J. Sep. Sci.*, **32**, 1087–1095 (2009).
39. Sheffner, A. L. The reduction in vitro in viscosity of mucoprotein solutions by a new mucolytic agent, *N*-acetyl-L-cysteine. *Ann. N. Y. Acad. Sci.* **106**, 298–310 (1963).
40. Turkevich, J., Stevenson, P. C. & Hillier, J. A study of the nucleation and growth processes in the synthesis of colloidal gold. *Discuss. Faraday Soc.* **11**, 55– 75 (1951).
41. Frens, G. Controlled Nucleation for the Regulation of the Particle Size in Monodisperse Gold Suspensions. *Nature* **241**, 20–22 (1973).
42. Yousef, F. O., Zughul, M. B. & Badwan, A. A. The modes of complexation of benzimidazole with aqueous β-cyclodextrin explored by phase solubility, potentiometric titration, 1H-NMR and molecular modeling studies. *J. Incl. Phenom. Macrocycl. Chem.* **57**, 519–523 (2007).
43. Sánchez, A., Díez, P., Martínez-Ruíz, P., Villalonga, R. & Pingarrón, J. M. Janus Au-mesoporous silica nanoparticles as electrochemical biorecognition-signaling system. *Electrochem*. *commun*. **30**, 51–54 (2013).
44. Akyildiz, I. F., Pierobon, M., Balasubramaniam, S. & Koucheryavy, Y. The internet of Bio-Nano things. *IEEE Commun. Mag.* **53**, 32–40 (2015).
45. Sancenón, F., Pascual, L., Oroval, M., Aznar, E. & Martínez-Máñez, R. Gated Silica Mesoporous Materials in Sensing Applications. *ChemistryOpen* **4**, 418–37 (2015).
46. Akyildiz, I. & Jornet, J. The Internet of nano-things. *IEEE Wirel. Commun.* **17**, 58–63 (2010).
47. Giménez, C. et al. Towards chemical communication between gated nanoparticles. *Angew. Chem. Int. Ed*. **53**, 12629–33 (2014).
48. Davis, B. G., Lloyd, R. C. & Jones, J. B. Controlled site-selective glycosylation ofproteins by a combined site-directed mutagenesis and chemical modification approach. *J. Org. Chem.* **63**, 9614–9615 (1998).

Acknowledgements

A.L.-L. is grateful to ‘La Caixa’ Banking Foundation for his PhD fellowship. We wish to thank the Spanish Government (MINECO Projects MAT2015-64139-C4-1, CTQ2014- 58989-P and CTQ2015-71936-REDT and AGL2015-70235-C2-2-R) and the Generalitat Valenciana (Project PROMETEOII/2014/047) for support. The Comunidad de Madrid (S2013/MIT-3029, Programme NANOAVANSENS) is also gratefully acknowledged.

Authors contributions

A.L.-L. and P.D. performed the experiments. A.L.-L., P.D., A.S., R.V. and R.M.-M. designed and conceived the experiments. A.L.-L. and R.M.-M. wrote the manuscript. F.S. revised and helped in the elaboration of the manuscript. M.D.M. and P.M.-R. helped in useful discussions and technical issues. All authors discussed the results and commented on the manuscript.

5.7 Supporting Information

Chemicals

Tetraethyl orthosilicate (TEOS), *n*-cetyltrimethylammonium bromide (CTABr), sodium hydroxide (NaOH), tris(2,2′-bipyridyl)dichlororuthenium(II) hexahydrate ($[Ru(bpy)_3]Cl_2$), (3-iodopropyl)trimethoxysilane, benzimidazole, triethylamine, (3-mercaptopropyl)trimethoxysilane, hydrogen tetrachloroaurate(III) ($HAuCl_4{\cdot}3H_2O$), sodium citrate tribasic dihydrate, paraffin wax, 3-mercatopropionic acid, potassium tert-butoxide, β-cyclodextrin, *N*-acetyl-L-cysteine, *N*-(3-dimethylaminopropyl)-*N*ꞌ-ethylcarbodiimide hydrochloride (EDC), *N*-hydroxysuccinimide (NHS), β-galactosidase from *Aspergillus oryzae*, glucose oxidase from *Arpergillus niger*, lactose monohydrate, maltose monohydrate, lactulose, 2,2′-Azino-bis(3-ethylbenzothiazoline-6-sulfonic acid) diammonium salt (ABTS), peroxidase from horseadish (HRP) and D-glucose were purchased from Sigma-Aldrich. Sodium dihydrogen phosphate monohydrate, disodium hydrogen phosphate heptahydrate, sodium sulfate anhydrous and solvents were provided by Scharlau.

General methods

Powder X-ray diffraction (PXRD), transmission electron microscopy (TEM), N_2 adsorption-desorption isotherms, UV-visible spectrophotometry, thermogravimetric and elemental analysis, techniques were employed for materials characterization. PXRD measurements were performed on a Seifert 3000TT diffractometer using CuK_α radiation. TEM images were acquired using a JEOL TEM-1010 Electron microscope working at 100 kV. N_2 adsorption-desorption isotherms were recorded on a Micromeritics TriStar II Plus automated analyzer. UV-visible spectra were recorded with a JASCO V-650 Spectrophotometer. Thermogravimetric analysis were carried out on a TGA/SDTA 851e Mettler Toledo equipment, using an oxidant atmosphere (Air, 80 mL/min) with a heating program consisting on a heating ramp of 10 °C per minute from 393 K to 1273 K. Elemental analysis was performed in a CE Instrument EA-1110 CHN Elemental Analyzer.

Characterization of nanoparticles

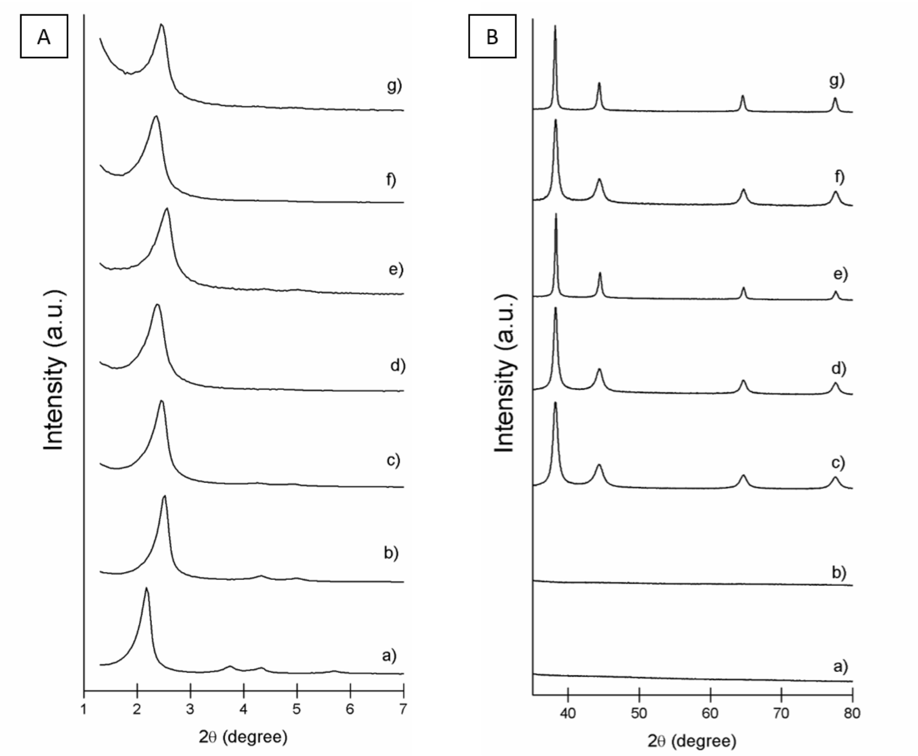

Supplementary Figure 1. Powder X-ray diffraction patterns of the solids (a) as-made MCM-41, (b) calcined MCM-41, (c) Janus Au-MS nanoparticles **S0**, (d) solid **S1**, (e) solid **S2**, (f) final nanodevice **S1$_{gal}$** and (g) final nanodevice **S2$_{gox}$** at low (A, left) and high (B, right) angles.

Solids were characterized by standard techniques. Supplementary Figure 1 shows powder X-ray diffraction patters at low (1.5 < 2θ > 7) and at high angles (35 < 2θ > 80). At low angles, the as-made MCM-41 mesoporous silica nanoparticles (curve a) shows characteristic low-angle reflections. For the calcined MCM-41 (curve b), we observed a slight displacement of the peaks related to the condensation of silanol groups during the calcination process. These low-angle typical peaks are preserved in the Au-MSN Janus colloids **S0** (curve c). The presence of the (100) peak in the PXRD patterns in the solids **S1**, **S2**, **S1$_{gal}$** and **S2$_{gox}$**

indicated that the different chemical modifications, functionalization and cargo loading had not damage the mesoporous structure. Moreover, the high-angle diffraction pattern of the all the Janus colloids showed the cubic gold characteristic (111), (200), (220) and (331) diffraction peaks, confirming the presence of gold nanocrystals and the Janus Au-MSN architecture.[1]

UV/vis measurements in aqueous solution were performed on the as-synthesized gold nanoparticles and on Janus Au-MS nanoparticles **S1** (by suspending 0.5 mg of solid in 1 mL of water). The starting gold colloid shows a single absorption band at 520 nm, characteristic of the surface plasmon resonance of spherically shaped nanospheres with an approximately 20 nm diameter. In the **S1** spectrum, there is a redshift of the absorbance maximum (535 nm) and a broadening of the band. These two facts can be ascribed to the increase in the refractive index around the gold nanospheres due to the MS attachment and to light refraction produced by silica.[2]

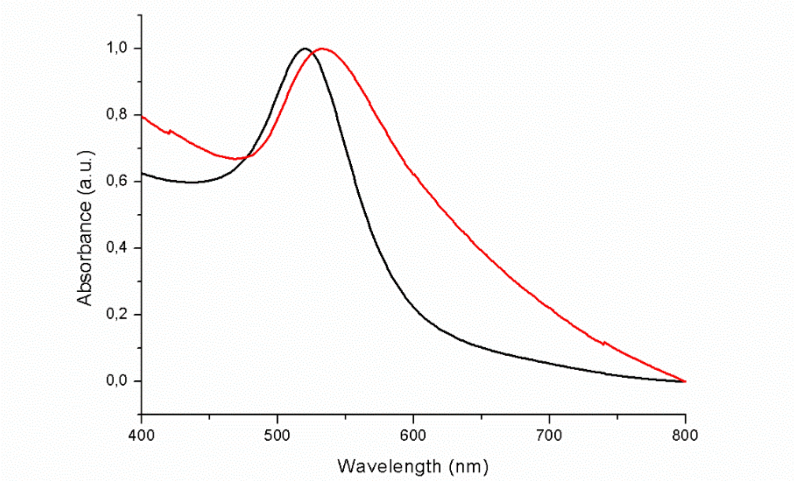

Supplementary Figure 2. Normalized UV-Visible spectra of the gold nanoparticles (black) and Janus Au-MS **S1** (red).

The N_2 adsorption-desorption isotherms of the calcined MCM-41 and Janus nanoparticles **S0** show an adsorption step at intermediate P/P_0 value 0.3, which is characteristic for mesoporous solids with empty pores (see Supplementary Figure 3). This step is related to the nitrogen condensation inside the mesopores by capillarity. The absence of a hysteresis loop in this interval and the narrow BJH pore distribution suggest the existence of uniform cylindrical mesopores. Application of the BET model results in a value for the total specific surface of 1093.9 m^2 g^{-1} for calcined MCM-41 and 879.1 $m^2 \cdot g^{-1}$ for **S0**. In contrast, N_2 adsorption-desorption isotherms for the functionalized and loaded solids **S1** and **S2** show a significant decrease in N_2 volume adsorbed and are flat when compared (at the same scale) to those from MCM-41 and **S0**. This indicates that there is a significant pore blocking as a consequence of the loading and capping processes. BET specific values, pore volumes and pore sizes calculated from N_2 adsorption-desorption isotherms for MCM-41, **S0**, **S1** and **S2** are listed in Table 1.

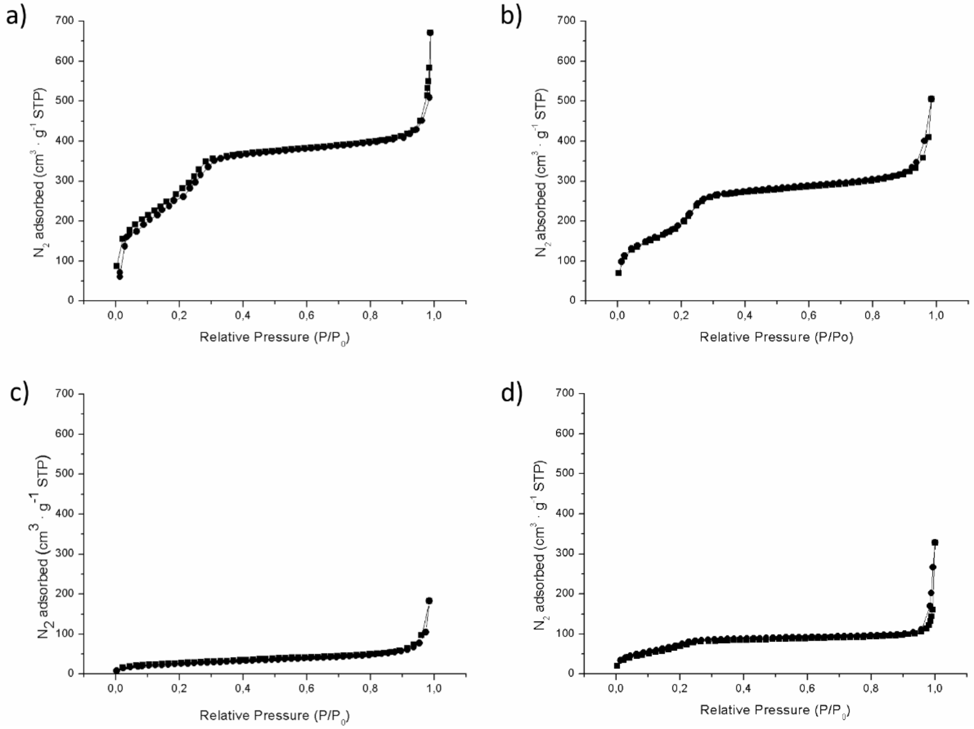

Supplementary Figure 3. The N_2 adsorption-desorption isotherms for (a) the calcined MCM-41 mesoporous material, (b) Janus Au-MS nanoparticles **S0** and loaded and capped solids (c) **S1** and (d) **S2**.

Supplementary Table 1. Elemental analysis for selected materials.

	%C	%H	%N	%S
MCM-41	--	0.60	--	--
S0	3.14	2.32	--	--
S1	13.39	2.49	1.56	4.04
S2	15.56	3.62	1.63	0.60

From the elemental analysis studies, the contents of [Ru(bpy)$_3$]Cl$_2$ and –(CH$_2$)$_3$-SS-CD on **S1** were determined as 119 mg and 78 mg per gram of solid, respectively. For **S2**, the *N*-acetyl-L-cysteine, benzimidazole and β-CD contents were determined as 31, 58 and 170 mg per gram of solid, respectively. This results correlate well with the thermogravimetric analysis in which a 20.4 % of organic content was determined for **S1** and 24.2 % for **S2** (Supplementary Figure 4).

[Ru(bpy)$_3$]Cl$_2$ and –(CH$_2$)$_3$-SS-CD contents on **S1** were calculated from Supplementary Equations 1 and 2:

$$[Ru(bpy)_3Cl_2] = \frac{1.56\ g\ of\ N}{100\ g\ of\ S1} \times \frac{1\ mol\ of\ N}{14\ g\ of\ N} \times \frac{1\ mol\ of\ Ru(bpy)_3Cl_2}{6\ mol\ of\ N} \times \frac{640.53\ g\ of\ Ru(bpy)_3Cl_2}{1\ mol\ of\ Ru(bpy)_3Cl_2} = \frac{0.119\ g\ Ru(bpy)_3Cl_2}{g\ of\ S1}\ \textbf{(Supplementary Equation 1)}$$

$$[-(CH_2)_3 - SS - CD] = \left(\frac{13.39\ g\ of\ C}{100\ g\ of\ S1} - \frac{3.14\ g\ of\ C}{100\ g\ of\ S0} - \frac{0.119\ g\ Ru(bpy)_3Cl_2}{g\ of\ S1} \times \frac{360\ g\ of\ C}{640.53\ g\ of\ Ru(bpy)_3Cl_2}\right) \times \frac{1\ mol\ of\ C}{12\ g\ of\ C} \times \frac{1\ mol\ of\ -(CH_2)_3-SS-CD}{45\ mol\ of\ C} \times \frac{1241\ g\ of\ -(CH_2)_3-SS-CD}{1\ mol\ of\ -(CH_2)_3-SS-CD} = \frac{0.082\ g\ of\ -(CH_2)_3-SS-CD}{g\ of\ S1}\ \textbf{(Supplementary Equation 2)}$$

N-acetyl-L-cysteine (NAC), benzimidazole (BZI) and β-CD contents on **S2** were calculated from Supplementary Equations 3, 4 and 5:

$$[NAC] = \frac{0.60\ g\ of\ S}{100\ g\ of\ S2} \times \frac{1\ mol\ of\ S}{32\ g\ of\ S} \times \frac{1\ mol\ of\ NAC}{1\ mol\ of\ S} \times \frac{163.2\ g\ of\ NAC}{1\ mol\ of\ NAC} = \frac{0.031\ g\ NAC}{g\ of\ S2}\ (\textbf{Supplementary Equation 3})$$

$$[BZI] = \left(\frac{1.63\ g\ of\ N}{100\ g\ of\ S2} - \frac{0.031\ g\ of\ NAC}{g\ of\ S2} \times \frac{14\ g\ of\ N}{163.2\ g\ of\ NAC}\right) \times \frac{1\ mol\ of\ N}{14\ g\ of\ N} \times \frac{1\ mol\ of\ BZI}{2\ mol\ of\ N} \times \frac{118.14\ g\ of\ BZI}{1\ mol\ of\ BZI} = \frac{0.058\ g\ of\ BZI}{g\ of\ S2}\ (\textbf{Supplementary Equation 4})$$

$$[\beta - CD] = \left(\frac{15.56\ g\ of\ C}{100\ g\ of\ S2} - \frac{0.031\ g\ NAC}{g\ of\ S2} \times \frac{60\ g\ of\ C}{163.2\ g\ of\ NAC} - \frac{0.058\ g\ BZI}{g\ of\ S2} \times \frac{72\ g\ of\ C}{118.14\ g\ of\ NAC} - \frac{3.14\ g\ of\ C}{100\ g\ of\ S0}\right) \times \frac{1\ mol\ of\ C}{12\ g\ of\ C} \times \frac{1\ mol\ of\ \beta{-}CD}{42\ mol\ of\ C} \times \frac{1135\ g\ of\ \beta{-}CD}{1\ mol\ of\ \beta{-}CD} = \frac{0.170\ g\ of\ \beta{-}CD}{g\ of\ S2}\ (\textbf{Supplementary Equation 5})$$

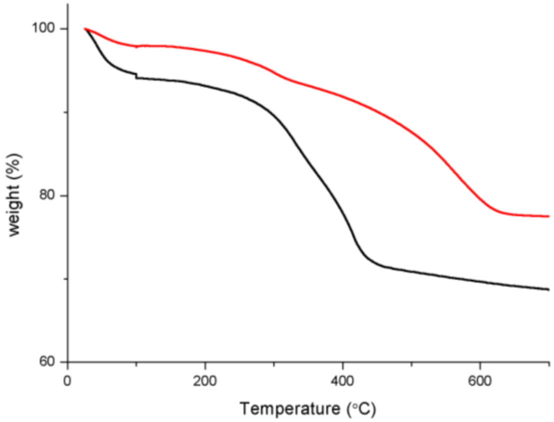

Supplementary Figure 4. Thermogravimetric analysis for **S1** (red curve) and **S2** (black curve).

Enzymatic assays

The immobilization of the enzymes was confirmed by running the corresponding enzyme activity assays on each nanodevice. The method we used in order to test glucose oxidase activity is based on the oxidation of glucose by glucose oxidase which gives gluconic acid and hydrogen peroxide. Then, hydrogen peroxide reacts with ABTS in the presence of peroxidase to form a yellow product

($ABTS^{2-}$) that can be followed UV-visible spectrophotometry (Suplementary Equations 6 and 7).

Reactions for assaying glucose oxidase activity:

$$D-glucose\ +\ O_2+\ H_2O\ \xrightarrow{glucose\ oxidase}\ D-gluconic\ acid+H_2O_2(\textbf{Supplementary Equation 6})$$

$$H_2O_2+ABTS\ \xrightarrow{peroxidase}\ ABTS^{2-}+H_2O\ (\textbf{Supplementary Equation 7})$$

In order to check glucose oxidase activity, 250 µL of 1 M of glucose (180 mg·mL^{-1}), 250 µL of ABTS solution (1 mg·mL^{-1}) and 50 µL of HRP solution (2 mg·mL^{-1}) were placed in a quartz cuvette. All solutions had been prepared in 100 mM sodium phosphate buffer at pH 7.5. Then, 10 µL of either buffer (for blank) or **S2$_{gox}$** suspension (7 mg·mL^{-1}) suspension were added. The mixture was shaken and absorbance at 418 nm was monitored as a function of time. Whereas no change was observed in the absence of nanoparticles, a strong yellow colour appeared in the presence of those. The increase in absorbance ($ABTS^{2-}$ formation) as a function of time in the presence of **S2$_{gox}$** is depicted in Supplementary Figure 5:

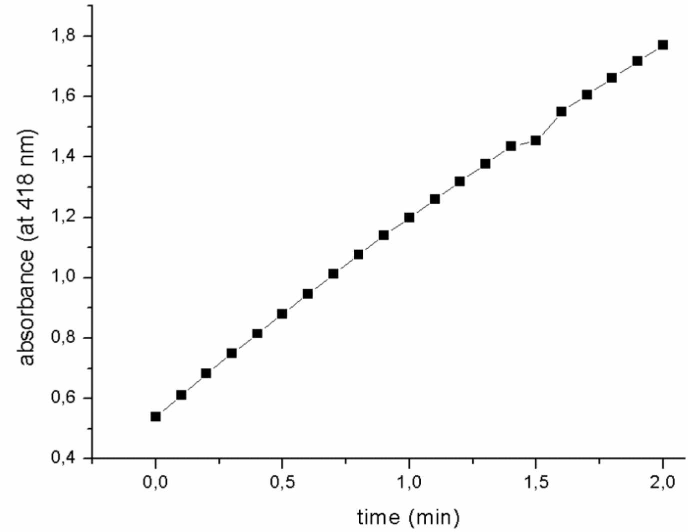

Supplementary Figure 5. Monitoring of $ABTS^{2-}$ formation due to glucose oxidase activity on **S2$_{gox}$**.

Glucose oxidase activity of **S2$_{gox}$** was estimated to be 0.8 U·mg^{-1}, by applying the Supplementary Equation 8:

$$\frac{\text{Enzyme Units}}{\text{g}} = \frac{(\Delta - \Delta_{\text{blank}}) * V_T * F_D}{\varepsilon_{TNB} * \text{l} * V_{NPs} * C_{NPs}} \ (\textbf{Supplementary Equation 8})$$

Where,
Δ is the slope of the graph (min^{-1})
Δ_{Blank} is the slope of the graph for the blank (min^{-1})
V_T is the total volume in the cuvette
ε_{TNB} is the molar extinction of ABTS^{2-} at 418 nm (36.000 M^{-1} · cm^{-1})^3
L is the optical path in the cuvette (1 cm)
V_{NPs} is the volume of nanoparticles added (mL)
C_{NPs} is the concentration of nanoparticles suspension added (g·mL^{-1}).

On the other hand, β-galactosidase activity on **S1$_{gal}$** was checked by a similar protocol taking into account that lactose is hydrolyzed into glucose and galactose by β-galactosidase (see Supplementary Equations 9, 10 and 11).

$$lactose + H_2O \xrightarrow{\beta-galactosidase} D - glucose + galactose \ (\textbf{Supplementary Equation 9})$$

$$D - glucose + O_2 + H_2O \xrightarrow{glucose\ oxidase} D - gluconic\ acid + H_2O_2 (\textbf{Supplemantary Equation 10})$$

$$H_2O_2 + ABTS \xrightarrow{peroxidase} ABTS^{2-} + H_2O \ (\textbf{Supplementary Equation 11})$$

In order to check β-galactosidase activity, 250 µL of lactose solution (1 mg·ml^{-1}), 250 µL of ABTS solution (1 mg·ml^{-1}), 50 µL of glucose oxidase solution (1 mg·ml^{-1}) and 50 µL of HRP solution (2 mg·ml^{-1}) were placed in a quartz cuvette. Next, 10 µL of either buffer (100 mM sodium phosphate, pH 7.5) or **S1$_{gal}$** suspension (8 mg·mL^{-1}) were added. The absorbance at 418 nm corresponding to the produced ABTS^{2-} was monitored. In this case, the β-galactosidase activity of **S1$_{gal}$** was determined to be 0.5 U·g^{-1}. This smaller value when compared to the glucose oxidase activity on **S2$_{gox}$** can be ascribed to the relatively low activity of commercial β-galactosidase. Using these procedures, the activity of commercial enzymes β-galactosidase and glucose oxidase were determined to be 30 U·g^{-1} and 115.7 U·mg^{-1} respectively.

Delivery studies from single nanodevices

Delivery experiments were carried out in order to study the envisioned capping-uncapping behavior with the aid of the dye-loaded nanoparticles **S1**$_{\mathbf{gal}}$ and **S2**$_{\mathbf{dye}}$ and UV-visible spectroscopy in the presence or in the absence of the corresponding molecular trigger.

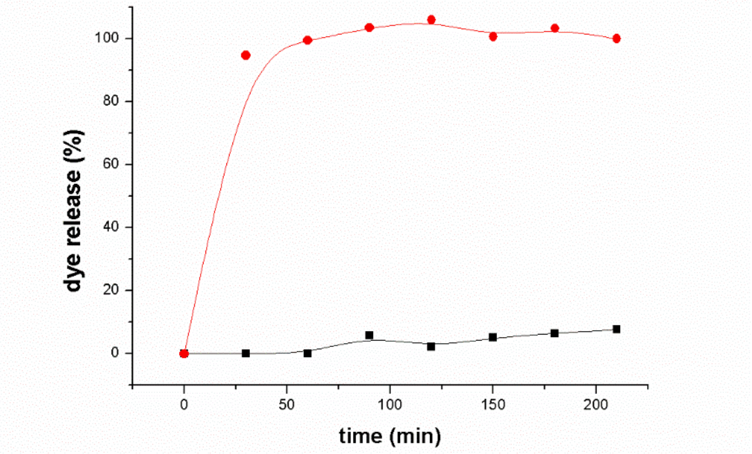

Supplementary Figure 6. Release of dye in aqueous solution at pH 7.5 from **S1**$_{\mathbf{gal}}$ in the absence (black curve) and in the presence (red curve) of *N*-acetyl-L-cysteine (1 mM) monitored by measuring the $[Ru(bpy)_3]^{2+}$ absorbance at 453 nm.

In a typical experiment, a refrigerated solution **S1**$_{\mathbf{gal}}$ was aliquoted, washed with freshly prepared aqueous solution at pH 7.5 (20 mM Na_2SO_4), divided in two fraction and finally brought to a concentration of 4 mg·mL^{-1} in aqueous media (20 mM Na_2SO_4, pH 7.5). Afterward, *N*-acetyl-L-cysteine (1 mM) was introduced to one of the suspensions and shaken over time. Aliquots were taken at scheduled times and centrifuged to remove the nanoparticles. Then, the absorbance at 453 nm corresponding to the $[Ru(bpy)_3]Cl_2$ released was measured. The results are shown in Supplementary Figure 6. From the kinetic curves it can be seen that solid **S1**$_{\text{gal}}$ was unable to release the cargo in absence on *N*-acetyl-L-cysteine, whereas in the presence of the input a remarkably cargo delivery was found.

Furthermore, delivery experiments were carried out using the capped material **S2**$_{\text{dye}}$ in the presence of D-glucose as trigger. In a typical experiment, a refrigerated solution of **S2**$_{\text{dye}}$ was aliquoted, washed with freshly prepared aqueous solution at pH 7.5 (20 mM Na_2SO_4), divided in two fraction and finally brought to a concentration of 1 mg·mL^{-1} in aqueous media (20 mM Na_2SO_4, pH 7.5). Then, D-glucose (5 mM) was introduced to one of the suspensions and shaken over time. Aliquots were taken at scheduled times, centrifuged to remove the nanoparticles, and the absorbance at 453 nm corresponding to the $[Ru(bpy)_3]Cl_2$ released was measured. As it can be seen in Supplementary Figure 7, in the absence of glucose a negligible dye release from **S2**$_{\text{dye}}$ was observed, whereas upon addition of D-glucose a remarkable release of cargo was found.

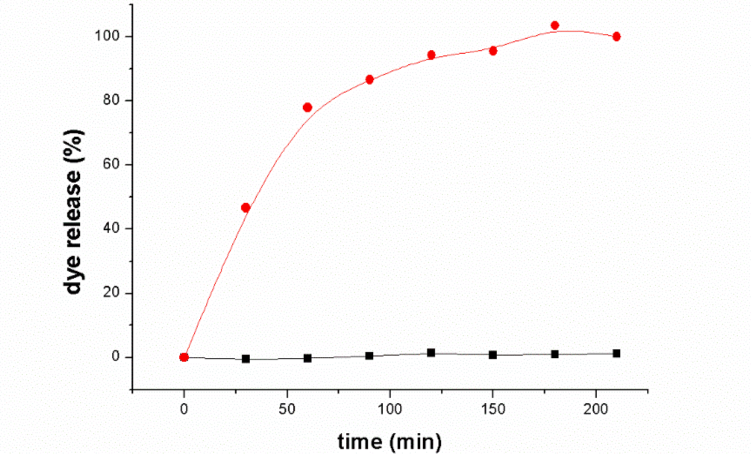

Supplementary Figure 7. Release of dye in aqueous solution at pH 7.5 from **S2**$_{\text{dye}}$ in the absence (black curve) and in the presence (red curve) of D-glucose (5 mM) monitored by measuring the ascribed $[Ru(bpy)_3]^{2+}$ absorbance at 453 nm.

---

1. Sánchez, A., Díez, P., Martínez-Ruíz, P., Villalonga, R. & Pingarrón, J. M. *Electrochem. commun.* **30,** 51–54 (2013).
2. Kelly, K.L., Coronado, E., Zhao,L.L. & Schatz, G.C.. *J. Phys. Chem. B* **107,** 668–677 (2003).
3. Shin, K-S. & Lee, Y-J. *Biochem. Biophys.* **384**, 109–115 (2000).

6. Hybrid Nanocarriers Act by Processing Logic Tasks: Toward the Design of Nanobots Capable of Reading Information from the Environment

Hybrid Nanocarriers Act by Processing Logic Tasks: Toward the Design of Nanobots Capable of Reading Information from the Environment

A. Llopis-Lorente,[a,b,c] B. De Luis,[a,b,c] A. García-Ferández,[a,b,d] S. Jimenez-Falcao,[e] M. Orzáez,[d] F. Sancenón,[a,b,c] R. Villalonga*[e] and R. Martínez-Máñez*[a,b,c]

[a] Instituto Interuniversitario de Investigación de Reconocimiento Molecular y Desarrollo Tecnológico (IDM), Universitat Politècnica de València-Universitat de València (Spain).

[b] Departamento de Química, Universitat Politècnica de València, Camino de Vera s/n, 46022 Valencia (Spain). E-mail: rmaez@quim.upv.es

[c] CIBER de Bioingeniería, Biomateriales y Nanomedicina (CIBER-BBN).

[d] Centro de Investigación Príncipe Felipe, Eduardo Primo Yúfera 3, 46012 Valencia (Spain).

[e] Nanosensors & Nanomachines Group. Department of Analytical Chemistry, Faculty of Chemistry, Complutense University of Madrid, 28040 Madrid (Spain). E-mail: rvillalonga@quim.ucm.es

(Reprinted with permission from ***ACS Appl. Mater. Interfaces*** **2018,** ***10,*** **26494-26500**. Copyright © 2018, American Chemical Society*)*

6.1 Abstract

Here, we present the design of smart nanodevices capable of reading molecular information from the environment and acting accordingly by processing Boolean logic tasks. As proof of concept, we prepared Au-mesoporous silica (MS) nanoparticles functionalized with the enzyme glucose dehydrogenase (GDH) on the Au surface and with supramolecular nanovalves as caps on the MS surface, which is loaded with a cargo (dye or drug). The nanodevice acts as an AND logic gate and reads information from the solution (presence of glucose and nicotinamide adenine dinucleotide (NAD^+)), which results in cargo release. We show the possibility of coimmobilizing GDH and the enzyme urease on nanoparticles to mimic an INHIBIT logic gate, in which the AND gate is switched off by the presence of urea. We also show that such nanodevices can deliver cytotoxic drugs in cancer cells by recognizing intracellular NAD^+ and the presence of glucose.

6.1 Introduction

A novel and ambitious approach in the nanotechnology field is to design smart nanobots (or nanorobots). Research activities in nanobotics comprise an emerging interdisciplinary technology area with new scientific challenges and promising revolutionary advancement in medicine.[1] Nanobots can be made by assembling abiotic and/or biological nanocomponents and can be considered as a possible way to enable the required manufacturing technology to move toward a new generation of smart nanodevices for applications such as drug delivery or diagnosis.[2] An appealing feature of such futuristic systems is their potential ability of reading information from the environment (e.g., diseased tissues or interior of cells) and acting accordingly. Inputs can, for instance, be combinations of certain molecules which abnormal levels can be indicative of a health disorder. As for macroscale devices, logic operators[3] could be potentially used to control nanobots capable of processing (bio)chemical inputs and producing outputs, like drug delivery, inducing apoptosis, and so on. Logic gates are operators used in electronics to process two binary inputs or more and produce a single binary output.[4] Current digital computers and electronic devices are programmed to process information inputs using algorithms based on logic gates. Although electronic logic gates cannot be incorporated into nanoparticles, one possible approach could be to use chemical systems that mimic the operation of their electronic counterparts.[5-8] Transferring these computing capabilities to nanoscale machines in relation to reading information from the environment is a key step to build advanced biomedical nanobots capable of performing complex tasks in biological settings.

From another point of view, stimuli-responsive delivery systems have recently gained much interest due to their potential application to develop better medical therapies and sensing protocols. Researchers are exploring the use of liposomes, metallic nanoparticles, and polymeric and inorganic materials as potential drug carriers.[9-12] Among them, mesoporous silica (MS) materials are appealing given their high loading capacity, stability, biocompatibility, and the possibility of functionalizing them with molecular gates or nanovalves on their outer surface.[13-17] These molecular gates are molecular or supramolecular ensembles that prevent the cargo from being released until an external stimulus is applied. Gated mesoporous materials responsive to physical (such as light, temperature, and magnetic fields)[18-20] and chemical (such as pH, enzymes, redox agents, and chemical species)[21-27] stimuli have been reported. However, comparatively few materials respond to small molecules of biological interest, and when this is the case, it is usually the presence of a single molecule to which the system responds.[16] In contrast, delivery nanodevices capable of reading information from the environment and delivering the cargo in Boolean logic terms with more than a single input are rare. However, the conceptual design (Figure 1) of such systems is interesting because diseases usually produce abnormal levels of a combination of molecules.[28,29]

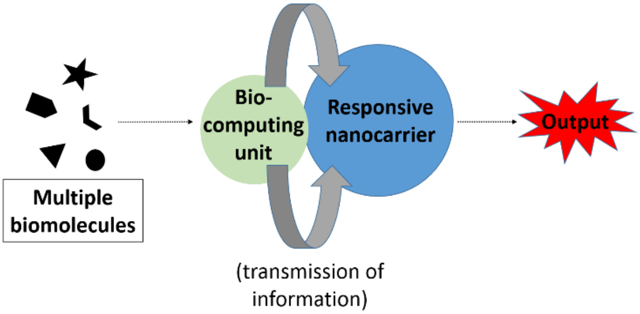

Figure 1. Conceptual representation of a smart nanodevice equipped with a biocomputing unit (capable of reading and processing molecular information from the environment and sending a chemical messenger to a responsive nanocarrier unit which can deliver a cargo (dye or drug)).

Given the potential benefits of developing nanodevices capable of sensing molecular information from the environment, we report herein the preparation of nanoparticles equipped with enzymatic logic gates that are able to perform biocomputing operations, which result in the programmed delivery of an entrapped cargo. The systems consist of Janus nanoparticles with gold and MS on opposites surfaces. The MS surface is loaded with a cargo (a dye or a drug) and is functionalized with a pH-responsive β-cyclodextrin (β-CD)/benzimidazole supramolecular nanovalve. The Au surface acts as a biocomputing unit and contains enzymes capable of “detecting” the simultaneous presence of certain biomolecules and transforming information into a local chemical messenger that is able to open the β-CD/benzimidazole nanovalve and induce cargo delivery. On the basis of this concept, nanoparticles that display AND or INHIBIT logic behaviour are prepared (Figure 2). In particular, the AND system contains the enzyme glucose dehydrogenase (GDH) and responds to the simultaneous presence of glucose and nicotinamide adenine dinucleotide (NAD^+). Although several glucose-responsive delivery systems have been reported,[30-32] they usually respond to the single presence of glucose, which is found in both extra- and intracellular environments. NAD^+ is found in the interior of living cells where it participates as a cofactor in a number of enzymatic reactions. Furthermore, both glucose uptake and NAD^+/NADH ratio are increased in cancer cells.[33,34] Thus, nanocarriers capable of performing AND logic analysis of glucose and NAD$^+$ could be advantageous for the construction of more selective glucose-responsive delivery systems. Additionally, we also report the possibility of coimmobilizing GDH and the enzyme urease on nanoparticles to mimic an INHIBIT logic gate, in which the AND gate is switched off by the presence of urea. Urea is a key biomolecule that is synthesized in liver cells and transported in the blood to the kidneys. Programming nanocarriers with INHIBIT logic functions could potentially be useful to design smart delivery systems that are switched off in particular regions or cells where certain biomolecules are expressed.

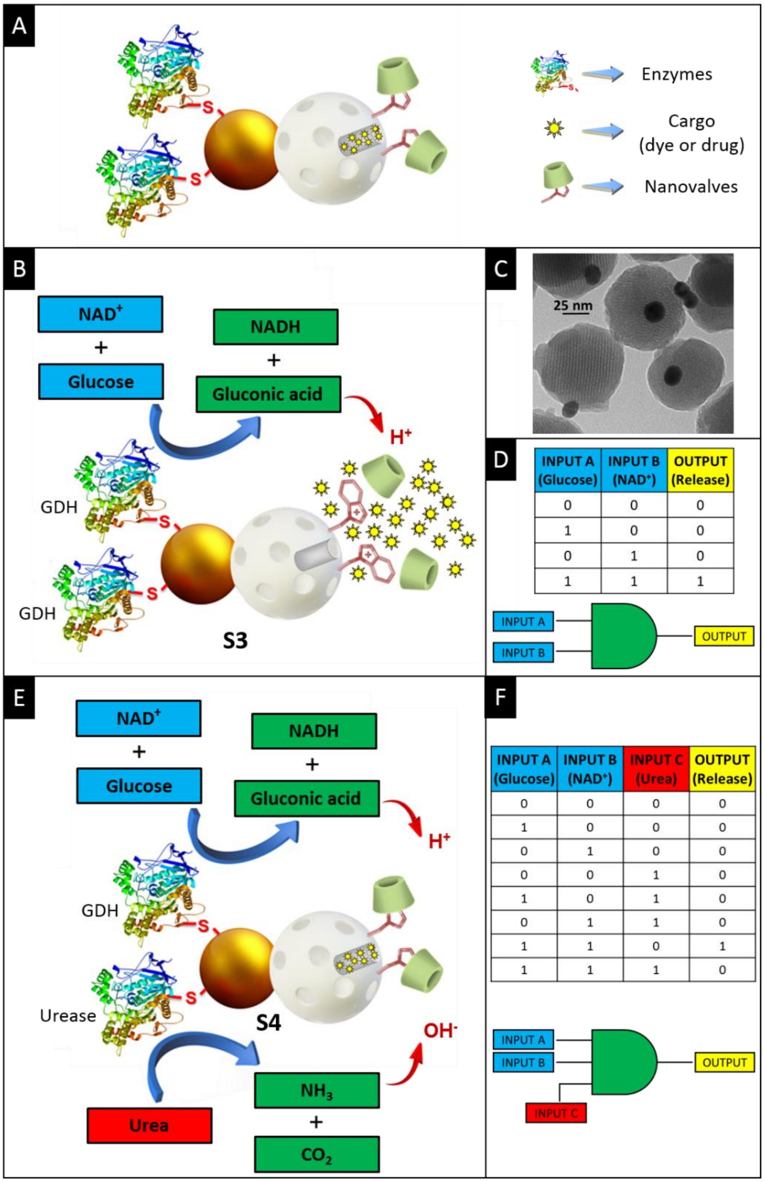

INPUT A (Glucose)	INPUT B (NAD+)	OUTPUT (Release)
0	0	0
1	0	0
0	1	0
1	1	1

INPUT A (Glucose)	INPUT B (NAD+)	INPUT C (Urea)	OUTPUT (Release)
0	0	0	0
1	0	0	0
0	1	0	0
0	0	1	0
1	0	1	0
0	1	1	0
1	1	0	1
1	1	1	0

Figure 2. The nanoparticles reported in this paper. (A) General representation. (B) Nanoparticles **S3** with an AND logic behavior. The combination of both inputs (glucose and NAD$^+$) is recognized by the biocomputing unit resulting in cargo release from the mesoporous surface. (C) The TEM image of the Au-MS scaffold (**S1**). (D) The Boolean logic table and scheme for an AND logic gate, as used in computing and electronics. (E) Representation of nanoparticles **S4** with an INHIBIT logic behavior. The system is switched off by the presence of urea. (F) The Boolean logic table and scheme for an INHIBIT logic gate, as used in computing and electronics.

6.3 Results and discussion

Mesoporous silica nanoparticles (MSNPs) were synthesized by a standard procedure, which employs cetyltrimethylammonium bromide as a directing agent for the condensation of inorganic precursor tetraethyl orthosilicate in basic media. The as-synthesized MSNPs were calcined in air to remove the surfactant. Gold nanoparticles (AuNPs) were synthesized by reducing Au(III) with sodium citrate. In another step, MSNPs were confined at the interface of a paraffin-water emulsion to partially functionalize them with (3-mercaptopropyl) trimethoxysilane (see the Supporting Information for details). AuNPs and MSNPs were then attached by the formation of S-Au bonds, which yielded the Janus Au–MS nanoparticles (**S1**). **S1** was loaded with fluorophore $[Ru(bpy)_3]Cl_2$, and the outer silica surface was functionalized with benzimidazole moieties by the nucleophilic substitution of the previously anchored (3- iodopropyl)trimethoxysilane. The gold surface was functionalized with carboxylic groups by a treatment with 3-mercaptopropionic acid, which finally yielded **S2**. The resulting nanoparticles were capped with β-CD, which forms inclusion complexes (K_f=104 M^{-1})[35] with benzimidazole (**S2-CD**). Finally, enzyme glucose dehydrogenase (GDH) was linked to carboxylic groups on the gold surface by using *N*-hydroxysuccinimide and ethyl(dimethylaminopropyl) carbodiimide, which yielded the final nanodevice **S3**. Additionally, the coimmobilization of GDH and urease yielded the nanodevice **S4**.

The prepared materials were characterized by standard procedures. The TEM images of Janus nanoparticles **S1** showed spherical MSNPs (ca. 100 nm) attached to AuNPs of ca. 20 nm (Figures 2C and S1). The as-synthesized AuNPs showed an absorption maximum at 523 nm, which was red-shifted in Au-MSNPs (**S1**) to 533 nm due to the change in the refractive index around the gold nanospheres because of the MS attachment (Figure S3). The powder X-ray diffraction (PXRD) patterns of the starting MSNPs and **S1** showed the characteristic (100) reflection peak of mesoporous silica around 2.4° (Figure S4). The preservation of this typical peak in **S2** confirmed that the cargo loading and surface functionalization processes did not damage the mesoporous scaffolding. Characteristic cubic gold peaks were observed at high-angle PXRD for **S1** and **S2**, which thus confirmed the presence of gold nanoparticles in these materials. From the N_2 adsorption−desorption isotherms (Figure S5), the total surface area of the starting MSNPs was 1018.70 m^2 g^{-1}, which diminished to 846.10 m^2 g^{-1} for **S1** and to 123.24 m^2 g^{-1} for **S2**. Pore size and pore volume were calculated by applying the Barrett-Joyner-Halenda model to the adsorption band of the isotherm and are summarized in Table S2. From the elemental analysis (Tables S3 and S4), the contents of benzimidazole, cargo, and β-CD in mmol per g of **S2-CD** were determined as 0.28 (3.3 wt %), 0.08 (4.3 wt %), and 0.10 (11.2 wt %), respectively. The activity of immobilized enzyme on **S3** was determined as 1.25 U mg^{-1}, which corresponds to 17.91 mg of GDH per g of solid (Figure S6). TEM-energy dispersive X-ray spectroscopy mapping of the final nanodevice, **S3**, was also carried out (Figure S2).

S3 was designed to monitor the environment and to deliver the cargo in the presence of glucose and NAD^+ following an AND logic behavior. In a typical experiment, **S3** was brought to 1 mg mL^{-1} concentration in an aqueous solution at pH 7.5 upon the application of different conditions: absence of glucose and NAD^+ (0,0), presence of both (1,1), and presence of only glucose (1,0) or only NAD^+ (0,1). Aliquots were taken at the scheduled times, centrifuged to remove nanoparticles, and the cargo release was evaluated by measuring the emission band of $[Ru(bpy)_3]Cl_2$ at 595 nm (λ_{exc} = 453 nm). The obtained payload delivery kinetics are shown in Figure 3. In the absence of both inputs (0,0) and in the presence of only glucose (1,0) or only NAD^+ (0,1), **S3** was capped and the cargo release was lower than 10% after 2.5 h. However, when **S3** sensed the presence of glucose and NAD^+ (1,1), a subsequent remarkable cargo delivery took place. This was attributed to GDH recognizing both substrates (glucose and NAD^+). GDH catalyzed the reaction between glucose and NAD^+ to give glucono-1,5-lactone and NADH. Glucono-1,5-lactone hydrolyzed in water to give gluconic acid (pK_a = 3.6) (internal chemical messenger), which induced the protonation of the benzimidazole groups (pK_a = 5.55)[36] on the MS surface, and the dethreading of the supramolecular nanovalve finally resulted in cargo delivery. NADH formation from glucose and NAD+ in the presence of **S3** was confirmed (Figure S6). Moreover, it was also confirmed that the cargo delivery from **S3** in the presence of NAD^+ was observed only with glucose, but not with other saccharides, such as fructose, galactose, mannose, sucrose, and lactose (Figure 4).

In another next step, we aimed to prepare a nanodevice capable of reading from the environment three different molecules that control cargo delivery. In this scenario, we constructed nanodevice **S4**, in which GDH and the enzyme urease were coimmobilized on the gold surface (Figure 2E). The amount of GDH immobilized on **S4** lowered to 9.87 mg g^{-1} (compared to 17.91 mg g^{-1} for **S3**) as a result of urease coimmobilization (Figure S6). Nanodevice **S4** mimicked an INHIBIT logic gate in which the AND gate was switched off by urea. In Boolean logic terms, an INHIBIT gate is represented, as shown in Figure 2F; input C (urea) disables the gate (no output signal) even if inputs A (glucose) and B (NAD^+) are present. However, in a 0 state (absence) of the INHIBIT input C (urea), the gate is enabled and the output is 1 (cargo delivery is observed) when both input A (glucose) and input B (NAD^+) are in state 1 (present). INHIBIT gates are used when logic signals are needed to be either enabled or inhibited, depending on certain control inputs. To demonstrate the INHIBIT-like behavior of the nanodevice, the release of **S4** suspensions (1 mg mL^{-1}) in the presence of (i) no inputs, (ii) glucose and NAD^+, and (iii) urea, glucose, and NAD^+ after 150 min was evaluated. As seen in Figure 5, whereas a remarkable release occurred in the presence of glucose and NAD^+ (1,1,0), dye delivery became negligible when urea was also added (1,1,1). This was ascribed to the presence of urease on **S4**, which catalyzed the transformation of urea into CO_2 and two equivalents of NH_3. The produced ammonia induced an increase in pH in the microenvironment of the nanoparticles and neutralized the effect of gluconic acid, thus inhibiting the release from the nanoparticles. With **S3**, addition of urea had no effect on the release (Figure S8), which indicated the key role played by urease in **S4**.

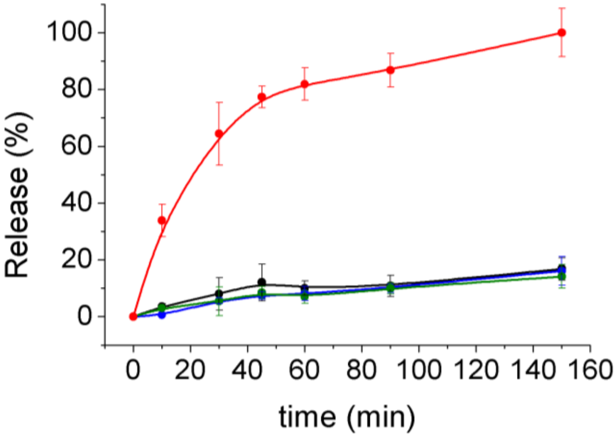

Figure 3. Normalized cargo release from **S3** determined by measuring [Ru(bpy)$_3$]Cl$_2$ fluorescence at 595 nm (λ_{exc} = 453 nm) versus time in aqueous solutions at pH 7.5: (black) in the absence of any input (0,0); (blue) in the presence of glucose (1,0); (green) in the presence of NAD$^+$ (0,1); and (red) in the presence of both NAD$^+$ and glucose (1,1). Substrates added at 1 mM concentration. Error bars as σ from three independent experiments.

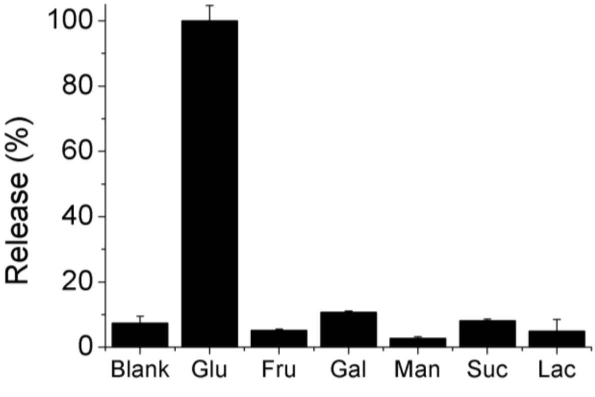

Figure 4. Normalized cargo release from **S3** in the presence of NAD$^+$ and different saccharides (glucose (Glu), fructose (Fru), galactose (Gal), mannose (Man), sucrose (Suc) and lactose (Lac)) at 1 mM concentration after 60 min. Error bars as σ from three independent experiments.

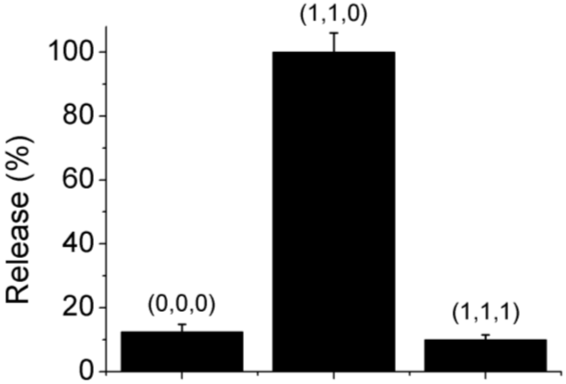

Figure 5. The INHIBIT-like behavior of **S4**. Normalized cargo release from **S4** in the absence of inputs (0,0,0); in the presence of glucose and NAD$^+$ and absence of urea (1,1,0); and in the presence of glucose, NAD$^+$ and urea (1,1,1) after 150 min. Substrates added at 1 mM concentration.

Encouraged by these findings, we aimed to demonstrate that such nanodevices can also read information, and act accordingly, in complex biological settings, such as cells. To this end, we prepared **S3$_{DOX}$** (similar to **S3**, but loaded with the cytotoxic drug doxorubicin) and tested its performance in human cervix adenocarcinoma (HeLa) cells. For these experiments, glucose was added as an external input, whereas the NAD$^+$ naturally produced in the cell interior was expected to be the second input. Controlled doxorubicin release from **S3$_{DOX}$** was studied by confocal microscopy by tracking doxorubicin-associated fluorescence and also by cell viability assays. For confocal microscopy experiments, HeLa cancer cells were incubated with 50 mg mL^{-1} of **S3$_{DOX}$** for 30 min, washed to remove noninternalized nanoparticles, and were further incubated with and without glucose (25 mM) for 24 h. Representative images of doxorubicin release (red), DNA marker Hoechst 3342 (blue), and merge for HeLa cells under different conditions are shown in Figure 6I. In the presence of glucose (and intracellular NAD$^+$), a significant doxorubicin release was observed (Figure 6Ib). In marked contrast, in the absence of glucose, the doxorubicin release became negligible (Figure 6Ic). Additionally, the WST-1 cell viability assays correlated well with the confocal microscopy studies. As seen in Figure 6II, treating HeLa cells with $\mathbf{S3}_{\mathbf{DOX}}$ in the presence of both glucose and intracellular NAD^+ led to cell viability considerably diminishing due to the doxorubicin release. When no glucose input was applied, no reduction in cell viability was observed. Therefore, these results confirmed that nanodevice $\mathbf{S3}_{\mathbf{DOX}}$ is able to read conditions in competitive media (presence of glucose and NAD^+) and to deliver a cytotoxic drug to reduce cell viability. In addition, to confirm that the decrease in cell viability was due to doxorubicin release from $\mathbf{S3}_{\mathbf{DOX}}$ and not to the acidic pH induced by the generated gluconic acid, we carried out additional viability experiments with $\mathbf{S3}_{\mathbf{Blank}}$ (a solid similar to $\mathbf{S3}_{\mathbf{DOX}}$ but without doxorubicin). Unlike $\mathbf{S3}_{\mathbf{DOX}}$, $\mathbf{S3}_{\mathbf{Blank}}$ did not produce any reduction in cell viability in the simultaneous presence of glucose and intracellular NAD^+ (Figure S9). On the other hand, although assessing the concentration of these elements in the body is difficult, it has been reported that glucose intracellular concentration is between 0 and 1 mM[37,38] and that the ratio between free NAD^+ and NADH in the cytoplasm is about 700,[39,40] with an estimated NAD^+ concentration of 0.3 mM.[41,42] However, it is known that in cancer cells glucose uptake is considerably increased[33] and the redox ratios NAD^+/NADH and $NADP^+$/NADPH are about 5-10 times higher.[34] In this scenario, advanced nanobots functionalized with targeting agents and capable of performing glucose-NAD^+ logic sensing could be an interesting tool as therapeutic agents.

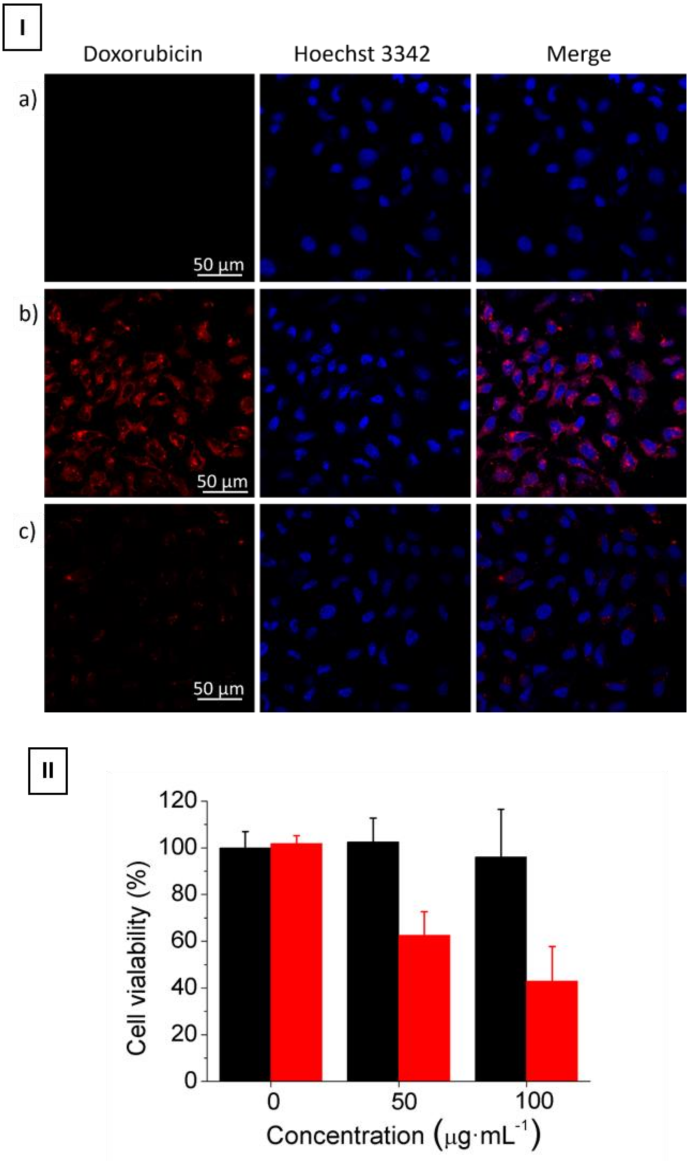

Figure 6. Experiments in cellular media. Top (I): confocal microscopy images of HeLa cells showing the controlled doxorubicin release from nanodevice **S3**$_{\mathbf{DOX}}$. a) HeLa cells with no treatment; b) HeLa cells treated with 50 μg·mL^{-1} of **S3**$_{\mathbf{DOX}}$ in a medium containing glucose (25 mM); c) HeLa cells treated with 50 μg·mL^{-1} of **S3**$_{\mathbf{DOX}}$ in the absence of glucose. From left to right: doxorubicin fluorescence, DNA marker (Hoechst 3342) fluorescence and combined (merge). Bottom (II): cell viability assays of HeLa cells treated with different **S3**$_{\mathbf{DOX}}$ concentrations (0, 50 and 100 μg·mL^{-1}) in the absence (black bars) or presence (red bars) of glucose (25 mM). Data shown as m±σ.

6.4 Conclusions

In conclusion, we show here the design of smart nanodevices capable of reading information from the environment (presence of glucose, NAD^+, and urea) and performing basic Boolean logic tasks that result in the programmed delivery of an entrapped cargo. Nanoparticles with AND or INHIBIT logic behavior were prepared. The Au-MS nanoparticles functionalized with the enzyme GDH on the gold surface and with supramolecular pH-responsive nanovalves on the MS surface mimicked an AND logic gate and required two biomolecules (glucose and NAD^+) to trigger cargo release. Specificity was due to the incorporation of GDH, which transformed glucose and NAD^+ into gluconic acid and NADH. Gluconic acid acted as a local chemical messenger that induced the protonation of benzimidazole in the nanovalve, which disrupted the supramolecular complex and induced cargo delivery. We also found that two enzymes (GDH and urease) can be combined in a single nanodevice to display a more complex behavior. When urease and GDH were coimmobilized, the system acted as an INHIBIT logic gate, in which the AND gate was switched off and on by the presence or absence of urea. We also showed that the nanoparticles can deliver a cytotoxic drug in cancer cells after detecting the presence of glucose and intracellular NAD^+ in the environment. Given that multiple small biomolecules are altered in diseased cells and the number of enzymes that can be tested, we hope that our results inspire the development of smart programmed nanobots for medical applications such as drug delivery. We believe that the systems reported herein could allow advances to be made in our knowledge of how molecular information recognition (via simple chemical or biochemical reactions) can be converted into specific actions of nanodevices.[43,44] The idea of having nanodevices capable of sensing the environment and acting accordingly (processing logic tasks) embraces an enormous potential for the design of more advanced complex nanoscale systems governed by the presence of multiple (bio)molecules, and it could be a promising first step to enable future nanoprocessors with increased complexity. Inspired by how biological communities sense the environment and act,[45] developing such nanodevices may open up new directions in nanobotics with a number of applications in different areas.

Acknowledgments

A.L.-L. is grateful to “La Caixa” Banking Foundation for his Ph.D. grant. A.G.-F. and B.de L. thank the Spanish government for FPU fellowships. The authors are grateful to the Spanish Government (MINECO Projects MAT2015-64139-C4-1, CTQ2014-58989-P, and CTQ2015-71936-REDT) and the Generalitat Valencia (Project PROMETEOII/2014/047 and PROMETEOII/2014/061) for support. The Comunidad de Madrid (S2013/MIT-3029, Programme NANOAVANSENS) is also gratefully acknowledged.

6.5 References

1. Kwon, E. J.; Lo, J. H.; Bhatia, S. N. Smart Nanosystems: Bio-Inspired Technologies that Interact with the Host Environment. *PNAS* **2015**, *112*, 14460-14466.
2. Hauert, S.; Bhatia, S. N. Mechanisms of Cooperation in Cancer Nanomedicine: Towards Systems Nanotechnology. *Trends Biotech.* **2014**, *32*, 448-455.
3. Deschamps, J. P.; Valderrama, E.; Terés, L. *Digital Sytems: From Logic gates to Processors*, Springer, **2017,** pp. 21-41.
4. Blundell, B. G.; Khan, N.; Lasebae, A.; Jabbar, M. *Computer Systems and Networks*, Thomson Learning: London, **2007**, pp. 17-39.
5. Filo, O.; Lotan, N. *Information Processing by Biochemical Systems: Neural Network-Type Configurations*, Wiley: New Jersey, **2010**.
6. Guliyev, R.; Ozturk, S.; Kostereli, Z.; Akkaya, E. U. From Virtual to Physical: Integration of Chemical Logic Gates. *Angew. Chem. Int. Ed.* **2011**, *50*, 9826-9831.
7. Katz, E.; Privman, V. Enzyme-Based Logic Systems for Information Processing. *Chem. Soc. Rev.* **2010**, *39*, 1835-1857.
8. Seelig, G.; Soleveichik, D.; Zhang, D. Y.; Winfree, E. Enzyme-Free Nucleic Acid Logic Circuits. *Science* **2006**, *314*, 1585-1590.
9. Kamaly, N.; Yameen, B.; Wu, J.; Farokhzad, O. C. Degradable Controlled-Release Polymers and Polymeric Nanoparticles: Mechanisms of Controlling Drug Release. *Chem. Rev.* **2016**, 116, 2602.
10. Mura, S.; Nicolas, J.; Couvreur, P. Stimuli-Responsive Nanocarriers for Drug Delivery. *Nat. Mater.* **2013**, *12*, 991-1003.
11. Mathiyazhakan, M.; Wiraja, C.; Xu, C. A Concise Review of Gold Nanoparticles-Based Photo-Responsive Liposomes for Controlled Drug Delivery. *Nano-Micro Lett.* **2018**, *10*, 1-10.

12. Knezevic, N. N. Z.; Durand, J.-O. Large Pore Mesoporous Silica Nanomaterials for Application in Delivery of Biomolecules. *Nanoscale* **2015**, *7*, 2199-2209.
13. Croissant, J. G.; Fatieiev, Y.; Almalik, A.; Khashab, N. Mesoporous Silica and Organosilica Nanoparticles: Physical Chemistry, Biosafety, Delivery Strategies, and Biomedical Applications. *Adv. Healthcare Mater.* **2017**, *7*, 1700831.
14. Castillo, R. R.; Colilla, M.; Vallet-Regí, M. Advances in Mesoporous Silica-Based Nanocarriers for Co-Delivery and Combination Therapy against Cancer. *Expert. Opin. Drug Deliv.* **2017**, *14*, 229-243.
15. Tarn, D.; Ashley, C. E.; Xue, M.; Carnes, E. C.; Zink, J. I.; Brinker, C. J. Mesoporous Silica Nanoparticle Nanocarriers: Biofunctionality and Biocompatibility. *Acc. Chem. Res.* **2013**, *46*, 792-801.
16. Aznar, E.; Oroval, M.; Pascual, L.; Murguía, J. R.; Martínez-Máñez, R.; Sancenón, F. Gated Materials for On-Command Release of Guest Molecules. *Chem. Rev.* **2016**, *116*, 561-718.
17. Song, N.; Yang, Y.-W. Molecular and Supramolecular Switches on Mesoporous Silica Nanoparticles. *Chem. Soc. Rev.* **2015**, *44*, 3474-3504.
18. Lv, Y.; Cao, Y.; Li, P.; Liu, J.; Chen, H.; Liu, W.; Zhang, L. Ultrasound-Triggered Destruction of Folate-Functionalized Mesoporous Silica Nanoparticle-Loaded Microbubble for Targeted Tumor Therapy. *Adv. Healthcare Mater.* **2017**, *6*, 1700354.
19. Martínez-Carmona, M.; Lozano, D.; Baeza, A.; Colilla, M.; Vallet-Regí, M. A Novel Visible Light Responsive Nanosystem for Cancer Treatment. *Nanoscale* **2017**, *9*, 15967-15973.
20. Tarn, D.; Ferris, P.; Barnes, J. C.; Ambrogio, M. W.; Stoddart, J. F.; Zink, J. I. A Reversible Light-Operated Nanovalve on Mesoporous Silica Nanoparticles. *Nanoscale* **2014**, *6*, 3335-3343.
21. Lu, C.-H.; Willner, I. Stimuli-Responsive DNA-Functionalized Nano-/Microcontainers for Switchable and Controlled Release. *Ang. Chem. Int. Ed.* **2015**, *54*, 12212-12235.
22. Gisbert-Garzarán, M.; Lozano, D.; Vallet-Regí, M.; Manzano, M. Self-Immolative Polymers as Novel pH-Responsive Gate Keepers for Drug Delivery. *RSC Adv.* **2017**, *7*, 132-136.
23. Llopis-Lorente, A.; Lozano-Torres, B.; Bernardos, A.; Martínez-Máñez, R.; Sancenón, F. Mesoporous Silica Materials for Controlled Delivery Based on Enzymes. *J. Mater. Chem. B* **2017**, *5*, 3069-3083.
24. Sancenón, F.; Pascual, L.; Oroval, M.; Aznar, E.; Martínez-Máñez, R. Gated Silica Mesoporous Materials in Sensing Applications. *ChemistryOpen* **2015**, *4*, 418-437.
25. Llopis-Lorente, A.; Díez, P.; de la Torre, C.; Sánchez, A.; Sancenón, F.; Aznar, E.; Marcos, M. D.; Martínez-Ruíz, P.; Martínez-Máñez, R.; Villalonga, R. Enzyme-Controlled Nanodevice for Acetylcholine-Triggered Cargo Delivery Based on Janus Au–Mesoporous Silica Nanoparticles. *Chem. Eur. J.* **2017**, *23*, 4276-4281.
26. Ding, C.; Tong, L.; Fu, J. Quadruple Stimuli-Responsive Mechanized Silica Nanoparticles: A Promising Multifunctional Nanomaterial for Diverse Applications. *Chem. Eur. J.* **2017**, *23*, 15041-15045.
27. Llopis-Lorente, A.; de Luis, B.; García-Férnández, A.; Díez, P.; Sánchez, A.; Marcos, M. D., Villalonga, R.; Martínez-Máñez, R., Sancenón, F. Au–Mesoporous Silica Nanoparticles Gated with Disulfide-Linked Oligo(Ethylene Glycol) Chains for Tunable Cargo Delivery Mediated by an Integrated Enzymatic Control Unit. *J. Mater. Chem. B* **2017**, *5*, 6734-6740.
28. Manesh, K. M.; Halámek, J.; Pita, M.; Zhou, J.; Tam, T. K.; Santhosh, P.; Chuang, M.-C.; Windmiller, J. R.; Abidin, D.; Katz, E.; Wang, J. Enzyme Logic Gates for the Digital Analysis of Physiological Level Upon Injury. *Biosens. Bioelectron.* **2009**, *24*, 3569-3574.

29. Zhou, J.; Halamek, J.; Bocharova, V.; Wang, J.; Katz. E. Bio-Logic Analysis of Injury Biomarker Patterns in Human Serum Samples. *Talanta* **2011**, *83*, 955-959.
30. Chen, M.; Huang, C.; He, C.; Zhu, W.; Xu, Y.; Lu, Y. A Glucose-Responsive Controlled Release System Using Glucose Oxidase-Gated Mesoporous Silica Nanocontainers. *Chem. Commun.* **2012**, *48*, 9522–9524.
31. Wu, S.; Huang, X.; Du, X. Glucose- and pH-Responsive Controlled Release of Cargo from Protein-Gated Carbohydrate-Functionalized Mesoporous Silica Nanocontainers. *Angew. Chem. Int. Ed.* **2013**, *52*, 5580-5584.
32. Oroval, M.; Díez, P.; Aznar, A.; Coll, C.; Marcos, M. D.; Villalonga, R.; Martínez-Máñez, R. Self-Regulated Glucose-Sensitive Neoglycoenzyme-Capped Mesoporous Silica Nanoparticles for Insulin Delivery. *Chem. Eur. J.* **2017**, *23*, 1353-1360.
33. Adekola, K.; Rosen, S. T.; Shanmugam, M. Glucose Transporters in Cancer Metabolism. *Curr. Opin. Oncol.* **2012**, *24*, 650-654.
34. da Veiga Moreira, J.; Hamraz, M.; Abolhassani, M.; Bigan, E.; Pèrés, S.; Pauvelé, L.; Nogueira, M. L.; Steyaert, J.-M.; Schwartz, L. The Redox Status of Cancer Cells Supports Mechanisms behind the Warburg Effect. *Metabolites* **2016**, *6*, 33-44.
35. Yousef, F. O.; Zughul, M. B.; Badwan, A. A. The Modes of Complexation of Benzimidazole with Aqueous β-Cyclodextrin Explored by Phase Solubility, Potentiometric Titration, ^{1}H-NMR and Molecular Modeling Studies. *J. Incl. Phenom. Macrocycl. Chem.* **2007**, *57*, 519-523.
36. Jerez, G.; Kaufman, G.; Prystai, M.; Schenkeveld, S.; Donkor, K. K.; Determination of Thermodynamic pK_a Values of Benzimidazole and Benzimidazole Derivatives by Capillary Electrophoresis. *J. Sep. Sci.* **2009**, *32*, 1087-1095.
37. Rodwell, V. W.; Bender, D. A.; Botham, K. M.; Kennelly, P. J.; Weil, P. A. Harper's Illustrated Biochemistry, 30th Edition, Mc Graw Hill, **2015**, pp. 477.
38. Xu, J.; Huang, P.; Qin, Y.; Jiang, D.; Chen, H. Analysis of Intracellular Glucose at Single Cells using Electrochemiluminescence Imaging. *Anal Chem* **2016**, *88*, 4609-4612.
39. Zhang, Q.; Piston, D.W.; Goodman, R.H. Regulation of Corepressor Function by Nuclear NADH. Science **2002**, *295*, 1895-1897.
40. Williamson, D.H., Lund P., Krebs H.A. The Redox State of Free Nicotinamide-Adenine Dinucleotide in the Cytoplasm and Mitochondria of Rat Liver. *Biochem. J.* **1967**, *103,* 514-527.
41. Yamada, K.; Hara, N.; Shibata, T.; Osago, H.; Tsuchiya, M. The Simultaneous Measurement of Nicotinamide Adenine Dinucleotide and Related Compounds by Liquid Chromatography/Electrospray Ionization Tandem Mass Spectrometry. Anal. Biochem **2006**, *352*, 282-285.
42. Yang, H.; Yang, T.; Baur, J. A.; Perez, E.; Matsui, T.; Carmona, J.J.; Lamming, D. W.; Souza-Pinto, N.C.; Bohr V.A.; Rosenzweig, A.; de Cabo, R.; Sauve, A.A.; Sinclair, D. A. Nutrient-Sensitive Mitochondrial NAD^+ Levels Dictate Cell Survival. *Cell* **2007**, *130* 1095-1107.
43. Llopis-Lorente, A.; Díez, P; Sánchez, A.; Marcos, M. D.; Sancenón, F.; Martínez-Ruíz, P.; Villalonga, R.; Martínez-Máñez, R. Toward Chemical Communication Between Nanodevices. *Nano Today* **2018**, *18*, 8-11.
44. Llopis-Lorente, A.; Díez, P; Sánchez, A.; Marcos, M. D.; Sancenón, F.; Martínez-Ruíz, P.; Villalonga, R.; Martínez-Máñez, R. Interactive Models of Communication at the Nanoscale Using Nanoparticles that Talk to One Another. *Nat. Commun.* **2017**, *8*, 15511.
45. Bonabeau, E.; Theraulaz, G.; Dorigo, M. *Swarm Intelligence: From Natural to Artificial Systems*, Oxford University Press, **1999.**

6.6 Supporting Information

Chemicals

Tetraethyl orthosilicate (98%), *n*-cetyltrimethylammonium bromide (CTAB) (≥99%), sodium hydroxide (NaOH) (≥98%), tris(2,2′-bipyridyl)dichlororuthenium(II) hexahydrate ($[Ru(bpy)_3]Cl_2$) (99.95%), (3-iodopropyl)trimethoxysilane (≥95%), benzimidazole (98%), trimethylamine (98%), (3-mercaptopropyl)trimethoxysilane (95%), hydrogen tetrachloroaurate(III) ($HAuCl_4{\cdot}3H_2O$) (≥99.9%), sodium citrate tribasic dehydrate (≥99%), paraffin wax (mp 53-57°C), β-cyclodextrin (98%), 3-mercaptopropionic acid (99%), glucose dehydrogenase from *Pseudomonas sp*., *N*-(3-dimethylaminopropyl)-N^{I}-ethylcarbodiimide hydrochloride (EDC) (≥98%), *N*-hydroxysuccinimide (NHS) (98%), β-nicotinamide adenine dinucleotide hydrate (NAD^+) (≥96.5%), urease from *Canavalia ensiformis* (type IX), glucose (≥99.5%), fructose, lactose monohydrate, galactose (≥99%), mannose (≥99%) and sucrose (≥99.5%) were purchased from Sigma-Aldrich. Sodium dihydrogen phosphate monohydrate, disodium hydrogen phosphate heptahydrate (analysis grade), sodium sulfate anhydrous (extra pure) and solvents were provided by Scharlau. Doxorubicin hydrochloride was purchased from Sequoia Research Products. For cell experiments, Dulbecco's Phosphate Buffered Saline (PBS), Dulbecco's Modified Eagle's Medium (DMEM) - high glucose, Fetal Bovine Serum (FBS) and Hoechst 33342 were purchased from Sigma-Aldrich. HeLa human cervix adenocarcinoma cells were purchased from the German Resource Centre for Biological Materials (DSMZ). Cell proliferation reagent WST-1 was obtained from Roche Applied Science (Madrid, Spain).

General methods

Powder X-ray diffraction (PXRD), transmission electron microscopy (TEM), N_2 adsorption-desorption isotherms, UV-visible and fluorescence spectrophotometry, and elemental analysis were employed for materials characterization. PXRD measurements were performed on a Seifert 3000TT diffractometer using CuK_α radiation at low angles ($1.3 < 2\theta < 8.3$, with steps of

0.04 degrees and 3 seconds for step) and high angles ($35 < 2\theta < 80$, with steps of 0.04 degrees and 1 second for step). For TEM imaging, samples were deposited on copper grids covered with carbon film provided by Electron microscopy sciences. TEM images were acquired using a JEOL TEM-1010 Electron microscope working at 100 kV. Furthermore, TEM coupled with energy dispersive X-ray spectroscopy (TEM-EDX) was used for element mapping using a JEOL TEM-2100F microscope. N_2 adsorption-desorption isotherms were recorded on a Micromeritics TriStar II Plus automated analyzer. Samples were previously degassed at 90 °C in vacuum overnight and measurements were performed at 77 K. UV-visible spectra were recorded with a JASCO V-650 Spectrophotometer at room temperature using a 1-mL quartz cuvette. Fluorescence measurements were carried out in a JASCO FP-8500 Spectrophotometer at room temperature using an excitation wavelength of 453 nm and emission was measured at 595 nm. Elemental analysis was performed using a LECO CHNS-932 Elemental Analyzer by combustion of small amounts of samples (1-2 mg). Cell viability measurements were taken with a Wallac 1420 workstation using cell proliferation reagent WST-1 solution (from Roche). Confocal microscopy imaging was performed with a Leica TCS SP2 AOBS (Leica Microsystems Heidelberg GmbH) inverted laser scanning confocal microscope.

Synthesis of the mesoporous silica nanoparticles (MSNPs)

1.00 g (2.74 mmol) of *n*-cetyltrimethylammonium bromide (CTAB) was dissolved in 480 mL of deionized water. Then, the pH was basified by adding 3.5 mL of a 2 $mol \cdot L^{-1}$ NaOH solution and the temperature was increased to 80 °C. Next, 5 mL of tetraethyl orthosilicate (22.4 mmol) were added to the solution. Magnetic stirring was kept for 2 hours to give a white suspension. Finally, the solid was isolated by centrifugation, washed several times with water and dried at 70 °C overnight (as-synthesized MSNPs). To obtain the final mesoporous nanoparticles (**MSNPs**), the as-synthesized solid was calcined at 550 °C in an oxidant atmosphere for 5 hours in order to remove the surfactant.

Synthesis of gold nanoparticles (AuNPs)

300 mL of a 0.3 mM $HAuCl_4 \cdot 3H_2O$ solution were brought to 100 °C under stirring and refluxing. Then, 4.5 mL of a 1% sodium citrate solution was added to yield 20 nm gold nanoparticles. The initially faint yellow colour turned to blue-black and finally red wine in 10 min. After this, the colloidal suspension was let to cool at room temperature.

Preparation of Au-MSNPs (S1)

180 mg of mesoporous silica nanoparticles (MSNPs) were dispersed in 9 mL of aqueous solution (6.7 % ethanol) followed by addition of *n*-cetyltrimethylammonium bromide (CTABr, 1 µM). The mixture was heated at 75 °C, and then 1 g of paraffin wax was added. Once the paraffin was melted, the mixture was vigorously stirred for 15 minutes using an homogenizer (Ultra-Turrax T-8, IKA). Afterward, the mixture was further stirred for 1 h at 75 °C using a magnetic stirrer. The resulting Pickering emulsion was then cooled to room temperature, diluted with 9 mL of methanol and reacted with 180 µL of (3-mercaptopropyl)trimethoxysilane for 3 hours. The solid was collected by centrifugation and washed with methanol. For gold attachment, the partially mercapto-functionalized nanoparticles were dispersed in 68 mL of methanol and added over 400 mL of the as-synthesized gold nanoparticles. The mixture was stirred overnight. Then, the solid was isolated by filtration and exhaustively washed with ethanol and with chloroform. The solid was dried and ground. This process finally yielded the Janus Au-MS nanoparticles (**S1**).

Preparation of S2

To prepare **S2**, first 100 mg of **S1** and 62.4 mg of $[Ru(bpy)_3]Cl_2 \cdot 6H_2O$ were suspended in 8 mL of acetonitrile and stirred for 24 h in order to load the pores of the mesoporous face. Afterward, an excess of (3-iodopropyl)trimethoxysilane (100 µL) was added and the suspension was stirred for 5.5 h. This solid was isolated by centrifugation and dried at 70 °C overnight (**S1-I**). Then, 0.5 mg of benzimidazole and 990 µL of triethylamine were mixed with 40 mL of toluene and heated for 20 min at 80 °C in order to prepare a saturated solution of benzimidazole. 20 mL of this suspension were added over 100 mg of **S1-I** and the mixture was stirred at 80 °C for three days. Afterward, the resulting solid was isolated by centrifugation and washed twice with toluene. Then, the solid was suspended in 10 mL of acetonitrile containing 50 mg of $[Ru(bpy)_3]Cl_2 \cdot 6H_2O$ and 100 µL of 3-mercaptopropionic acid in order to functionalize the gold face with carboxylic groups. The mixture was stirred for 1 h, washed twice with toluene and dried overnight at 70 °C. This protocol finally yielded solid **S2**.

Preparation of S3

To prepare **S3**, 70 mg of **S2** were suspended in 22 mL of 50 mM sodium phosphate buffer at pH 7.5 containing β-cyclodextrin (35.25 mg) and $[Ru(bpy)_3]Cl_2 \cdot 6H_2O$ (40 mg). The suspension was stirred overnight at room temperature, then washed with 50 mM sodium phosphate buffer (pH 7.5) and dried under vacuum which yielded **S2-CD**. In order to attach the enzyme, 8 mg of this solid, 2.5 mg of EDC, 2.5 mg of NHS and 2 mg of glucose dehydrogenase (GDH) were mixed in 4 mL of 50 mM sodium phosphate buffer at pH 7.5. The mixture was stirred overnight in an ice bath and the solid was isolated by centrifugation, exhaustively washed with 50 mM sodium phosphate buffer (pH 7.5) and kept in refrigeration until use. This protocol finally yielded the nanodevice **S3**.

Preparation of $S3_{DOX}$

A material similar to **S3** but loaded with doxorubicin (Doxo) instead of $[Ru(bpy)_3]Cl_2$ was also prepared (solid **$S3_{DOX}$**). For this purpose, and in a first step, 50 mg of **S1** were suspended in 4 mL of anhydrous acetonitrile under stirring and treated with an excess of (3-iodopropyl)trimethoxysilane (50 µL). The suspension was stirred for 5.5 hours and then the solid was isolated by centrifugation, washed with toluene and dried at room temperature overnight. The resulting solid was suspended in 10 mL of toluene saturated with benzimidazole and containing triethylamine (prepared by mixing 0.5 mg of benzimidazole and 990 µL of tryethylamine in 40 mL of toluene and heating at 80 °C for 20 min). The mixture was stirred and heated at 80 °C for three days. Then, the solid was isolated by centrifugation, suspended in 10 mL of acetonitrile and treated 100 µL of 3-mercaptopropionic acid in order to functionalize the gold face with carboxylic groups. After this, the resulting solid was centrifuged, washed with acetonitrile and dried at 70 °C overnight. 8 mg of this solid, 2.5 mg of EDC, 2.5 mg of NHS and 2 mg of GDH were suspended in 4 mL of 50 mM sodium phosphate buffer (pH 7.5) and stirred overnight in an ice bath. Next, the solid was isolated by centrifugation and washed with phosphate buffer exhaustively. Then, the material was suspended in 2 mL of 50 mM sodium phosphate buffer (pH 7.5) and 4 mg of Doxo were added in order to load the pores of the mesoporous face. After 7 hours stirring in an ice bath, 3.2 mg of β-cyclodextrin were added and the sample was further stirred overnight. The resulting solid **S3$_{\mathbf{DOX}}$** was isolated by centrifugation, exhaustively washed with 50 mM sodium phosphate buffer (pH 7.5) and kept in the refrigerator until use.

Preparation of S3$_{Blank}$

In order to confirm that the decrease in cell viability induced by **S3$_{\mathbf{DOX}}$** in the presence of glucose and intracellular NAD$^+$ was due to doxorubicin release, a similar solid to **S3$_{\mathbf{DOX}}$** but without doxorubicin was prepared (solid **S3$_{\mathbf{Blank}}$**). After functionalization of **S1** with benzimidazole groups and 3-mercaptopropionic acid (as described above for **S3$_{\mathbf{DOX}}$**), 2 mg of this solid, 0.63 mg of EDC, 0.63 mg of NHS and 0.5 mg of GDH were suspended in 1 mL of 50 mM phosphate buffer (pH 7.5) and stirred overnight at 4 °C. Afterward, the solid was exhaustively washed by centrifugation with phosphate buffer and further stirred at 4 °C in 0.5 mL of buffer containing 0.8 mg of β-cyclodextrin. The mixture was stirred overnight and the resulting solid **S3$_{\mathbf{blank}}$** was isolated by centrifugation, exhaustively washed with 50 mM sodium phosphate buffer (pH 7.5) and kept in the refrigerator until use.

Preparation of S4

A material similar to **S3** but functionalized with both GDH and urease was also prepared (solid **S4**). In order to attach both enzymes, 8 mg of **S2-CD**, 2.5 mg of EDC, 2.5 mg of NHS, 1 mg of GDH and 1 mg of urease were mixed in 4 mL of 50 mM sodium phosphate buffer at pH 7.5. The mixture was stirred overnight in an ice bath and the solid was isolated by centrifugation, exhaustively washed with 50 mM sodium phosphate buffer (pH 7.5) and kept in refrigeration until use. This protocol finally yielded the nanodevice **S4**.

Materials Characterization

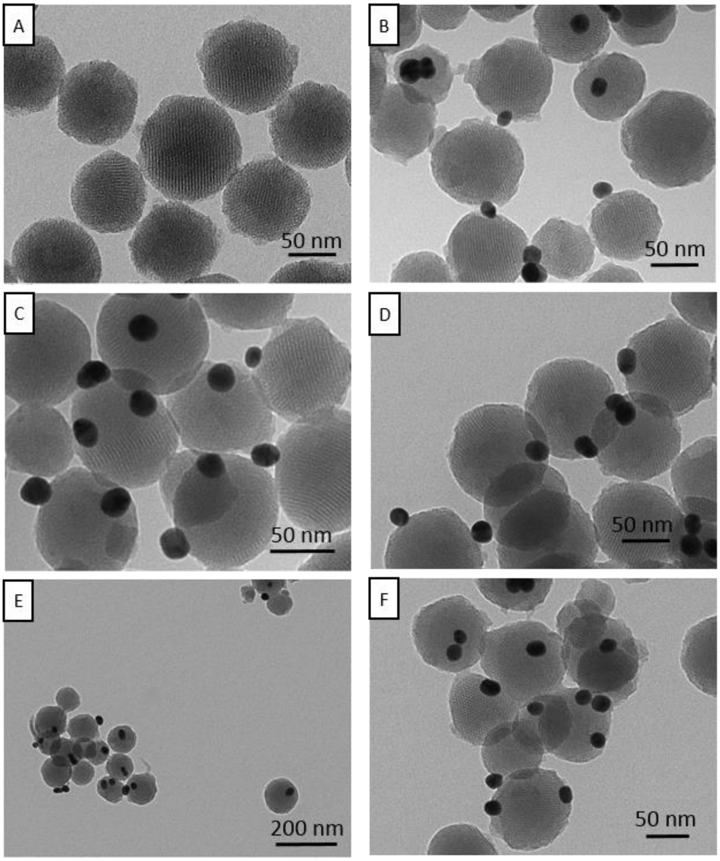

Figure S1. Representative TEM images of: (A) calcined MSNPs and (B-F) Au-MS nanoparticles (**S1**).

Table S1. Summary of distribution of AuNPs-MSNPs ratio as determined by analysis of TEM images.

Au-Si	Number	Percentage
0:1	11	16.92 %
1:1	40	61.54 %
2:1	14	21.54 %
Total NPs	65	100.00 %

TEM-EDX mapping of the final nanodevice **S3** showed the presence of Si and O atoms that can be ascribed to the silica support and the presence of Au atoms, due to the Au nanosphere. In addition, although the mapping of the atoms of the organic moieties is more challenging and it is more affected by background noise, it can be appreciated that S-counts (associated to enzymes) are mainly located on the gold surface and that the N-counts (associated to the cargo and enzymes) are higher on the silica and gold surface than on the backgrounds (see Figure S2).

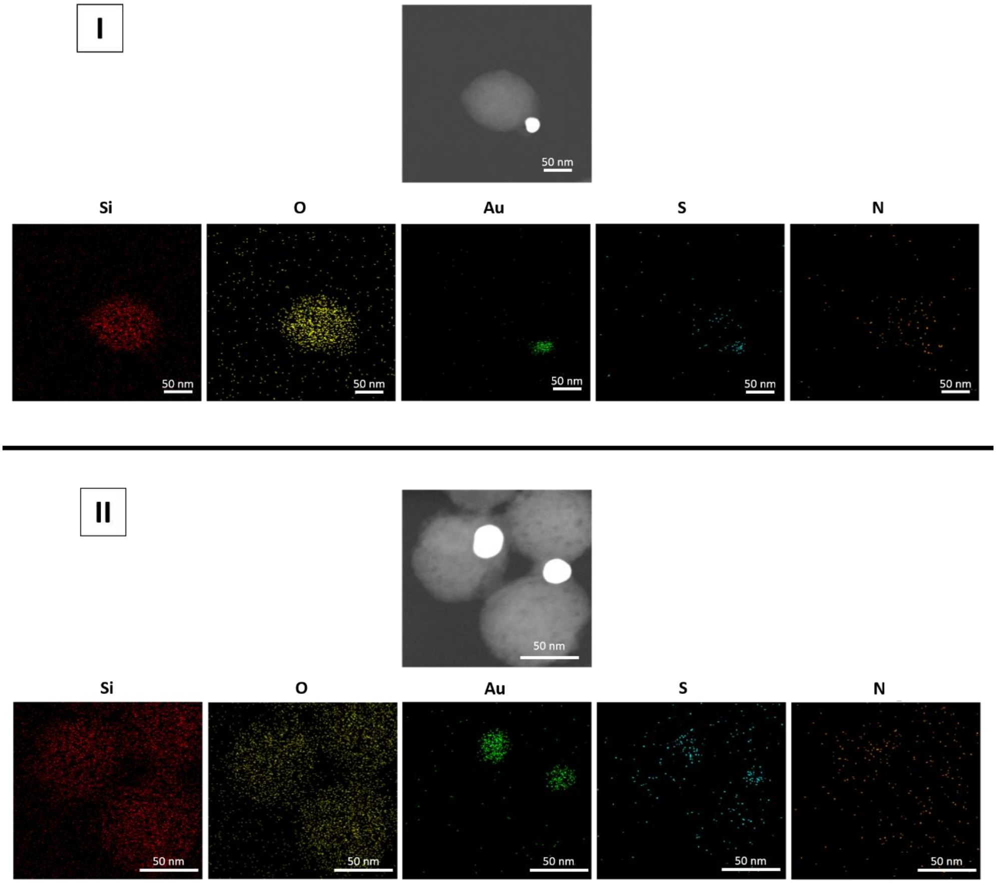

Figure S2. Mapping of different atoms on the Janus nanodevice **S3**, obtained using TEM coupled with energy dispersive X-ray spectroscopy (EDX).

UV/vis spectrum of the as-prepared AuNPs and of the Au-MS nanoparticles **S1** (1 mg of suspended in 2 mL of water) were acquired (see Figure S3). AuNPs showed a single absorption band at 523 nm, which perfectly agrees with the typical colour and surface plasmon resonance band shown by those gold nanoparticles smaller than 25 nm.[1] In the **S1** spectrum, there is a broadening of the absorption band due to light diffraction produced by silica and a 10 nm redshift of the absorbance maximum due to the change in the refractive index around the gold nanospheres due to the MS attachment.[2]

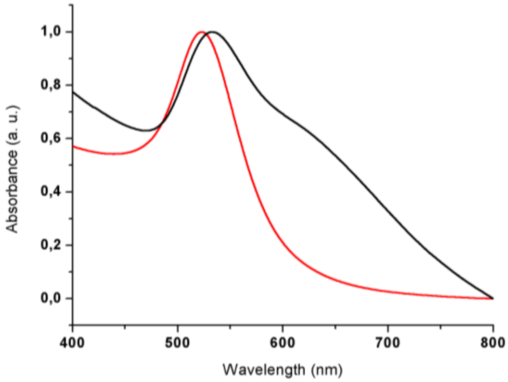

Figure S3. Normalized UV-Visible spectra of AuNPs (red) and Au-MSNPs **S1** (black).

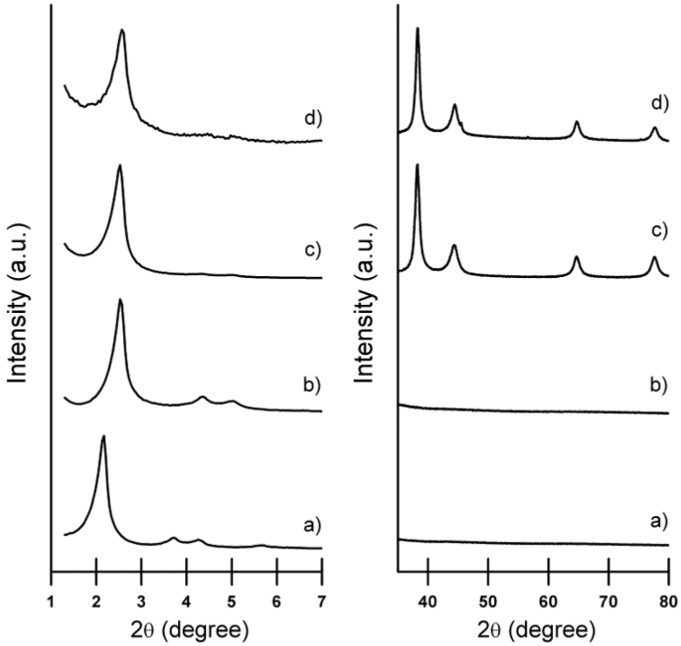

Figure S4. Powder X-Ray diffraction patterns at low (left) and high (right) angles of: (a) as-synthesised MSNPs, (b) calcined MSNPs, (c) **S1** nanoparticles and (d) functionalized nanoparticles **S2**.

At low angles ($1.5 < 2\theta < 7$), powder X-Ray diffraction pattern of the as-made MSNPs (Figure S4, a) showed the typical reflection peaks characteristics of materials with a 3-D porous structure of the MCM-41 type ((100), (110) and (200)

Bragg peaks). After calcination, there was a slight displacement of these peaks related to the removal of the surfactant and to the condensation of silanol groups during the calcination process (see Figure S4, b). The preservation of the main peak at 2.4° in **S1** and **S2** confirmed that gold attachment, surface functionalization and cargo loading processes did not damage the mesoporous scaffolding (see Figure S4, c and d). At high angles (35 < 2θ < 80), cubic gold characteristic (111), (200), (220) and (331) diffraction peaks appeared for **S1** and **S2**, thus confirming the presence of gold nanocrystals and the Janus Au-MS architecture.

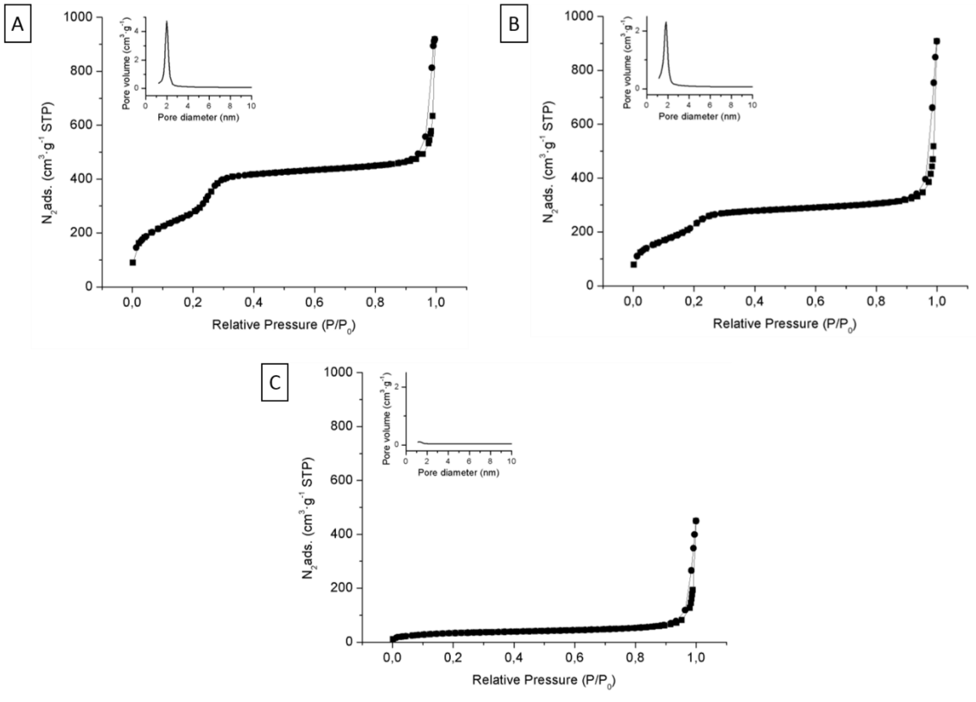

Figure S5. N_2 adsorption-desorption isotherms for (A) the calcined MSNPs, (B) Au-MS nanoparticles **S1** and (c) **S2** loaded solid. Inset: Pore size distribution.

N_2 adsorption-desorption isotherms for MSNPs and Au-MSNPs **S1** showed an adsorption step at P/P_0 below 0.3 which is ascribed to the nitrogen condensation inside the empty pores (see Figure S5). Additionally, the narrow pore size distribution and the absence of hysteresis indicate the formation of uniform cylindrical mesopores. Total surface specific area was calculated by applying the BET model and are summarized in Table S2. Whereas a slight decrease was observed from 1018.70 $m^2 \cdot g^{-1}$ for MSNPs to 846.10 $m^2 \cdot g^{-1}$ for **S1** due to the attachment of non-porous gold nanoparticles, total specific surface area for **S2** significantly decreased to 123.63 $m^2 \cdot g^{-1}$ as a consequence of cargo loading inside the mesopores. In order to calculate pore size and total pore volume, BJH model was applied on the adsorption band of the isotherm for $P/P_0 < 0.6$ (associated to adsorption inside the pores).

Table S2. BET specific surface values, pore volumes and pore sizes calculated from N_2 adsorption-desorption isotherms for selected materials.

Sample	S_{BET} [$m^2\ g^{-1}$]	Pore Volume [$cm^3 g^{-1}$]	Pore size [nm]
MSNPs	1018.70	0.77	2.38
S1	846.10	0.55	2.34
S2	123.63	0.06	--

From elemental analysis data (Table S3), composition of solids was calculated and is summarized in Table S4. First the quantity of 3-iodopropyl moieties and dye ($[Ru(bpy)_3]Cl_2$) was calculated from the increase in C and N percentage from **S1** to **S1-I**. The amount of benzimidazole anchored on **S2** was calculated by taking into account the increase in N percentage (and that there was not any leakage of $[Ru(bpy)_3]Cl_2$ since it is not soluble in toluene). For **S2-CD**, dye content was calculated from the N percentage and taking into account that benzimidazole content remained constant. β-CD content was calculated from C percentage and dye and benzimidazole content.

Table S3. Elemental analysis data.

Sample	% C	% H	% N
MSNPs	0.74	0.76	0.12
S1	2.53	1.96	0.18
S1-I	12.14	2.55	2.59
S2	18.79	2.59	3.37
S2-CD	10.04	2.67	1.42

Table S4. Content of each component according to elemental analysis data. Values expressed as mmol of component per gram of solid and as weight percentage in brackets.

Solid	3-iodopropyl	Benz.	dye	β-CD
S1-I	0.29 (4.9%)	--	0.31 (17.6%)	--
S2	--	0.28 (3.3%)	0.31 (17.6%)	--
S2-CD	--	0.28 (3.3%)	0.08 (4.3%)	0.10 (11.2%)

Table S5. GDH activity and corresponding GDH content on enzyme functionalized solids.

Sample	Δ (min^{-1})	Enzymatic Activity (U·mg^{-1})	mg GDH / g solid
S3	0.2421	1.25	17.91
S4	0.1334	0.69	9.87

Glucose dehydrogenase (GDH) immobilization on the nanoparticles was confirmed by a specific enzymatic assay. The assay is based on monitoring the production of NADH catalyzed by glucose dehydrogenase as a function of time.[3] NADH formation can be monitored by measuring its light absorption at 340 nm. In order to carry out the assay, 475 µL of 50 mM sodium phosphate buffer (pH 7.5), 250 µL of glucose 1 M and 25 µL of NAD$^+$ 20 mM were added in a quartz cuvette. Then, 5 µL of either buffer (for blank) or nanoparticles solution (5 mg·mL^{-1}) were added. The mixture was shaken and absorbance at 340 nm was measured for 2 min in intervals of 5 seconds. As can be seen in Figure S6, no increase in absorbance (no NADH formation) occurred in the absence of GDH-functionalized nanoparticles. When **S3** or **S4** were added, absorbance at 340 nm rapidly increase due to their GDH activity.

Glucose dehydrogenase activity (Table S5) on the nanoparticles was calculated by applying the following formula:

$$\frac{\text{Enzyme Units}}{\text{g}} = \frac{(\Delta - \Delta_{\text{blank}}) * V_T * F_D}{\varepsilon_{NADH} * l * V_{NPs} * C_{NPs}}$$

Where,

Δ is the slope of the graph (min^{-1})

Δ_{blank} is the slope of the graph for the blank (min^{-1})

V_T is the total volume in the cuvette

ε_{NADH} is the molar extinction of NADH at 340 nm (6220 $M^{-1} \cdot cm^{-1}$)

L is the optical path in the cuvette (1 cm)

V_{NPs} is the volume of nanoparticles added (mL)

C_{NPs} is the concentration of nanoparticles suspension added (g/mL).

Additionally, the activity of commercial GDH was determined to be 70 U·mg^{-1}. From this data, the corresponding amount of GDH on **S3** was calculated to be 17.91 mg per g of solid (see also Table S5). For **S4**, the amount of GDH (9.87 mg·g^{-1}) reduced almost by half due to the co-immobilisation of urease.

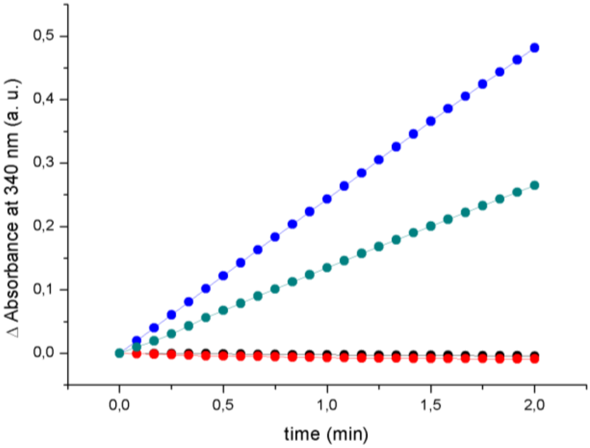

Figure S6. Monitoring of absorbance at 340 nm (NADH formation) due to GDH activity on nanoparticles **S3** (blue), **S4** (green), **S2-CD** (red, without activity), and blank (black).

Release experiments

For release experiments, the corresponding refrigerated solutions of nanoparticles were washed with an aqueous solution (pH 7.5, 20 mM Na_2SO_4), divided into fractions and brought to a final concentration of 1 mg·mL^{-1}. The corresponding inputs (solutions previously adjusted at pH 7.5) were introduced and samples were shaken over time. Aliquots were taken at scheduled times and centrifuged to remove the nanoparticles. Then, the emission at 595 nm of the $[Ru(bpy)_3]Cl_2$ dye released was measured ($\lambda_{exc} = 453$ nm).

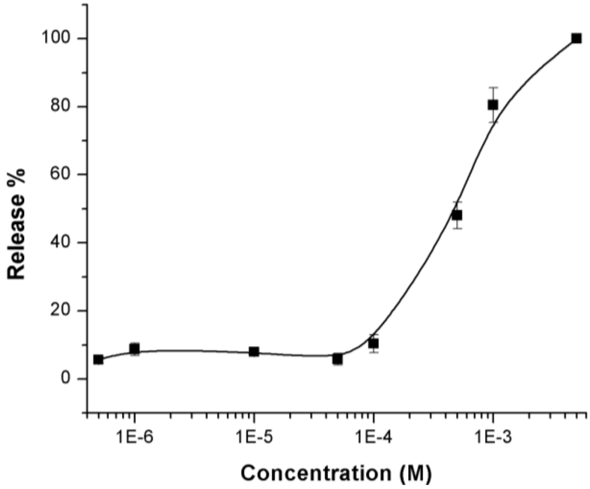

Figure S7. Calibration curve obtained upon addition of different equivalent concentrations of glucose and NAD^+ to suspensions of **S3** (1 mg·mL^{-1}).

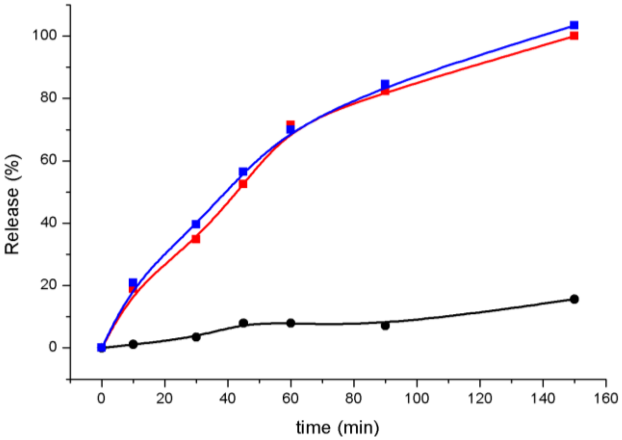

Figure S8. Normalized cargo release from **S3** in the absence of input (black curve), in the presence of glucose and NAD^+ (blue curve), and in the presence of glucose, NAD^+ and urea (red curve). Substrates added at 1 mM concentration.

Cell culture experiments

Cell culture conditions

HeLa human cervix adenocarcinoma cells were purchased from the German Resource Centre for Biological Materials (DSMZ) and were grown in DMEM supplemented with 10% FBS. Cells were incubated at 37 °C in an atmosphere of 5% carbon dioxide and 95% air and underwent passage twice a week.

Confocal microscopy

HeLa cells were seeded on glass coverslips at 250,000 cells/mL in a 6-well plate and incubated at 37 °C for 24 h. Then, the medium was changed to fresh PBS (10% FBS) and cells were incubated with $\mathbf{S3}_{\mathbf{DOX}}$ (50 $\mu g \cdot mL^{-1}$) at 37 °C for 30 min. Afterward, cells were washed several times with PBS in order to remove non-internalized nanoparticles and further incubated for 24 h in a fresh medium in the absence or in the presence of glucose (25 mM). Next, cells were washed several times with PBS and DNA marker Hoechst 33342 was added at 2 $\mu g \cdot mL^{-1}$. Finally, slides were visualized using a confocal microscope Leica TCS SP2 AOBS.

Cell viability assays

HeLa cells were seeded in a 24-well plate at 50,000 cells/well and incubated at 37 °C for 24 h. Then, medium was changed to fresh PBS (10% FBS) and cells were incubated (30 min, 37 °C) with $\mathbf{S3}_{\mathbf{DOX}}$ and $\mathbf{S3}_{\mathbf{Blank}}$ at 50 and 100 $\mu g \cdot mL^{-1}$. After 30 min, cells were washed several times with PBS in order to remove non-internalized nanoparticles and cells were further incubated for 24 h in the presence or in the absence of glucose (25 mM). Finally, cell viability was evaluated by incubation with the cell proliferation WST-1 reagent for 1h and measuring the absorbance at 595 nm. The obtained results are shown in Figure S9.

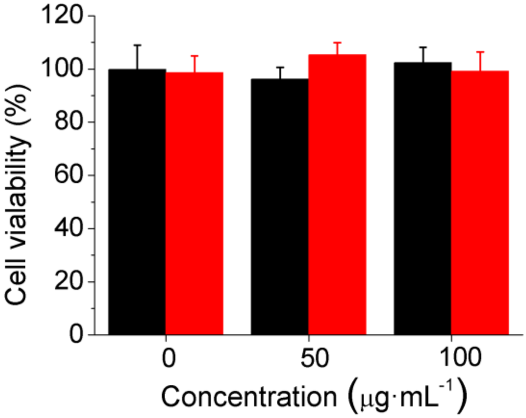

Figure S9. Cell viability assays of HeLa cells treated with different **S3**$_{\mathbf{Blank}}$ concentrations (0, 50 and 100 µg·mL^{-1}) in the absence (black bars) or presence (red bars) of glucose (25 mM). Data shown as m±σ.

---

1. Haiss, W.; Thanh, N. T. K.; Aveyard, J.; Fernig, D. G. Determination of size and concentration of gold nanoparticles from UV− Vis spectra. *Anal. Chem.* **2007**, *79*, 4215-4221.
2. Kelly, K. L.; Coronado, E.; Zhao, L. L.; Schatz, G. C. The optical properties of metal nanoparticles: the influence of size, shape, and dielectric environment. *J. Phys. Chem. B* **2003**, *107*, 668-677.
3. Smith, L. D.; Budgen, N.; Bungard, S.J.; Danson, M. J.; Hough, D.W. Purification and characterization of glucose dehydrogenase from the thermoacidophilic archaebacterium Thermoplasma acidophilum. *Biochem. J.* **1989**, 261, 973-977.

7. Versatile New Paradigm for the Design of Optical Nanosensors Based on Enzyme-Mediated Detachment of Labelled-Reporters: The Example of Urea Detection

Versatile New Paradigm for the Design of Optical Nanosensors Based on Enzyme-Mediated Detachment of Labelled-Reporters: The Example of Urea Detection

A. Llopis-Lorente,[a,b,c] R. Villalonga,*[d] M. D. Marcos,[a,b,c,e,f] R. Martínez-Máñez*[a,b,c,e,f] and F. Sancenón[a,b,c,e,f]

[a] Instituto Interuniversitario de Investigación de Reconocimiento Molecular y Desarrollo Tecnológico (IDM), Universitat Politècnica de València-Universitat de València (Spain).

[b] Departamento de Química, Universitat Politècnica de València, Camino de Vera s/n, 46022 Valencia (Spain). E-mail: rmaez@quim.upv.es

[c] CIBER de Bioingeniería, Biomateriales y Nanomedicina (CIBER-BBN).

[d] Department of Analytical Chemistry, Faculty of Chemistry, Complutense University of Madrid, 28040 Madrid (Spain). E-mail: rvillalonga@quim.ucm.es

[e] Unidad Mixta de Investigación en Nanomedicina y Sensores. Universitat Politècnica de València, Instituto de Investigación Sanitaria La Fe, Valencia (Spain).

[f] Unidad Mixta UPV-CIPF de Investigación en Mecanismos de Enfermedades y Nanomedicina, Valencia, Universitat Politècnica de València, Centro de Investigación Príncipe Felipe, Valencia (Spain).

(Reprinted with permission from ***Chem. Eur. J.*** **2018, DOI 10.1002/chem.201804706**.

7.1 Abstract

Here we present a novel bio-inspired nanoarchitectonics approach for the design of optical probes. It is based on nanodevices that combine (i) an enzymatic receptor subunit, (ii) a signalling subunit (consisting of a labelled-reporter attached to a silica surface), and (iii) a mechanism of communication between the two sites founded on the production of chemical messengers by the enzymatic subunit that induces the detachment of the reporter molecules from the silica surface. As a proof of concept, a urea nanosensor based on the release of Alexa Fluor 647-labelled oligonucleotide from enzyme-functionalized Janus Au-MSNPs (gold-mesoporous silica nanoparticles) has been developed. Janus Au-MSNPs are functionalized on the silica face with amino groups to which the labelled oligonucleotide is attached by electrostatic interactions, whereas the gold face is used for grafting the urease enzyme. The nanodevice is able to release fluorescent-oligonucleotide via enzyme-mediated hydrolysis of urea to ammonia and the subsequent deprotonation of amino groups on the silica face. This simple nanodevice has been applied for the flurorimetric detection of urea in real human blood samples and for the identification of adulterated milk. Given the large variety of enzymes and reporter species that could be combined, we believe this is a general new paradigm that could applied to the design of a number of optical probes for the detection of target analytes.

7.2 Introduction

The chromo-fluorogenic detection of analytes (cations, anions and neutral molecules) of biomedical and environmental interest is a primary research topic due to their potential applications in different fields.[1] Chromo-fluorogenic probes (also called chemosensors) offer certain advantages such as no need to use sophisticated equipment or highly-trained personnel, low cost, rapid response and *in situ* detection.[2] Most chemosensors are usually molecular entities that incorporate (i) a receptor subunit (that interacts with the analyte), (ii) a signalling subunit (usually a fluoro-chromophore group) and (iii) a mechanism of communication between the two subunits (e.g. photoinduced electron transfer (PET), electronic energy transfer (EET), etc.) (Figure 1a).[3] A key step when designing an optical probe is to find the receptor group that interacts specifically with the target analyte.

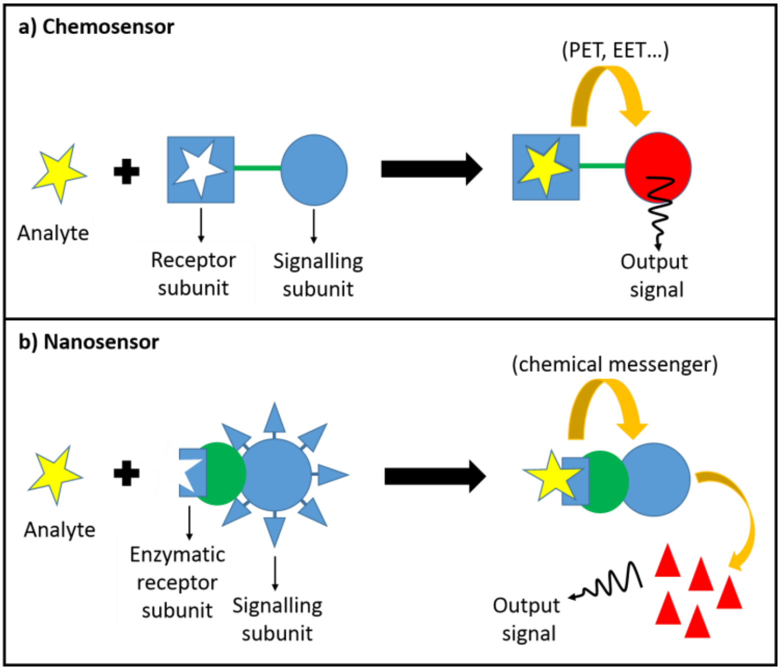

Figure 1. a) Schematic of a typical chromo-fluorogenic probe containing a receptor subunit and a signalling subunit. b) Schematic of the bio-inspired nanoarchitectonics approach proposed in this paper for the design of nanosensors combining an enzymatic receptor subunit and a hybrid signalling subunit.

When talking about chromo-fluorogenic chemosensors, the design of probes for small neutral biomolecules is challenging due to their lower reactivity compared to cations and anions. In natural systems, recognition of small biomolecules is accomplished by antibodies, enzymes and other bioreceptors.[4]

Whereas antibodies bind to the target molecule, enzymes transform their specific substrates into new chemicals. On the other hand, nanoarchitectonics has been regarded as a promising approach to develop advanced nanoscale materials based on the synergic combination of different nano-(bio)-components using nanotechnology, supramolecular and molecular chemistry, and bio-related technologies.[5] Inspired by both traditional chemosensors and the role of enzymes in living systems, we envisioned a new versatile paradigm for the design of optical probes based on hybrid nanodevices incorporating (i) enzymes as receptor subunit, (ii) fluoro-chromogenic species linked to a silica surface as the signalling subunit and (iii) a mechanism of communication between the two subunits based on the production of “chemical messengers” by the enzymes that induce the detachment and release of the fluoro-chromophore. As a proof of concept, we present here a urea nanosensor based on Janus Au-MSNPs (gold-mesoporous silica nanoparticles) functionalized with Alexa Fluor 647-labelled oligonucleotide on the silica surface and with urease on the gold surface (Figure 2).

In the scientific literature, the term Janus is used to define particles that have two (or more) surfaces with different chemical and physical properties.[6] Janus particles with different morphologies and 3D architectures have been designed such as half-and-half hemispheres, rods, dumbbell-, acorn- or (like in the present study) snowman-shaped particles.[7] Besides, the integration of metal nanoparticles and silica materials in Janus or core-shell structures for detection applications has been reported in several studies.[8]

Urea [$(NH_2)_2CO$] is a key molecule in human, animal and plant metabolism. It is a major component of blood plasma and urine and its determination is of considerable interest in clinical and agricultural settings.[9] In humans, urea is synthesized in the livers for the removal of ammonia generated from the breakdown of proteins and amino acids. From the liver, urea is transported by the blood to the kidneys and finally excreted in urine. In plasma, urea normal levels are from 2.5 mM to 7.5 mM and concentrations above this range can be indicative of renal dysfunctions, liver disease or dietetic problems.[10] On the other hand, urea has been identified amongst the most common chemicals used in milk adulteration, especially in developing countries.[11] It is added with the aim of increasing the solid non-fat content determined by conventional tests and consumption of milk adulterated with urea can cause serious health problems. Furthermore, urea levels in cattle milk are a useful parameter to control animal health, and levels above 40 mg·dL^{-1} (6.6 mM) can be indicative of disease.[12] In the last 3 years, the development of simple methodologies for urea detection has attracted considerable attention and several studies have been reported (see Table SI-1),[13] most of them based on electrochemical sensing.[13a-j] Whereas previous electrochemical sensors have generally required two enzymes (urease and glutamate dehydrogenase) and mediators (e.g., NADH, L-glutamate, ferrocene) to complete electron transfer to the electrode,[14] recent studies aim to reduce complexity and the number of chemicals needed by using polymer composites and graphene modified electrodes.[13a-j] Furthermore, a colorimetric method based on the aggregation of unmodified gold nanoparticles with a detection limit of 20 mM,[13k] and a urea probe based on the magnetization of iron nanoparticles in oil-in-water emulsions have been reported.[13l] Despite these advances, the development of simple methods for urea sensing in complex matrices (i.e. plasma, milk) to reduce analysis time and avoid the use of sophisticated equipment remains a topic of interest.

7.3 Results and discussion

The design and sensing paradigm of the urea nanosensor (**S1**) based on the release of labelled-oligonucleotide from Janus-type Au-mesoporous silica nanoparticles mediated by an integrated enzymatic unit (urease) are depicted in Figure 2. The silica face, in the Janus nanoparticles, is functionalized with amino moieties (positively charge at neutral pH) to which oligonucleotide strand attach via electrostatic interactions.[15] The oligonucleotide strand contains 20 nucleotides and is labelled with a fluorescent dye (Alexa Fluor 647) on its 5’-end. Moreover, the gold face is used for immobilizing urease enzyme. The nanosensor produces a strong fluorescent signal in the presence of urea as a consequence of its recognition by the enzyme and transformation into ammonia and CO_2. This induces a local decrease of the pH and deprotonation of the amino moieties on the silica face that results in the release of the labelled-oligonucleotide to the solution.

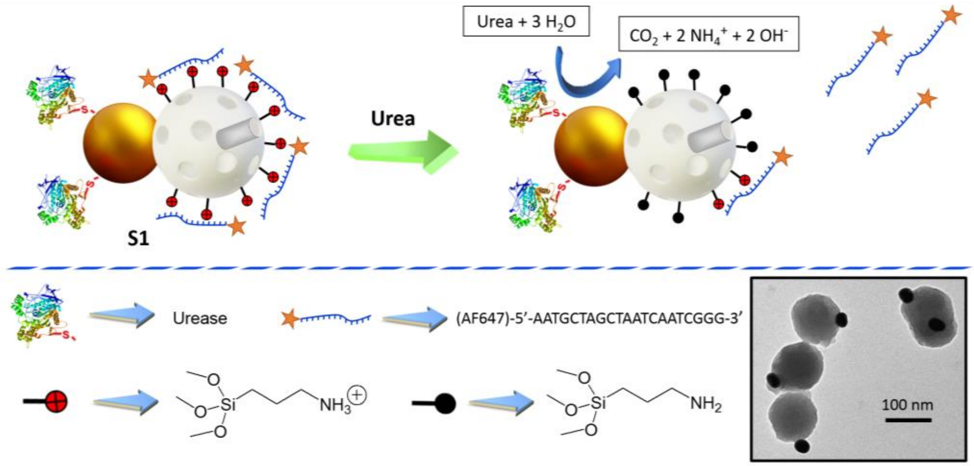

Figure 2. Representation of the design and sensing performance of the nanosensor **S1**. Inset: TEM image of Janus **Au-MSNPs**.

In order to prepare the nanosensor, firstly, mesoporous silica nanoparticles (**MSNPs**) were synthesized by condensation of tetraethyl orthosilicate in alkaline media using *n*-cetyltrimethylammonium bromide (CTAB) micelles as a template. Gold nanoparticles (**AuNPs**) were synthesized by reduction of Au(III) with sodium citrate. Next, **MSNPs** were partially functionalized with (3-mercaptopropyl) trimethoxysilane by confinement at the interface of an emulsion between paraffin wax and an aqueous phase, and **AuNPs** were then attached to **MSNPs** by the formation of Au-S bonds with thiols on the silica surface. The paraffin wax was removed by washing the nanoparticles with $CHCl_3$, which yielded the Janus Au-mesoporous silica nanoparticles (**Au-MSNPs**).[16] Then, the gold face was functionalized by treatment with 3-mercaptopropionic acid and afterward the silica surface was functionalized with amino moieties by treatment with an excess of (3-aminopropyl)triethoxysilane. The resulting solid (**S0**) was stirred in a solution of a labelled oligonucleotide ((Alexa Fluor 647)-5’-AATGCTAGCTAATCAATCGGG-3’) in phosphate buffer at pH 7.5 for 30 min, washed, and further functionalized with urease by coupling the enzyme with carboxylic groups on the gold face via the use of ethyl(dimethylaminopropyl)carbodiimide (EDC) and *N*-hydroxysuccinimide (NHS). This process finally yielded the sensing nanodevice **S1** (Figure 2), which was kept in the refrigerator in phosphate buffer solutions (pH 7.5) until use.

The prepared materials were characterized using standard procedures (see Supporting Information). TEM images (inset in Figure 2 and Figure SI-1) confirmed the linkage between **MSNPs** nanoparticles (ca. 80-100 nm) and **AuNPs** (ca. 20 nm) yielding the Janus-type Au-MS structure. Absorption spectra showed the characteristic gold surface plasmon resonance at 525 nm for **AuNPs**, with a red-shift to 532 nm for **Au-MSNPs** due to the increase in the refractive index around the gold surface induced by the coupling with the mesoporous silica (Figure SI-2). Additionally, low-angle powder X-ray diffraction (PXRD) patterns (Figure SI-3) of the **MSNPs** and **Au-MSNPs** showed the (100) reflection peak that is characteristic of mesoporous silica materials. At high angles, the PXRD pattern of the **Au-MSNPs** Janus colloids showed the cubic gold (111), (200), (220), and (311) peaks which confirmed the presence of gold nanocrystals observed by TEM. Conservation of low- and high-angles peaks in **S0** confirmed that the functionalization processes did not damage the 3D structure. The total surface area of starting **MSNPs** was 1299.86 $m^2 \cdot g^{-1}$, determined from N_2 adsorption-desorption isotherms, and reduced to 974.28 $m^2 \cdot g^{-1}$ for **Au-MSNPs** due to the incorporation of non-porous gold nanoparticles (Figure SI-4). The zeta potential of the **MSNPs** and **Au-MSNPs** was -39.9 and -39.4 mV (at pH 7.5) respectively and for **S0** the total charge was reduced (-16 mV) due the functionalization of the silica face with aminopropyl groups. For the final nanodevice **S1**, the negative charge increased to -30 mV due to the attachment of oligonucleotide strands on the silica face and to the immobilization of urease on the gold surface. From dynamic light scattering measurements, the hydrodynamic diameter for the sensing nanoparticles **S1** was determined to be 111±20 nm (Figure SI-5). From elemental analysis of **S0**, the amount of anchored aminopropyl moieties was determined to be 1.6 mmol per gram of solid. The amount of labelled-oligonucleotide on the final nanodevice **S1** was 2 µmol per gram of solid, as determined by fluorescence. The activity of immobilized urease on **S1** was 820 U·g^{-1}, as determined using a standard assay (see Experimental Section and Figure SI-6), which corresponds to 12.7 mg of commercial enzyme per g of **S1**.

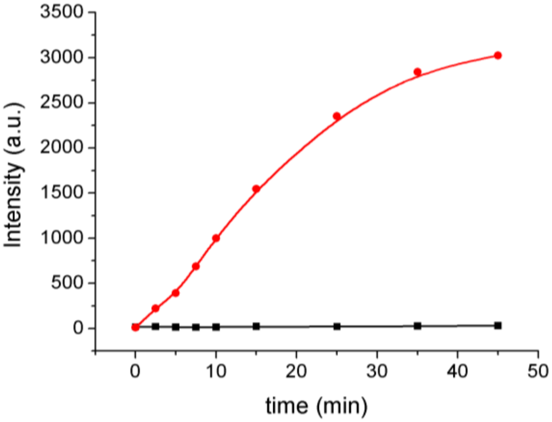

Figure 3. Labelled-oligonucleotide release from **S1** determined by measuring emission at 664 nm (λ_{exc} = 649 nm) in water solutions (PBS, pH 7.5) in the absence (black curve) and in the presence (red curve) of urea (5 mM).

To assess the feasibility of the proposed nanosensor, we first monitored the release of labelled-oligonucleotide from **S1** in aqueous media in the absence and presence of urea. For these experiments, **S1** aliquots were brought to a concentration of 0.3 mg·mL^{-1} in phosphate buffer solution (PBS, pH 7.5) containing either 0 or 5 mM of urea and stirred at room temperature (25 °C). At scheduled times, aliquots were taken, centrifuged to remove the nanoparticles and the release of labelled-oligonucleotide to the solution was evaluated by measuring the emission band of Alexa Fluor 647 at 664 nm (λ_{exc} = 649 nm). The oligonucleotide release kinetics are displayed in Figure 3. As can be seen, in the absence of urea, the fluorescence emission was negligible since amino moieties on the silica surface are protonated (pk_a = 9.6)[17] and the oligonucleotide remains attached by the formation of electrostatic interactions.[18] In contrast, in the presence of urea a strong fluorescence signal was observed due to the release of labelled-oligonucleotide from **S1** to the solution. This emission enhancement was ascribed to the recognition of urea by the enzymatic unit on **S1**, which catalysed the formation of carbon dioxide and ammonia. In turn, ammonia induced the deprotonation of amino moieties on **S1**, which broke the electrostatic interactions with phosphate groups and produced the release of labelled-oligonucleotide. Besides, an increase in the pH of the media was observed as a result of ammonia formation. In order to confirm the sensing mechanism, we checked that the fluorescence of (Alexa Fluor 647)-labelled oligonucleotide alone was not affected by the pH of the media or the presence of urea. In addition, urea did not induce any increase in fluorescence when Janus nanoparticles containing the labelled-oligonucleotide but without urease enzyme were used.

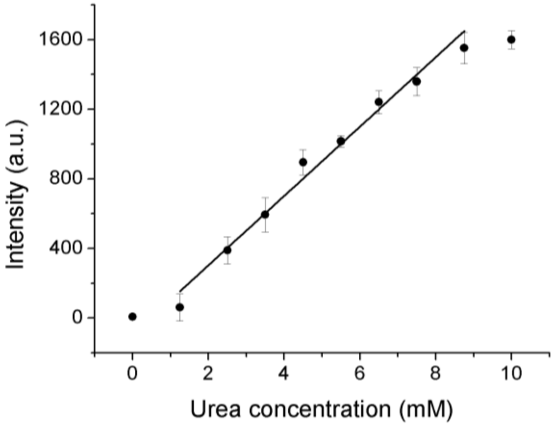

Figure 4. Emission at 664 nm (λ_{exc} = 649 nm) associated with the release of labelled-oligonucleotide release from **S1** as a function of urea concentration in water solutions (PBS, pH 7.5) after 10 min of incubation.

In a next step, we studied the response of the nanosensor **S1** as a function of urea concentration. **S1** nanoparticles were suspended in PBS (0.3 mg·mL^{-1}, pH 7.5) with different concentrations of urea, incubated for 10 min and afterward the fluorescence of the released labelled-oligonucleotide was measured. As can be seen in Figure 4, a gradual enhancement in fluorescence was observed upon increasing the amount of urea. Particularly, a linear increase occurred in the range 1.25-8.75 mM and a limit of detection of 0.5 mM was calculated from the calibration curve. In terms of clinical applications, the linear range of nanosensor **S1** confers it a competitive basis to monitor urea within the normal clinical range found in blood plasma (2.5-7.5 mM). Additionally, the nanosensor **S1** may also be employed for the analysis of higher urea concentrations, such as that found in plasma of patients with renal problems or the normal concentrations in urine (700-130 mM),[19] by simply performing dilutions of the samples.

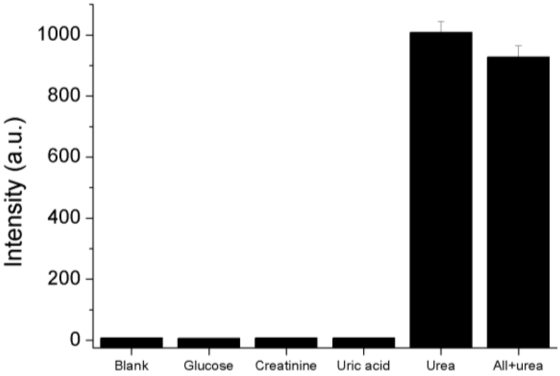

Figure 5. Emission at 664 nm (λ_{exc} = 649 nm) associated with the labelled-oligonucleotide release from **S1** in the presence of different biomolecules at physiological concentrations (glucose (5 mM), creatinine (80 µM), uric acid (0.3 mM)), in the presence of urea (5 mM) and in a mixture of these potential interferents and urea (5 mM).

In a further step, we confirmed the selectivity of the sensing nanodevice by evaluating the response of **S1** in the presence of other biomolecules such as glucose, creatinine and uric acid at physiological concentrations. For these experiments, **S1** (0.3 mg·mL^{-1}) was suspended in aqueous solutions at pH 7.5 (PBS) in the presence of each chemical and incubated for 10 minutes. Then, the fluorescence of the released labelled-oligonucleotide was determined. As can be seen in Figure 5, these biomolecules did not produce any appreciable increase in fluorescence which indicated that the oligonucleotide remained attached to **S1**. In an additional experiment, the response of **S1** was tested in a solution containing a mixture of these potential interferences and urea, and a clear fluorescent signal was observed indicating the selective recognition of urea with the subsequent release of oligonucleotide in this complex mixture.

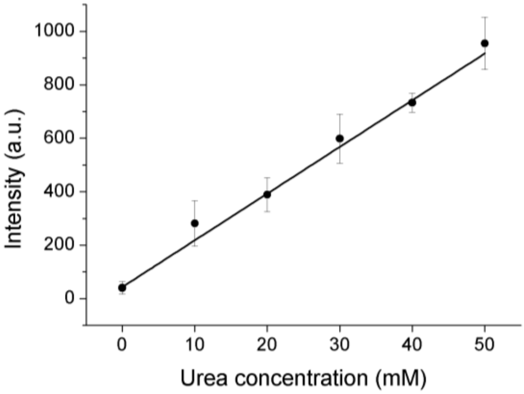

Figure 6. Emission at 664 nm (λ_{exc} = 649 nm) as a function of spiked urea concentration in human blood plasma associated with the release of labelled-oligonucleotide from **S1** after 10 min of incubation.

Encouraged by the above mentioned results, we decided to evaluate the potential use of nanosensor **S1** for the detection of urea in real human blood samples. Blood samples were obtained from a healthy volunteer, and were centrifuged to separate the plasma (see Experimental Section and Figure SI-7 for details). In order to perform the analysis, 15 µL of plasma samples spiked with different amounts of urea were added over 135 µL of a **S1** suspension (0.3 mg·mL^{-1}) and incubated for 10 minutes. After this, aliquots were centrifuged to eliminate the nanoparticles and the fluorescence of the supernatant was then measured.

Remarkably, as can be seen in Figure 6, a significant and proportional increase in fluorescence was observed as a function of the urea concentration in plasma. The analysed range was selected taking into account that in patients with renal dysfunctions urea concentration in blood is in the 20-50 mM range and that it decreases to less than 10 mM after dialysis.[20] The obtained response clearly indicated that plasma samples with abnormal levels of urea can be analysed by adding small amounts of the sample (15 µL) over a suspension containing **S1**. Additionally, from the intercept of the resulting calibration line (y=60.93 + 17.54x) with the x-axis, a urea concentration of 3.5 mM in the original (non-spiked) blood was determined, which is a normal value for a healthy person. Furthermore, we used this calibration to estimate the concentration of two samples spiked with urea (with a final concentration of 23.5 mM and 43.5 mM respectively). Using the procedure described above, urea concentration was determined to be 26.4 and 42.6 mM respectively, with recovery ratios of 112 and 98 %, respectively.

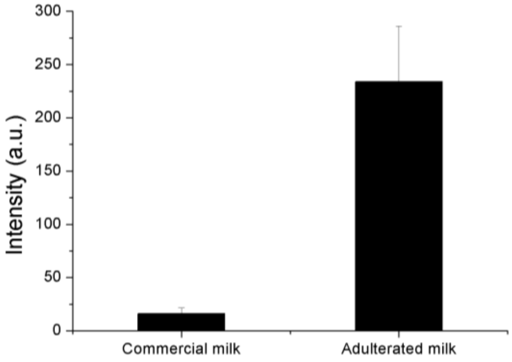

Figure 7. Discrimination between adulterated (containing 20 mM of urea) and non-adulterated milk using **S1**. Emission at 664 nm (λ_{exc} = 649 nm) associated with the labelled-oligonucleotide release from **S1** after 10 min of incubation with adulterated and non-adulterated milk.

Finally, we tested the potential use of **S1** to detect urea in adulterated milk. For these experiments, we used commercial milk that had been either spiked or not with urea (20 mM). In a similar way to the experiments performed in human blood, 15 µL of milk (previously centrifuged using centrifugal filters to remove turbidity) were added over aqueous solutions of **S1** (0.3 mg·mL^{-1}) and stirred for 10 minutes at room temperature. As can be seen in Figure 7, a remarkable difference in the supernatant fluorescence was observed between adulterated and non-adulterated milk samples. This fact points out the ability of **S1** to identify abnormal urea levels in milk (indicative of adulteration).

7.4 Conclusions

In summary, we report here a new nanoarchitectonics-based approach for the design of optical probes that combine (i) an enzymatic receptor subunit, (ii) a hybrid signalling subunit (consisting of labelled-reporter molecules attached to a silica surface by labile interactions), and (iii) a mechanism of communication between the two sites founded on the production of chemical messengers by the enzymatic subunit that induces the detachment of reporter molecules from the silica surface. As a proof-of-concept, the design, preparation and characterization of a nanodevice for urea detection based on the release of fluorescent-oligonucleotide from enzyme-functionalized Janus Au-mesoporous silica nanoparticles has been presented. The nanosensor consists of Janus-type Au-mesoporous silica nanoparticles functionalized with a fluorescent-oligonucleotide (on the silica face via electrostatic interactions with previously anchored 3-aminopropyl moieties) and with urease (by coupling the enzyme with carboxylic groups on the gold face). The sensing mechanism is based on the recognition of urea by the enzymatic unit and the production of ammonia (chemical messenger), which induces the detachment of the fluorescent oligonucleotide strand from the silica surface. The nanosensor was able to detect the presence of urea and a linear response was observed in the 1.25-8.75 mM concentration range, which covers the normal clinical range in plasma (from 2.5 mM to 7.5 mM). We demonstrated the applicability of the nanosensor for the detection of urea in human blood samples and for the identification of adulterated milk. Regarding the sensing of urea, this fluorescent nanosensor represents a simple and novel alternative to previously reported electrochemical and optical sensors and allows urea detection in real samples. Notwithstanding, given the knowledge acquired in the field of chemosensors and supramolecular chemistry in the design of labile linkages that can be broken by common enzymatic products (e.g. H_3O^+, OH^-, H_2O_2, nucleophiles, etc.), this approach could open new directions towards the development of novel optical sensors. Furthermore, mesoporous silica offers the additional possibility of loading an additional cargo (dye) in the pores interior and we envision that this could be taken advantage of to develop multisignalling nanosensors that combine the detachment of labelled-reporters from the external surface with the release of cargos from the pores interior. From a broad perspective, we believe that these results could inspire the development of nanodevices based on the combination of enzymatic effectors and the detachment of different reporter species for the design of easy-to-use detection kits of analytes of biomedical and environmental interest.

7.5 Experimental Section

Chemicals

Tetraethyl orthosilicate (TEOS), *n*-cetyltrimethylammonium bromide (CTABr), sodium hydroxide (NaOH), (3-mercaptopropyl)trimethoxysilane, hydrogen tetrachloroaurate(III) ($HAuCl_4·3H_2O$), sodium citrate tribasic dihydrate, paraffin wax, 3-mercaptopropionic acid, urease from Jack Beans (type IX), (3-aminopropyl)triethoxysilane, *N*-(3-dimethylaminopropyl)-*N*ˡ-ethylcarbodiimide hydrochloride (EDC), *N*-hydroxysuccinimide (NHS), urea, glucose, creatinine hydrochloride, uric acid, and urease assay kit were purchased from Sigma-Aldrich. Sodium chloride, potassium chloride, sodium dihydrogen phosphate monohydrate, potassium dihydrogen phosphate, disodium hydrogen phosphate heptahydrate, ethanol, chloroform and acetonitrile were provided by Scharlau.

Oligonucleotide (Alexa Fluor 647)-5'-AATGCTAGCTAATCAATCGGG-3' was provided by Thermo Fisher.

General Methods

Powder X-ray diffraction (PXRD), transmission electron microscopy (TEM) , N_2 adsorption-desorption isotherms, UV-visible and fluorescence spectrophotometries, dynamic light scattering (DLS), and elemental analysis were employed for materials characterization. PXRD measurements were performed on a Seifert 3000TT diffractometer using CuK_α radiation. TEM images were acquired using a JEOL TEM-1010 Electron microscope. N_2 adsorption-desorption isotherms were recorded using a Micromeritics TriStar II Plus automated analyzer. UV-visible spectra were recorded with a JASCO V-650 Spectrophotometer. Fluorescence measurements were carried out on a JASCO FP-8500 Spectrophotometer. DLS experiments were performed with a ZetaSizer Nano ZS (Malvern). Elemental analysis was performed using a CE Instrument EA-1110 CHN Elemental Analyzer.

Synthesis of mesoporous silica nanoparticles (MSNPs)

First, 1.00 g (2.74 mmol) of *n*-cetyltrimethylammonium bromide (CTABr) was dissolved in 480 mL of deionized water. Next, 3.5 mL of a 2 $mol{\cdot}L^{-1}$ NaOH were added and the temperature was increased to 80 °C. Then, 5.0 mL of TEOS (22.4 mmol) were added to the stirring solution. The mixture was further stirred for 2 hours at 80 °C which yielded a white precipitate. Afterward, the solid was isolated by centrifugation, washed several times with water and dried at 70 °C overnight. Finally, CTABr was removed by heating the solid at 550 °C (in an oxidant atmosphere for 5 hours) which yielded the starting **MSNPs**.

Synthesis of gold nanoparticles (AuNPs)

Gold nanoparticles were obtained by reduction of Au(III) with citrate. First, 100 mL of $HAuCl_4{\cdot}3H_2O$ solution (1.16×10^{-2} %) were refluxed under magnetic stirring. Then, 1.5 mL of 1% sodium citrate solution were added to induce the formation 20 nm gold nanoparticles. The initially faint yellow colour turned to blue-black and finally to red wine in a few minutes. After 10 minutes refluxing, the colloidal suspension was let to cool at room temperature. This process was repeated four times.

Synthesis of Janus Au-MSNPs

180 mg of **MSNPs** were dispersed in 9 mL of aqueous solution (6.7 % ethanol) and *n*-cetyltrimethylammonium bromide (CTABr) was added for a 1 µM final concentration. The mixture was heated at 75 °C, and then 1 g of paraffin wax was added. Once the paraffin was melted, the mixture was vigorously stirred for 15 minutes using an Ultra-Turrax T-8 homogenizer (IKA). Afterward, the mixture was further stirred for 1 h and 75 °C using a magnetic stirrer. The resulting Pickering emulsion was then cooled to room temperature, mixed with 9 mL of methanol and reacted with 180 µL of (3-mercaptopropyl)trimethoxysilane for 3 hours. The solid was collected by centrifugation and washed twice with methanol. Then, the resulting **MSNPs** were dispersed in 68 mL of methanol and added over 400 mL of the as-synthesized **AuNPs**. The mixture was stirred overnight. Afterward, the solid was isolated by filtration and exhaustively washed with ethanol and with chloroform in order to remove the paraffin. The solid was dried at room temperature and ground. This process finally yielded the Janus **Au-MSNPs**.

Synthesis of S0

A suspension of 30 mg of **Au-MSNPs** in 5 mL of acetonitrile was treated with 50 µL of 3-mercaptopropionic acid in order to functionalize the gold face. The mixture was stirred at room temperature for 1 h. Afterward, nanoparticles were isolated by centrifugation, washed exhaustively with acetonitrile and dried at room temperature overnight. The next day, the solid was suspended in 2.5 mL of acetonitrile and reacted with 60 µL of (3-aminopropyl)triethoxysilane for 5.5 h in order to functionalize the mesoporous face with amino groups. The solid was isolated by centrifugation, washed once with acetonitrile and once with ethanol and was dried at room temperature. This process finally yielded the solid **S0**.

Preparation of S1

In order to prepare the sensing nanodevice, 1 mg of **S0** was dispersed in 450 µL of sodium phosphate buffer (pH 7.5, 50 mM) and mixed with 50 µL of labelled-oligonucleotide solution (100 µM). The solution was placed in a shaker at 37 °C for 30 minutes. Afterward, the excess of oligonucleotide was removed by centrifugation and the solid was mixed with 0.5 mg of urease, 0.35 mg of EDC and 0.35 mg of NHS in sodium phosphate buffer (500 µL, pH 7.5, 50 mM). The sample was placed in a shaker a 4 °C overnight. Finally, the nanoparticles were isolated by centrifugation, washed several times with buffer and kept in the refrigerator until use.

Enzymatic assay

Urease activtiy of **S1** was evaluated using a commercial kit provided by Sigma-Aldrich. It is based on measuring the ammonia produced by the enzymatic reaction using the Berthelot's reagent (an alkaline solution of phenol and hypochlorite) which results in the formation of the colored indophenol blue.[21] First, samples are incubated 10 minutes with a urea solution, followed by stopping the reaction and further incubation for 30 minutes with the Berthelot's reagent. Following the technical procedure, the absorbance at 670 nm for the ammonium standards was measured to obtain the calibration curve showed in Figure SI-6. From the absorbance of indophenol blue obtained by incubation with **S1** (0.01 $mg \cdot mL^{-1}$) or with commercial enzyme (0.2 $\mu g \cdot mL^{-1}$), we calculated their urease activity by applying the formula:

$$Urease\ activity\ \left(\frac{units}{g}\right) = \frac{(A_{670})_{sample} - (A_{670})_{blank}}{Slope \cdot t \cdot C}$$

Where:

t = incubation time of with urea (10 min)

$(A_{670})_{sample}$ = Absorbance value for sample

$(A_{670})_{blank}$ = Absorbance value for assay blank (0.06)

Slope= slope of the calibration line in Figure SI-6 (0.0015 μM^{-1})

C= concentration of the sample.

The determined urease activity for **S1** was 830 U·g^{-1} and for the commercial enzyme was 65333 U·g^{-1}, from which an equivalent amount of 12.7 mg of enzyme per g of **S1**, was calculated.

Sensing experiments

In a typical experiment, refrigerated solutions of **S1** were brought to a concentration of 0.3 mg·mL^{-1} in aqueous solution (PBS, pH 7.5) containing the corresponding amount of urea and were stirred at room temperature (25 °C) in a thermoshaker. Aliquots were taken at scheduled times, centrifuged (2 min) to remove the nanoparticles and then the emission of fluorescent-DNA at 664 nm was measured (λ_{exc} = 649 nm). On the other hand, human blood samples were obtained from a healthy volunteer thanks to the support of our university health centre. Red blood cells were separated from serum by centrifugation (10 min at 11000 rpm) and serum samples were further centrifuged (5 min, 11000 rpm) using Amicon Ultra-05 centrifugal filters units with Ultracel-10 membranes to remove proteins (see Figure SI-7). For analysis, 15 µL of serum spiked with the corresponding amount of urea were added over 135 µL of **S1** aqueous solution (0.3 mg·mL^{-1}). After 10 minutes of incubation, samples were centrifuged to remove the nanoparticles and the emission at 664 nm (λ_{exc} = 649 nm) was measured. Milk samples were also centrifuged (5 min, 11000 rpm) with Amicon Ultra-05 centrifugal filters units with Ultracel-10 membranes to remove turbidity and then 15 µL of sample were added over 135 µL of **S1** aqueous solution and incubated for 10 minutes before measuring the emission spectra.

Acknowledgements

A. Llopis-Lorente is grateful to “La Caixa” Banking Foundation for his PhD fellowship. The authors thank to the Spanish Government (MINECO Projects MAT2015-64139-C4-1, AGL2015-70235-C2-2-R, CTQ2014-58989-P and CTQ2015-

71936-REDT) and the Generalitat Valencia (Project PROMETEOII/2014/047) for support. The Comunidad de Madrid (S2013/MIT-3029, Programme NANOAVANSENS) is also gratefully acknowledged.

7.6 References

1. a) T. D. Ashton, K. A. Jolliffe, F. M. Pfeffer, *Chem. Soc. Rev.* **2015**, *44*, 4547-4595; b) X. Zhou, S. Lee, Z. Xu, J. Yoon, *Chem. Rev.* **2015**, *115*, 7944-8000; c) L. E. Santos-Figueroa, M. E. Moragues, E. Climent, A. Agostini, R. Martínez-Máñez, F. Sancenón, *Chem. Soc. Rev.* **2013**, *42*, 3489-3613; d) M. H. Lee, J. S. Kim, J. L. Sessler, *Chem Soc. Rev.* **2015**, *44*, 4185-4191.
2. a) W. Sun, S. Guo, C. Hu, J. Fan, X. Peng; *Chem. Rev.* **2016**, *116*, 7768-7817; b) E. Garrido, L. Pla, B. Lozano-Torres, S. El Sayed, R. Martínez-Máñez, F. Sancenón, *ChemistryOpen* **2018**, *7*, 401-428.
3. a) D. Wu, A. C. Sedgwick, T. Gunnlaugsson, E. U. Akkaya, J. Yoon, T. D. James, *Chem Soc. Rev.* **2017**, *46*, 7105-7123; b) R. Martínez-Máñez, F. Sancenón, *Chem. Rev.* **2003**, *103*, 4419-4476; c) J. Wu, B. Kwon, W. Liu, E. V. Anslyn, P. Wang, J. Seung-Kim. *Chem. Rev.* **2015**, 115, 7893-7943; d) Y. Ding, W.-H. Zhu, Y. Xie, Chem. Rev. **2017**, *117*, 2203-2256.
4. a) E. Persch, O. Dumele, F. Diederich, *Angew. Chem. Int. Ed.* **2015**, *54*, 3290-3327; b) D. Bray, *Nature* **1995**, *376*, 307-312.
5. a) K. Ariga, D. T. Leong, T. Mori, *Adv. Funct. Mater.* **2018**, *28*, 1702905; b) M. Komiyama, K. Yoshimoto, M. Sisido, K. Ariga, *Bull. Chem. Soc. Jpn.* **2017**, *90*, 967-1004.
6. Y. Yi, L. Sanchez, Y. Gao, Y. Yu, *Analyst* **2016**, *141*, 3526-3539.
7. a) A. Walther, A. H. Müller, *Chem. Rev.* **2013**, *113*, 5194-5261; b) A. Walther, A. H. Müller, *Soft Matter* **2008**, *4*, 663-668.
8. a) Y. Song, S. Chen, *Chem. Asian J.* **2014**, *9*, 418-430; b) A. Sánchez, P. Díez, P. Martínez-Ruiz, R. Villalonga, J. M Pingarrón, *Electrochem. Commun.* **2013**, *30*, 51-54; c) C. Lu, X. Liu, Y. Li, F. Yu, L. Tang, Y. Hu Y. Ying, *ACS Appl. Mater. Interfaces* **2015**, *7*, 15395-15402; d) A. Burns, H. Owiesner, *Chem. Soc. Rev.* **2006**, *35*, 1028-1042; e) K. Aslan, M. Wu, J. Lakowicz, C. D. Geddes, *J. Am. Che. Soc.* **2007**, *129*,1524-1525; S. A. Kalene, S.S. Ashaputre, N. Y. Hebalkar, S. W. Gosavi, D. N. Deobagkar, D. D. Deobagkar, S. K. Kulkarni, *Chem. Phys. Lett.* **2005**, *404*, 136-141; f) Z. Wang, X. Yang, J. Feng, Y. Tang, Y. Jiang, N. He, *Analyst* **2014**, *139*, 6088-6091.
9. G. Dhawan, G. Sumana, B.D. Malthotra, *Biochem. Eng. J.* **2009**, *44*, 42-52.
10. a) T. W. Meyer, T. H. Hoestetter, *N. Engl. J. Med.* **2007**, *13*, 1315-1325; b) A. J. Taylor, P. Vadgama, *Ann. Clin. Biochem.* **1992**, *29*, 245-264; c) M. Singh, N. Verma, A. K. Garg, N. Redhu, *Sens. Actuators B Chem.* **2008**, *134*, 345-351.
11. a) J. Qin, K. Chao, M. S. Kim, *Food Chemistry* **2013**, *138*, 998-1007; b) C. F. Nascimiento, P. M. Santos, E. Rodrigues Pereira-Filho, F. R. P. Rocha, *Food Chemistry* **2017**, *221*, 1232-1244.

12. a) U. B. Trivedia, D. Lakshminarayana, I. L. Kothari, N. G. Patel, H. N. Kapse, K. K. Makhija, P. B. Patel, C. J. Panchal, *Sens. Actuators B Chem.* **2009**, *1*, 140-266; b) W. Butler, J. Calaman, S. Beam, *J. Anim. Sci.* **1996**, *74*, 858–865.
13. a) V. Kumar, R. Mahajan, I. Kaur, K.-Y. Kim, *ACS Appl. Mater. Interfaces* **2017**, *9*, 16813-16823; b) N. S. Nguyen, G. Das, H. H. Yoon, *Biosens. Bioelectron.* **2016**, *77*, 372-377; c) Z. Yang, X. Liu, C. Zhang, B. Liu, *Biosens. Bioelectron.* **2015**, 74, 85-90; d) S. Jakhar, C. S. Pundir, *Biosens. Bioelectron.* **2018**, *100*, 242-250; e) E. Dervisevic, M. Dervisevic, J. K. Nyangwebah, M. Senel, *Sens. Actuators B Chem.* **2017**, *246*, 920-926; f) M. Dervisevic, E. Dervisevic, M. Senel, *Sens. Actuators B Chem.* **2018**, *254*, 93-101; g) T. Alizadeh, M. R. Ganjali, F. Rafiei, *Anal. Chim. Acta* **2017**, *974*, 54-62; h) R. Sha, K. Komori, S. Badhulika, *Electrochim. Acta* **2017**, *233*, 44-51; i) V. Kumar, A. Chopra, S. Arora, S. Yadav, S. Kumar, I. Kaur, *RSC Adv.* **2015**, *5*, 13278-13284; j) S. V. Marchenko, I. S. Kucherenko, A. N. Hereshko, I. V. Pansiuk, O. O. Soldatkin, A. V. El´skaya, A. P. Soldatkin, *Sens. Actuators B Chem.* **2015**, *207*, 981-986; k) P. Kumar, P. R. Lambadi, N. K. Navani, *Biosens. Bioelectron.* **2015**, *72*, 340-347; l) A. W. Zaibudeen, J. Philip, *Sens. Actuators B Chem.* **2018**, *255*, 720-728.
14. R. K. Srivastava, S. Srivastava, T. N. Narayanan, B. D. Mahlotra, R. Vajtai, P. M. Ajayan, A. Srivastava, *ACS Nano* **2012**, *1*, 168-175.
15. a) E. Climent, R. Martínez-Máñez, F. Sancenón, M. D. Marcos, J. Soto, A. Maquieira, P. Amorós, *Angew. Chem.* **2010**, *122*, 7439-7441; b) M. Oroval, C. Coll, A. Bernardos, M. D. Marcos, R. Martínez-Máñez, D. G. Shchukin, F. Sancenón, *ACS Appl. Mater. Interfaces* **2017**, *9*, 11332-11336; c) M. Oroval, E. Climent, C. Coll, R. Eritja, A. Aviñó, M. D. Marcos, F. Sancenón, R. Martínez-Mañez, P. Amorós. *Chem. Commun.* **2013**, *49*, 5480-5482.
16. A. Llopis-Lorente, P. Díez, A. Sánchez, M. D. Marcos, F. Sancenón, P. Martínez-Ruíz, R. Villalonga, R. Martínez-Mañez, *Nat. Commun.* **2017**, *8*, 15511.
17. A. L. Doadrio, J. M. Sánchez-Montero, J. C. Doadrio, A. J. Salinas, M. Vallet-Regí, *Micropor. Mesopor. Mater.* **2014**, *195*, 43-49.
18. V. Balladur, A. Theretz and B. Mandrand, *J. Colloid Interface Sci.*, 1997, **194**, 408.
19. L. Liu, H. Mo, S. Wei, D. Raftery, *Analyst* **2012**, *137*, 595-600.
20. P. S. Francis, S. W. Lewis, K. F. Lim, *Trends Analyt. Chem.* **2002**, *21*, 389-400.
21. Y. Moliner-Martínez, R. Herráez-Hernández, P. Campíns-Falcó, *Anal. Chim. Acta* **2005**, *534*, 327-334.

7.7 Supporting Information

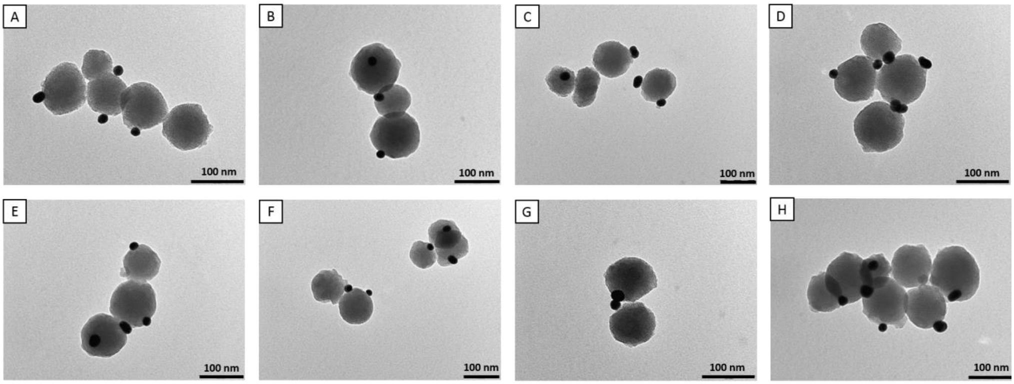

Figure SI-1. Additional TEM images of the Janus **Au-MSNPs**.

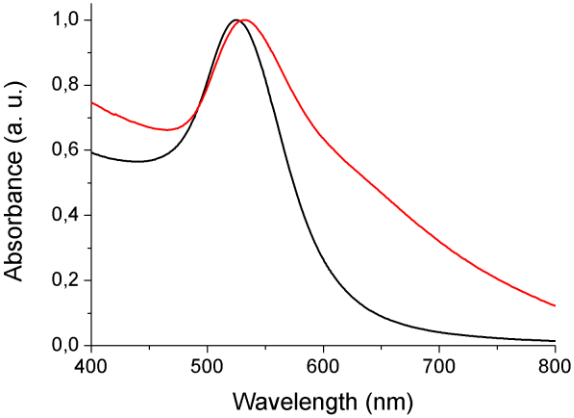

Figure SI-2. Normalized absorbance spectra of the as-synthesized **AuNPs** (black curve) and of Janus **Au-MSNPs** (red curve).

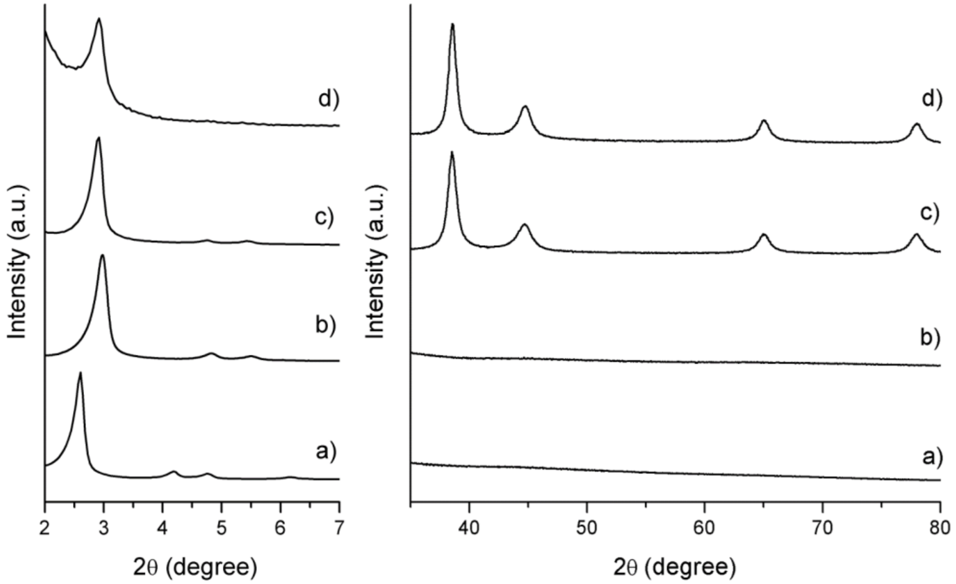

Figure SI-3. Powder X-Ray patterns at low (left) and high (right) angles of: (a) as-synthesised **MSNPs**, (b) calcined **MSNPs**, (c) **Au-MSNPs** and (d) functionalized **S0** nanoparticles.

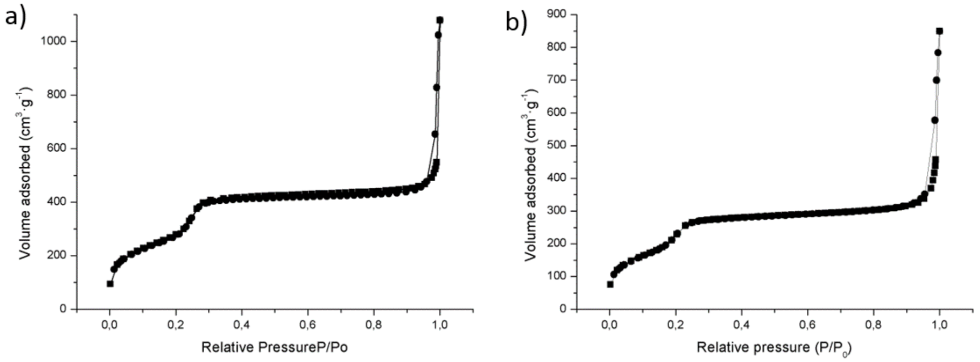

Figure SI-4. N_2 adsorption-desorption isotherms for (a) calcined **MSNPs** and (b) Janus **Au-MSNPs**.

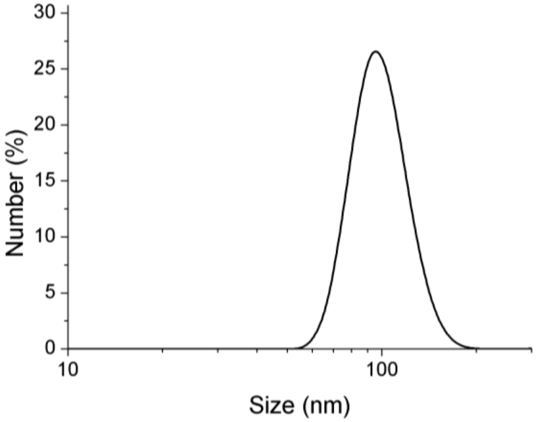

Figure SI-5. Hydrodynamic diameter distribution of the sensing nanodevice **S1** determined by DLS.

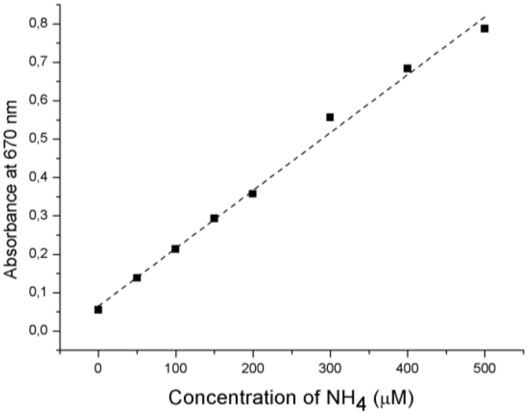

Figure SI-6. Urease activity assay. Absorbance at 670 nm for ammonium standards (calibration curve).

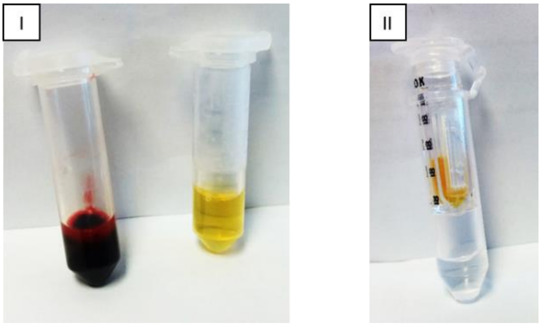

Figure SI-7. Images illustrating the procedure followed for measuring urea in real human blood. First, blood was centrifuged to separate serum (yellow phase) from red blood cells (I). Next, proteins were removed from serum using centrifugal filters giving a colorless solution (II), which was then analyzed.

Table SI-1. Systems for the selective detection of urea recently reported (last three years).

Publication	**Sensor type**	**Application in real matrices**	**LOD**	**Linear range**
This work	Optical (fluorescent)	Blood and milk	0.5 mM	1.25-8.75 mM
P. Kumar *et al*., *Biosens. Bioelectron.*, 2015, **72**, 340	Optical (colorimetric)	Milk	20 mM	20-100 mM
A. W. Zaibudeen and J. Philip, *Sens. Actuators B Chem.*, 2018, **255**, 720	Magneto-Optical	Not shown	0.03, 1.5, or 20 mM depending on the surfactant used	0.05-10, 3-555, or 40-5567 mM depending on the surfactant used
V. Kumar *et al*., *ACS Appl. Mater. Interfaces*, 2017, **9**, 16813	Electrochemical (amperometric)	Not shown	0.83 mM	1.6-15 mM
N. S. Nguyen *et al*., *Biosens. Bioelectron.*, 2016, **77**, 372	Electrochemical (voltammetric)	Urine	5 µM	0.06-0.30 mM
Z. Yang *et al*., *Biosens. Bioelectron.*, 2015, **74**, 85	Piezoelectric	Urine	0.01 µM	0.04-120 µM
S. Jakhar and C. S. Pundir, *Biosens. Bioelectron.*, 2018, **100**, 242	Electrochemical (potentiometric)	Blood	1 µM	2-80 µM
E. Dervisevic *et al*., *Sens. Actuators B Chem.*, 2017, **246**, 920	Electrochemical (amperometric)	Blood	0.05 mM	0.2-1.8 mM
M. Dervisevic *et al*., Sens. Actuators B Chem., 2018, 254, 93	Electrochemical (amperometric)	Blood	0.4 mM	1-20 mM
T. Alizadeh *et al*., *Anal. Chim. Acta*, 2017, **974**, 54	Electrochemical (voltammetric)	Blood and urine	0.05 µM	10^{-5} – 10 mM
R. Sha *et al*., *Electrochim. Acta*, 2017, **233**, 44	Electrochemical (voltammetric)	Milk	6 µM	0.01-0.2 mM
V. Kumar *et al*., *RSC Adv.*, 2015, **5**, 13278	Electrochemical (amperometric)	Not shown	1.6 mM	1.6-13.3 mM
S. V. Marchenko *et al*., *Sens. Actuators B Chem.*, 2015, **207**	Electrochemical (potentiometric)	Blood	0.1 mM	0.5-15 mM

Chapter 8: Conclusions and Perspectives

The development of stimuli-responsive materials and delivery systems is an exciting area of nanotechnology. In this regard, mesoporous silica materials equipped with molecular gates, that can release chemicals or drugs upon application of a certain stimulus, have attracted considerable attention due to their potential application in nanomedicine and sensing. Despite the advances made in the last decade, the design of gated materials that respond to small molecules of biological interest has been less explored compared to other types of stimuli. In this context, this PhD thesis has explored the construction of stimuli-responsive nanodevices based on Janus gold-mesoporous silica nanoparticles that combine enzymes, molecular gates and chromo-fluorogenics species or drugs.

The first chapter of this PhD thesis has been dedicated to introducing concepts and recent developments related with nanotechnology, supramolecular chemistry, mesoporous silica materials, stimuli-responsive gated materials, Janus particles and enzymes.

In the second chapter, the objectives attempted in the following experimental chapters have been stated.

In the third chapter, a nanodevice based on Janus gold-mesoporous silica nanoparticles for controlled release in response to the neurotransmitter acetylcholine has been reported. The design is based on the incorporation of acetylcholinesterase as recognition element on the gold face and a supramolecular complex (between β-cyclodextrin and benzimidazole) as bulky cap on the silica surface. Acetylcholinesterase mediates the transformation of acetylcholine into acetic acid and choline, locally lowering the pH and opening the supramolecular nanovalve. Although the way from these studies to the *in vivo* use of similar nanocarriers remains long and uncertain, the design and development of delivery systems that respond to neurotransmitters could be an interesting tool in the treatment of neurodegenerative disorders and other nervous system diseases.

In the fourth chapter, an enzyme-controlled Janus nanocarrier based on the opening of a thiol-responsive molecular gate has been reported. In particular, the nanodevice is functionalized with disulfide-linked oligo(ethylene glycol) chains on the mesoporous face, whereas the gold face is functionalized with acetylcholinesterase. The enzyme mediates the recognition of acetylthiocholine and the formation of thiocholine as the thiol-bearing molecule. Additionally, it has been showed that the enzymatic activity and, as a result, the payload delivery is tuned by the presence of enzymatic inhibitors. The nanodevice shows an enhanced payload delivery in cancer cells in the presence of acetylthiocholine.

In the fifth chapter, a chemical communication system between enzyme-functionalized Janus nanoparticles has been developed. The system mimics an interactive model of communication, in which the sender sends a message to the receiver, and the receiver then channels a message back to the original sender. Cargo delivery from the first nanoparticle occurs after biunivocal communication with the second nanoparticle, which involves two enzymatic processes and the interchange of two chemical messengers. The conceptual idea of establishing communication between nanodevices opens the opportunity to develop cooperative systems in which different nanoparticles share information and act synergically to perform advanced tasks.

In the sixth chapter, it has been shown that nanocarriers can be programmed to read molecular information from the environment and act accordingly by processing logic tasks. Specifically, nanoparticles with AND or INHIBIT logic behavior have been prepared. AND logic behavior using glucose and NAD^+ as inputs is achieved by incorporating the enzyme GDH on gold-mesoporous silica nanoparticles capped with pH-responsive nanovalves. Furthermore, it has also been shown that two enzymes (GDH and urease) can be combined in a single nanodevice to implement an INHIBIT logic behavior (in which the system is switched off by urea). Remarkably, experiments with cells showed that such nanodevices can make use of intracellular NAD^+ to deliver a cytotoxic drug in the simultaneous presence of glucose.

In the seventh chapter, a new approach for the design of optical probes based on the enzyme-mediated detachment of labelled-reporters has been presented. Based on this idea, a urea nanosensor has been developed using Janus nanoparticles functionalized with fluorescent oligonucleotide strands (attach through electrostatic interactions) on the silica surface and with urease on the gold surface. In the presence of urea, the fluoresecent oligonucleotide is detached due to the enzyme-mediated transformation of urea to ammonia and the subsequent rupture of the electrostatic interactions. From a broad perspective, this general paradigm could be used to develop a variety of nanosensors by selecting other enzymes and reporter molecules attached through labile linkages responsive to common enzymatic subproducts (such as H_3O^+, OH^-, H_2O_2, redox species and nucleophiles).

A general conclusion that can be extracted from this PhD thesis is that the incorporation of enzymes on nanodevices allows to perform certain functions that would be very difficult or impossible to achieve using artificial components. The use of enzymes as functional components can provide gated hybrid nanodevices with high specific recognition capabilities toward selected biomolecules. As illustrative examples, we have presented in this PhD thesis several hybrid nanodevices for sensing, controlled release and chemical communication processes.

As additional future perspectives, the results achieved in this PhD thesis open and encouraged us to pursue new research opportunities and projects. On the one hand, there are plenty of combinations of enzymes and molecular gates that could be tested. In this regard, several delivery and sensing systems responsive to selected molecules of biomedical and environmental interest could be developed. On the other hand, there is the possibility to employ the incorporation of enzymes on nanodevices to introduce self-propulsion capabilities based on the catalytic production of a gas or chemical. This could lead to the development of nanorobots capable of exhibiting autonomous motion, cargo transport and stimuli-responsive delivery. Additionally, nanoreactors could be designed based on nanoparticles loaded with prodrugs and equipped with enzymes for the *in situ* synthesis of drugs in physiological environments. Moreover, an extra direction is to explore the use of the gold surface on Janus nanoparticles to incorporate cell-targeting ligands or to perform SERS or hyperthermia.

It is our hope that the results presented in this PhD thesis will inspire the development of new smart materials with application in different areas such as nanomedicine and sensing.

Gracias a la Obra Social "la Caixa" por concederme
una beca de doctorado.